SYNTHESIS AND ADSORPTIVE PROPERTIES OF METAL-LOADED NANO-SIZED ZINC ZEOLITIC 2-METHYLIMIDAZOLATE FRAMEWORKS (ZIF-8) WITH APPLICATIONS IN HETEROGENEOUS CATALYSIS

A dissertation submitted in accordance with the requirements for the degree

Magister Scientiae

in the

Department of Chemistry

Faculty of Natural and Agricultural Sciences

at the

University of the Free State

by

Chih-Wei Tsai

Supervisor

Dr. E.H.G. Langner

2014

Acknowledgements

I would hereby like to thank all my friends, family and colleagues for their friendship, guidance, motivation amd support throughout my studies. Special appreciation must be made to the following people:

My utmost repsect, acknowledgement and thank you to my promoter (Dr. Ernie Langner) for all your excellent guidance, patience, leadership, diligence and preseverance throughout the duration of my studies and the time devoted to my studies. You pull me throught the toughest time of my project.

I would like to acknowledge the head of the Physical chemistry group Prof. J.C. Swarts for his leadership, guidance and advice during my studies.

I would like to thank Dr. Elizabeth Erasmus for XPS analysis and Dr. Melanie Rademeyer for PXRD measurements.

To my parents, Kuo-Tsung and Feng-Chi Tsai, thank you for your support, guidance, patience and motivation throughout especially during tough times during my studies.

The Physical Chemistry group, thank you all for support, guidance and the good times we spend together not only as fellow work colleagues but as good friends throughout this study.

The Chemistry department and the University of the Free State, thank you for available resources and facilities.

To my friends Alex Huang and Uwe Siegert, for reading the dissertation and help with language and grammar.

The National Research Foundation and the University of the Free State, thank you for the financial support, without it I would not have achieve anything.

Table of Contents.

Table of Contents

Opsomming

List of Abbreviations

acac	Acetylacetonate
ASAP	Accelerated Surface Area and Porosity
BET	Brunauer-Emett-Teller
CCDC	Cambridge Crystallographic Data Centre
CLD	Chemical Liquid Deposition
CTAB	Cetyltrimethylammonium bromide
CVD	Chemical Vapour Deposition
DEF	*N*,*N*-Diethylformamide
DMF	*N*,*N*-Dimethylformamide
EDS	Energy-dispersive X-ray Spectroscopy
eV	Electron Volts
FcCHO	Ferrocenecarboxaldehyde
FTIR	Fourier Transform Infrared
ICP-OES	Inductively Coupled Plasma – Optical emission spectrometry
IM	Imidazolate
IMes.HCl	1,3-bis-(2,4,6-trimethylphenyl)imidazole-2-ylidene
Ir(COD)(MeCp)	(methylcyclopentadienyl)(1,5-cyclooctadiene)iridium(I))
MeIM	2-methylimidazolate
MeOH	Methanol
MIL	Matériaux de l'Institut Lavoisier
MOF	Metal Organic Framework
MS	Mass Spectrometry
nBuLi	*n*-Butyllithium
NMR	Nuclear Magnetic Resonance
nZIF-8	Nanoparticles Zeolitic Imidazolate Framework 8
OAc	Acetate
PhIM	Benzimidazolate
PSM	Post Synthetic Modification
PXRD	Powder X-ray Diffraction
SALE	Solvent Assisted Ligand Exchange

List of Abbreviations

SAXS/WAXS	Small Angle and Wide Angle X-ray Scattering
SEM	Scanning Electron Microscopy
SOD	Sodalite
STP	Standard Temperature Pressure
TEA	Triethylamine
TEM	Transmission Electron Microscopy
TGA	Thermal Gravimetric Analysis
THF	Tetrahydrofuran
TOF	Turnover Frequency
XPS	X-ray Photoelectron Spectroscopy

1 Introduction

1.1 Introduction

Microporous and mesoporous materials contain pores with diameters of less than 2 nm and 2 to 50 nm respectively. Aluminosilicates are examples of such materials, consisting of silicon, aluminium and oxygen. Since the discovery of zeolites or crystalline aluminosilicates, they have been widely used extensively in many industrial processes as catalyst or heterogeneous catalyst support, in gas separation, water purification, ion exchange, medicine and agriculture. There are over 40 different types of zeolites from both natural and synthetic origin. The discovery of zeolites sparked interest in developing new microporous materials and in the modification or improvement of existing materials, en route to catalyst regeneration or prevent agglomeration and sintering of metals on the zeolites.

With this aside, the high demand for porous materials has led to the development of Metal-Organic Frameworks or MOFs, coordination polymers with unique porous structures and crystalline properties. MOFs are hybrid materials formed during the crystallization of transition metal clusters and functionalized organic ligands coordinating to form one, two and three dimensional porous rigid structures.[1] MOF synthesis only started in the early 1990s but has since then greatly increased to over 6000 known MOF structures in 2010. The large number of possible metal centre and organic ligand combinations resulted in MOFs with surface areas from 1000 to 10000 $m^2 g^{-1}$, much larger than for zeolites and activated carbon. Generally MOFs exhibit high chemical and thermal stability, with the ability to undergo post synthetic modification by solid state chemistry on the organic ligands within the MOF, a procedure not possible with zeolites. MOFs have been investigated as heterogeneous catalysts or as supports for metal particles and organic moieties.[2] MOF based catalysts may be used to improve selectivity during reactions with multiple products or reduce the formation of side-products.[3]

The main focus of this study is on Zeolitic Imidazolate Frameworks (ZIFs) which were first reported in 2006, and represented a new subclass of porous metal organic frameworks. ZIF materials have a unique bonding angle of 145° between the metal and the imidazolate linker (M-Im-M angle), which is similar to the Si-O-Si angle of zeolites.[4] Therefore, the structural

classifications of ZIFs are based on that of the zeolites.Various ZIFs (e.g. ZIF-8) can be synthesized in both micro- and nano-sized particles. This study will focus on the synthesis of nano ZIF-8, aiming at its possible application in Nanotechnology. Nanotechnology is fast moving towards potential application in industry because of the unique properties of nano-sized materials when compared to their microsized analogues. Nanotechnology and nanoparticles are being investigated in fields like nanomedicine, electronics and nano engineering. Although micro-sized ZIF-8 is available commercially as Basolite Z1200 by BASF, ZIF-8 nanocrystals (nZIF-8) was only recently synthesized, and will be the main focus in this study.[5]

ZIF-8 has a porous polymeric network structure made up from zinc metal centres tetrahedrally coordinated to 2-methylimidazole ligands, giving a SOD topology with a surface area of ~1600 $m^2 g^{-1}$ and a six-ring pore aperture of 3.4 Å. ZIF-8 has a high thermal stability up to 400 °C.[4] Over the years micro-sized ZIF-8 has been reported as having impressive potential applications in gas storage or separation, drug delivery, chemical sensing and catalysis.[4,6] ZIF-8 displays good mechanical behaviour and showed excellent anti-wear results as a lubricant additive to oil.[7] The surface of ZIF-8 contains Lewis acid and basic active sites for catalysis of reactions like Knoevenagel condensation and transesterification.[8] Control of particle size and particle size distribution is important since it will influence the external surface area available for catalysis as well as the active site density. Surfactants and polymers have been used as additives to assist in particle size control during ZIF-8 synthesis. In attempts to improve the catalytic properties of ZIF-8 various techniques such as chemical vapour deposition (CVD) and chemical liquid deposition (CLD) have been implemented to load the pores of ZIF-8 with metal nanoparticles. The cage structure prevents the metal nanoparticles from being leached out or to agglomerate easily in repeated catalytic cycles. Another technique to chemically enhance the ZIF-8 structure is by solvent assisted ligand exchange (SALE) where the 2-methylimdazole ligand of ZIF-8 can be exchanged by imidazole without changing the SOD topology of the ZIF. After the exchange, the imidazolate ligands can undergo post synthetic modification (PSM) by lithiation to form carbene-like moieties on the ZIF-8 surface for its use as a potential catalyst.[3]

1.2 Aims of this Study

With the above background, this study will focus on the following:

1) Catalytic activity of ZIF-8 nanoparticles occurs on their external surface. Smaller crystallite sizes may thus result in increased external surface area and subsequently to higher catalytic activity. The effect of synthesis temperature on particle size and size

distribution will be investigated. A preliminary catalytic study with nZIF-8 as catalyst in the Knoevenagel condensation reaction between malononitrile and ferrocene-carboxaldehyde will be done, to determine catalytic activity of the nano-sized ZIF-8 compared to that of the micro-sized particles.

2) Since ZIF-8 is a porous material it may be impregnated by metal salts in solution. Upon reduction of these metal salts after impregnation, metal nanoparticles may be deposited inside the pores of ZIF-8. The impregnation of nZIF-8 with silver and palladium precursors by chemical liquid deposition, followed by reduction, will be attempted. The products will be characterized by X-ray photoelectron spectroscopy (XPS) and inductively coupled plasma – optical emission spectrometry (ICP-OES).
3) ZIF-8 may undergo solvent assisted ligand exchange (SALE) with imidazole in solution. The effect of exchange time on the structure and chemical composition of the resultant products (SALEM-2) will be investigated.
4) The imidazolate ligand of the SALEM-2 products possesses a labile hydrogen atom bound to the C2 carbon atom in the 5-membered ring. An attempt will be made to lithiate this position on the ring in order to activate it for further functionalization by alkyl halide moieties.
5) Characterization of the synthesized nZIF-8, Metal@ZIF-8 and SALE products of nZIF-8 using different methods such as infrared spectroscopy, transmission electron microscopy (TEM), powder X-ray diffraction (PXRD) and nuclear magnetic resonance (NMR) spectroscopy.
6) Porosity analysis on nZIF-8, Metal@nZIF-8 and SALE product of nZIF-8 can be used to determine their BET surface areas and t-plot external surface areas.
7) Thermal analysis will be performed on all ZIF-8 derivatives to determine their thermal stability.

---

[1] S. L. James, *Chem. Soc. Rev.*, 2003, **32**, 276-288.
[2] H. Furukawa, K. E. Cordova, M. O'Keeffe and O. M. Yaghi, *Science*, 2013, **341**, 1230444-1.
[3] D. Farrusseng, S. Aguado and C. Pinel, *Angew. Chem. Int. Ed.*, 2009, **48**, 7502-7513.
[4] K. S. Park, Z. Ni, A. P. Cote, J. Yong, R. Huang, F. J. Uribe-Romo, H. K. Chae, M. O'Keeffe, O. M. Yaghi, *PNAS*, 2006, **103**, 10186-10191.
[5] D. Farrusseng, *Metal-Organic Framworks Applications from Catalysis to Gas Storage (WILEY-VCH)*, 2011, 344-346.
[6] G. Lu and J. T. Hupp, *J. Am. Chem. Soc.*, 2010, **132**, 7832-7833.
[7] Q. Shi, Z. Chen, Z. Song, J. Li and J. Dong, *Angew. Chem. Int. Ed.*, 2011, **50**, 672-675.
[8] P. Valvekens, F. Vermoortele and D. De Vos, *Catal. Sci. Technol.*, 2013, **3**, 1435.

INTRODUCTION

2 Literature Survey

2.1 Introduction

Since the discovery of crystalline microporous materials such as zeolites, it has been largely used in industry for gas separation, petroleum cracking, ion exchange, water purification, drug delivery and catalysis.[1,2] The use of zeolitic catalysts greatly increased the conversion and yield during fuel synthesis in comparison with existing clay catalysts. A decrease in coke formation was observed but also a low octane count. Y-zeolites are the most frequently used with some of the aluminium removed from the framework.[3] Recently there was an interest to develop new porous coordination polymers, also known as metal organic frameworks (MOFs), using easily accessible metal ions and functionalizable organic linkers to make up the integral part of the framework that can mimic the topologies of zeolites to further improve or match properties (chemical resistance, pore size , thermal stability).[3,4] MOFs have great capability to be used in catalysis and can be used as Lewis acid catalysts, Brønsted acid catalysts, basic catalysts, enantioselective catalysts or C-C bond formation and polymerization catalysts. Nano-metallic particles and organometallic moieties supported on MOFs may also act as catalysts.[5] The zeolitic imidazolate frameworks (ZIFs) is a subclass of metal organic frameworks (MOFs) with unique properties from both MOFs and zeolites combined (**Figure 2.1**, p **6**). These properties include very high surface area monodisperse micropores, structural flexibility and tuneable structures.[6] ZIFs consist of bivalent metal (M^{2+}) cations (usually zinc or cobalt) linked together by imidazolate anions in a tetrahedral manner around the metal centre. Although a number of new Fe(II), Co(II), Cu(II) and Zn(II) compounds where synthesized to have similar zeolite-like tetrahedral nets, many of the ZIFs are nonporous (high density) with low-symmetry structures and only a few such as ZIF-8 were found be porous.[2]

ZIF structures adapts to topologies analogous to those of the zeolites since the 145° angle between the nitrogen's on the 1,3-positions of the imidazolate anion ring and the metal centre mimics the Si-O-Si angle found in zeolites (**Scheme 2.1**, p **6**). The organic linkers of the ZIF give cages or channels rather than the silicate oxide surfaces found in conventional zeolites.[2] Within 5 years since 2010 more than 90 ZIF compounds have been synthesized compared to over 190 zeolites.[1,7]

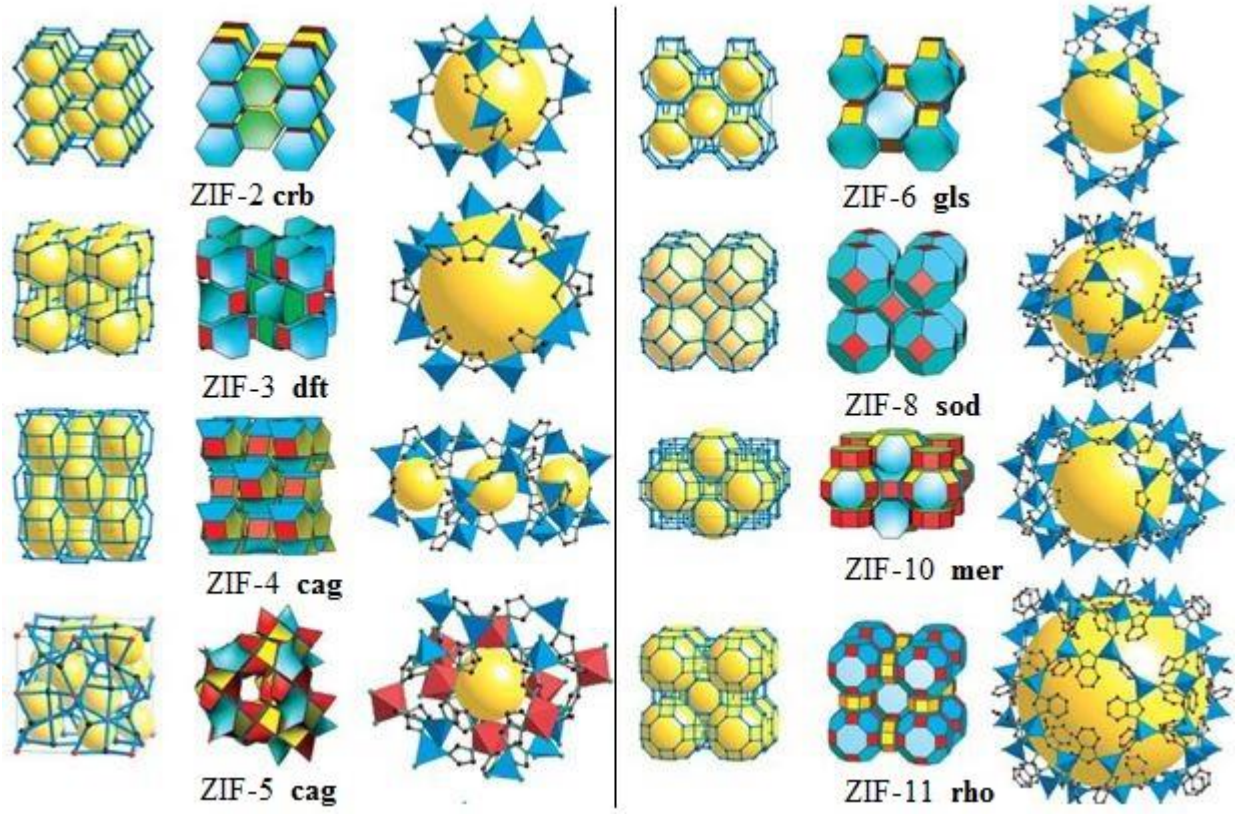

Figure 2.1 Single crystal X-ray structures of selected ZIFs: The network topology is shown as a stick diagram (left) and with tiling (center). The largest cage is represented by a yellow ball (right), with ZnN_4 tetrahedra shown in blue and, octahedra for ZIF-5, InN6 shown in red. H atoms are omitted for clarity.[2] (Reprinted (adapted) with permission from K. S. Park, Z. Ni, A. P. Cote, J. Yong, R. Huang, F. J. Uribe-Romo, H. K. Chae, M. O'Keeffe, O. M. Yaghi, PNAS, 2006, **103**, 10186-10191. Copyright (2006) PNAS.)

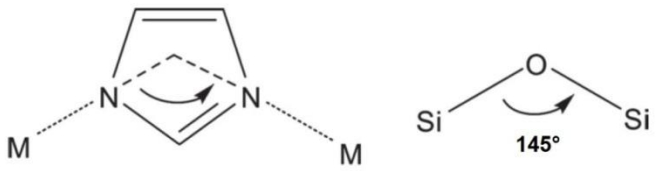

Scheme 2.1 Bridging angles 1) between the metal center and imidazole ligand in ZIFs 2) between Silicon and oxygen in zeolites.[2] (Reprinted (adapted) with permission from K. S. Park, Z. Ni, A. P. Cote, J. Yong, R. Huang, F. J. Uribe-Romo, H. K. Chae, M. O'Keeffe, O. M. Yaghi, PNAS, 2006, **103**, 10186-10191. Copyright (2006) PNAS.)

Recent studies in 2007 by Wu *et al.* showed that by using neutron powder diffraction and computational calculations that the strongest attraction site of the ZIF is on the imidazole organic linker itself (**Figure 2.2**, p **7**) rather than on the tetrahedral ZnN_4 triangular faces.[8] The hydrogen adsorbs mainly on the C=C bond and on both sides of the organic linker and then form secondary adsorption sites in the pore channel.[9]

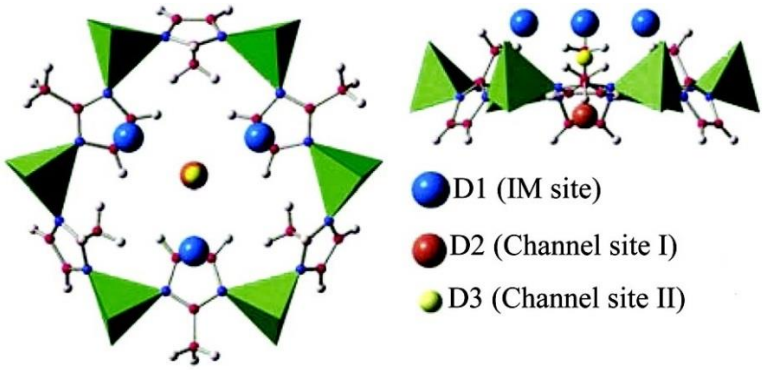

Figure 2.2 Hydrogen adsorption sites on the 2-methylimidazole of ZIF-8 obtained from Fourier difference analysis. Hydrogen atoms represented by blue (D1), red (D2) and green (D3) balls. Zinc metal tetrahedral coordination is represented by the green pyramids.[8] (Reprinted (adapted) with permission from H. Wu, W. Zhou, T. Yildirim, *J. Am. Chem. Soc.*, 2007, **129**, 5314-5315. Copyright (2007) American Chemical Society.)

2.2 History and Synthesis

To the best of our knowledge the first twelve micro sized Zeolitic imidazolate framework series from 1 to 12 (**Table 2.1**, p **9**) was synthesized in 2006 by Park *et al.*, but the first $Zn(im)_2$ crystalline polymeric structure was synthesized in the 1980s.[2,7] The synthesis was performed using solvothermal methods by combining the required hydrated metal salt or complex and a suitable imidazole linker. The syntheses were performed in an amide solvent such as *N,N*-Diethylformamide (DEF) or *N,N*-Dimethylformamide (DMF) at temperature close to 150°C. The ZIF product was easily isolated by centrifugation or filtration after 48-96 hours.[2] Under these conditions the deprotonation of the imidazole was achieved by the amines obtained from the thermal degradation of the solvent and during the cooling process crystals are obtained in moderate to high yields.[1] The concentration of the metal ions, organic linkers and the temperature plays an important role to synthesize monocrystalline materials. The organic linker is expected to play a secondary role in directing the topology. Therefore a large selection of imidazole derivatives, to list a few in (**Figure 2.3**, p **8**), was used to synthesize ZIFs. In some cases only small scale synthetic reactions with yields sufficient for single crystal analysis was

possible.[2,1,7] The SOD geometry of ZIF-8 is an exception amongst other ZIFs because the SOD geometry is found to be less stable amongst other high end geometries in the $Zn(im)_2$ polymorphs that has been synthesized. The density of ZIF-8 is substantially less than most of the scalable and non-scalable ZIFs or polymorphs. Therefore to synthesize SOD geometry form of $Zn(im)_2$ polymorphs or ZIFs is most unlikely to happen with direct solvothermal, ionothermal or similar methods.[7]

The ZIF products were characterized with PXRD as well as single crystal X-ray diffraction.[1] Utilizing bulky substituents leads to large cages or structures and it can also lead to unstable or metastable open structures which may be blocked, for example ZIF-20 with a purine ligand have pores of 2.8 Å that not even molecular nitrogen can access, or lead to nonporous materials.[7,10] It is also possible to synthesise ZIFs from mixing the linkers to form single phase materials and more than 15 mixed linker (heterolink) structures has been reported.[1] For the case of ZIF-5 two different metals namely zinc and indium can be mixed to synthesize ZIFs with octahedral and tetrahedral coordination environments which has the same topology as the (4,6)-coordinated gar net structure found in $Ca_3Al_2Si_3O_{12}$.[1,2] These structures can become very complex, for example ZIF-100, synthesized with linker 5-chlorobenzimidazole (cbIm), of which the unit cell is a giant cage with 264 vertices comprising of 7524 atoms.

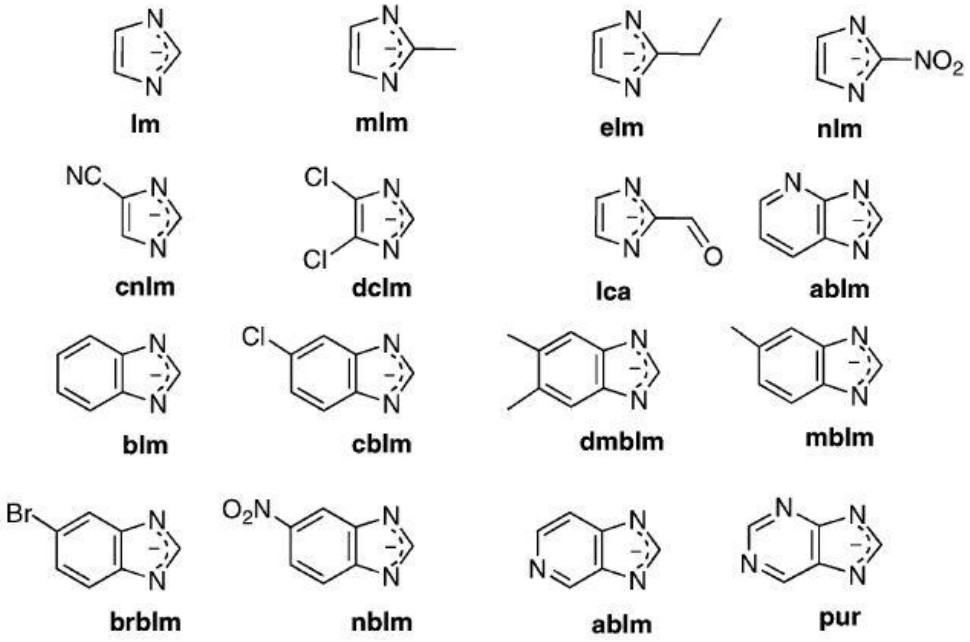

Figure 2.3 Examples of imidazole linkers used to synthesize ZIFs.[1] (Reprinted (adapted) with permission from A. Phan, C.J. Doonan, F. J. Uribe-Romo, C. B. Knobler, M. O'Keeffe, O. M. Yaghi, *Acc. Chem. Res.*, 2009, 43, 58-67. Copyright (2009) American Chemical Society.)

Table 2.1 List of ZIF compounds: their composition, structure and net parameters.[2]

ZIF-n	Composition	Net*	Zeolite	d,§ Å	N¶
ZIF-1	$Zn(IM)_2$	crb	BCT	6.94	12
ZIF-2	$Zn(IM)_2$	crrb	BCT	6.00	12
ZIF-3	$Zn(IM)_2$	dft	DFT	8.02	16
ZIF-4	$Zn(IM)_2$	cag	-	2.04	20
ZIF-5	$In_2Zn_3(IM)_{12}$	gar	-	3.03	20
ZIF-6	$Zn(IM)_2$	gls	GIS	8.80	20
ZIF-7	$Zn(PhIM)_2$	sad	SOD	4.31	24
ZIF-8	$Zn(MeIM)_2$	sad	SOD	11.60	24
ZIF-9	$Co(PhIM)_2$	sad	SOD	4.31	24
ZIF-10	$Zn(IM)_2$	mer	MER	12.12	24
ZIF-11	$Zn(PhIM)_2$	rho	RHO	14.64	48
ZIF-12	$Co(PhIM)_2$	rho	RHO	14.64	48

*Definition of the three letter abbreviation, see Reticular Chemistry Structure Resource (http://okeeffe-ws1.la.asu.edu/RCSR/home.htm).

§d is diameter of largest sphere that will fit in the framework.

¶ N is number of vertices of the largest cage.

The largest sphere to fit in the cavity of the ZIF-8 is 11.6 Å, shown in **Table 2.1**, and illustrated (**Figure 2.4**, p **10**). All the ZIFs from ZIF-1 to ZIF12 have zeolite topologies except for ZIF-4 and ZIF-5, with ZIF-8 having a SOD topology (**Table 2.1**). The ZIFs are microporous with an average cavity width of less than 20 Å.[3] The largest pore aperture diameter for ZIF-8 was reported to be 3.4 Å for the 6 membered ring (**Figure 2.4**, p **10**), much less than Y zeolites with a micropore of 8 Å.[3,2] Interestingly the pore sizes of the ZIF-8 is approximately twice as large as that of its zeolite counterpart, due to the larger imidazole linking unit. Although ZIFs are not as flexible as other MOFs (MIL-53) the ZIF-8 aperture is found to have a high degree of flexibility and is able to open up to 5.8 Å as compared to the rigid zeolites.[11] The position of the zinc nodes in the framework is quite rigid but rotation or transitional tilt of the imidazole linkers on the metal-metal axis, thus opening the aperture size by a factor of almost 2, allowing larger molecules such as methane (3.80 Å) and nitrogen (3.60 Å) to diffuse or be adsorbed.[11,12,13] The pores of ZIF-8 can sustain very high pressures up to 1.47 GPa and it was found that the pore volume increase with high pressures takes place by reorientation of the imidazole ligand.[14]

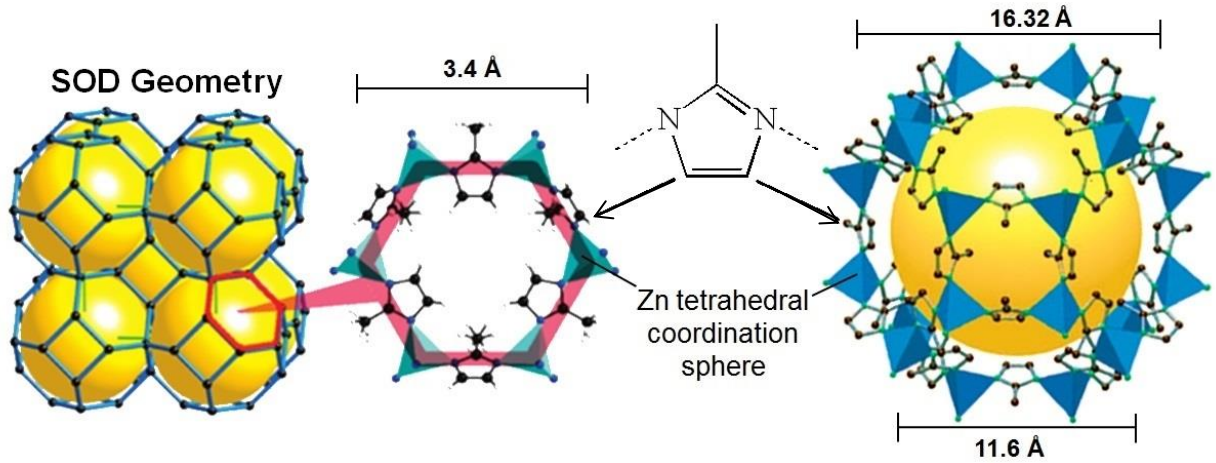

Figure 2.4 The SOD geometry of ZIF-8 showing the 3.4 Å pore aperture of the 6 membered ring, as well as the 11.6 Å pore volume (yellow sphere) and 16.3 Å unit cell size. Zinc tetrahedral coordination sphere (blue) and the organic linker (black).[2,15] (Reprinted (adapted) with permission from K. S. Park, Z. Ni, A. P. Cote, J. Yong, R. Huang, F. J. Uribe-Romo, H. K. Chae, M. O'Keeffe, O. M. Yaghi, PNAS, 2006, 103, 10186-10191 and Copyright (2006) PNAS.). (Reprinted (adapted) with permission from H. Bux, F. Liang, Y. Li, J. Cravillon, M. Wiebcke and J. Caro, *J. Am. Chem. Soc*., 2009, **131**, 16000-16001. Copyright (2009) American Chemical Society.)

Various methods have been used to synthesize ZIF-8. Seoane *et al.* synthesized a series of ZIFs by ultrasonification in which the cavitation of the liquid medium provides high temperatures and pressures. The PXRD pattern of ZIF-8 synthesized with ultrasounds up to 12 hours corresponds to that of the ZIF-8 from solvothermal synthesis. However, from the SEM pictures it was found that as the sonocrystallization time increases, the particle size increases with a narrow particle size distribution, due to the promotion of the nucleation process by ultrasound.[16] ZIF-8 is relatively stable with 5 minutes of ultrasonification, but after 10 minutes of ultrasonification Ostwald ripening led to the formation of larger particles, while maintaining crystallinity and porosity.[17] In 2013 Cho *et al.* synthesized micro-sized ZIF-8 using pH-adjusted sonocrystallization under achieving a yield of 85 %. Different ratios of triethylamine and NaOH were investigated. This yield was reached at a pH of 9.0 resulting in particles with an average size of 200 nm, after increasing the concentration of Zn^{2+} in the sonochemical method.[18] After the addition of ammonium hydroxide with a nonionic triblock polymer (Pluronic) to the reaction mixture in aqueous medium, ZIF-8 was produced with 98 % yield and particle sizes of 200 to 400 nm.[19] Joaristi *et al.* in 2012 obtained ZIF-8 with a particle size of <1 µm *via* anodic dissolution in an electrochemical cell.[20] Microwave assisted heating has also been used to

synthesize ZIF-8 with particle size of 300 μm.[15] Modified liquid-assisted mechanochemistry with the use of ZnO as a zinc source can be used to produce ZIF-8 with the SOD topology. A rapid reaction between 30 to 60 minutes gave quantitative yields with ammonium salts assisting the formation of ZIF-8 without a liquid. Later Tanaka and Beldon reported that solvent and salt free mechanochemical dry synthesis of ZIF-8 yield core-shell structures with an approximate depth of 10 nm below the ZnO crystals with overall particle size of 30 to 150 nm was obtained.[21]

A nanoparticle is defined as a structure with a size between 1 to 100 nm. To the best of our knowledge the first nano-sized nZIF-8 was synthesized by Cravillon *et al.* by rapid room-temperature colloidal chemistry, using a methanol solution with ratio 1:8:700 for Zn^{2+}, 2-methylimidazole and methanol respectively. Other polar solvents such as DMF may also be used to synthesis nanoparticles of ZIF-8. Using XRD peak broadening a particles size of 46 nm was determined and with SEM and HRTEM a size of 40 nm (**Figure 2.5**, p **11**). Lattice fringes of 1.2 nm can be observed on the HRTEM image accounting for the (110) planes. A ζ potential of +55 mV was determined for the nZIF-8 suspension in methanol.[22]

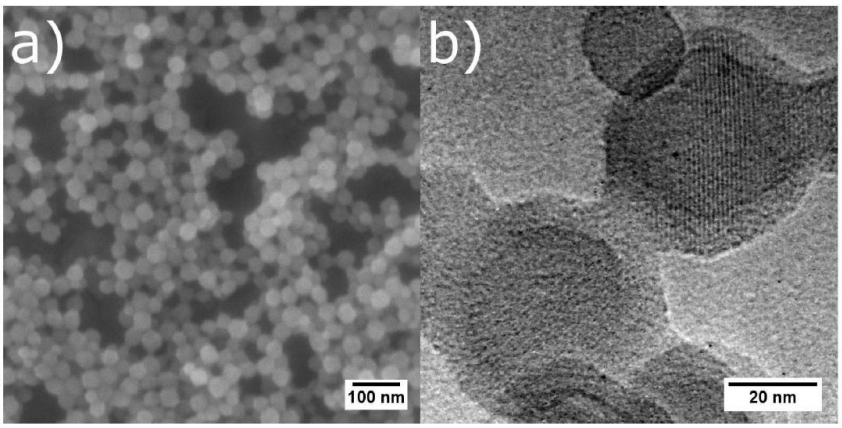

Figure 2.5 nZIF-8 synthesized in methanol a) SEM image b) HRTEM image.[22] (Reprinted (adapted) with permission from J. Cravillon, S. Münzer, K. Huber and M. Wiebcke, *Chem. Mater.*, 2009, **21**, 1410-1412. Copyright (2009) American Chemical Society.)

In 2011 Pan *et al.* were the first to successfully synthesize nZIF-8 in an aqueous medium. The nZIF-8 was synthesized with a molar ratio of Zn^{2+}: 2-methylimidazole: H_2O = 1:70:1238 and performed at room temperature. After 5 min the nZIF-8 was isolated with 80 % yield. A particle size of 70 nm was calculated from the Scherrer equation and TEM measurements estimated the size to be 85 nm. When the 2-methylimidazole ratio was increased from 70 to 200, the particle size decreased to 50 nm.[23] However, aqueous system requires over 40 time excess of imidazole

to zinc in order to synthesize pure phase ZIF-8 without any zinc hydroxide compounds by-products as compared to organic solvents.[24]

Recently in 2013 Marquez *et al.* and Carné-Sánchez *et al.* propose a spray drying/EISA (Evaporated Induced Self Assembly) technique with methanol and water respectively, a cheap and environmentally friendly method to synthesize nZIF-8 with a particle size ~100 nm.[25]

2.3 Structure of ZIF-8

2.3.1 Crystallographic Characterization of ZIF-8

The use of single crystal X-ray diffraction (XRD) and powder X-ray diffraction (PXRD) is one of the most important characterization techniques when characterizing ZIFs. These techniques serve as ways to establish the product's fingerprint, the topology and structure of the ZIFs, as well as assisting in the detection of impurities during synthesis. Park *et al.* was the first to grow ZIF crystals for single crystal X-ray diffraction. The presence of the organic ligand such as imidazole or 2-methylimidazole, in some cases, lowers the space group symmetry of the ZIF compared to zeolites but the net from the linking of the metal atom nodes with the organic linkers matches that of the zeolites. Crystallographic detail of the ZIF-8 structure can be found in (**Appendix C**).[2,26]

PXRD patterns (**Figure 2.6**, p **13**) was obtained for the as-synthesized ZIF-8. The simulated PXRD pattern was determined by using the single crystal data. The comparison shows that the peak positions from both patterns are very similar to one another and that the synthesized bulk ZIF-8 has the same SOD geometry as the single crystal. Although the positions are slightly deviated this is due to the fact that the single crystal was measured at cryogenic temperatures and the PXRD at room temperature.[2]

The nano crystallite size of nanoparticles smaller than 100 nm can be theoretically calculated by the peak broadening of the PXRD of nZIF-8 (**Figure 2.7**, p **13**) using the Scherrer equation (1) developed by Paul Scherrer in 1918.

$$D = \frac{K\lambda}{\beta \cos\theta} \quad (1)$$

Where D = particle diameter, K = the shape factor a typical value of 0.9, λ = X-ray wavelength, β = line broadening at half the maximum intensity (FWHM) and θ = Bragg angle.[27]

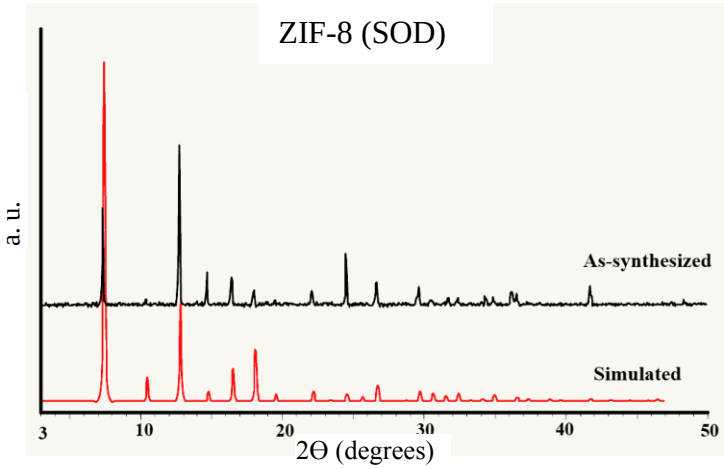

Figure 2.6 PXRD scans of as-synthesized (top) and simulated (bottom) ZIF-8.[2] (Reprinted (adapted) with permission from K. S. Park, Z. Ni, A. P. Cote, J. Yong, R. Huang, F. J. Uribe-Romo, H. K. Chae, M. O'Keeffe, O. M. Yaghi, *PNAS*, 2006, **103**, 10186-10191. Copyright (2006) PNAS.)

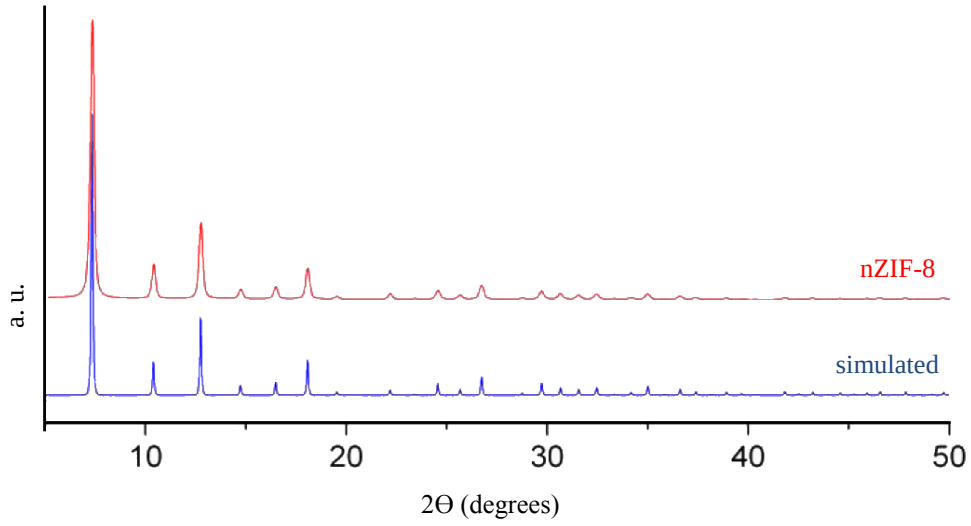

Figure 2.7 PXRD with peak broadening of nZIF-8 (red) compared to simulated ZIF-8 (blue).[22] (Reprinted (adapted) with permission from J. Cravillon, S. Münzer, K. Huber and M. Wiebcke, Chem. Mater., 2009, **21**, 1410-1412. Copyright (2009) American Chemical Society.)

In this thesis PXRD will mainly be used as a tool to characterize the ZIF-8 structure and to calculate the particle size of nanoparticles.

2.3.2 Infrared Spectroscopy of ZIF-8

Vasconcelos *et al.* and Hu *et al.* were able to identify the peaks in the infrared spectrum which is associated to the ligand and Zn-N bonds of ZIF-8, correlating well to the spectrum obtained by K.S. Park (see **Figure 2.8**, p **14**).[2,28,29]

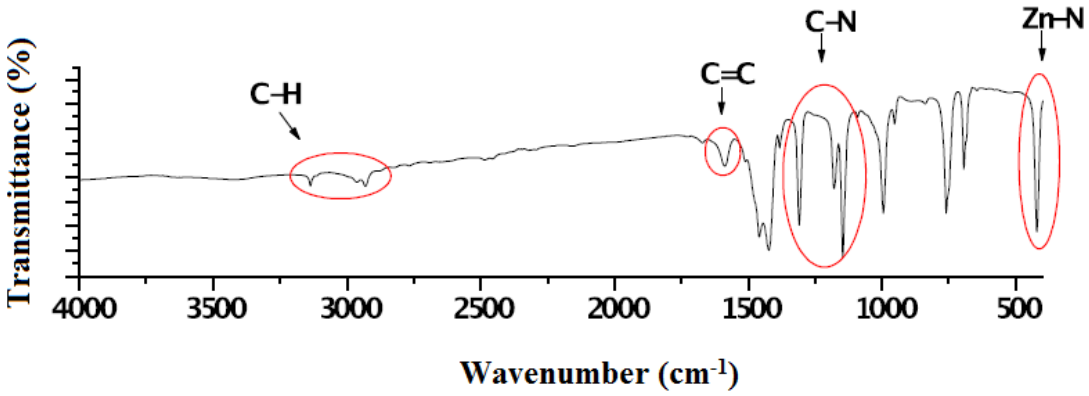

Figure 2.8 Infrared spectrum of ZIF-8.[28] (Reprinted (adapted) with permission from I. B. Vasconcelos, T. G. da Silva, G. C. G. Militão, T. A. Soares, N. M. Rodrigues, M. O. Rodrigues, N. B. da Costa Jr., R. O. Freire and S. A. Junior, *RSC Adv.*, 2012, **2**, 9437-9442. Copyright (2012) The Royal Society of Chemistry.)

The infrared spectrum of ZIF-8 shows two bands at 3135 and 2928 cm^{-1} which is the stretching frequencies for the aromatic C-H and the aliphatic C-H bonds respectively, and the peak at 1606 cm^{-1} is related to the C=C stretch. The peaks found between 1100 and 1400 cm^{-1} represents the C-N adsorption bands. The peaks found between 900 to 1350 cm^{-1} represents the in plane bending of the ring, and those below 800 cm^{-1} is for the out of plane bending. The Zn-N stretching band is observed at 421 cm^{-1}. [2,2829,30]

2.3.3 Porosity of ZIF-8

ZIF-8 porosity was first characterized by the gas-sorption measurements of Park *et al.* The type 1 (**Figure 2.9**, p **15**) isotherm proved that ZIF-8 is microporous with a Langmuir surface area of 1810 $m^2 g^{-1}$, a Brunauer-Emett-Teller (BET) surface area of 1630 $m^2 g^{-1}$ and a micropore volume of 0.636 $cm^3 g^{-1}$. The calculated surface area of 1947 $m^2 g^{-1}$ and micropore volume of 0.663 $cm^3 g^{-1}$ obtained by single crystal X-ray analysis, both correspond to the experimental results.[2] The surface area obtained greatly surpasses the surface area found in zeolites with similar geometry. Although many ZIFs were synthesized, only a few are porous. ZIF-11, with the benzimidazole

organic linker, was found to be non-porous to nitrogen because the pore aperture for ZIF-11 is only 3.0 Å compared to the kinetic diameter of nitrogen, reported to be 3.6 Å. With these results in mind the pore aperture size can be controlled by using different organic linkers, thus restricting the adsorption of molecules in the ZIF particle. The aperture of ZIF-8 as well as ZIF-11 was big enough for hydrogen to be taken up. Both ZIF-8 and ZIF-11 shows reversibility to hydrogen adsorption (**Figure 2.9**, p **15**). ZIF-11 was able to take up more hydrogen than ZIF-8 because of the unique cage interior containing benzene rings which is more favourable towards hydrogen adsorption. When the pressure reaches 760 torr the amount of hydrogen adsorbed by ZIF-8 (145 cm^3 g^{-1} at STP) is very close to the amount adsorbed by ZIF-11 (154 cm^3 g^{-1} at STP), because ZIF-8 has a much higher surface area and micropore volume.[2]

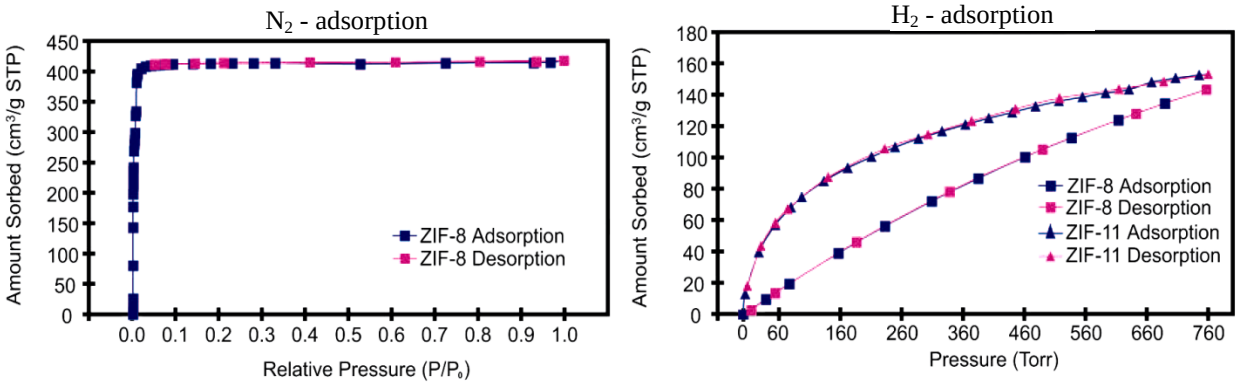

Figure 2.9 Nitrogen isotherm of ZIF-8 at 77 K (left) and hydrogen isotherm of ZIF-8 and ZIF-11 at 77 K (right).[2] (Reprinted (adapted) with permission from K. S. Park, Z. Ni, A. P. Cote, J. Yong, R. Huang, F. J. Uribe-Romo, H. K. Chae, M. O'Keeffe, O. M. Yaghi, PNAS, 2006, **103**, 10186-10191. Copyright (2006) PNAS.)

An important application for ZIFs is their ability to selectively separate gases, especially CO_2, from industrially relevant gas mixtures containing CH_4, N_2, O_2 and CO.[1] It was found that some ZIFs have a high uptake capacity, high selectivity and affinity for CO_2. CO_2 is retained in the ZIF while other gases are able to pass through the ZIF particle packed in a column without hinderance.[1]

ZIF-8 was soaked in various solvents with different kinetic diameter to examine whether their molecules would pass through the aperture of the framework. ZIF-8 was covered with *n*-hexane (kinetic diameter 4.3 Å), cyclohexane (kinetic diameter 6.0 Å) and toluene (kinetic diameter 6.1 Å) and afterwards TGA-MS was used to determine the escape of solvents from the pores. Only *n*-hexane was released from the pores of ZIF-8 proving that cyclohexane and toluene with their

larger kinetic diameter do not enter the pores of ZIF-8.[7] TGA-MS also showed the release of *n*-hexane above its boiling temperature which is expected as molecules with sizes close to that of the aperture requires additional thermal energy.[2] Peralta *et al.* performed a series of separations with combinations of two hydrocarbons solvents (aromatics, alkane and alkene). It was found that ZIFs without any functional groups, such as ZIF-8, behave like apolar adsorbents which have an affinity for the solvents in the following order: alkane > alkene > aromatics.[11]

Küsgens *et al.* compared ZIF-8 to other MOFs with regard to water physisorption. The isotherms (**Figure 2.10**, p **16**) showed that ZIF-8 is hydrophobic, with only 10 $cm^3 g^{-1}$of water adsorbed at $p/p_0 = 0.6$. The heat of adsorption for water on ZIF-8 is 44.68 KJ mol^{-1} which is very close to the molar enthalpy of water evaporation (40.69 KJ mol^{-1}).[31]

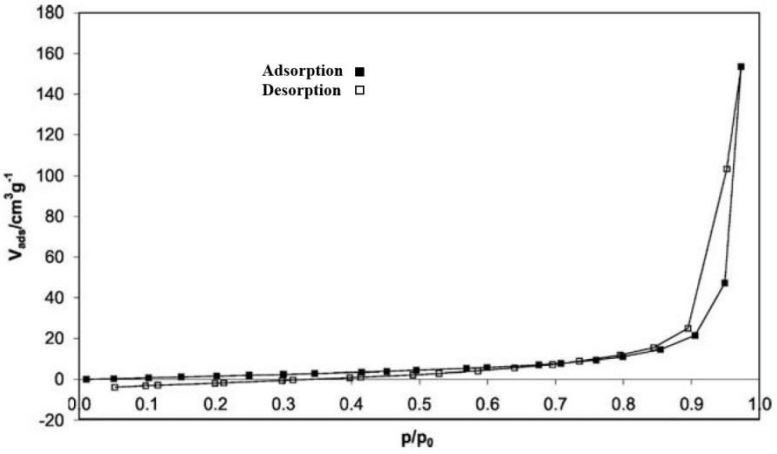

Figure 2.10 Water physisorption isotherm of ZIF-8 at 298K showing adsorption (solid) and desorption (open).[31] **(**Reprinted from Publication P. Küsgens, M. Rose, I. Senkovska, H. Fröde, A. Henschel, S. Siegel and S. Kaskel, *Microporous and Mesoporous Materials*, 2009, **120**, 325-330, Copyright (2009), with permission from Elsevier)

In 2013 Zhang *et al.* performed alcohol/water adsorption on ZIF-8 and further proved that ZIF-8 is hydrophobic. ZIF-8 was found to be efficient in the separation of 1-butanol/water and 1-propanol/water mixtures with a higher initial adsorption step for alcohols. Smaller alcohol molecules, such as methanol, show higher adsorption in ZIF-8. The filling of the cages with alcohols does not depend on the size of the pores of the ZIF, but is more dependent on the nature of the linker.[32]

McCarthy *et al.* showed that the selectivity of a ZIF-8 film coated on α-alumina for H_2/CH_4 mixture is 13.0 and for H_2/N_2 is 11.6, thus exhibiting molecular sieving capability favouring smaller molecules. O_2 has a higher affinity for ZIF-8 than CO_2 because oxygen undergoes charge

transfer with the framework, resulting in higher adsorption selectivity for oxygen than CO_2. In general the small gas molecules have a higher selectivity in ZIF-8 than larger molecules. [33] In CO_2/CH_4 mixtures, CO_2 hinder the CH_4 molecules by window blocking on ZIF-8 therefore permeance of CH_4 are lower which prevent inter-cage movement.[34]

Chang *et al.* coated a capillary with nZIF-8 and has a strong ability to sieve a mixture of branch alkanes and linear alkanes. The narrow pore size and hydrophobicity of ZIF-8 is excellent to separate alkane mixtures by the van de Waal forces of linear alkanes. Branched alkanes elute much faster than linear alkanes and short chain elute faster than longer chains for both branched and linear alkanes with a broad range of boiling points.[35]

2.4 Thermal Stability of ZIF-8

Thermal gravimetric analysis (TGA) was first performed by Park *et al.* on micro sized ZIF-8, synthesized in DMF under solvothermal conditions. The TGA curve (**Figure 2.11**, p **18**) of the as-synthesized ZIF-8 showed a weight loss of 28 % between of 25℃ and 450℃, accounting for the slow escape of guest molecules from the pores. It is less than the calculated amount of guest molecules (35.9 %), due to the fact that the guest molecules leave the pores much slower and carbonization occurs within the pores at high temperatures, as seen by the change of ZIF-8 to a darker colour at 500℃. After 600℃ the structure decomposes. The escaping of the guest molecules does not damage the framework as the samples were heated between 200℃ and 500℃ in a nitrogen atmosphere. The SOD topology of ZIF-8 was preserved and corresponds to the simulated PXRD patterns from single crystal structures (**Figure 2.11**, p **18**). With this high thermal stability ZIF-8 is only matched by a few highly dense MOFs.[2] The last decomposition step yields ZnO which was determined to be 21 %.[23,28]

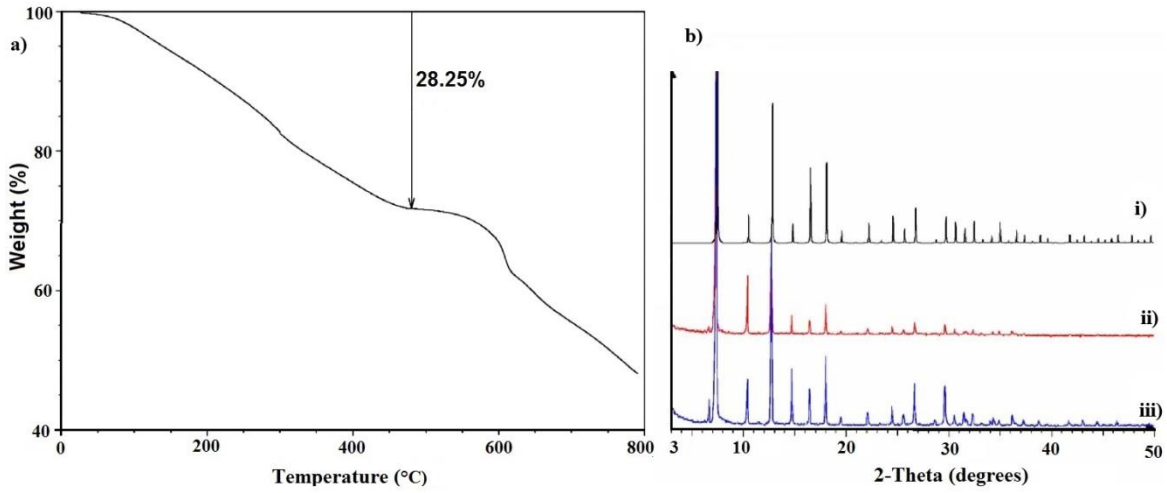

Figure 2.11 TGA of ZIF-8 as-synthesized in DMF (a) and PXRD patterns of ZIF-8 (b) as-synthesized (i), after heating to 500℃ in nitrogen flow (ii) and activated ZIF-8 (iii).[2] (Reprinted (adapted) with permission from K. S. Park, Z. Ni, A. P. Cote, J. Yong, R. Huang, F. J. Uribe-Romo, H. K. Chae, M. O'Keeffe, O. M. Yaghi, PNAS, 2006, **103**, 10186-10191. Copyright (2006) PNAS.)

The use of the following solvents to clean the pores of as-synthesized ZIF-8 was investigated: THF, acetonitrile, dichloromethane and methanol. TGA (**Figure 2.12**, p **19**) showed that after exchanging the DMF (from synthesis) with methanol or dichloromethane, a more simple thermogravmetric behaviour was observed. The initial mass loss (**Figure 2.11**, p **18**) of 28.25 % up to 450℃ from the as-synthesized ZIF-8 was replaced with a very small initial step of 7.6 % from 200 to 450℃ after solvent exchange with methanol.[2]

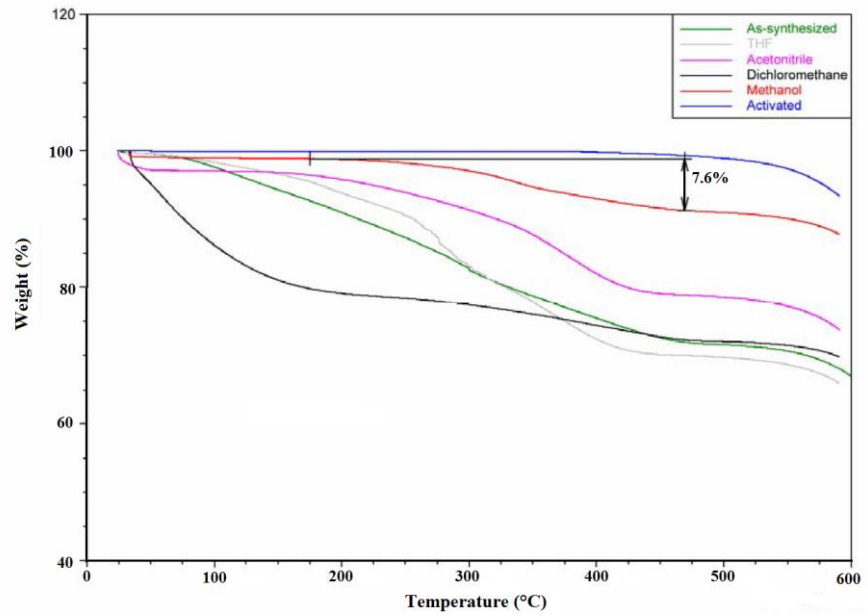

Figure 2.12 TGA of ZIF-8 of as-synthesized (green), activated (blue) and as-synthesized ZIF-8 after solvent exchange by various solvents.[2] (Reprinted (adapted) with permission from K. S. Park, Z. Ni, A. P. Cote, J. Yong, R. Huang, F. J. Uribe-Romo, H. K. Chae, M. O'Keeffe, O. M. Yaghi, PNAS, 2006, **103**, 10186-10191. Copyright (2006) PNAS.)

2.5 Chemical Stability of ZIF-8

One of the key properties of ZIF-8 is its high chemical stability in ambient and harsh conditions reflecting extreme operational parameters used in industrial chemical processes. These conditions included boiling in solvents such as benzene, methanol, water and also low and high concentrations of aqueous sodium hydroxide. During the tests it was found that the ZIF-8 maintained its full crystallinity while boiling in organic solvents (benzene and methanol) for 7 days as shown from the PXRD patterns (**Figure 2.13**, p **20**). It was stable in water at room temperature, 50℃ and 100℃ for 7 days as well as 0.1 M and 8 M aqueous sodium hydroxide solutions at 100℃ for 24 hours.[2,36] The high resistance of ZIF-8 to hydrolysis is a combination of two phenomena: The hydrophobicity of the ZIF structure prevents the dissolution of the framework. The stability of the Zn-N bond also contributes to the hydrothermal stability of the ZIF-8 which is similar to that of covalent solids.[2] Nano crystallites of ZIF-8 were tested for chemical stability and similar results to micro sized ZIF-8 were obtained.[23] Interestingly the nZIF-8 was stable in ethanol for 3 weeks, after it was found to aggregate by the formation of hydrogen bonds between the protonated imidazole on the surface.[37]

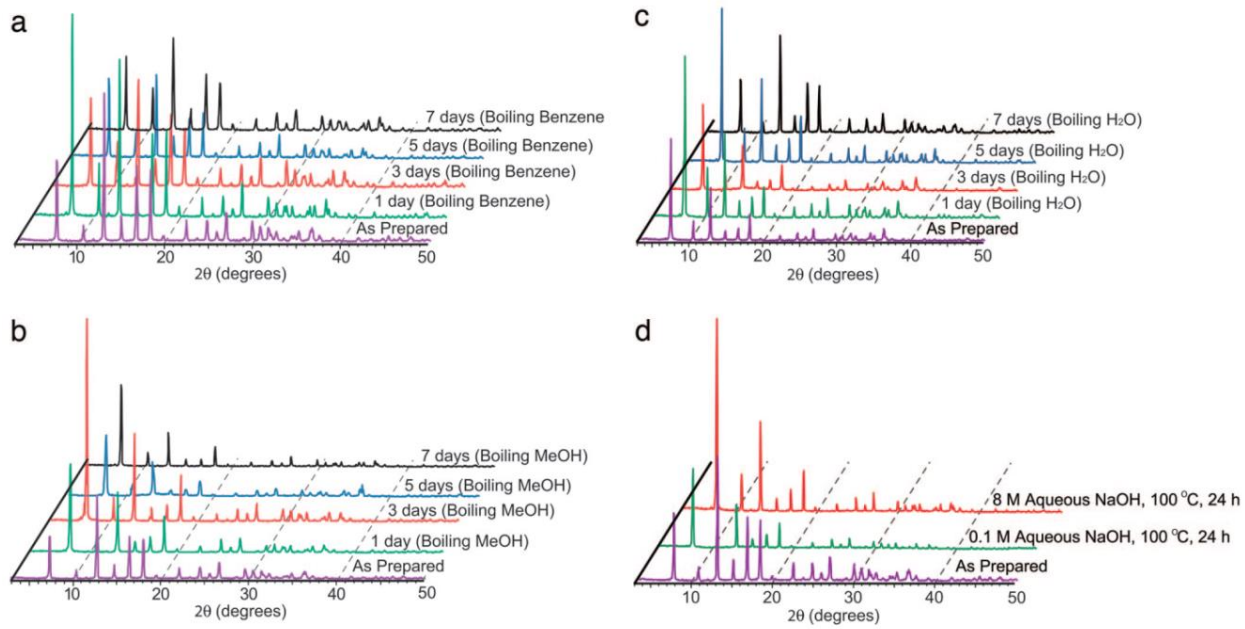

Figure 2.13 PXRD patterns of ZIF-8, refluxed in: a) benzene for 7 days at 80℃ b) methanol for 7 days at 60℃ c) H_2O for 7 days at 100℃ and d) Aqueous NaOH for 24 hours at 100℃.[2] (Reprinted (adapted) with permission from K. S. Park, Z. Ni, A. P. Cote, J. Yong, R. Huang, F. J. Uribe-Romo, H. K. Chae, M. O'Keeffe, O. M. Yaghi, PNAS, 2006, **103**, 10186-10191. Copyright (2006) PNAS.)

2.6 Synthesis of ZIF-8 Nanoparticles with Size Control

Since the discovery of ZIF-8, different methods have been employed to control the particle size of ZIF-8 during synthesis, and by doing so, improve physical properties such as surface area and diffusion resistance of the MOF. Smaller particles will have a larger external surface area per gram than larger particles, increasing the number of active sites on the external surface available for e.g. catalysis. A conventional size for ZIF-9 nanoparticles of 40 nm (Chapter **2.2**) was previously reported by Cravillon *et al.*.[22]

Although the nucleation, growth and crystallization of nano ZIF-8 (nZIF-8) has not been widely investigated, understanding the formation mechanism is important to improve and control the structure and morphology of nZIF-8. Venna *et al.* followed the synthesis reaction of nZIF-8 with ex situ PXRD up to 24 hours and found that the crystal growth of ZIF-8 can be divided into three stages:

1) Nucleation stage of ZIF-8 from 0 to 10 min, giving particles of 50 nm in diameter.
2) Growth Stage from 10 to 60 min, giving particles to 230 nm.

3) Stationary phase > 60 min where the metastable phase is consumed. Particles reach 500 nm with a narrow size distribution after 12 hours.

TEM images were taken at each time interval of the PXRD pattern (**Figure 2.14**, p **21**). The significant size increase can be explained as a result of Ostwald ripening, where the spontaneous and thermodynamically driven consuming of smaller particles to grow larger ones are energetically favoured (lower energy states).[26]

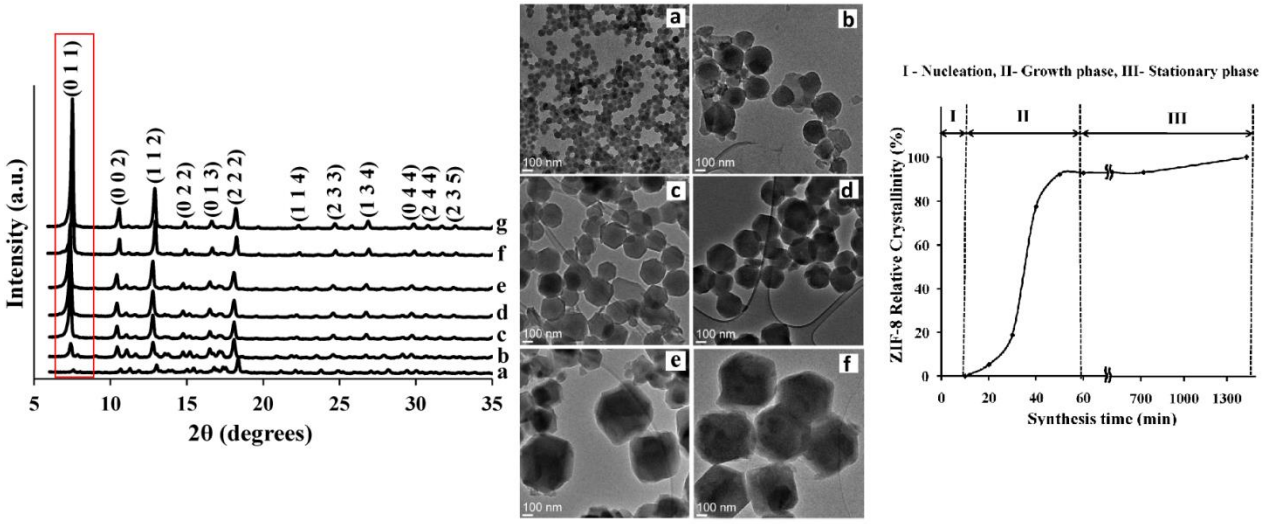

Figure 2.14 PXRD patterns of ZIF-8 with TEM images taken during synthesis after a) 20 min, b) 30 min, c) 40 min, d) 50 min, e) 60 min, f) 12 h and g) 24 h. Graph of relative crystallinity *vs.* synthesis time of ZIF-8 showing the three different phases.[26] (Reprinted (adapted) with permission from S. R. Venna, J. B. Jasinski and M. A. Carreon, *J. Am. Chem. Soc*, 2010, **132**, 18030-18033. Copyright (2010) American Chemical Society.)

In 2011 Cravillon *et al.* further monitored the fast nucleation and crystal growth of ZIF-8 by in situ small angle and wide angle X-ray scattering (SAXS/WAXS) and found that pure-phase ZIF-8 nanoparticles are formed in the early stages without the occurrence of other transient crystalline phases. Similarly it was observed that a fast crystallization stage is followed by a slower stage. The cluster forms initially and gets nearly consumed rapidly within 60 seconds with the formation of particles with the particle density approaching a constant value, indicating that nucleation has stopped. The nucleation rate can be increased by an excess amount of imidazole reagent. After 1 hour a particle diameter of 55 nm was observed which is smaller than those produced by Venna *et al.*, because a stop-flow device and different conditions was implemented.[22,38] Another study by J. Cravillon using in situ Static Light Scattering (SLS) showed that slow nucleation occurs together with fast crystal growth and that the two processes are not separated from each other.[39]

The 2-methyl imidazole reagent can act as a linker unit when deprotonated or as a stabilizing unit when neutral.[22] During the synthesis a change in pH from 7.8 to 7.2 corresponds to an increase in the crystallinity of ZIF-8, suggesting that as the pH decreases it promotes crystallization of the framework. Both neutral and deprotonated linkers coexists at equilibrium and a lower pH indicates a lower concentration of deprotonated linkers, allowing stabilization from the neutral linkers which prevents further phase change transformation (terminating crystal growth).[26] Deprotonation of the 2-methylimidazole ligand with a base, provides a faster nucleation rate, resulting in smaller crystals.[39]

2.6.1 Particle Size Control by Surfactants

In 2011 Pan *et al.* successfully used surfactants as capping agents to control the particle size of ZIF-8 during synthesis.[40] With the surfactant cetyltrimethylammonium bromide (CTAB) an increase of its wt %, from 0.0025 to 0.025, resulted in a decrease in particle size from 4000 nm to 110 nm (**Figure 2.15**, p **23**). The different size ZIF-8 synthesized with CTAB all had identical topology to the ZIF-8 without the CTAB as shown in the PXRD (**Figure 2.15.a**, p **23**), but the crystal shape changed from a truncated rhombic dodecahedron to a truncated cube with as the crystal size decreased (**Figure 2.15.e**, p **23**). The long hydrophobic hydrocarbon chains of CTAB absorbed on the ZIF-8 surface hinders the reagents attachment to the surface thus slowing down the growth rate of the crystals. The ZIF-8 synthesised with CTAB was re-dispersed and the crystal was seen to continue growing due to Ostwald ripening since the CTAB on the surface was dissolved in the solvent.[40]

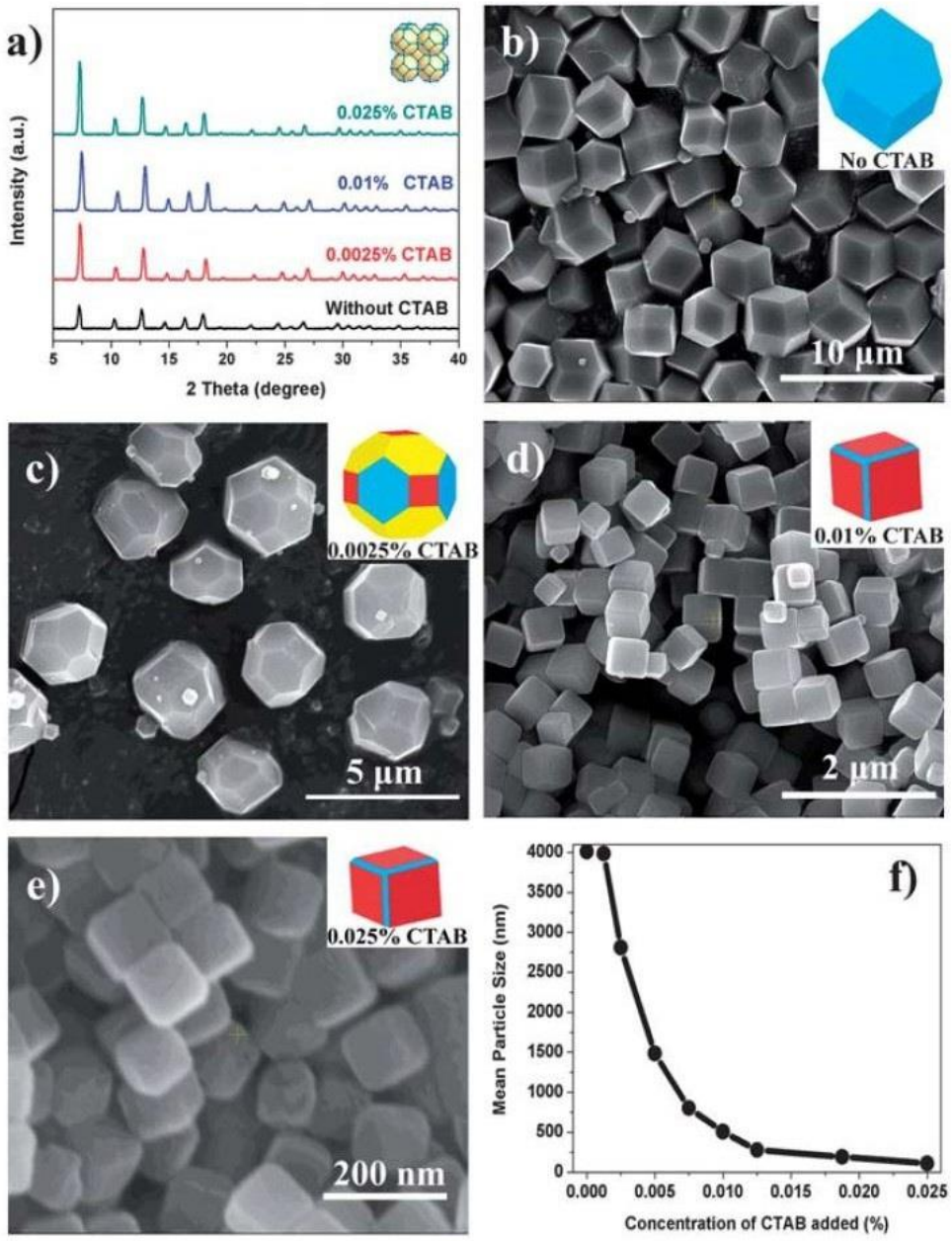

Figure 2.15 Characterization, using PXRD and SEM, of ZIF-8 synthesized in the presence of different concentrations of cetyltrimethylammonium bromide (CTAB): a) XRD patterns; b) no CTAB; c) 0.0025 % CTAB; d) 0.01 % CTAB; e) 0.025 % CTAB f) ZIF-8 mean particle size *vs.* CTAB concentration. Schematic diagrams displaying crystal morphology {110}, {100} and {111} facets as cyan, red and yellow respectively.[40] (Reprinted (adapted) with permission from Y. Pan, D. Heryadi, F. Zhou, L. Zhou, G. Lestari, H. Su, Z. Lai, *CrystEngComm*, 2011, **13**, 6937-6940. Copyright (2012) The Royal Society of Chemistry.)

2.6.2 Particle Size Control by Modulating Ligand and Polymers

In 2010 Nune *et al.* managed to control the particle size of nZIF-8 by the addition of 1 % high molecular weight (M_w 400 000 - 500 000) poly(diallyldimethylammonium chloride) polymer to the reaction mixture in methanol. A very narrow size distribution was obtained after 24 hours at room temperature with an average particle size of 57 nm.[41]

nZIF-8 synthesized without modulating ligands gave ~45 nm particles as previously reported by Cravillon *et al.*.[22] In 2011 his group introduced a coordination modulation method to control the size and shape of nZIF-8. By addition of *n*-butylamine to the reaction mixture in methanol at room temperature in different ratios, particle sizes between 9 to 55 nm were obtained (**Table 2.2, p 24**). The modulating ligand acts both as a competitive ligand at the metal centres as well as a base to deprotonate bridging ligands.[39]

Table 2.2 Synthesis of nZIF-8 with different ratios of (Zinc) Zn, 1-methylimidazole (Hmim), *n*-Butylamine (*n*-$BuNH_2$) in methanol at room temperature with average particle diameter determined by XRD and small angle X-ray scattering (SAXS).[39]

Zn:Hmim:*n*-$BuNH_2$:MeOH	**Diameter by XRD (nm)**	**Diameter by SAXS (nm)**
1:4:2:5000	9	9
1:4:2:1000	10	9
1:4:2:500	10	8
1:4:4:500	16	16
1:4:4:1000	18	17
1:4:4:5000	24	20
1:2:4:500	43	42
1:2:4:1000	45	39
1:2:4:5000	55	40

2.6.3 Particle Size Control by Concentration

In 2012 Tanaka *et al.* reported a method to control the particle size of ZIF-8 in aqueous solutions at room temperature. Different 2-methylimidazole/zinc (mim/Zn) ratios ranging from 4 to 100 were employed whilst keeping the water and zinc concentration constant. [6]

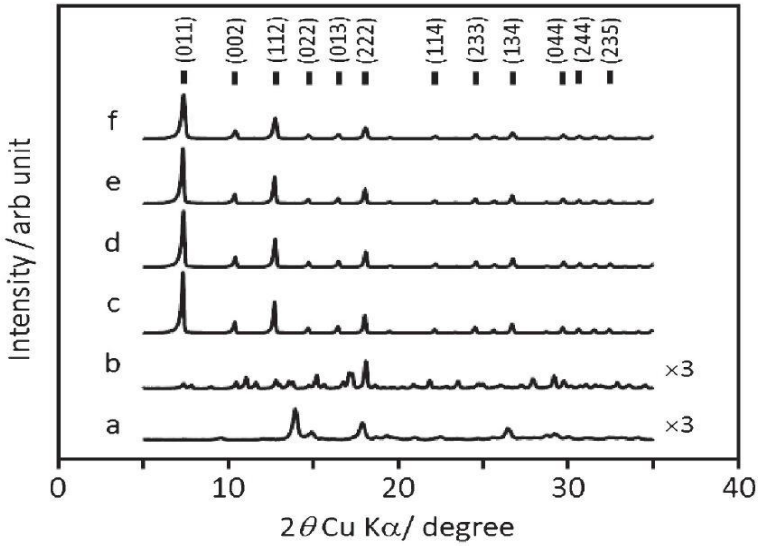

Figure 2.16 PXRD patterns of ZIF-8 from syntheses with different 2-methylimidazole/Zn ratios a) 4, b) 20, c) 40, d) 60, e) 80 and f) 100 with a) and b) repeated 3 times.[6] (Reprinted (adapted) from S. Tanaka, K. Kida, M. Okita, Y. Ito, Y. Miyake, *Chem. Let.* 2012, **41**, 1337-1339. Copyright (2012) The Chemical Society of Japan.)

From **Figure 2.16** (**p 25**) it can be seen that as the mim/Zn ratio was increased the crystallinity increased to be pure phase ZIF-8 from a mim/Zn ratio of 40 (c). SEM analysis of the products from different mim/Zn ratios showed that particle diameter was inversely proportional to mim/Zn ratio (**Table 2.3, p 25**).

Table 2.3 Different mim/Zn ratio with the resulted ZIF-8 particle diameter as determined by SEM.

mim/Zn ratio	Particle diameter (μm)
40	3.4
60	1
100	0.32

The reason for the decrease is that the imidazole molecules exist in tautomeric form. Any of its two nitrogen atoms can be deprotonated giving a symmetrical imidazolium anion.[6] By increasing the 2-methylimidazole concentration the concentration of free imidazolate ions is increased.[33] Therefore, as the concentration of imidazolate ions increase, the nuclei for complex formation will increase, leading to smaller particles, thus suggesting a high nucleation rate in the early stage of the reaction. Interestingly, as the particle size decrease the BET surface areas increased

from 1520 $m^2 g^{-1}$ (for 3.4 µm particles) to 1600 $m^2 g^{-1}$ (for 0.32 µm particles), but the Langmuir surface area remains relatively the same for all the different particle sizes: 1860 $m^2 g^{-1}$.[6]

In 2013 Yamamoto *et al.* was able to successfully control the particle size of ZIF-8 by altering the concentration ratio of 2-methylimidazole/Zn and flow rates during synthesize using a micromixer in an aqueous solution. A slower flow rate of 1 $cm^3 min^{-1}$ produced larger particles of 465 nm and a faster flow rate of 25 $cm^3 min^{-1}$ smaller particles (150 nm).[42] This minimum size is still much larger than the particles synthesized during this study.

2.7 Metals Loaded in ZIF-8

The synthesis of metal nanoparticles has been widely investigated and only recently MOFs have been used as a host matrix to stabilize well-defined metal nanoparticles and thus prevent agglomeration. ZIF-8, one of the popular MOFs to be used for this purpose, with its pore width of 11.6 Å and openings of 3.4 Å, is suitable for impregnation by molecules and metals in order to improve its gas adsorption and catalytic properties. Different techniques have been used to load ZIFs with metals, namely chemical liquid deposition (CLD), chemical vapour deposition (CVD), solid grinding and ion exchange.[43] The following notation: M@ZIF-8, will be used, where M represents the metal being incorporated (@) within the pores of ZIF-8. In this study the impregnation of ZIF-8 nanoparticles with silver as well as palladium was studied.

2.7.1 Au@ZIF-8 and Ag@ZIF-8

Noble metals have been well known as effective catalysts. Gold and Ruthenium has recently been loaded into a variety of MOFs.[44] Gold metal nanoparticles were deposited in ZIF-8 by Jiang *et al.* in 2009 using a solid grinding technique and volatile dimethyl Au(III) acetylacetonato ($Me_2Au(acac)$) precursor. The product was reduced by H_2 to obtain Au@ZIF-8 with loadings between 0.5 to 5 wt %. The Au nanoparticles were too small for detection by XRD, but the higher loading of Au lowers the amount if N_2 physisorbed on ZIF-8 at 77K indicating that the particles are highly dispersed in the framework. Au@ZIF-8 also showed considerable activity towards gas phase CO oxidation.[45] Esken *et al.* reported the impregnation of ZIF-8 by chemical vapour deposition (CVD) using chlorocarbonylgold (Au(CO)Cl). They obtained gold nanoparticle of 1 to 2 nm homogeneously dispersed in ZIF-8 with loadings of 5 to 30 wt %.[46]

In 2011 Jiang *et al.* loaded ZIF-8 with silver nanoparticles and also formed bimetallic silver/gold cores in ZIF-8 (**Figure 2.17**, p **27**). Both metals were loaded in succession *via* chemical vapour

deposition (CVD) using silver nitrate and hydrogen tetrachloroaurate (III) tetrahydrate ($HAuCl_4.4H_2O$). The products were chemically reduced with sodium borohydride to give ZIF-8 containing both 2 % Au and 2 % Ag. The bimetallic core was formed with two approaches: ZIF-8 was first loaded with gold then with silver (**Figure 2.1.a)**, p **27**) and vice versa (**Figure 2.17.b)**, p **27**). Both approaches produced similar compositions with metal nanoparticle sizes of 2-6 nm. The N_2 physisorption isotherm of the metal-containing ZIF-8 showed a decrease in surface area compared to ZIF-8, an indication that the pores were blocked. Bimetallic systems have improved catalytic activity over monometallic and alloy counterparts in the reduction of 4-nitrophenol by $NaBH_4$.[47]

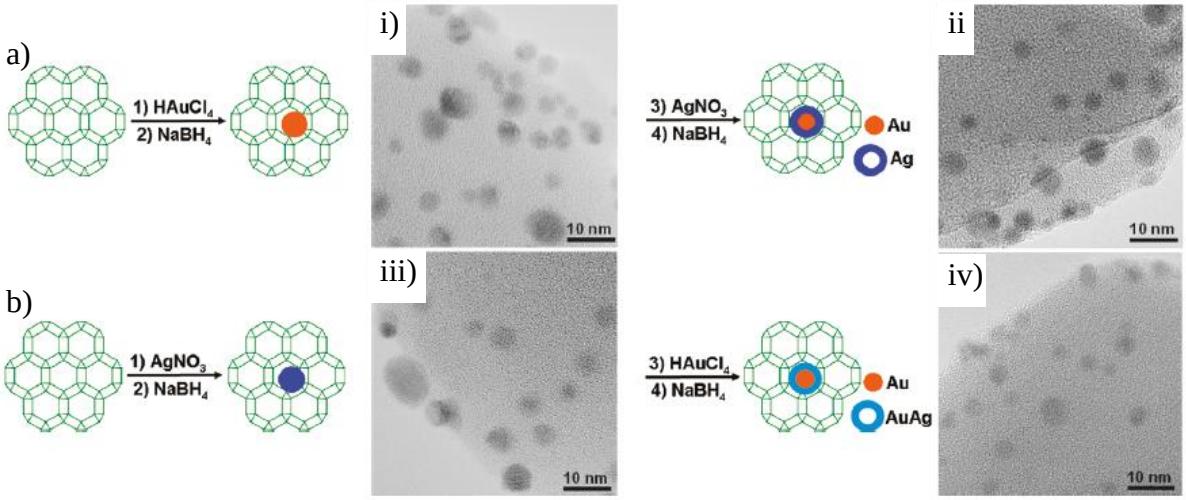

Figure 2.17 Schematic representation and TEM images of two approaches to form bimetallic Au/Ag@nZIF-8: a) 2 %Au@ZIF-8 (i) 2%Au-2%Ag@ZIF-8 (ii), b) 2%Ag@ZIF-8 (iii), 2%Ag-2 %Au@ZIF-8 (iv), with metal nanoparticles between 2 to 6 nm.[47] (Reprinted (adapted) with permission from H-L Jiang, T. Akita, T. Ishida, M. HAruta and Q. Xu, J. Am. Chem. Soc., 2010, **133**, 1304-1306. Copyright (2010) American Chemical Society.)

2.7.2 Pd@ZIF-8

Over the years the use of platinum group metals as supported catalyst have been widely investigated because these metals are expensive and in most cases cannot be recycled or easily separated. Out of this group palladium has been a popular choice, e.g. in the Heck reaction, Suzuki reaction and the Sonogashira coupling reaction.[48] Ever since the discovery of MOFs, catalytic studies where different single Pd precursors or, in some cases bi-metallic precursors are supported on a wide variety of MOFs, have been conducted.[43,49]

Palladium can be easily loaded into ZIF-8 pores by chemical liquid deposition methods as reported by Yuan *et al.* using a $Pd(NO_3)_2$ in DMF solution. The loaded ZIF-8 was isolated from

the solution and treated with H_2 at 200℃ to yield Pd@ZIF-8 with a loading of 0.95 wt % as measured by XPS.[50] Palladium can also be supported on ZIF-8 using K_2PdCl_4 in solution followed by the addition of polyvinyl alcohol (stabilizer) and hydrazine (reductant) to obtain a loading of 0.92 wt % by ICP analysis. TEM and SEM images (**Figure 2.18**, p **28**) show palladium particles with sizes of 4 to 9 nm, highly dispersed on the external surface area of ZIF-8 crystals. Pd@ZIF-8 is air stable and no significant change in the porosity of the support was observed after the loading of Pd nanoparticles.[51]

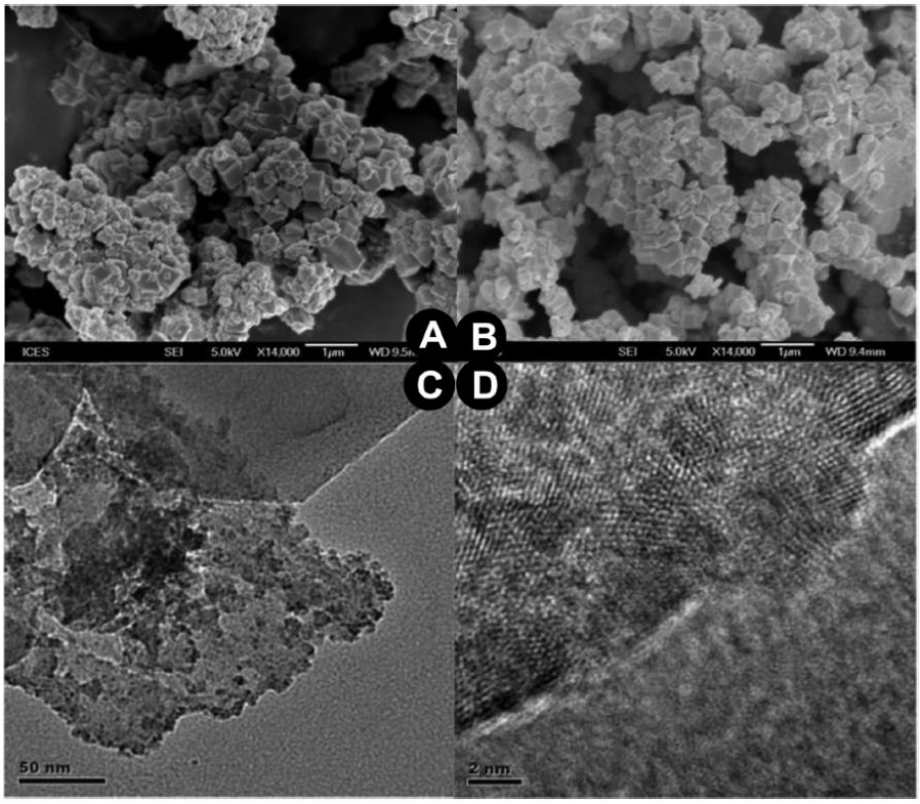

Figure 2.18 SEM images of a) ZIF-8 and b) Pd@ZIF-8. TEM images of c) ZIF-8 and d) Pd@ZIF-8.[51] (Reprinted (adapted) with permission from T. T. Dang, Y. Zhu, J. S. Y. Ngiam, S. C. Ghosh, A. Chen and A. M. Seayad, *ACS Catal.*, 2013, **3**, 1406-1410. Copyright (2013) American Chemical Society.)

In this study Pd will be loaded onto nano-sized ZIF-8, which has a larger external surface area, compared to the commercially available ZIF-8.

2.7.3 Other Metals Loaded in ZIF-8

A variety of other metal nanoparticles has also been loaded into micro sized ZIF-8, using chemical vapour deposition and chemical vapour deposition. In (**Table 2.4**, p **29**) a summary of metals and metal salts other than Ag, Au and Pd, which were loaded onto ZIF-8, is given.

Table 2.4 Summary of metals loaded into ZIF-8 showing metal precursor, technique and metal wt %. COD = 1,5-cyclooctadiene; MeCp = methylcyclopentadienyl.

Name	Metal Precursor	Technique	Loading %	Reference
Ni@ZIF-8	$Ni(C_5H_5)_2$	Chemical Liquid Deposition	22 wt %	**52**
Ni@ZIF-8	$Ni(C_5H_5)_2$	Chemical Vapour Deposition	19 wt %	**52**
GaN@ZIF-8	$(CH_3)_3NGaH_3$	Chemical Vapour Deposition	13 wt %	**53**
ZnO@ZIF-8	$Zn(C_2H_5)_2$	Chemical Vapour Deposition	9 wt %	**54**
AlH_3@ZIF-8	$C_2H_5N(CH_3)_2 \cdot AlH_3$	Chemical Liquid Deposition	1.14 wt %	**55**
Co_3O_4@ZIF-8	$Co(NO_3)_2$	Chemical Liquid Deposition	22 wt %	**56**
Ir@ZIF-8	Ir(COD)(MeCp)	Chemical Vapour Deposition	1.5 wt %	**57**

Both chemical vapour deposition and chemical liquid deposition methods are effective ways to load the ZIF-8 with well dispersed metal nanoparticles. ZIF-8 is stable enough for further reduction or oxidation procedures of the metal.

Some alternative approaches metal nanoparticles are encapsulated by growing ZIF-8 around the metal. E.g. encapsulated magnetic Fe_3O_4 allows the ZIF-8 particles to be magnetic and they can thus be easily separated using a magnetic field. Similarly, ZIF-8 encapsulated lanthanide doped ($NaYF_4$) rods and CdTe quantum dots are photoluminescent.[58] Encapsulated Pt@ZIF-8 showed enhanced catalytic activity and selectivity over Pd/C in hydrogenation of 1-hexene.[59] By encapsulating Cu_2O with ZIF-8 a hollow yolk-shell particle with a thickness of 100 nm was formed during synthesis. During the formation of ZIF-8 around the Cu_2O nanoparticle the pH reduces from 7 to 5 and thus the Cu_2O is etched off simultaneously. With this method metals such as palladium can be pre-coated with Cu_2O and after encapsulation with ZIF-8 only the Pd remains within the yolk-shell ZIF-8. Higher catalytic activity was observed from the yolk-shell Pd@ZIF-8 than core-shell ZIF-8 without Cu_2O etched off.[60]

2.8 Post Synthetic Modification by Ligand Exchange of ZIF-8

In 2008 the concept of using ZIF crystals as molecules in typical organic reactions were developed by W. Morris.[61] ZIF-90 with imidazolate-2-carboxyaldehyde as organic linker and having a SOD geometry was reacted in organic reaction conditions with $NaBH_4$ reducing the aldehyde ligand into an alcohol thus producing ZIF-91, or was refluxed with an amine to give ZIF-92 (**Figure 2.19**, p **30**). Both reactions were successful with conversions of 80 %. PXRD measurements produced identical patterns for ZIF-90, ZIF-91 and ZIF-92 all maintaining high crystallinity and showing no structural transformation. This was consistent with porosity measurements.[61]

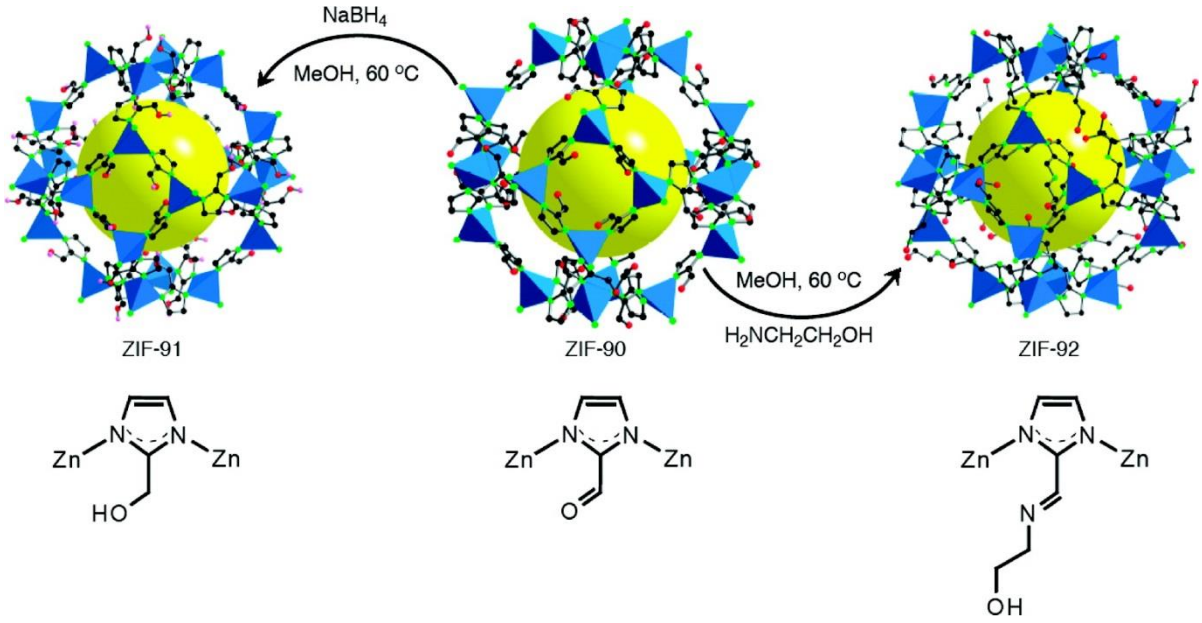

Figure 2.19 Postsynthetic modification of ZIF-90 (middle) to ZIF-91 by reduction with $NaBH_4$ (left) and to ZIF-92 by reaction with ethanolamine (right). (C, black; N, green; O, red).[1,61] (Reprinted (adapted) with permission from A. Phan, C.J. Doonan, F. J. Uribe-Romo, C. B. Knobler, M. O'Keeffe, O. M. Yaghi, *Acc. Chem. Res.*, 2009, **43**, 58-67. Copyright (2009) American Chemical Society.)

Kim *et al.* recently exchanged linkers and metals of a variety of robust MOFs (MIL, UiO, ZIF). A solid-solid mixture of two solid similar MOFs and a solid-liquid mixture were used to successfully exchange either the metal or the ligand under mild conditions whilst maintaining crystallinity of the original MOF.[62] In this study the focus is only on the exchange of the organic linker. Exchange of the metal center will thus not be further discussed.

In 2012 Karagiaridi *et al.* initially used a solvent assisted linker exchange (SALE) method on a cadmium based ZIF (CdIF-4) with large apertures (9.6 Å) and a RHO topology containing a 2-ethylimidazole linker. The linker was successfully exchanged with 2-methylimidazole to produce SALEM-1 and with 2-nitroimidazole to yield CdIF-9. Both SALEM-1 and CdIF-9 retained the RHO topology of the original CdIF-4 after a 100 % exchange of ligands as observed by PXRD and ^{1}H NMR measurements (**Figure 2.20**, p **31**).[63] The PXRD patterns of all three structures (**Figure 2.20.a**, p **31**) are identical (RHO topology) and thus prove that no structural changes occur during the ligand exchange procedure. The ^{1}H NMR spectra represented in (**Figure 2.20.b**, p **31**) shows that all compounds are pure in their composition and that CdIF-4 was fully converted to CdIF-9 (**Figure 2.20.b.ii**, p **31**) and SALEM-1 (**Figure 2.20.b.iii**, p **31**) respectively. Furthermore, the particle size distribution remained constant during the exchange process and the BET surface areas of CdIF-9 and SALEM-1 matches that of the CdIF-4.[63]

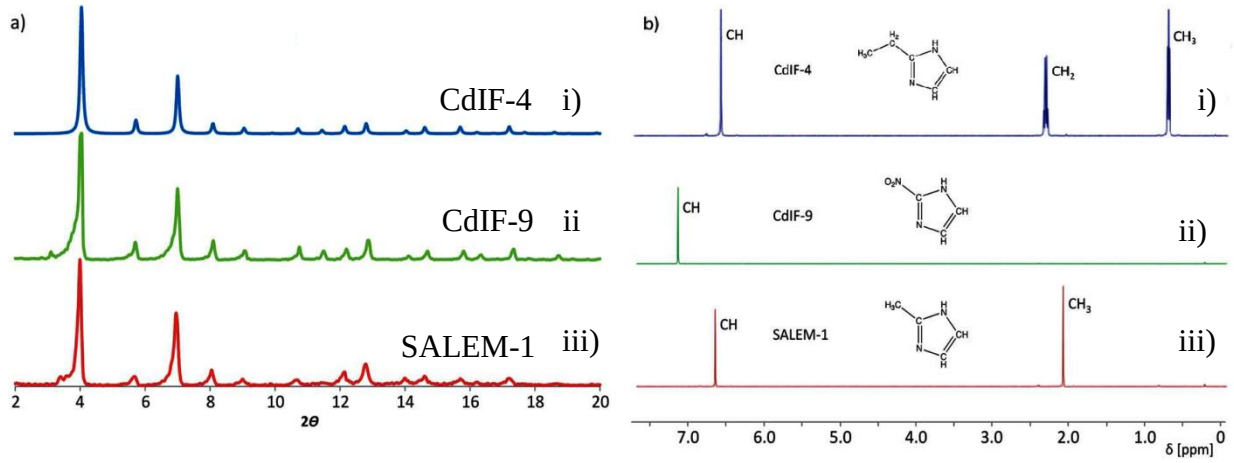

Figure 2.20 a) PXRD patterns of CdIF-4 (i, blue), CdIF-9 (ii, green) and SALEM-1 (iii, red) b) ^{1}H NMR spectrum after dissolution in D_2SO_4: CdIF-4 (i, blue), CdIF-9 (ii, green) and SALEM-1 (iii, red).[63] (Reprinted (adapted) with permission from O. Karagiaridi, W. Bury, A. A. Sarjeant, C. L. Stern, O. K. Farha and J. T. Hupp, *Chem. Sci*., 2012, **3**, 3256-3260. Copyright (2012) The Royal Society of Chemistry.)

Karagiaridi *et al.* reported a SALE reaction where the 2-methylimidazole linkers in ZIF-8 were exchanged with imidazole ligands (**Scheme 2.2,** p **32**), to produce SALEM-2 with retention of the SOD topology of the starting material (ZIF-8).

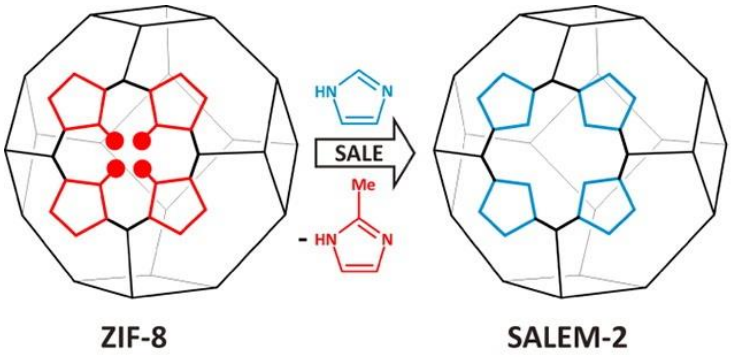

Scheme 2.2 ZIF-8 undergoes a solvent assisted ligand exchange (SALE) reaction, where the 2-methylimidazole linkers of ZIF-8 are replaced by imidazole ligands to give SALEM-2.[7] (Reprinted (adapted) with permission from O. Karagiaridi, M. B. Lalonde, W. Bury, A. A. Sarjeant, O. K. Farha and J. T. Hupp, *J. Am. Chem. Soc.*, 2012, **134**, 18790−18796. Copyright (2012) American Chemical Society.)

A PXRD study (**Figure 2.21.a**, p **33**) showed that the spectra of ZIF-8 and SALEM-2 are identical indicating that the SOD topology was retained during the SALE reaction. Up to 85 % of the linkers were exchanged as determined from the proton ratio in the ^{1}H NMR spectrum of SALEM-2 (**Figure 2.21.b**, p **33**). The porosity of ZIF-8 (250 cm^3 of N_2 adsorbed with a BET surface area of 1080 $m^2\ g^{-1}$) was lowered during the exchange with the imidazole linker to SALEM-2 (225 $cm^3$of N_2 adsorbed with a BET surface area of 830 $m^2\ g^{-1}$), as seen in (**Figure 2.21.c**, p **33**). The shape and size of ZIF-8 crystals remained the same during the SALE reaction, as determined with TEM (**Figure 2.21.d**, p **33**).[7]

The SALE reaction of ZIF-8 is solvent dependent, since *N*,*N*-Dimethylformamide and *N*,*N*-Dimethylacetamide, as solvents, lead to the degradation of the ZIF-8 SOD topology, while the less basic *n*-butanol was found to be more effective. The molar ratio between the exchanging imidazole linker and the ZIF-8 is also important as a ratio higher than 7:1 lead to the loss of the SOD geometry while a ratio of less than 3:1 resulted in no exchange. The chemical and thermal stability of the SALEM-2 product is similar to that of ZIF-8.[7] Conventional solvothermal synthesis procedures, using the imidazole ligand (instead of 2-methylimdazole, as with ZIF-8) yields ZIF-10, a nonporous material with a MER topology. In this study the SALE reaction was performed for the first time on nano-sized ZIF-8.

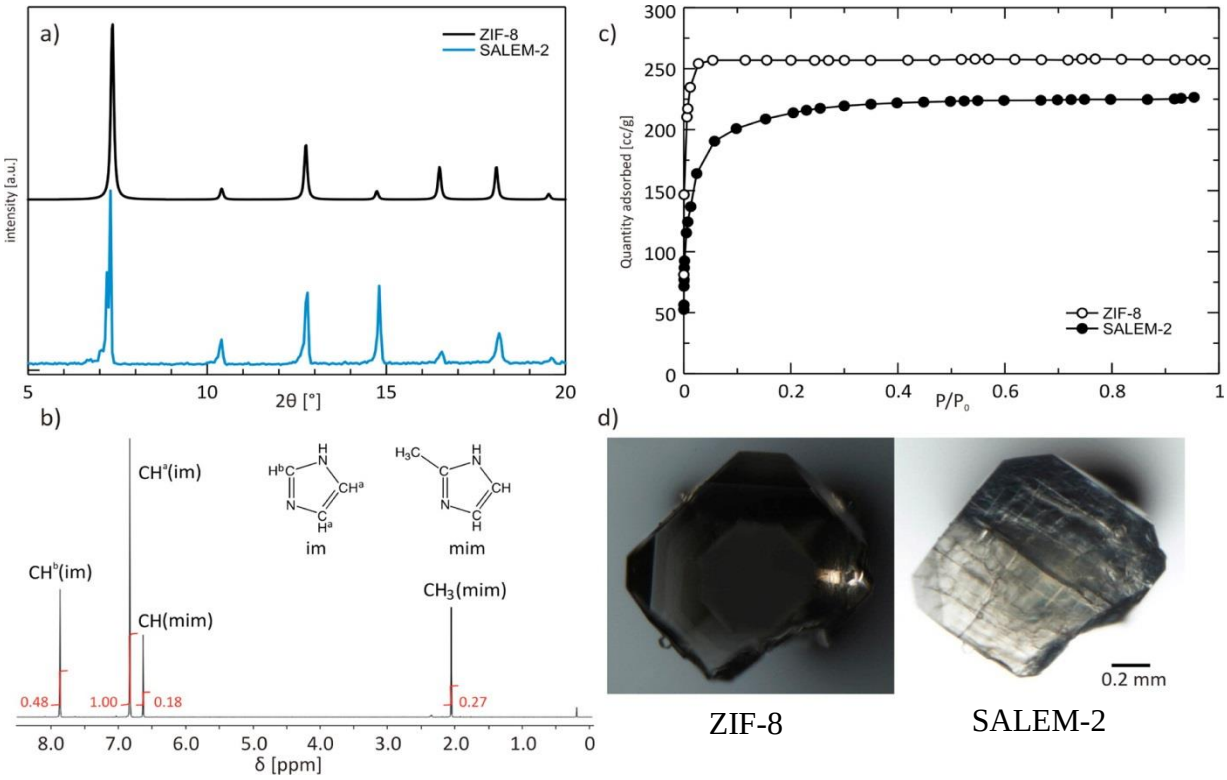

Figure 2.21 Comparison of ZIF-8 and SALEM-2: a) PXRD of ZIF-8 (top) and SALEM-2 (bottom) b) ^{1}H NMR analysis of SALEM-2 digested in D_2SO_4 (1:9 in D_2O) c) N_2 isotherms at 77 K for ZIF-8 (top) and SALEM-2 (bottom) c) TEM images of a ZIF-8 crystals (left) and the same crystal after 7 days in SALE reaction (right).[7] (Reprinted (adapted) with permission from O. Karagiaridi, M. B. Lalonde, W. Bury, A. A. Sarjeant, O. K. Farha and J. T. Hupp, J. Am. Chem. Soc., 2012, **134**, 18790−18796. Copyright (2012) American Chemical Society.)

2.9 Catalytic Studies with ZIF-8

After the external surface of ZIF-8 was probed with CO adsorption and computed using DFT calculations it was found that ZIF-8 not only has Lewis acid and basic sites but also Brønsted acid sites.[64] ZIF-8 is known to catalyse reactions such as the Knoevenagel reaction[18,65], transesterification[64] and Friedel Craft acylation[30]. These reactions were all performed using micro-sized ZIF-8. The catalytic test reaction performed in this study focused on the active sites on the external surface of nano-sized ZIF-8.

2.9.1 Knoevenagel Condensation Reaction

The Knoevenagel condensation is a well-known reaction for the formation of carbon-carbon bonds by the reaction of an aldehyde with an activated methylene group (**Scheme 2.3**, p **34**) and is catalysed by weak bases such as primary, secondary or tertiary amines of which piperidine was regarded as the best.[66]

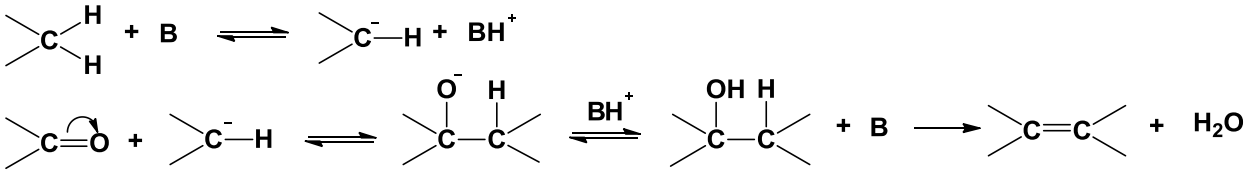

Scheme 2.3 A general mechanism for the Knoevenagel condensation reaction between a methylene group and an aldehyde catalyzed with a base (B=base).[66]

Homogeneous catalysts (like piperidine) are difficult to remove and recycled and require a high mol percentage of catalyst in the reaction.[67,68] In 2011 Tran *et al.* employed ZIF-8 as a heterogeneous catalyst for the Knoevenagel Reaction between benzaldehyde and malononitrile at room temperature in toluene as shown in **Scheme 2.4**.[65]

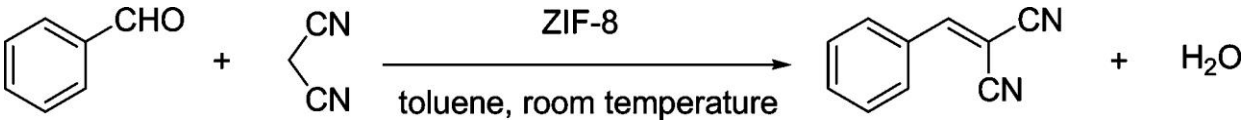

Scheme 2.4 Knoevenagel reaction of benzaldehyde and malononitrile in toluene with ZIF-8 catalyst at room temperature.[65] (Reprinted (adapted) with permission from U. P. N. Tran, K. K. A. Le and N. T. S. Phan , *ACS Catalysis.*, 2011, **1**, 120-127. Copyright (2011) American Chemical Society.)

The hexagonal pore entrance of 3.4 Å prevents larger molecules from entering and therefore the reaction takes place on the external surface of ZIF-8. The catalytic activity of ZIF-8 with crystal sizes between 100 to 200 µm was determined by GC-MS. No leaching of the catalyst was detected and ZIF-8 was easily separated from the reaction mixture without poisoning of the catalyst. After five runs with recycled ZIF-8 the conversion remains high, proving that ZIF-8 is stable and shows no degradation.[65]

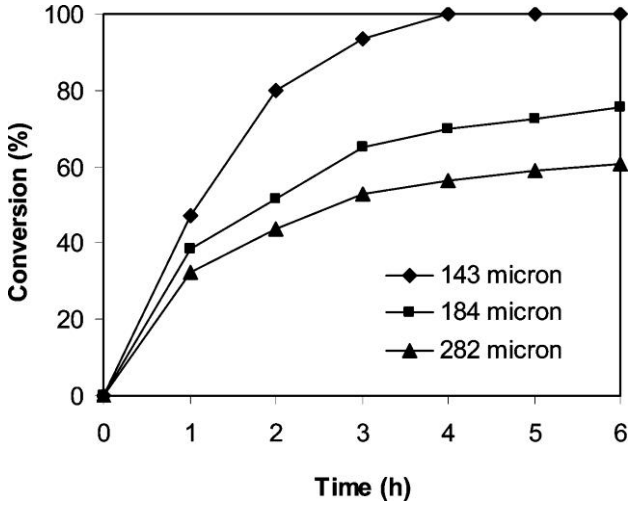

Figure 2.22 The effect of different ZIF-8 particle size on the conversion during the Knoevenagel condensation between benzaldehyde and malonitrile.[65] (Reprinted (adapted) with permission from U. P. N. Tran, K. K. A. Le and N. T. S. Phan , *ACS Catalysis.*, 2011, **1**, 120-127. Copyright (2011) American Chemical Society.)

In (**Figure 2.22** The effect of different ZIF-8 particle size, p **35**) it can be seen that during the Knoevenagel condensation of benzaldehyde and malonitrile, ZIF-8 particles with a smaller size (143 micron) exhibit a higher catalytic activity (100 % conversion after 4 hours) than larger particles (282 micron) with only 55 % conversion after 4 hours, because smaller particles have a larger external surface area with more available active sites.[65] This trend will form the bases of the study on the catalytic activity of ZIF-8 nanoparticles performed in this investigation.

ZIF-8 also provides high catalytic activity for aldehyde substituents with both electron donating and withdrawing groups (**Figure 2.23**, p **36**). The electron withdrawing NO_2 of 4-nitrobenzaldehyde accelerates the reaction between the aldehyde and the activated methylene group with a 100 % conversion time of 1 hour, much faster than the other benzaldehyde in the investigation. The ZIF-8 catalyst can be used in quantities as little as 3 mol % to the aldehyde to obtain a 100 % conversion in 4 hours under mild conditions without an inert atmosphere.[65]

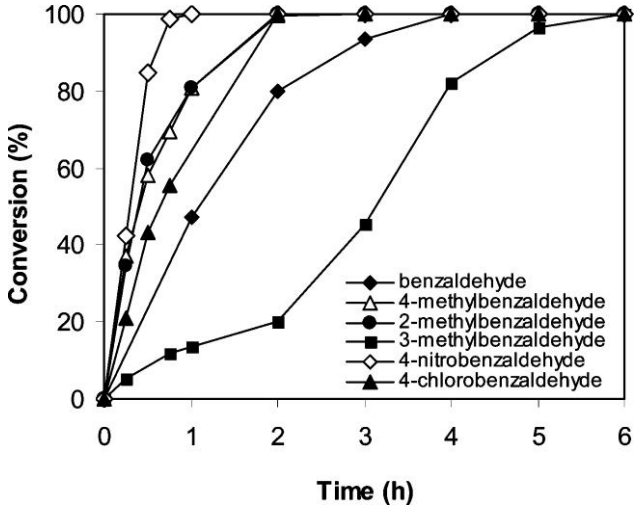

Figure 2.23 Conversion rates of Knoevenagel condensation with different substituents on the aldehyde using ZIF-8.[65] (Reprinted (adapted) with permission from U. P. N. Tran, K. K. A. Le and N. T. S. Phan , *ACS Catalysis.*, 2011, **1**, 120-127. Copyright (2011) American Chemical Society.)

2.9.2 Other Catalytic Studies with ZIF-8

In 2010 Chizallet *et al.* showed that the acid and basic sites on the external surface of ZIF-8 can catalyse the transesterification of vegetable oils (rapeseed oil) into alkyl esters. With improved results compared to known catalysts (e.g. $ZnAl_2O_4$), ZIF-8 allows the use of other alcohols besides methanol.[64] In general, Friedel-Crafts acylation of an aromatic ring with an acyl chloride needs a strong Lewis acid and inert atmosphere. ZIF-8 with its Lewis acid and base properties was shown to be an effective heterogeneous catalyst in the Friedel-Crafts acylation between anisole and benzyl chloride (**Scheme 2.5**). ZIF-8 can be used in a low mol % without the need of an inert atmosphere, and can be separated with ease from the reaction mixture.[30]

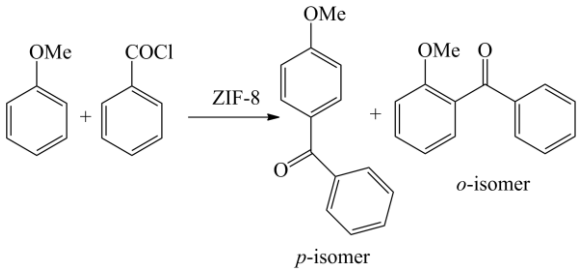

Scheme 2.5 Friedel-Crafts acylation of anisole and benzyl chloride with ZIF-8 as a catalyst.[30]

A selectivity of over 90 % of the *p*-isomer was obtained throughout the catalytic testing, 90 % and 70 % conversion after 6 hours for particle size of 92 μm and 210 μm respectively (**Figure 2.24**, p **37**).[30]

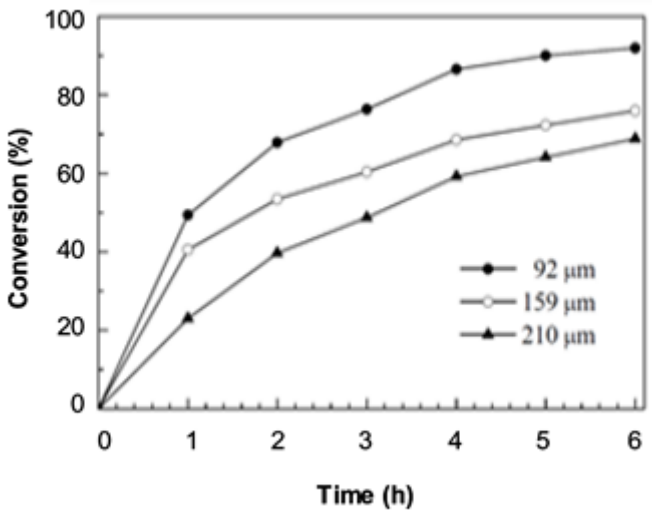

Figure 2.24 The effect of ZIF-8 catalyst with different particle sizes on the conversion during the Friedel-Craft acylation of anisole with benzyl chloride.[30] (Reprinted (adapted) from L. T. L. Nguyen, K. K. A. Le and T. S. Phan, *Chin. J. Catal.*, 2012, **33**, 688-696. Copyright (2012) Dalian Institute of Chemical Physics, Chinese Academy of Sciences.)

2.9.3 Catalysis with Ligand Exchanged ZIF-8 (SALEM-2)

In the previous (**Section 2.8, p 30**), 85 % of the ZIF-8 linkers were exchanged with imidazole to form SALEM-2. The imidazole linker was then deprotonated on the C_2 site by *n*-butyllithium (**Scheme 2.6**, p **37**) to form N-heterocyclic carbene-like moeities on the external surface area of SALEM-2.

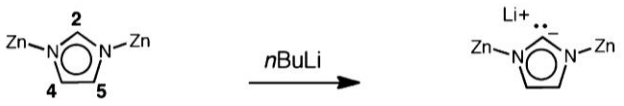

SALEM-2 **Li-SALEM-2**

Scheme 2.6 Lithiation of SALEM-2 with nBuLi.[7] (Reprinted (adapted) with permission from O. Karagiaridi, M. B. Lalonde, W. Bury, A. A. Sarjeant, O. K. Farha and J. T. Hupp, *J. Am. Chem. Soc.*, 2012, 134, 18790−18796. Copyright (2012) American Chemical Society.)

This surface lithiated product (Li-SALEM-2) was tested as a base catalyst in the conjugated addition of alcohols to 4-hexen-3-one (**Scheme 2.7**, p **38**). It was assumed that because of the steric demands of the alcohol reactants, 4-hexen-3-one, *n*-butyllithium and the product, the catalytic activity only takes place on the external surface area of the catalyst particles.

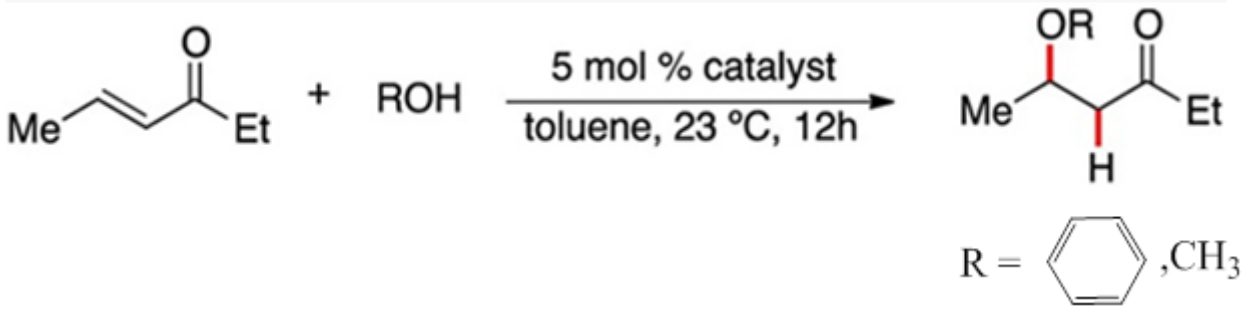

Scheme 2.7 Conjugated addition of an alcohol to 4-hexane-3-one with a lithiated SALEM-2 catalyst.[69] (Reprinted (adapted) with permission from S M. B. Lalonde, O. K. Farha, K. A. Scheidt and J. T. Hupp, *ACS Catal*., 2012, **2**, 1550-1554. Copyright (2010) American Chemical Society.)

Two different alcohols, benzyl alcohol and methanol, were used in the conjugated carbon addition. With the use of GC, Li-SALEM-2 showed to be an efficient catalyst with a conversion of 94 % for methanol and 81 % for benzyl alcohol, and can be separated like a heterogeneous catalyst. Li-SALEM-2 performed much better than the homogeneous catalyst 1,3-bis-(2,4,6-trimethylphenyl)imidazole-2-ylidene (IMes.HCl) with conversion of only 72 % with benzyl alcohol and 77 % for methanol. When ZIF-8 which was put through the same reaction conditions, it showed no catalytic activity in the conjugated addition of these alcohols.[7]

2.9.4 Catalysis with Pd@ZIF-8

Palladium loaded ZIF-8, Pd@ZIF-8, prepared by Yuan *et al.*, had very low catalytic activity in Suziki-Miyaura and Ullmann coupling reactions of aryl chlorides. This can be ascribed to the difficulty of aryl chlorides reactants and products to diffuse in and out of the 3.4 Å pore openings.[50] Pd@ZIF-8 performed well as catalyst for aminocarbonylation (**Scheme 2.8**, p **39**) under mild conditions with yields over 80 % and a turnover number (TON) of 2540. When recycled, Pd@nZIF-8 showed negligible change in activity. Both bromoarene and iodoarenes with various amines under mild conditions proved Pd@ZIF-8 to be a stable and active heterogeneous catalyst with low levels of leaching. A large variety of pharmaceutically important compounds such as cyclic amides, primary amides and carboxylic esters can potentially be synthesized with Pd@ZIF-8 as catalyst.[51]

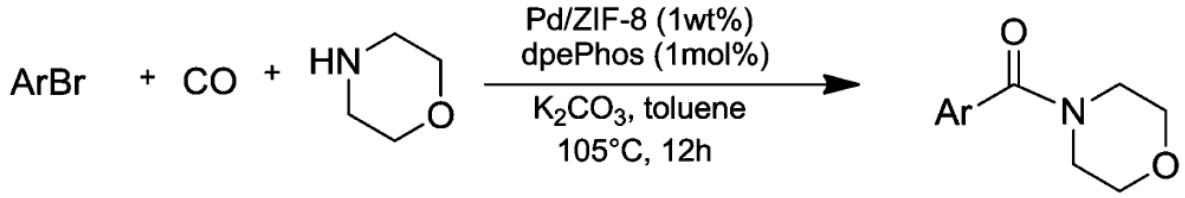

Scheme 2.8 Typical scheme for the aminocarbonylation of aryl bromides and morpholine with Pd@ZIF-8, dpePhos ((Oxydi-2,1-phenylene)bis(diphenylphosphine)) and K_2CO_3 in toluene.[51] (Reprinted (adapted) with permission from T. T. Dang, Y. Zhu, J. S. Y. Ngiam, S. C. Ghosh, A. Chen and A. M. Seayad, *ACS Catal.*, 2013, **3**, 1406-1410. Copyright (2013) American Chemical Society.)

References

[1] A. Phan, C.J. Doonan, F. J. Uribe-Romo, C. B. Knobler, M. O'Keeffe, O. M. Yaghi, *Acc. Chem. Res.*, 2009, **43**, 58-67.

[2] K. S. Park, Z. Ni, A. P. Cote, J. Yong, R. Huang, F. J. Uribe-Romo, H. K. Chae, M. O'Keeffe, O. M. Yaghi, *PNAS*, 2006, **103**, 10186-10191.

[3] J. Scherzer, *Catal. Rev.- Sci. Eng*, 1989, **31(3)**, 215-354.

[4] M. Schröder, *Functional Metal-Organic Frameworks: Gas Storage, Separation and Catalysis (Springer)*,2010, ch 14, 39-79.

[5] D. Farrusseng, S. Aguado and C. Pinel, *Angew Chem. Int. Ed.*, 2009, **48**, 7502-7513.

[6] S. Tanaka, K. Kida, M. Okita, Y. Ito, Y. Miyake, *Chem. Let.* 2012, **41**, 1337-1339.

[7] O. Karagiaridi, M. B. Lalonde, W. Bury, A. A. Sarjeant, O. K. Farha and J. T. Hupp, *J. Am. Chem. Soc*., 2012, **134**, 18790−18796.

[8] H. Wu, W. Zhou, T. Yildirim, *J. Am. Chem. Soc.*, 2007, **129**, 5314-5315.

[9] M. Zhou, Q. Wang, L. Zhang, Y-C Liu and Y. Kang, *J. Phys. Chem. B*, 2009, **113 (32)**, 11049-11053.

[10] B. Wang, A. P. Côté, H. Furukawa, M. O'Keeffe and O. M. Yaghi, *Nature*, 2008, **453**, 207-211.

[11] D. Peralta, G. Chaplais, A. Simon-Masseron, K. Barheket, C. Chizallet, A-A Quineaud and G. D. Pirngruber, *J. Am. Chem. Soc*, 2012, **134**, 8115-8126.

[12] D. Fairen-Jimenez, S. A. Moggach, M. T. Wharmby, P. A. Wright, S. Parsons and T. Düren, *J. Am. Chem. Soc*, 2011, **133**, 8900-8902.

[13] E. Haldoupis, T. Watanabe, S. Nair and D. S. Sholl, *ChemPhysChem*, 2012, **13(15)**, 3449-3452.

[14] S. A. Moggach, T. D. Bennett and A. K. Cheetham, *Angew. Chem.*, 2009, **121**, 7221-7223.

[15] H. Bux, F. Liang, Y. Li, J. Cravillon, M. Wiebcke and J. Caro, *J. Am. Chem. Soc*., 2009, **131**, 16000-16001.

[16] B. Seoane, J. M. Zamaro, C. Tellez and J. Coronas, *CrystEngComm*, 2012, **14**, 3103-3107.

[17] J. A. Thompson, K. W. Chapman, W. J. Koros, C. W. Jones and S. Nair, *Microporous and Mesoporous Materials*, 2012, **158**, 292-299.

[18] H-Y Cho, J Kim, S-N Kim and W-S Ahn, *Microporous and Mesoporous Materials*, 2013, **169**, 180-184.

[19] J. Yao, M. He, K. Wang, R. Chen, Z. Zhong and H. Wang, *CrystEngComm*, 2013, **15**, 3601-3606.
[20] A. M. Joaristi, J. Juan-Alcñiz, P. Serra-Crespo, F. Kapteijn and J. Gascon, *Cryst. Growth Des.*, 2012, **12**, 3489-3498.
[21] a) P. J. Beldon, L. Fábián, R. S. Stein, A. Thirumurugan, A. K. Cheetham and T. Friščić, *Angew. Chem. Int. Ed.*, 2010, **49**, 9640-9643; b) S. Tanaka, K. Kida, T. Nagaoka, T. Ota and Y. Miyake, *Chem. Commun*, 2013, **49**, 7884-7886.
[22] J. Cravillon, S. Münzer, K. Huber and M. Wiebcke, *Chem. Mater.*, 2009, **21**, 1410-1412.
[23] Y. Pan, Y. Liu, G. Zeng, L. Zhao and Z. Lai, *Chem. Commun.*, 2011, **47**, 2071-2073 .
[24] K. Kida, M. Okita, K. Fujita, S. Tanaka and Y. Miyake, *CrystEngComm*, 2013, **5,** 1794-1801.
[25] a) A. G. Marquez, P. Horcajada, D. Grosso, G. Ferey, C. Serre, C. Sanchez and C. Boissiere, *Chem. Commun.*, 2013, **49**, 3848-3850; b) A. Carné-Sánchez, I. Imaz, M. Cano-Sarabia and D. Maspoch, *Nature Chemistry*, 2013, **5**, 203-211.
[26] S. R. Venna, J. B. Jasinski and M. A. Carreon, *J. Am. Chem. Soc*, 2010, **132**, 18030-18033.
[27] a) P. Scherrer, *Nachr. Ges. Wiss. Göttingen*, 1918, **2**, 98-100; b) J. I. Langford and A. J. C. Wilson, *J. Appl. Cryst.*, 1978, **11**, 102-113; c) A. Monshi, M. R. Foroughi and M. R. Monshi, *World Journal of Nano Science and Engineering*, 2012, **2**, 154-160.
[28] I. B. Vasconcelos, T. G. da Silva, G. C. G. Militão, T. A. Soares, N. M. Rodrigues, M. O. Rodrigues, N. B. da Costa Jr., R. O. Freire and S. A. Junior, *RSC Adv.*, 2012, **2**, 9437-9442.
[29] Y. Hu, and H. Kazemian, S. Rohani, Y. Huang and Y. Song, *Chem. Commun.*, 2011, **47**, 12694-12696.
[30] L. T. L. Nguyen, K. K. A. Le and T. S. Phan, *Chin. J. Catal.*, 2012, **33**, 688-696.
[31] P. Küsgens, M. Rose, I. Senkovska, H. Fröde, A. Henschel, S. Siegel and S. Kaskel, *Microporous and Mesoporous Materials*, 2009, **120**, 325-330.
[32] K Zhang, R. P. Lively, M. E. Dose, A. J. Brown, C. Zhang, J. Chung, S. Nair, W. J. Koros and R. R. Chance, *Chem. Commun*, 2013, **49 (22)**, 3245-3247.
[33] M. C. McCarthy, V. Victor-Guerrero, G. V. Barnett, H. K. Jeong, *Langmuir*, 2010, **26**, 14636-14641.
[34] C. Chmelik, J. van Baten and R. Krishna, *Journal of Membrane Science*, 2012, **397**-**398**, 87-91.
[35] N. Chang, Z-Y Gu and Y-P Yan, *J. Am. Chem. Soc*, 2010, **132**, 13645-13647.
[36] K. A. Cychosz and A. J. Matzger, *Langmuir*, 2010, **26**, 17198-17202.
[37] A. Demessence, C. Boissière, D. Grosso, P. Horcajada, C. Serre, G. Férey, G. J. A. A. Soler-Illia and C. Sanchez, *J. Mater. Chem.*, 2010, **20**, 7676-7681.
[38] J. Cravillon, C. A. Schröder, R. Nayuk, J. Gummel, K. Huber and M. Wiebcke, *Angew. Chem. Int. Ed.*, 2011, **50**, 8067-8071.
[39] J. Cravillon, R. Nayuk, S. Springer, A. Feldhoff, K. Huber and M. Wiebcke, *Chem. Mater.*, 2011, **23**, 2130-2141.
[40] Y. Pan, D. Heryadi, F. Zhou, L. Zhou, G. Lestari, H. Su, Z. Lai, *CrystEngComm*, 2011, **13**, 6937-6940.
[41] S. K. Nune, P. K. Thallapally, A. Dohnalkova, C. Wang, J. Liu and J. Exarhos, *Chem. Commun.*,2010. **46**, 4878-4880.
[42] D. Yamamoto, T. Maki, S. Watanabe, H. Tanaka, M. T. Miyahara and K. Mae, *Chemical Engineering Journal*, 2013, **227**, 145-150.
[43] M. Meilikhov, K. Yusenko, D. Esken, S. Turner, G. van Tendeloo and R. A. Fischer, *Eur. J. Inorg. Chem.*, 2010, **24**, 3701-3714.
[44] a) T. Ishida, M. Nagaoka, T. Akita and M. Haruta, *Chem. Eur.*, 2008, **14**, 8456-8460; b) F. Schröder, D. Esken, M. Cokoja, M. W. E. van den Berg, O. I. Lebedev, G. van Tendeloo, B. Walaszek, G. Buntkowsky, H-H Limbach, B. Chaudret and R. A. Fischer, *J. Am. Chem. Soc.*, 2008, **130**, 6119-6130; c) M. Müller, S. Turner, O. I. Lebedev, Y. Wang, G. van Tendeloo and R.

A. Fischer, *Eur. J. Inorg. Chem.*, 2011, **12**, 1876-1887 d) H. Liu, Y. Liu, Y. Li, Z. Tang and H. Jiang, *J. Phys. Chem. C*, 2010, **114**, 13362-13369.
[45] H-L Jiang, B. Liu, T. Akita, M. Haruta, H. Sakurai and Q. Xu, *J. Am. Chem. Soc.*, 2009, **131**, 11302-11303.
[46] D. Esken, S. Turner, O. I. Lebedev, G. van Tendeloo and R. A. Fischer, *Chem. Mater.*, 2010, **22**, 6393-6401.
[47] H-L Jiang, T. Akita, T. Ishida, M. Haruta and Q. Xu, *J. Am. Chem. Soc.*, 2010, **133**, 1304-1306.
[48] N. Miyaura and A. Suzuki, *Chem. Rev.*, 1995, **95**, 2457-2483.
[49] a) A. Henschel, K. Gedrich R. Kraehnert and S. Kaskel, *Chem. Commun.*, 2008, **35**, 4192-4194; b) S. Hermes, F. Schröder, S. Amirjalayer, R. Schmid and R. A. Fischer, *J. Mater. Chem.*, 2006, **16**, 2464-2472; c) M. Sabo, A. Henschel, H. Frödem E. Klemm and S. Kaskel, *J. Mater. Chem.*, 2007, **17**, 3827-3832; d) D. Esken, X. Zhang, O. I. Lebedev, F. Schroöder and R. A. Fischer, *J. Mater. Chem.*, 2009, **19**, 1314-1319; e) X. Gu, Z-H Lu, H-J Jiang T. Akita and Q. Xu, *J. Am. Chem. Soc.*, 2011, **133**, 11822-11825; f) Y. E. Cheon and M. P. Suh, *Angew. Chem. Int. Ed.*, 2009, **48**, 2899 –2903.
[50] B. Yuan, Y. Pan, Y. Li B. Yin and H. Jiang, *Angew. Chem. Int. Ed.*, 2010, **49**, 4054-4058.
[51] T. T. Dang, Y. Zhu, J. S. Y. Ngiam, S. C. Ghosh, A. Chen and A. M. Seayad, *ACS Catal.*, 2013, **3**, 1406-1410.
[52] P-Z Li, K. Aranishi and Q. Xu, *Chem. Commun*., 2012, **45**, 3173-3175.
[53] D. Esken, S. Turner, C. Wiktor, S. B. Kalidindi, G. van Tendeloo and R. A. Fischer, *J. Am. Chem. Soc*, 2011, **133**, 16370-16373.
[54] D. Esken, H. Noei, Y. Wang, C. Wiktor, S. Turner, G. van Tendeloo and R. A. Fischer, *J. Mater. Chem.*, 2011, **21**, 5907-5915.
[55] E. M. Banach, H. A. Stil and H. Geerlings, *J. Mater. Chem.*, 2012, **22**, 324-327.
[56] W. Wang, Y. Li, R. Zhang, D. He, H. Liu and S. Liao, *Catalysis Communications*, 2011, **12**, 875-879.
[57] M. Zahmakiran , *Dalton Trans.*, 2012, **41**, 12690-12696.
[58] G. Lu, S. Li, Z. Guo, O. K. Farha, B. G. Hauser, X. Qi1, Y. Wang, X. Wang, S. Han, X. Liu, J. S. DuChene, H. Zhang, Q. Zhang, X. Chen, J. Ma, S. C. J. Loo, W. D. Wei, Y. Yang, J. T. Hupp and F. Huo, *Nature Chemistry*, 2012, **4**, 310-316.
[59] P. Wang, J. Zhao, X. Li, Y. Yang, Q. Yang and C. Li, *Chem. Commun.*, 2013, **49**, 3330-3332.
[60] C-H Kuo, Y. Tang, L-Y Chou, B. T. Sneed, C. N. Brodsky, Z. Zhao and C-K Tsung, *J. Am. Chem. Soc*, 2012, **134 (35)**, 14345-14348.
[61] W. Morris, C. J. Doonan, H. Furukawa, R. Banerjee and O. M. Yaghi, , *J. Am. Chem. Soc.*, 2008, **130**, 12626-12627.
[62] M. Kim, J. F. Cahill, H. Fei, K. A. Prather and S. M. Cohen, *J. Am. Chem. Soc.*, 2012, **134**, 18082-18088.
[63] O. Karagiaridi, W. Bury, A. A. Sarjeant, C. L. Stern, O. K. Farha and J. T. Hupp, *Chem. Sci*., 2012, **3**, 3256-3260.
[64] C. Chizallet, S. Lazare, D. Bazer-Bachi and Fabien Bonnier, *J. Am. Chem. Soc.*, 2010, **132**, 12365-12377.
[65] U. P. N. Tran, K. K. A. Le and N. T. S. Phan , *ACS Catalysis.*, 2011, **1**, 120-127.
[66] I. Vogel, *A Text-book of Practical Organic Chemistry Including Qualitative Organic Analysis third edition (Longmans),*1961, 710-711.
[67] A. M. Asiri, *Appl. Organometal. Chem.* 2001, **15**, 907-915.
[68] L. T. L. Nguyen, K. K. A. Le, H. X. Truong and N. T. S. Phan, *Catal. Sci. Technol*, 2011, **2**, 521-528.
[69] S M. B. Lalonde, O. K. Farha, K. A. Scheidt and J. T. Hupp, *ACS Catal*., 2012, **2**, 1550-1554.

3 Result and Discussion

3.1 Introduction

In this chapter, the synthesis and characterization of nano-sized Zeolitic Imidazolate Framework -8 (nZIF-8) with particle size control are described first. Thereafter the impregnation of nZIF-8 with silver and palladium metals will be discussed. Solvent assisted ligand exchange (SALE) reactions of nZIF-8 with imidazole as well as further post synthetic modification on the exchanged linkers will be discussed.

Characterizations of the above ZIFs include Fourier transform infrared (FT-IR), Powder X-ray diffraction (PXRD), accelerated surface area and porosity analysis (ASAP), Transmission Electron Microscopy (TEM) with Energy-dispersive X-ray spectroscopy (EDS), Thermo-gravimetric analysis (TGA), X-ray Photoelectron Spectroscopy (XPS), inductively coupled plasma – optical emission spectrometry (ICP-OES) and Nuclear magnetic resonance (NMR) where appropriate.

Lastly, the catalysis of a Knoevenagel condensation reaction by nZIF-8 will be discussed.

3.2 Synthesis of Nano-sized ZIF-8 (nZIF-8)

3.2.1 Synthesis

ZIF-8 nanoparticles (nZIF-8) were synthesized using a rapid isothermal bench top reaction open to the atmosphere.[1] $Zn(NO_3)_2.4H_2O$ (2,48 mmol) and 2-methylimidazole (MeIM, 19.99 mmol) was dissolved separately in methanol (50 cm^3) at the specified reaction temperature. The MeIM solution was added rapidly into the Zn^{2+} solution and stirred vigorously for 1h while maintaining the temperature constant (see **Scheme 3.1**, p **44**). To control the particle size eight isothermal syntheses between -15℃ and 60℃ (see **Table 3.1**, p **45**) with a set ratio of Zn^{2+}:MeIM:MeOH of 1:8:1000 were performed in triplicate. Immediately after the addition the solution turned into a white milky suspension. At synthesis temperature between -15℃ and 2℃ the solutions turn

milky much slower than the reactions at higher temperatures. The reaction starts withthe deprotonation of MeIM which then coordinates to the Zn^{2+} ions in a tetrahedral manner. The excess of MeIM assists in the formation of nanoparticles by the neutral 2-methylimidazole ligand which shields the particles from growing further. The maximum temperature of 60 ℃ was chosen to prevent the evaporation of the solvent and avoid reflux conditions.

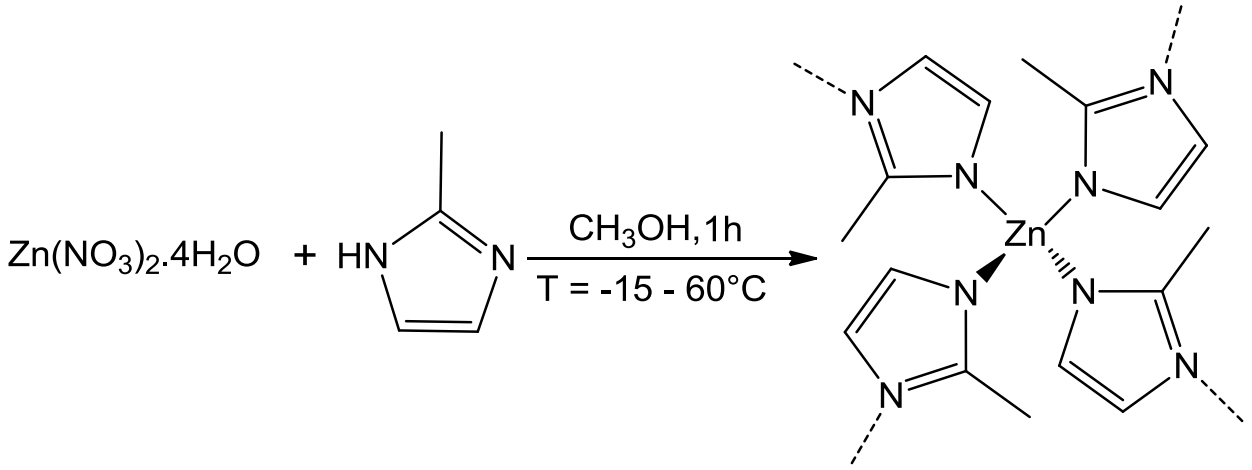

Scheme 3.1 General method to synthesize ZIF-8 nanoparticles isothermally at various temperatures (-15, -5, 2, 25, 30, 40, 50 and 60 °C) from zinc nitrate and 2-methylimidazole.

The nZIF-8 was in all cases isolated by centrifugation and washed with methanol. Thereafter nZIF-8 nanoparticles were dried and activated under vacuum at 100 ℃ to remove solvent and excess starting material from the pores. The resultant white powder is hydrophobic fairly stable and can be stored at ambient conditions without the need for reactivation prior to further use. For each temperature the synthesis was done in triplicate. Reproducible yields between 28 and 45 % were achieved, except for the nZIF-8 synthesized at -15 ℃ (9 %) (see **Table 3.1**, p **45**). The poor yield could be attributed to the lower solubility of reagents in methanol at this low temperature.

Table 3.1 Results of nZIF-8 synthesized at various temperatures from $Zn(NO_3)_2.4H_2O$ (2.46 mmol) and 2-methylimidazole (20 mmol) in methanol (100 cm^3). Syntheses were performed in triplicate to obtain average values. Particle sizes were measured indirectly by PXRD and directly by TEM.

Synthesis Temperature/ °C		**-15**	**-5**	**2**	**25**	**30**	**40**	**50**	**60**
Average Yield/ %		9	28.5	28.2	34.6	35.7	41.5	39.7	45.8
Particle Diameter by PXRD/ nm	**Average**	29.48	29.60	29.33	26.86	25.57	23.09	21.53	19.81
	Std. Dev.	3.22	3.11	4.21	1.69	2.47	1.88	2.01	1.34
Particle Diameter by TEM/ nm	**Average**	77.76	58.84	55.76	41.80	40.36	30.34	26.22	26.70
	Std. Dev.	15.45	11.60	9.72	7.79	7.95	5.36	4.11	4.08
	Minimum	39.02	31.57	29.76	22.76	21.75	14.84	15.84	14.88
	Maximum	115.47	82.37	76.20	58.95	55.65	43.23	35.99	39.23

3.2.2 Characterization

3.2.2.1 ATR-FTIR

All the nZIF-8 products were characterized by Fourier transform infrared spectroscopy (FTIR). In **Figure 3.1** (p **46**) the IR spectra of 2-methylimidazole (MeIM) starting material (a), commercial ZIF-8 (b) and the products of the -15 °C (c) and 60 °C (d) syntheses are compared. The MeIM spectrum (a) shows a broad peak between 2500 and 3000 cm^{-1}, associated with the NH stretching frequency. After nZIF-8 formation (c, d) it can be seen that this peak is no longer present indicating that the NH bond has been deprotonated and coordinated with the Zn metal. The FTIR spectra for the nZIF-8 synthesized at -15 °C (c) and 60 °C (d) is identical to that of the commercially available micro-sized ZIF-8 (Basolite Z1200)(b). This is true for all the products of all the other nZIF-8 syntheses as seen in **Appendix A.1 and Appendix A.2**. All nZIF-8 synthesized at different temperatures shows a weak stretching frequency at 3136 cm^{-1} for the methyl ($-CH_3$) group and the C=N stretching frequency at 1583 cm^{-1}. The fingerprint region below 1500 cm^{-1} is identical amongst all the nZIF-8 products.

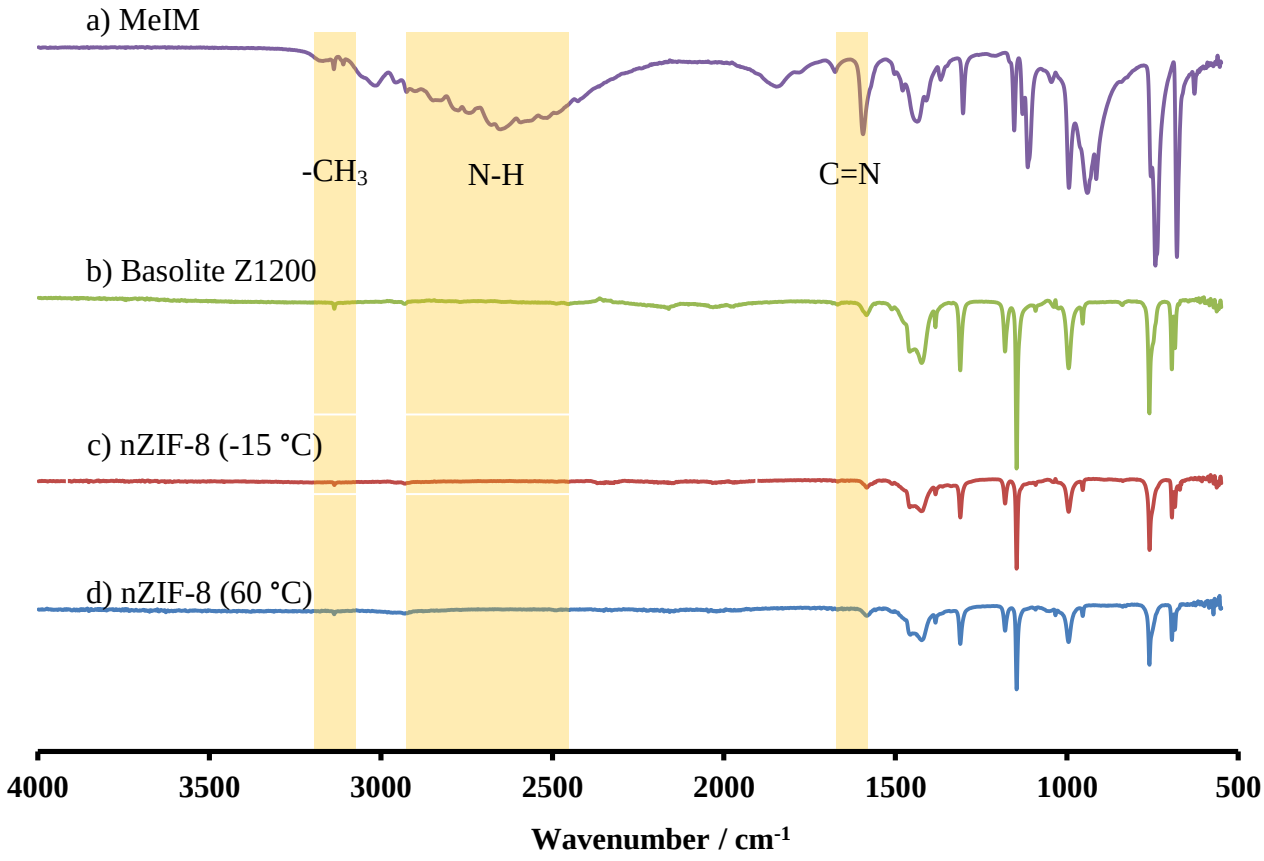

Figure 3.1 Comparison Transmission FTIR spectra of a) 2-methylimidazole (MeIM, purple), b) commercial ZIF-8 (Basolite Z1200) (green), c) nZIF-8 (synthesized at -15 °C; red) and d) nZIF-8 (synthesized at 60 °C; green).

3.2.2.2 PXRD

All the nZIF-8 products synthesized were characterized by Powder X-ray diffraction (PXRD), an efficient technique to verify the structure of the product. PXRD not only gives information about the structure, topology or crystallinity of the compound but can also detect some impurities. PXRD performed on commercial Basolite Z1200 as well as the simulated spectrum by X-ray crystallography was used as references (see **Figure 3.2**, p **47**). The PXRD patterns of nZIF-8 synthesized at -15 ℃ (a) and 60 ℃ (b) are identical with respect to peak positions to all the other nZIF-8 products (see **Appendix C.1**) and to the references (c, d). The well-defined PXRD patterns show that the synthesized nZIF-8 particle are highly crystalline (**Figure 3.2**, p **47)** and all have SOD (Sodalite) topology, showing that synthesis temperature has no influence on the structure.

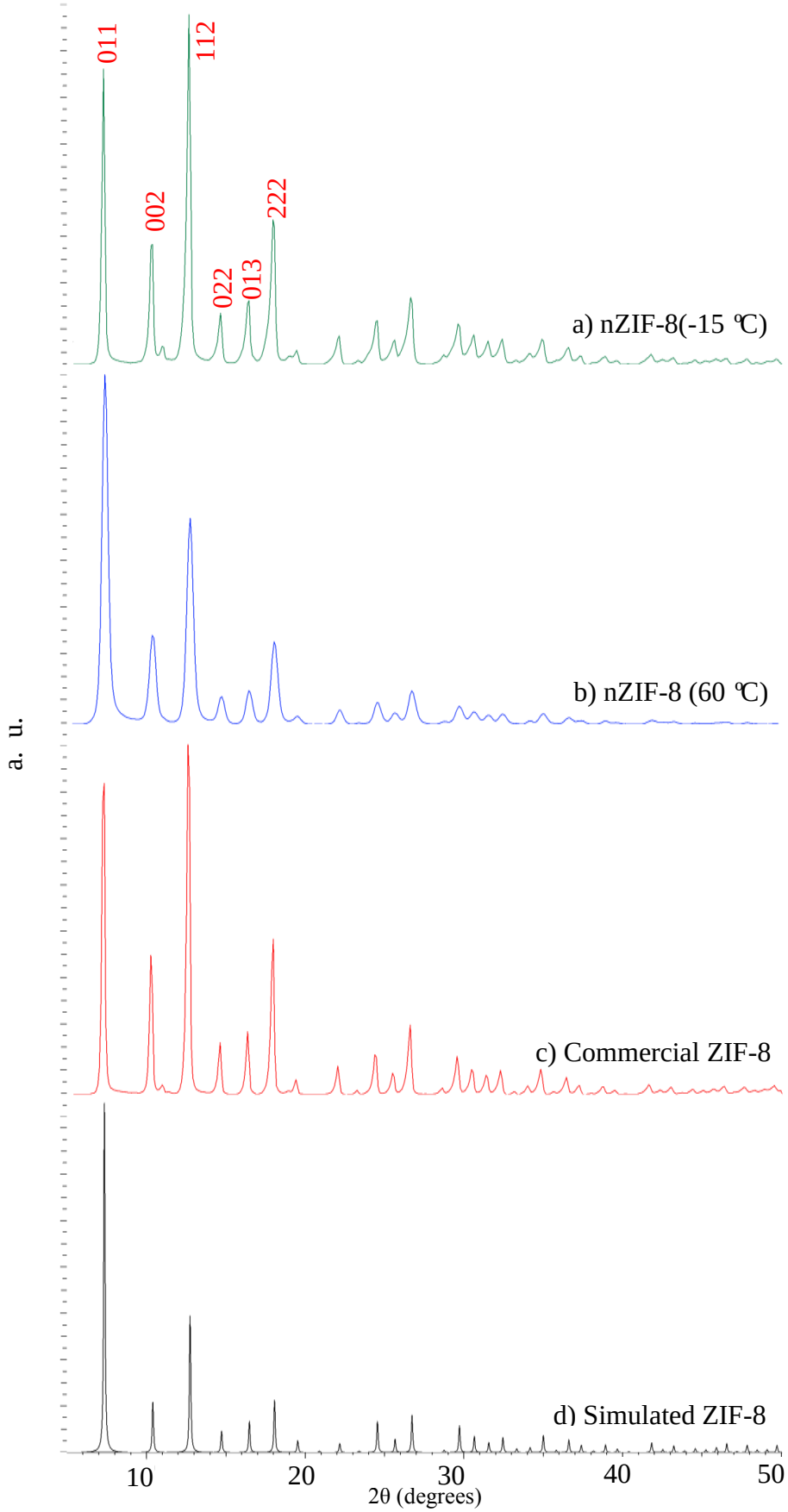

Figure 3.2 Powder X-ray Diffraction patterns of as-synthesized nZIF-8 synthesized at a) -15 ℃ (green) b) 60 ℃ (blue) c) commercial ZIF-8 (red) and d) simulated ZIF-8 (black). The Miller-indices of the first six signals are indicated.

When the PXRD spectra of all nZIF-8 synthesized at room temperature are compared to the simulated spectrum (d), obtained from ZIF-8 crystal data, it shows that these products are single phase ZIF-8. A slight shift in the peak positions may be due to the difference in measurement conditions, as the PXRD measurements of all nZIF-8 products were done at 25 ℃, while the crystal data used to generate the simulated PXRD pattern was obtained at 0 ℃. A difference in peak height between corresponding peaks of the different samples is caused by difference in sample preparation such as the grinding method which can influence the crystal packing in the sample cell.

When comparing the PXRD peaks of nZIF-8 (a and b) in (see **Figure 3.2**, p **47**) to those of the commercial sample (c) a slight broadening of the peaks is observed due to the nano crystalline nature of the nZIF-8. This peak broadening increases as the synthesis temperature increases. The nZIF-8 synthesized at 60 ℃ (b) shows the largest peak broadening compared to the commercial ZIF-8 (c). The Scherrer equation (1) can thus be implemented to calculate the average minimum particle sizes from this peak broadening for particles smaller than 100 nm.

$$D = \frac{K\lambda}{\beta \cos\theta} \quad (1)$$

Where D = particle diameter, K = the shape factor a typical value of 0.9, λ = X-ray wavelength, β = line broadening at half the maximum intensity (FWHM) and θ = Bragg angle. The FWHM (full width at half maximum) of the peak was determined assuming that the nZIF-8 particles are nearly of spherical shape with a shape factor (K) of 0.94. The FWHM of the peaks representing the 110, 200 and 211 faces on the PXRD patterns (see **Figure 3.2**, p **47**) were measured and used to calculate the average minimum crystallite size of nZIF-8, for each synthesis temperature (see **Table 3.1**, p **45**). Each isothermal synthesis was performed in triplicate and is reflected in the average values (**Appendix F.2 to F.4**). The minimum average crystalline size was observed to decrease as the synthesis temperature was increased (see **Table 3.1**, p **45**, PXRD average). A difference of ~10 nm was observed between nZIF-8 synthesized at -15 ℃ and 60 ℃. At synthesis temperatures below 2 ℃ the minimum particle size stayed relatively constant at ~29 nm but at synthesis temperatures higher than 25 ℃ a decrease in particle size till 20 nm was seen.

3.2.2.3 Electron Microscopy

Transmission electron microscopy (TEM) of the nZIF-8 synthesized at different temperatures was performed to obtain a direct measurement of the particle sizes and their size distribution. After a drop of nZIF-8 nanoparticle suspension in methanol was dropped onto a Formvar®

coated copper grid, the methanol was allowed to evaporate at room temperature. The organic linkers in the nZIF-8 particles cause sensitivity to the strong electron beam and therefore make it difficult to obtain high magnifications or multiple images on the same spot. TEM images at 64000x magnification of nZIF-8 synthesized at -15 ℃, 25 ℃ and 60 ℃ can be seen in **Figure 3.3** (p **49**) and the other nZIF-8 products in **Appendix B.1 to B.8**.

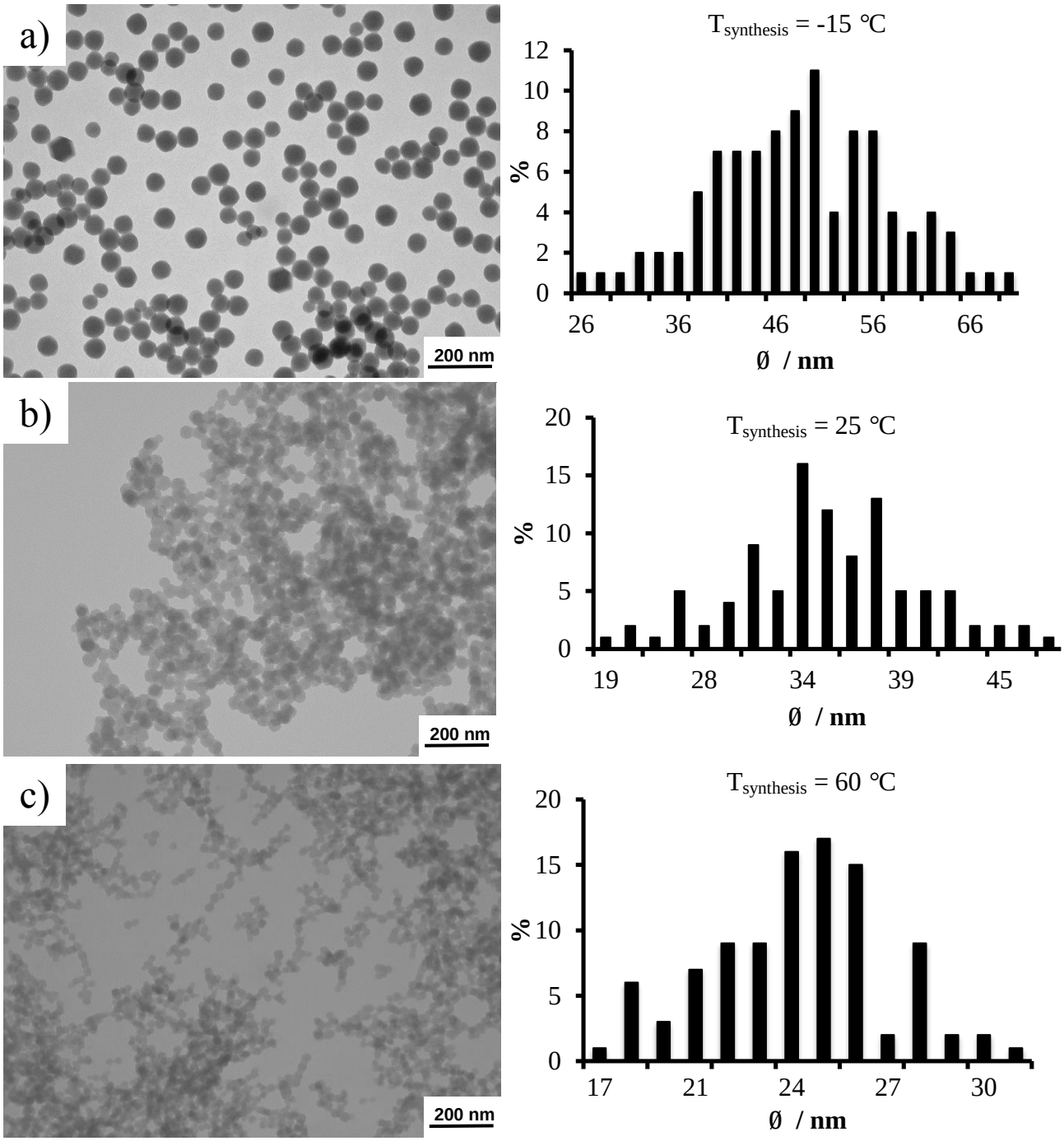

Figure 3.3 TEM images (left) accompanied by their respective particle size (Ø) histogram (right) of nZIF-8 particles synthesized at a) -15℃ b) 25℃ and c) 60℃ in methanol.

The observed particle sizes as determined by TEM, and summarized in **Table 3.1** (p **45**), are larger after low temperature syntheses than from higher temperature syntheses. This observation correlates to the minimum particle diameters calculated with the Scherrer equation from the PXRD patterns as seen in **Figure 3.5** (p **51**). The shape of the larger nanoparticles of nZIF-8 (-15 ℃ syntheses) have a rounder spherical shape than the smaller nZIF-8 particles (60 ℃ syntheses) which has a more hexagonal shape as seen in two dimensions (see **Figure 3.4**, p 50). This observation correlates to the three dimensional truncated octahedron shape of ZIF-8.[2,3]

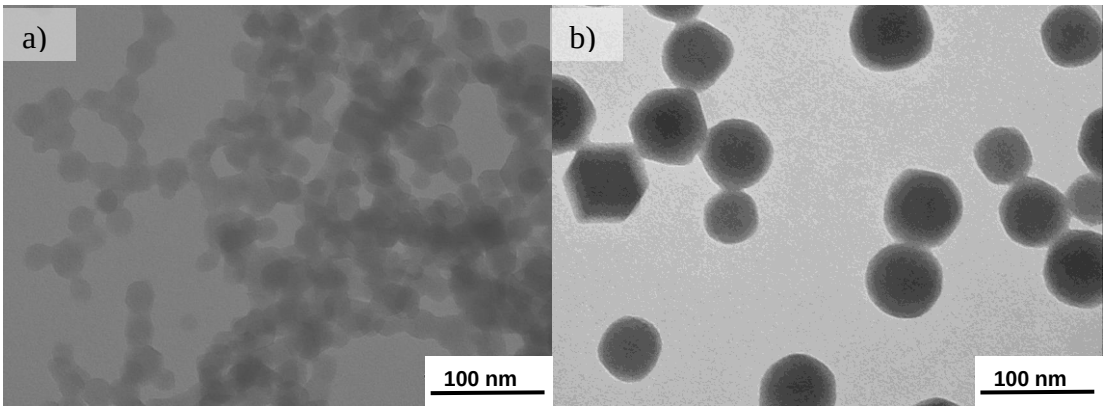

Figure 3.4 TEM images of nZIF-8, synthesized at a) 60 °C and b) -15 °C.

The particle size distribution histograms (see **Figure 3.3** (right), p **49**) were determined by statistically measuring 100 particles at random to determine the average particle size and particle size distribution, which became narrower as the synthesis temperature increased. The average crystallite size for each temperature, determined in triplicate, is represented in **Appendix F.5 to F.7**. A good correlation between the analysis by TEM and PXRD was observed (see **Figure 3.5**, p **51**). From the TEM measurements a decrease in average particle size from ~78 nm to ~26 nm can be seen. The advantage of using TEM rather than PXRD, is the ability to determine the exact particle sizes without the limitations of the Scherrer equation which only determine the average minimum crystallite size. As the synthesis temperature was increased the difference between the maximum and minimum particle size decreased from 78 nm (-15 ℃) to 24 (60 ℃) (see **Figure 3.5**, p **51**). With this set of results, the particle size and the particle size distribution of nZIF-8 can be controlled via synthesis temperature in methanol.

As reported earlier, the synthesis of nZIF-8 consists of slow nucleation accompanied by fast crystal growth.[4] In this study it was found that the size of nZIF-8 nanoparticles decreased as the synthesis temperature increased. This phenomenon can be explained as follows: Faster nucleation at high synthesis temperatures leads to a high concentration of nanoparticles by

consuming the majority of the starting material which inhibits crystal growth and results in small particles. The narrow size distribution, seen at higher synthesis temperatures, is also a result of the inhibited crystal growth. At low temperatures nucleation is slowed down, resulting in fewer particles which can grow larger (with a larger size distribution) in the abundance of starting material. The rate of nucleation is thus directly dependent on synthesis temperature, which could also be observed by the decreasing yield at lower synthesis temperatures (see **Table 3.1**, p **45**).

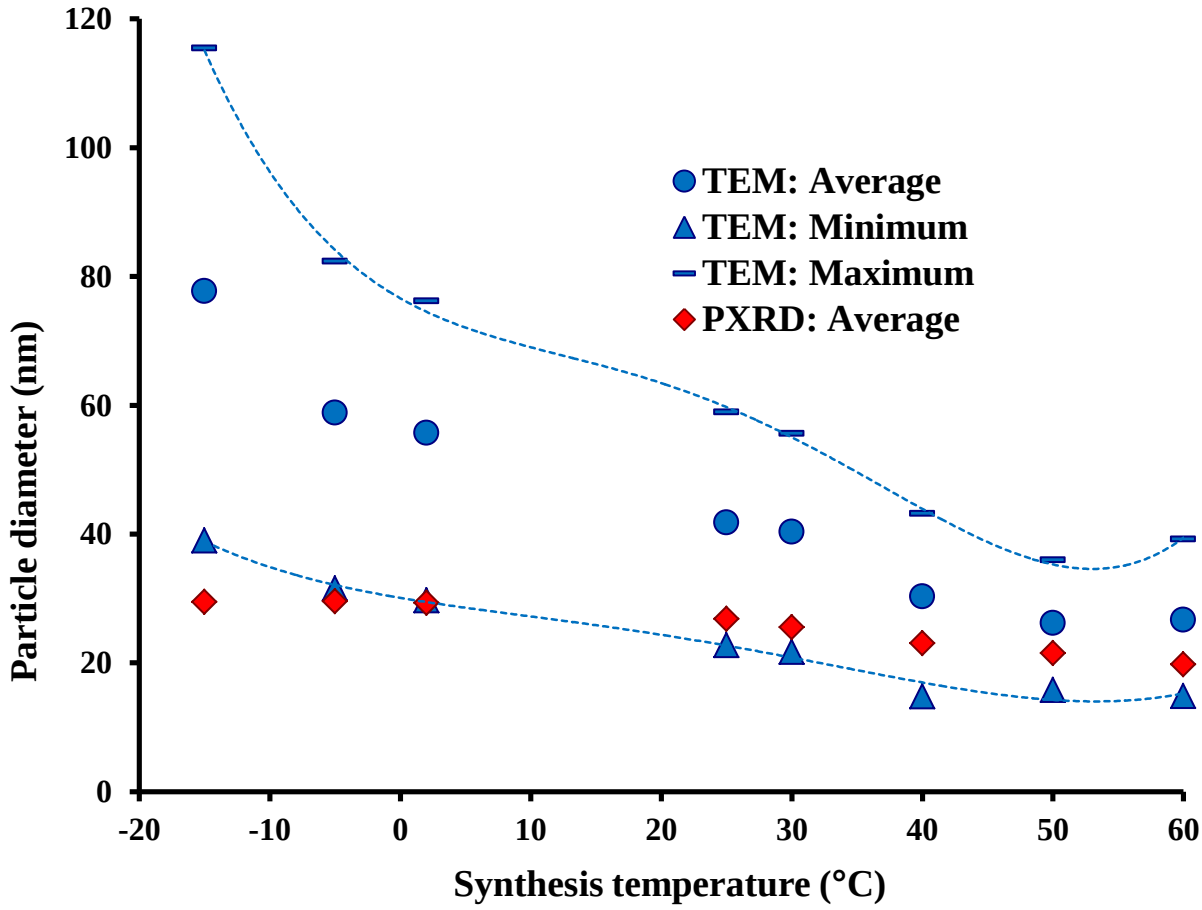

Figure 3.5 Graph of Particle diameter *vs.* synthesis temperature obtained from TEM measurements (blue): average particle diameter (circle), minimum diameter (triangle) and maximum diameter (dash). Average particle size from PXRD measurements is also represented (red).

3.2.2.4 Porosity Analysis

All the nZIF-8 batches synthesized from -15 ℃ till 60 ℃ gave similar N_2 isotherms after accelerated surface area and porosity analyses with N_2 at 77 K, as represented by the isotherm of nZIF-8 from the 60 ℃ synthesis (see **Figure 3.6.a**, p **52**). A typical Type-1 isotherm was obtained, proving that nZIF-8 is indeed microporous. The nZIF-8 is capable of adsorbing 400

cm^3 of nitrogen at (STP) per gram of nZIF-8 material at 77 K and a relative pressure of ~0.1 (p/p^0 with p^0 = 742.1 mmHg). The nZIF-8 isotherms correlates very well to the isotherm of commercial ZIF-8 obtained under the same conditions (see **Figure 3.6.b**, p **52**). The desorption isotherm shows no hysteresis with the adsorption isotherm (see **Figure 3.6**, p **52**) indicating that the sample was well evacuated and the activation period is sufficient.

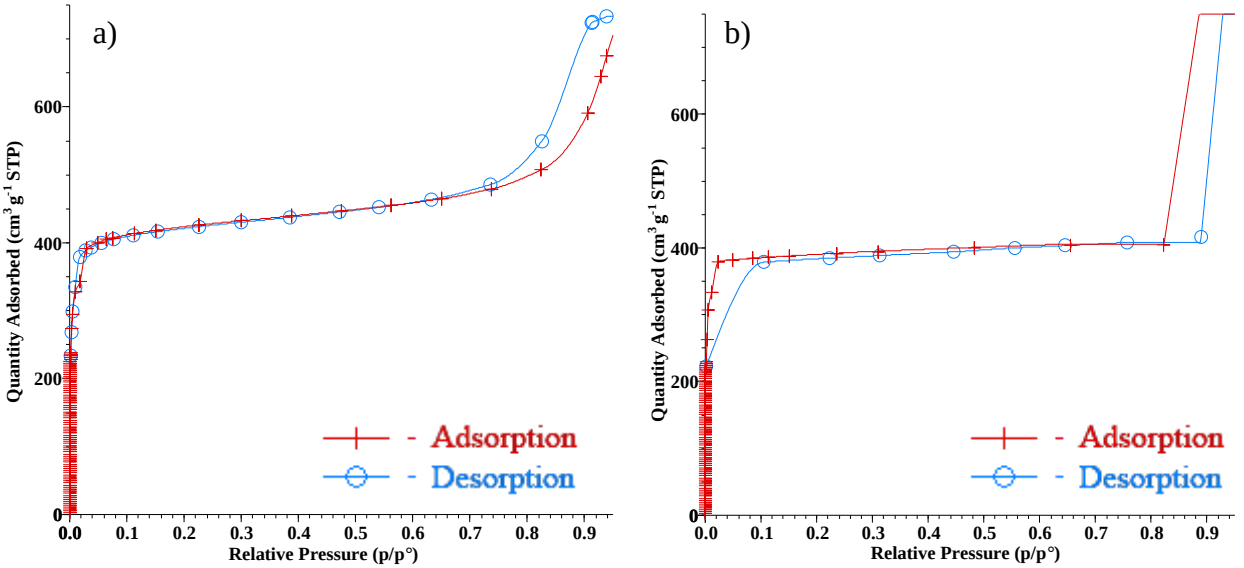

Figure 3.6 Adsorption and desorption N_2 isotherm at 77 K of nZIF-8 synthesized at a) 60 °C and b) commercial ZIF-8.

The isotherms of all the synthesized nZIF-8 (also see **Appendix G.1 to G.8)** were used to calculate their BET surface areas representing multilayer adsorption using the following linear expression:

$$\frac{P}{V_a(P_0 - P)} = \frac{1}{V_m C} + \frac{C - 1}{V_m C}\left(\frac{P}{P_0}\right)$$

Where V_a is the quantity gas adsorbed, pressure P, V_m gas quantity adsorbed for a monomolecular layer coverage, constant C and P_0 the saturation pressure. A nitrogen molecule, which covers 16.2 $Å^2$, was used to calculate the molecular layer at 77 K. Within the relative pressure range of 0.0032-0.05, the BET surface areas were calculated with a correlation of 0.999 (see **Table 3.2**, p **53**). The surface areas found for nZIF-8 is between ~1600 $m^2 g^{-1}$ and 1800 $m^2 g^{-1}$, corresponding to the BET surface area of commercial ZIF-8.

Table 3.2 Results of N_2 sorption measurements of nZIF-8 synthesized at different temperatures as well as commercial ZIF-8: BET surface area, micropore volume and external surface area (measured and calculated).

Sample (Synthesis Temperature)	Average Particle Size/ nm	BET Surface Area/ $m^2 g^{-1}$	t-plot Micropore Volume/ $cm^3 g^{-1}$	t-plot External Surface Area/ $m^2 g^{-1}$	Theoretical External Surface Area/ $m^2 g^{-1}$
nZIF-8 (-15°C)	78	1637 ± 43	0.50	254	174.0
nZIF-8 (-5°C)	59	1711 ± 26	0.52	266	229.9
nZIF-8 (2°C)	56	1816 ± 32	0.55	285	242.6
nZIF-8 (25°C)	42	1528 ± 39	0.44	300	323.6
nZIF-8 (30°C)	40	1858 ± 28	0.56	305	335.1
nZIF-8 (40°C)	30	1653 ± 24	0.49	315	445.9
nZIF-8 (50°C)	26	1783 ± 28	0.53	326	516.0
nZIF-8 (60°C)	27	1724 ± 37	0.51	336	506.7
ZIF-8 (commercial)	4900	1626 ± 28	0.55	116	2.8

The consistent range of BET surface area measurements and good correlation with that of the commercial ZIF-8, is also seen in the t-plot micropore volume, ranging from 0.44 – 0.56 $cm^3 g^{-1}$ and matching that of commercial ZIF-8 at 0.55 $cm^3 g^{-1}$. It was demonstrated that by synthesizing the nZIF-8 particles at different temperatures in methanol, the particle size can be controlled from 80 to 25 nm. As particle size decrease their external surface area per gram should increase. From the measured isotherms thickness curves, (t-plots) giving the thickness of the adsorbed layer can be obtained with the assumption that the nitrogen monolayer is 3.54 Å thick. The t-plot analyses were used to determine the t-plot external surface areas and t-plot micropore volumes of the nZIF-8 products (see **Table 3.2**, p **53**), using the Harkins and Jura thickness approximation.[5] The theoretical external surface areas (last column, **Table 3.2**, p **53**) were calculated using the average particle size, the volume of a truncated octahedron and a ZIF-8 density of 0.35 g cm^{-3} where a = length (see **Figure 3.7**, p **54**):

$$Volume = \left(8\sqrt{2}\right)a^2$$

$$Area = \left(6 + 12\sqrt{3}\right)a^2$$

$$Mass = Density\ x\ Volume$$

$$External\ Surface\ Area = \frac{Area}{Mass}$$

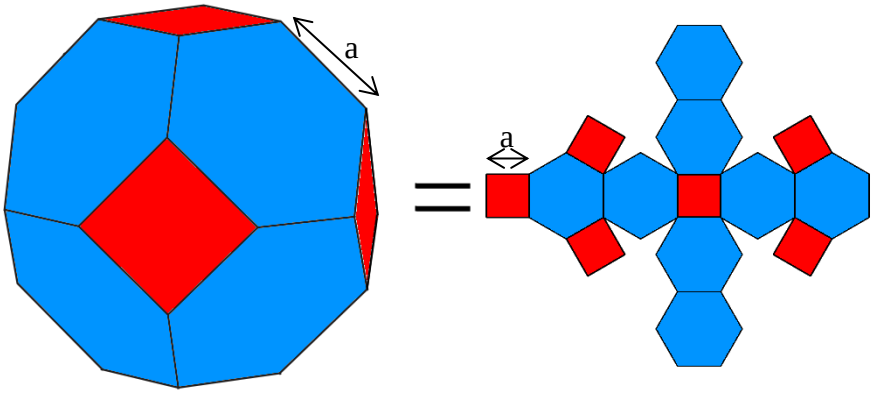

Figure 3.7 image of a truncated octahedron and open up to show the 6 squares and 8 hexagons.

As the nZIF-8 particle size decreases (from top to bottom), it was seen that the external surface area (measured and theoretical) increases (see **Table 3.2**, p **53**). This trend is represented in (see **Figure 3.8**, p **54**), where the t-plot external surface area decreases from 336 m^2 g^{-1} to 254 m^2 g^{-1} as the nanoparticles increase in size. This confirms that the smaller particles have increased external surface areas compared to the larger particles. The sharp increase in the theoretical surface area is because a flat model equation was used to determine the external surface area where as the t-plot model uses the thickness of the nitrogen atoms arranged on the external surface area.

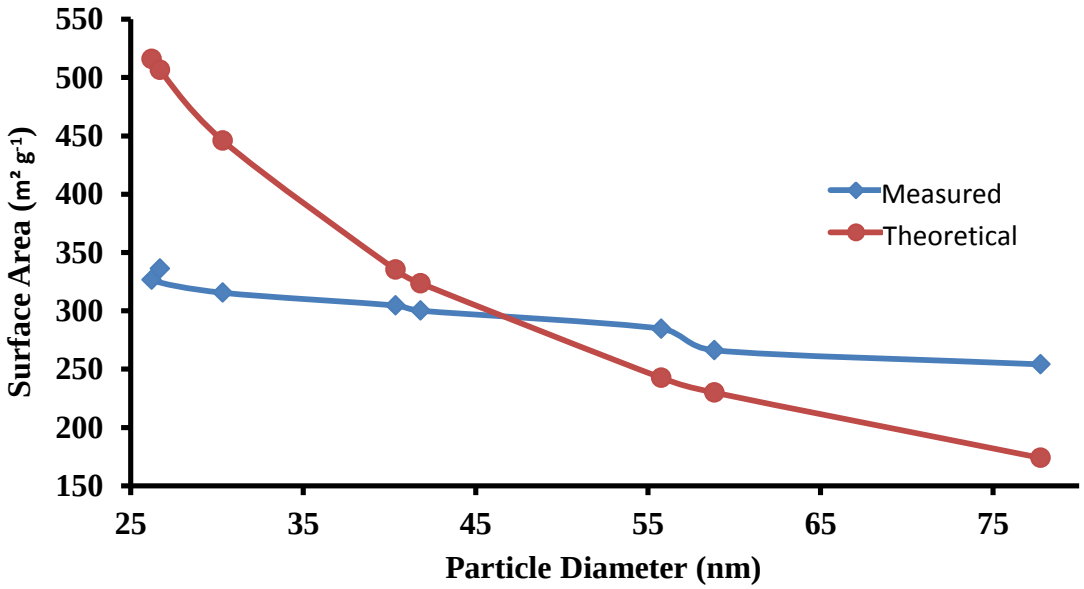

Figure 3.8 Graph of external surface area *vs.* particle diameter of nZIF-8 particles, from t-plot analyses after surface area measurements (blue) and theoretical calculations using particle diameter and the truncated octahedron particle shape (red).

3.2.2.5 Thermal Gravimetric Analysis (TGA)

TGA analyses were performed under argon atmosphere on all the nZIF-8 products, and gave identical TGA curves (see **Appendix E.1 to E.8**). The TGA thermogram of nZIF-8 synthesized at 60 ℃ (see **Figure 3.9**, p **55**) shows that nZIF-8 is stable up to 400 ℃ in argon where after the organic linkers begin to decompose with a weight loss of ~18 % followed by a continued collapse of the nZIF-8 structure after 600 ℃.

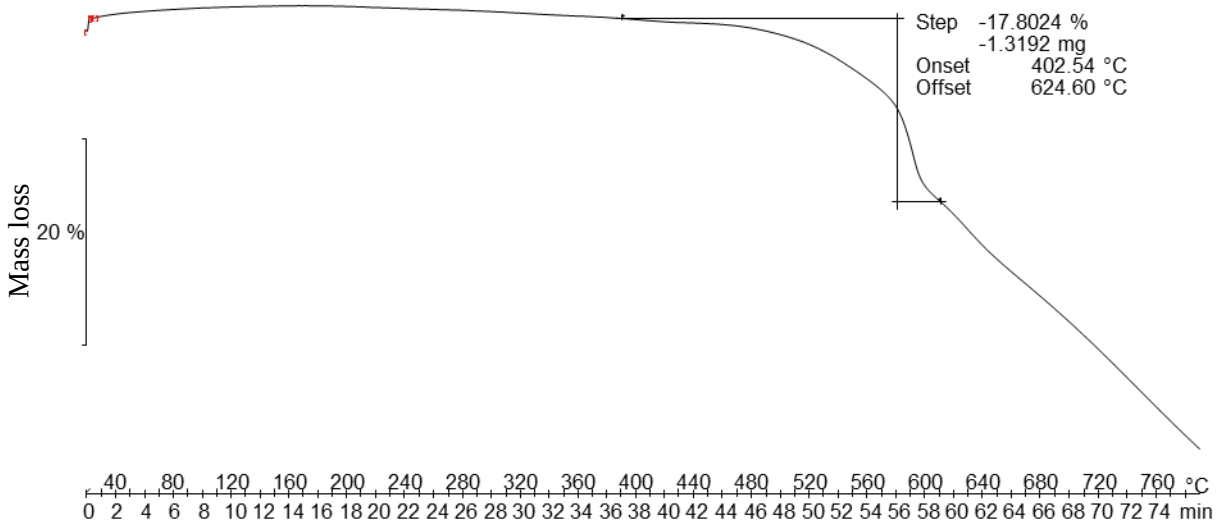

Figure 3.9 TGA thermogram in Ar of nZIF-8 synthesized at 60 ℃.

3.3 Metal Impregnation of nZIF-8

3.3.1 General Synthesis

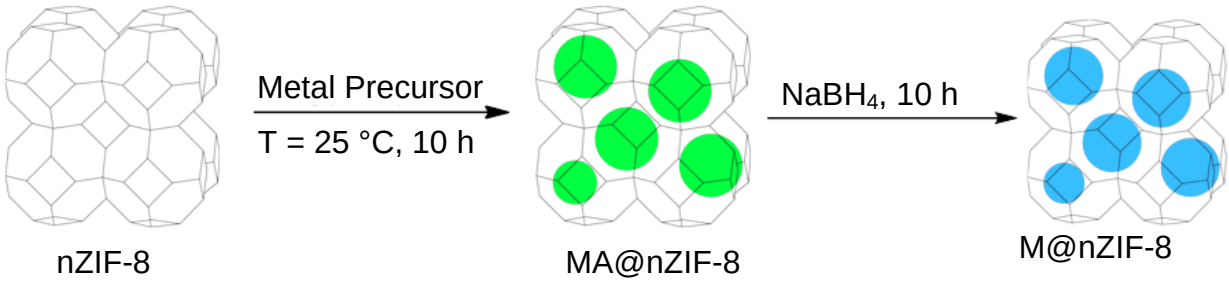

Scheme 3.2 General schematic representation of the synthesis of M@nZIF-8. MA = metal salt precursor; M = metal

The nZIF-8 synthesized at room temperature in bulk and activated at 120℃ for 6 hours under vacuum, was used for all the metal impregnation procedures, adapted from H-L Jiang's chemical liquid deposition method as shown in (**Scheme 3.2**, p **55**).[6] In this study metal impregnation was

performed on nano-sized ZIF-8, using metal salts, where after the loaded salts were subjected to chemical reduction by $NaBH_4$. The two metals used in this study were: silver, for its catalytic oxidation of ethylene[7], and palladium for its well-known catalytic activity in hydrogenation and C-C coupling reactions.[8] Silver nitrate was chosen as the silver precursor. Palladium nitrate, palladium acetate and palladium acetylacetonate as palladium precursors. Typically the nZIF-8 material was dispersed in methanol by ultra-sonification, whereafter the metal precursor, dissolved in methanol, was added and the mixture stirred for 10 hours. After that the products were isolated by centrifugation, washed with methanol and dried in air. Only the silver nitrate and palladium nitrate loaded nZIF-8 were isolated as intermediates ($AgNO_3$@nZIF-8 and $Pd(NO_3)_2$@nZIF-8 respectively). The other metal salts ($Pd(acac)_2$ and $Pd(OAc)_2$) were loaded into the nZIF-8 structure and subjected to reduction directly, without isolation of the intermediates.

Table 3.3 Summary of metal impregnation products of nZIF-8: Amount isolated and colour of dry powders.

Compound	Metal Salt Precursor	$C_{Metal\ Salts}$/ mM	Amount isolated/ %	Colour
$AgNO_3$@nZIF-8	$AgNO_3$	9.28	86 %	White
$Pd(NO_3)_2$@nZIF-8	$Pd(NO_3)_2$	9.28	91%	Light grey
Ag@nZIF-8	$AgNO_3$	9.28	91 %	Green
Ag_{high}@nZIF-8[a]	$AgNO_3$	18.56 (high)	89 %	Dark green
Pd@nZIF-8	$Pd(NO_3)_2$	9.28	95 %	Light grey
Pd@nZIF-8	$Pd(OAc)_2$	9.28	96 %	Light grey
Pd@nZIF-8	$Pd(acac)_2$	9.28	95 %	Dark grey

[a] This compound was impregnated using a high concentration (18.56 mM) of $AgNO_3$ in methanol.

After stirring of the metal precursor with nZIF-8 for 10 hours an excess of sodium borohydride ($NaBH_4$) was added to the mixture and stirred for another 10 hours before isolation (as described above). A summary of the metal impregnation procedures can be seen in (**Table 3.3,** p **56**). The $AgNO_3$@nZIF-8 was obtained after using a $AgNO_3$ solution with a concentration of either 9.28 mM or 18.56 mM. After loading with a double concentration of $AgNO_3$, the $NaBH_4$ concentration was also doubled during reduction. The white reaction mixture immediately turned green during reduction with the higher load of $AgNO_3$ results in a dark green suspension. Similarly, with the loading of $Pd(acac)_2$ and $Pd(OAc)_2$ in nZIF-8, the addition of the excess

$NaBH_4$ also lead to a change in colour. $Pd(OAc)_2$ loaded nZIF-8 changed from an orange to a cream suspension, while $Pd(acac)_2$ loaded nZIF-8 showed a colour change from light yellow to dark grey immediately after the addition of $NaBH_4$. All products were separated by centrifugation, washed with methanol and dried in air.

3.3.2 Ag@nZIF-8

During the impregnation procedure nZIF-8 was exposed to $AgNO_3$ in solution, followed by $NaBH_4$ as reducing agent. PXRD measurements were used to confirm the structural integrity of the framework after impregnation. The identical PXRD patterns for nZIF-8, $AgNO_3$@nZIF-8 and Ag_{high}@nZIF-8 (see **Figure 3.10**, p **57**) show no structural change of nZIF-8 during the chemical liquid deposition and chemical reduction procedure. nZIF-8 is thus resistant to the strong reducing agent, $NaBH_4$. No change in peak intensity or position was detected also for Ag@nZIF-8 (see **Appendix C.3**)**.** No reflection peaks were observed for silver particles due to their small size (< ~3 nm) and low concentration (< ~4 wt %).

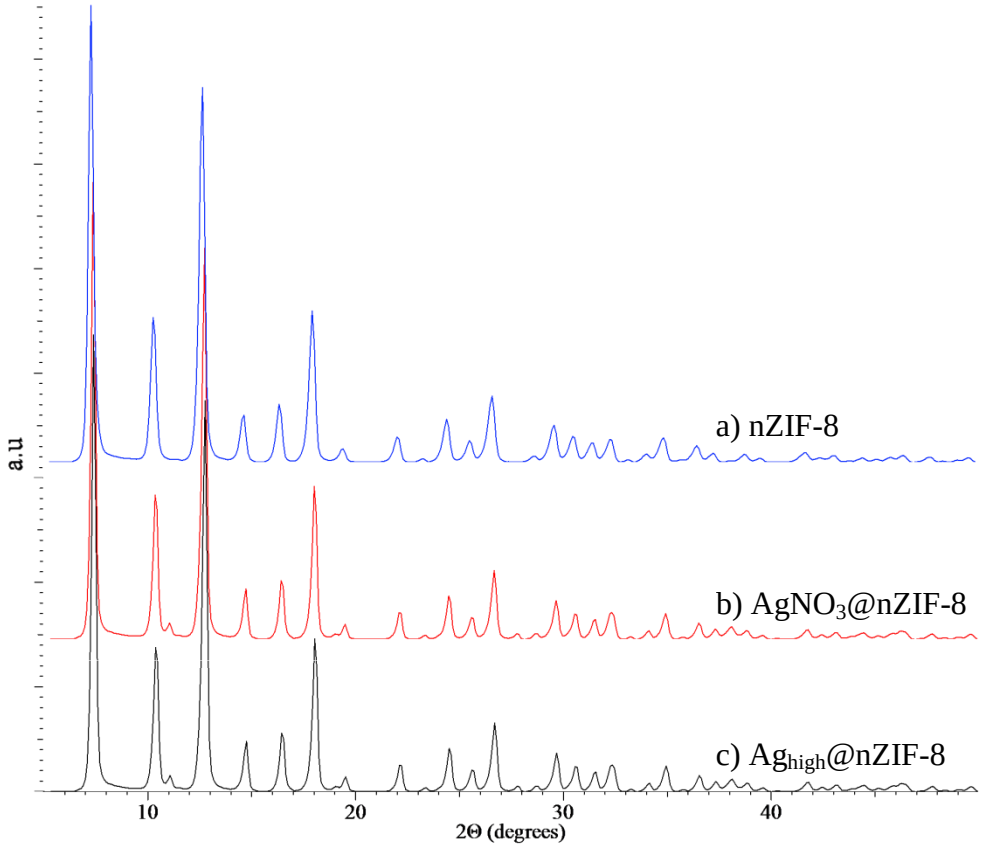

Figure 3.10 PXRD patterns of a) nZIF-8, b) $AgNO_3$@nZIF-8 and c) Ag_{high}@nZIF-8. $AgNO_3$@nZIF-8 is the intermediate and Ag_{high}@nZIF-8 the final product of the impregnation procedure of nZIF-8 with silver.

TGA analyses (see **Figure 3.11**, **p 58**)of the intermediate ($AgNO_3$@nZIF-8) and final product (Ag_{high}@nZIF-8) of the impregnation procedure show that these compounds remain stable up 400 ℃ in Argon, just like the starting material, nZIF-8 (see **Figure 3.9**, p **55**). This thermal stability was also observed for Ag@nZIF-8 (see **Appendix E.16**).

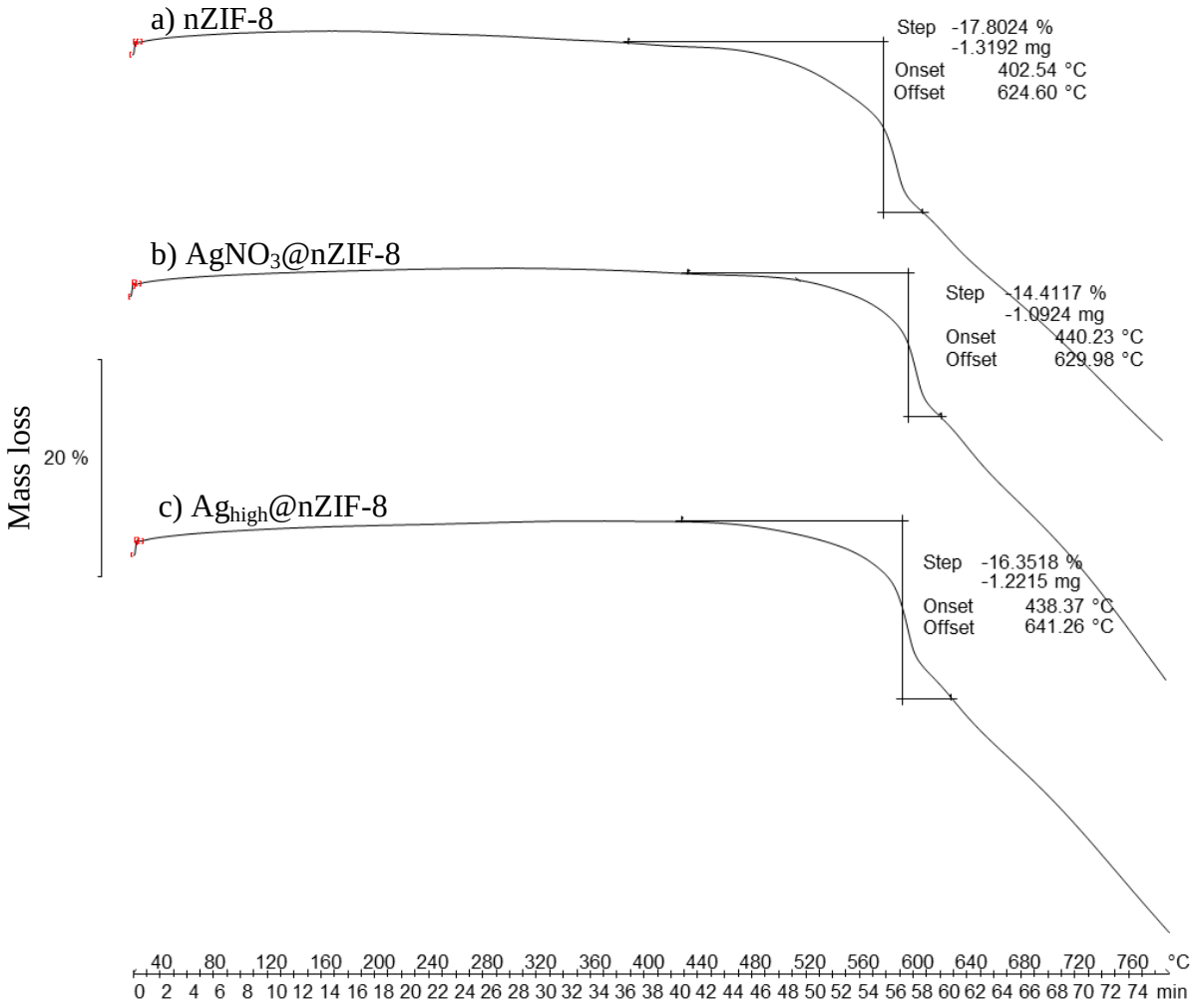

Figure 3.11 TGA thermograms of a) nZIF-8, b) $AgNO_3$@nZIF-8 and c) Ag_{high}@nZIF-8 taken in an Argon atmosphere.

Energy-dispersive X-ray Spectroscopy (EDS) coupled to Transmission Electron Microscopy (TEM) was used to qualitatively determine the presence of silver in the nZIF-8 structure after the impregnation procedure followed in (**Chapter 3.3.1**, p **55**). With the TEM-EDS the elements present in a selected area of a TEM image can be detected. The TEM images together with the EDS taken for $AgNO_3$@nZIF-8, Ag@nZIF-8 and Ag_{high}@nZIF-8 are shown in **Figure 3.12** (p **59**). For all there materials the EDS confirmed the presence of silver at ~3 keV (a.ii, b.ii and c.ii). It was observed that $AgNO_3$ form crystallites upon isolation and is not impregnated in the nZIF-8 framework (a.i).

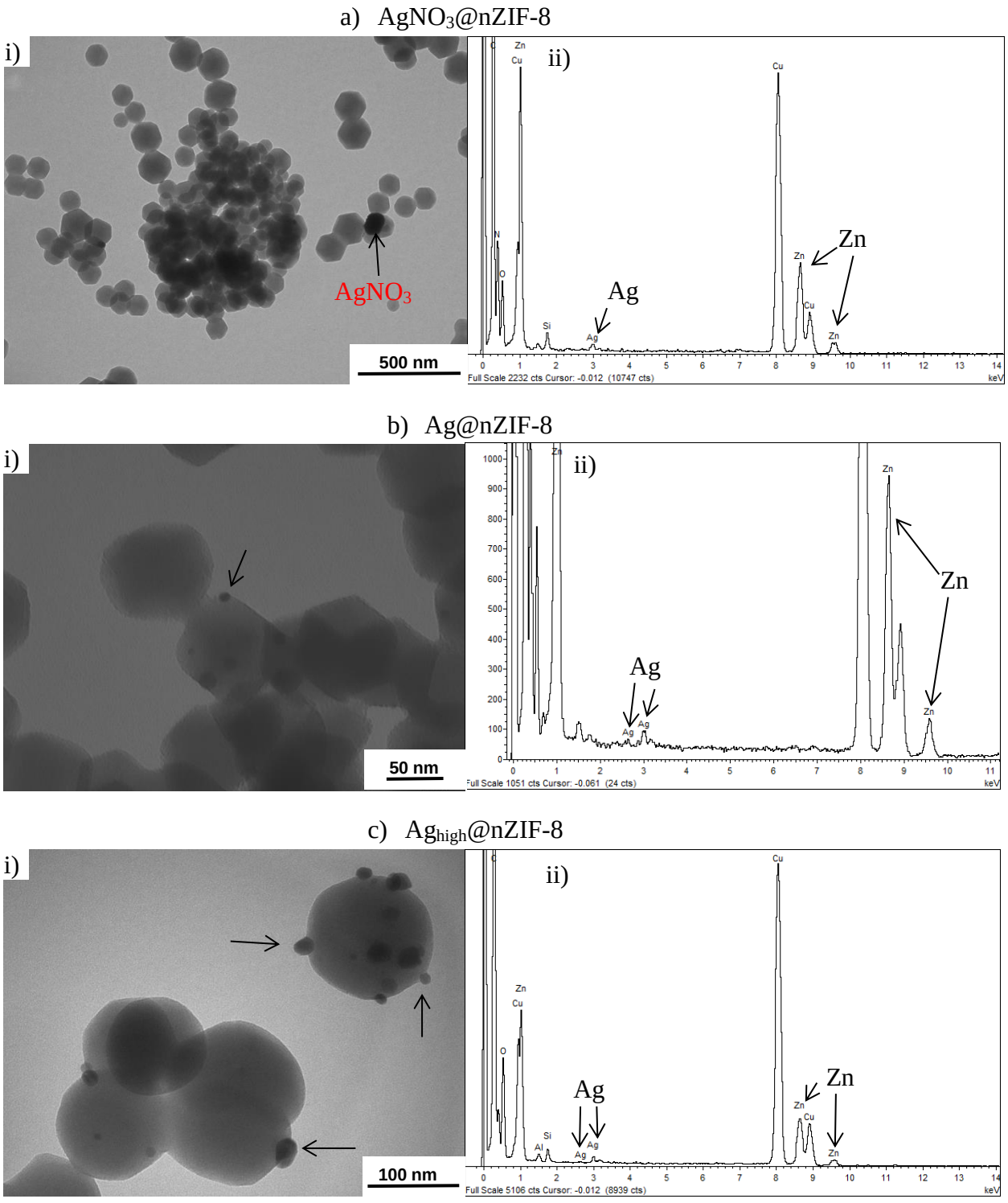

Figure 3.12 TEM images, accompanied by EDS spectra of a) $AgNO_3$@nZIF-8, b) Ag@nZIF-8 and c) Ag_{high}@nZIF-8.

This observation of silver nitrate crystals prompted the use of a one pot synthesis procedure whereby the $AgNO_3$ impregnated in nZIF-8 was reduced by $NaBH_4$ while still in a methanol suspension. After reduction, both the TEM images (b.i and c.i) show silver particles loaded onto the nZIF-8 particles without the presence of any large crystallite as in the case of $AgNO_3$@nZIF-

8 (a.i). The TEM images (b.i and c.i) show that the silver particles are mainly attached to the external surface of the nZIF-8 particles. The TEM images of Ag@nZIF-8 (b.i) shows that silver particles of ~5 nm were formed after reduction. When the silver nitrate concentration for impregnation was doubled a larger number of silver nanoparticles with average size of ~10-20 nm were observed (c.i). With an increased amount of silver, the silver agglomerates or grows to form larger particles. From the TEM images it can be seen that the nZIF-8 particles retain their shape and size (~100 nm as synthesized by the bulk reaction) and show no sign of agglomeration during the impregnation process. The copper signal seen in all the EDS spectra originates from the sample holder grid.

X-ray photoelectron spectroscopy (XPS) analyses performed on the silver loaded nZIF-8 samples ($AgNO_3$@nZIF-8, Ag@nZIF-8 and Ag_{high}@nZIF-8) showed that the samples contained large amounts of carbon and oxygen, due to the fact that the nZIF-8 samples could not be sputtered during the measurement. It also meant the atomic ratios of C, N, Zn and Ag were not accurate in some cases. As example the wide scan survey of Ag_{high}@nZIF-8 is shown in (see **Figure 3.13** (p **60**), displaying the relative low intensities of the twin 3d peaks of silver metal close to 400 eV.

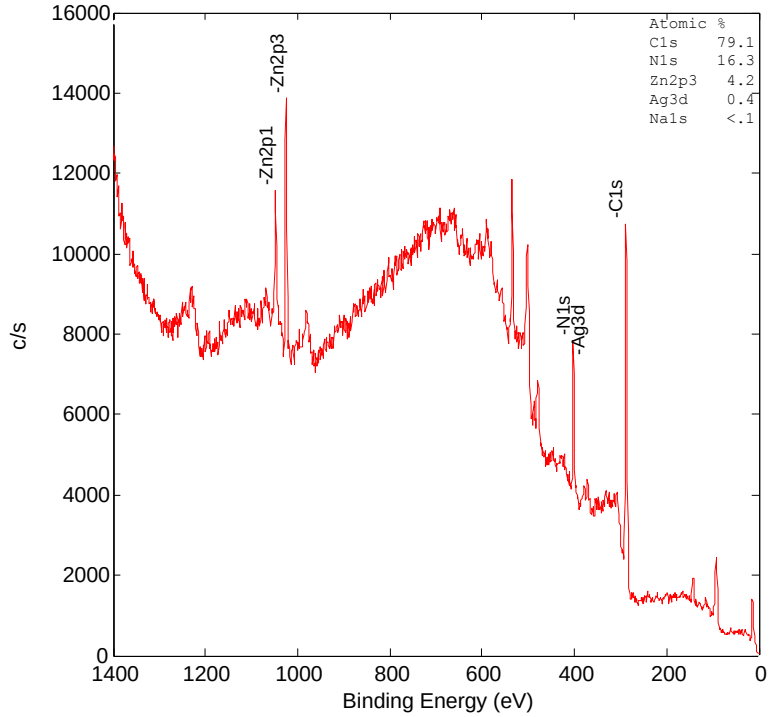

Figure 3.13 XPS wide scan Binding Energy of Ag_{high}@nZIF-8 showing the photoelectron and Auger peaks of the constituent atoms in the material. For clarity purposes the other peaks are not labeled.

The high resolution XPS scans of the three silver containing nZIF-8 materials ($AgNO_3$@nZIF-8, Ag@nZIF-8 and Ag_{high}@nZIF-8) showed identical signals for N (1s) as well as Zn (2p), as represented by (a) and (b) (see **Figure 3.14**, p **61**) respectively. The Ag (3d) signals for the three compounds are shown in (c), (d) and (e).

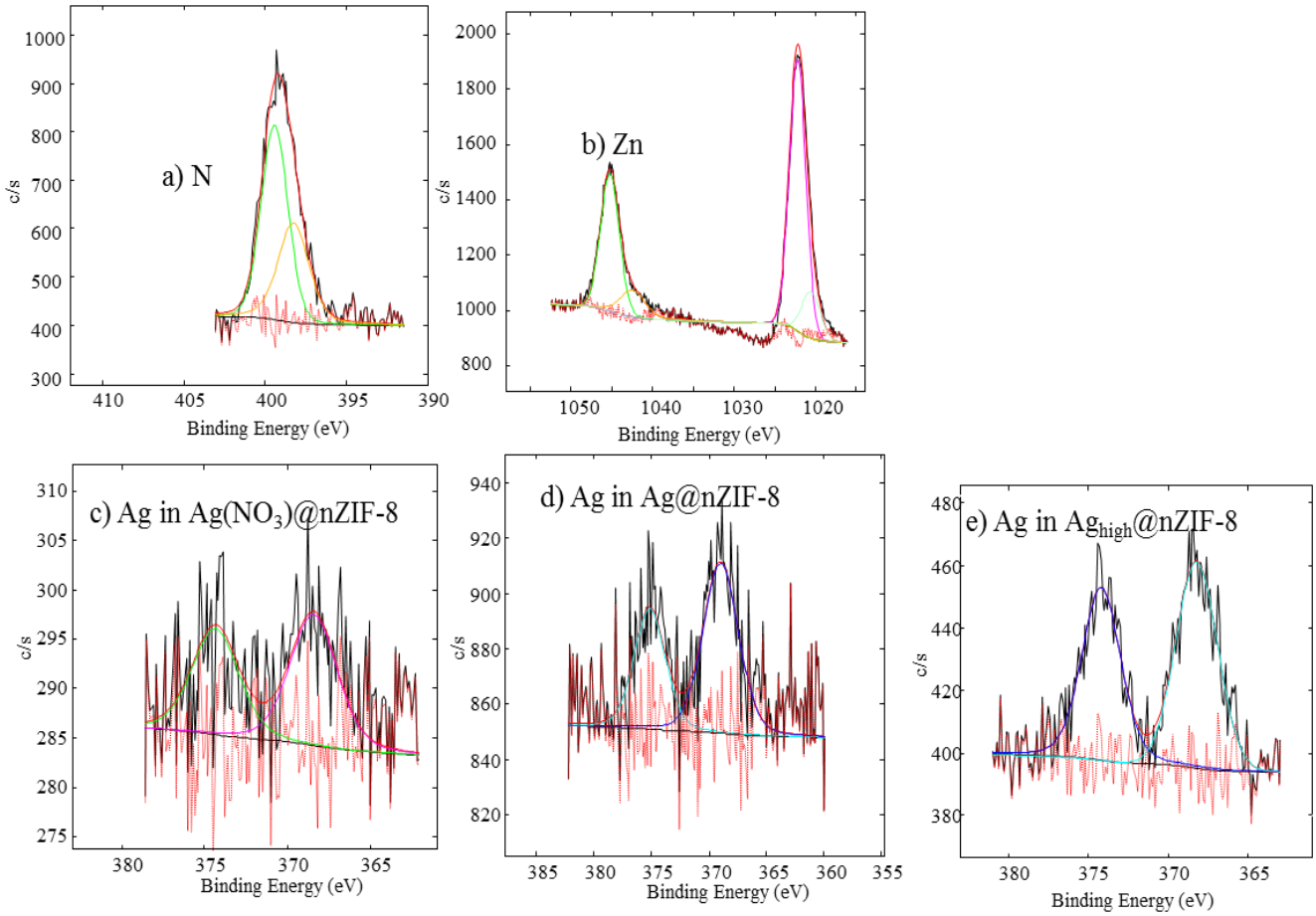

Figure 3.14 High resolution XPS scans of a) N (1s) and b) Zn (2p) in Ag_{high}@nZIF-8 as well as for Ag in c) $AgNO_3$@nZIF-8, d) Ag@nZIF-8 and e) Ag_{high}@nZIF-8.

By deconvolution of the N (1s) signal (a) the binding energy for the 1s orbital of N was shown to be a compliment of two separate peaks which is probably the result of the 399.44 eV for the C-N bonds and 398.27 eV for Zn-N bonds in the nZIF-8.[9] The Zn signal (b) appears as two separate peaks for the $2p_{1/2}$ (1045.24 eV) and $2p_{3/2}$ (1022.20 eV) orbitals. The silver signal appears as two peaks for $3d_{3/2}$ and $3d_{5/2}$ orbitals as seen in (c – e), with binding energies of 374.21 eV and 368.23 eV respectively, implying that Ag^0 is present for Ag_{high}@nZIF-8. The noise level for the silver signals of Ag@nZIF-8 (d) and $AgNO_3$@nZIF-8 (c) is very close to that of the base line

making an accurate determination of the binding energies impossible. Minute amounts of sodium (<0.1 %) was detected in the wide scan which is attributed to the $NaBH_4$ during reduction.

XPS gave qualitative proof of the association of Ag^0 with nZIF-8. Only for Ag_{high}@nZIF-8 the Ag:Zn ratio could be determined as 0.13 (see **Table 3.4**, p **62**) by XPS. In order to determine the silver content with greater accuracy, Inductively Coupled Plasma – Optical Emission Spectrometry (ICP-OES) analyses were performed in duplicate on $AgNO_3$@nZIF-8, Ag@nZIF-8 and Ag_{high}@nZIF-8. The Ag content was reported with a 95 % confidence and summarized **Table 3.4** (p **62**). The 0.61 % Ag content of $AgNO_3$@nZIF-8 is less than half that of the silver in Ag@nZIF-8 (reduced in a one pot synthesis) proving that $AgNO_3$ was leached from the pores by methanol washings during the isolation of $AgNO_3$@nZIF-8. After impregnation of nZIF-8, using an $AgNO_3$ solution with standard concentration (9.28 mM), followed by reduction, a 1.31 % load of Ag was reported for Ag@nZIF-8. By doubling the concentration of the silver precursor and after reduction, approximately 3 times the amount of silver (3.8 %) was reported for Ag_{high}@nZIF-8, which is also1.8 % higher than the 2 % load of Ag reported for micro-sized ZIF-8 in literature.[6] A difference of wt % between XPS and ICP is due to the fact that XPS analyzed the surface and the ICP analyzed the bulk of the sample.

Table 3.4 The Ag content of the silver impregnated derivatives of nZIF-8 as determined by XPS and ICP.

Sample	XPS atomic ratio Ag:Zn (wt %)	ICP/ wt %
$AgNO_3$@nZIF-8	-	0.61
Ag@nZIF-8	-	1.31
Ag_{high}@nZIF-8	0.13 (5.76)	3.80

3.3.3 Pd@nZIF-8

The same procedure followed for the silver impregnation in nZIF-8 was adapted for palladium. During the impregnation procedure nZIF-8 was exposed to the following palladium precursors ($Pd(NO_3)_2$, $Pd(OAc)_2$ and $Pd(acac)_2$) in solution. Only the $Pd(acac)_2$ was reduced by $NaBH_4$. The other impregnated products ($Pd(NO_3)_2$@nZIF-8 and $Pd(OAc)_2$@nZIF-8) could not be reduced in this manner, as determined during preliminary studies. The prepared palladium loaded nZIF-8 samples were characterized with PXRD in order to establish whether the nZIF-8 structure was

affected by exposure to the palladium precursors and strong reducing agent, $NaBH_4$. The identical PXRD patterns (see **Figure 3.15**, p **63**) show that no structural changes occurred and that the framework remains intact when compared to the nZIF-8 (a) starting material. nZIF-8 is thus resistant to chemical liquid deposition with palladium precursors and chemical reduction by $NaBH_4$. Neither of the peak intensities or positions was changed. The 2θ reflection peak for elemental palladium at ~40 º, as reported in literature, was not observed here because the palladium particles in the nZIF-8 structure are too small (< ~3 nm, **Figure 3.17.c**, p **65**) and the palladium concentration is too low to be detected by PXRD measurements.[10]

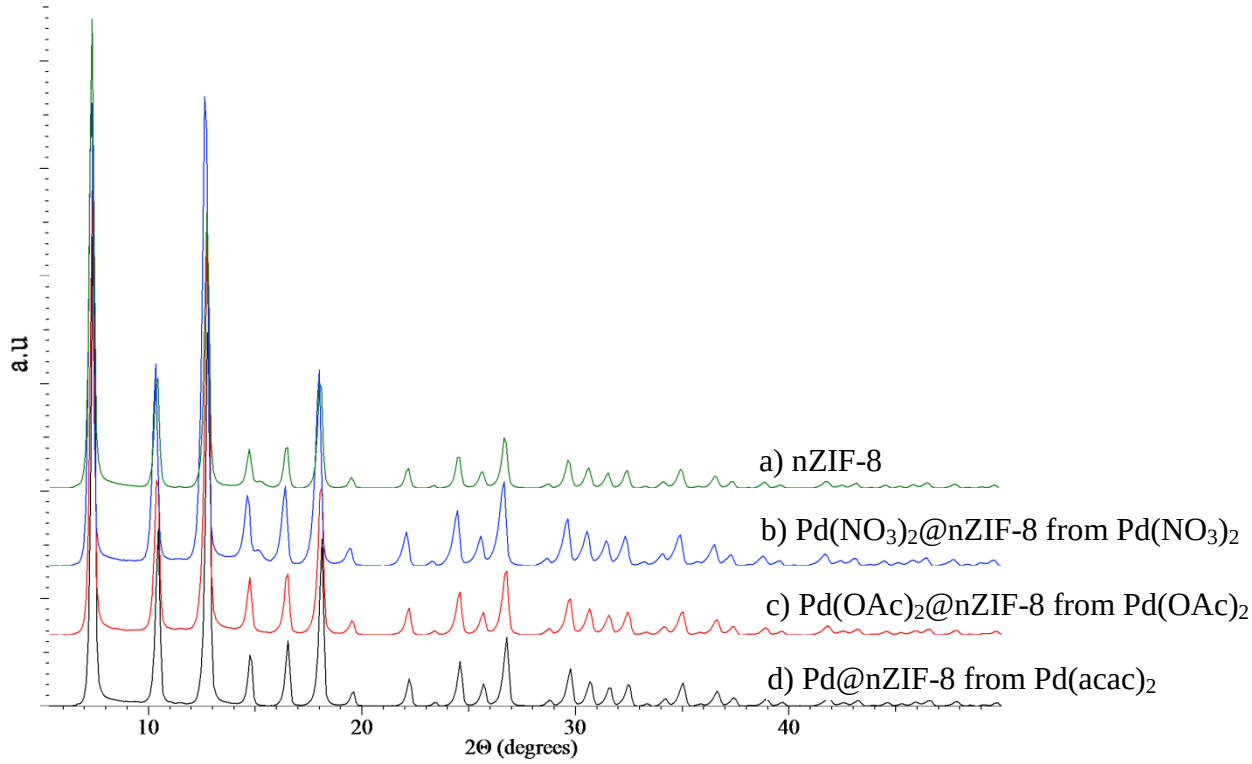

Figure 3.15 PXRD patterns of a) nZIF-8 and palladium loaded nZIF-8: b) $Pd(NO_3)_2$@nZIF-8 from $Pd(NO_3)_2$; c) $Pd(OAc)_2$@nZIF-8 from $Pd(OAc)_2$ and d) Pd@nZIF-8 from $Pd(acac)_2$. acac = acetylacetonate, OAc = acetate.

TGA analyses of the Pd impregnated nZIF-8 compounds were performed under identical conditions as for nZIF-8 in (**Chapter 0,** p **55**). By loading the nZIF-8 with palladium salts, the thermal stability of the nZIF-8 structure is maintained as seen from the TGA curves (b and c) in **Figure 3.16** (p **64**). Even after the reduction with $NaBH_4$ as in the case of Pd@nZIF-8 (d) obtained by impregnation of nZIF-8 with $Pd(acac)_2$, the structure only starts to decompose after 450 °C, like the non-impregnated nZIF-8 (a). Prior to the thermal collapse of the nZIF-8 structure, the TGA curves of the non-reduced $Pd(NO_3)_2$@nZIF-8 (b) and $Pd(OAc)_2$@nzif-8 (c)

both show an initial mass loss step of 2.75 % from 430 °C for $Pd(NO_3)_2$@nZIF-8 (i) and 3.04 % from 326 °C for $Pd(OAc)_2$@nZIF-8 (ii). These two mass losses can be attributed to the thermal decomposition of the nitrate (in $Pd(NO_3)_2$@nZIF-8) and acetate (in $Pd(OAc)_2$@nZIF-8) respectively. Pd@nZIF-8 shows the lowest weight loss of 1.56 % (iii) prior to the final decomposition, an indication that not all the Pd was fully reduced.

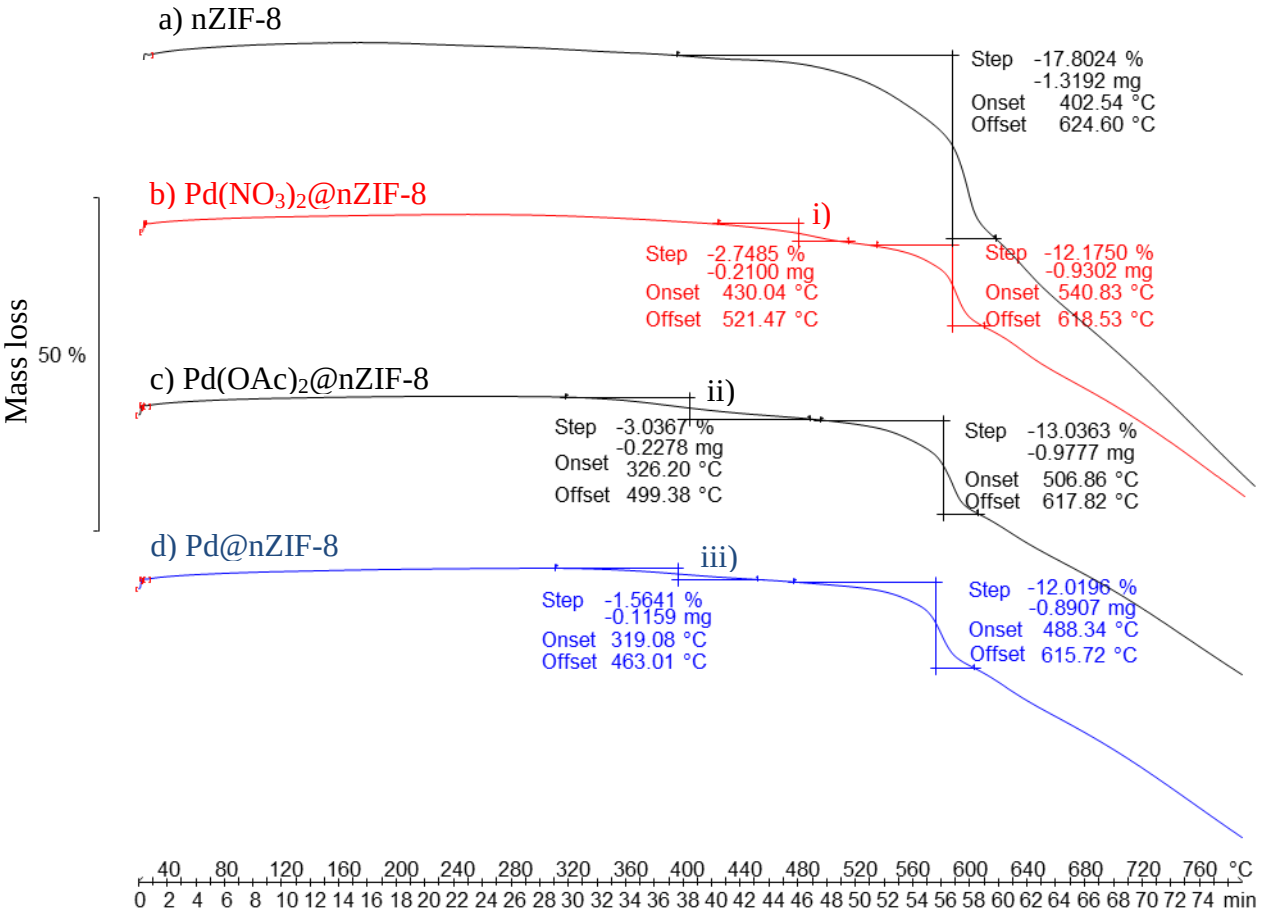

Figure 3.16 TGA thermograms in Ar of: a) nZIF-8 and palladium loaded nZIF-8: b) $Pd(NO_3)_2$@nZIF-8 from $Pd(NO_3)_2$; c) $Pd(OAc)_2$@nZIF-8 from $Pd(OAc)_2$ and d) Pd@nZIF-8 from $Pd(acac)_2$. acac = acetylacetonate, OAc = acetate.

Energy-dispersive X-ray spectroscopy (EDS) coupled to transmission electron microscopy (TEM) was performed on all the palladium-containing nZIF-8 compounds in order to obtain qualitative elemental analyses and visual evidence of the palladium particles present in the nZIF-8 framework, and displayed in **Figure 3.17** (p **65**). In all the TEM images it can be seen that the nZIF-8 particles retain their hexagonal shape and size after loading with palladium salts and even after reduction (c). The TEM image of $Pd(NO_3)_2$@nZIF-8 (a, i) shows $Pd(NO_3)_2$ as needle like

crystallites between the nZIF-8 particles as indicated by the arrows. The EDS confirms the presence of palladium at ~2.9 keV (a.ii). After impregnation of nZIF-8 with $Pd(OAc)_2$, the TEM image (see **Figure 3.17.b.i**, p **65**) shows no $Pd(OAc)_2$ crystallites, although the EDS spectrum (b.ii) confirmed the presence of palladium at ~2.9 keV.

a) $Pd(NO_3)_2$@nZIF-8

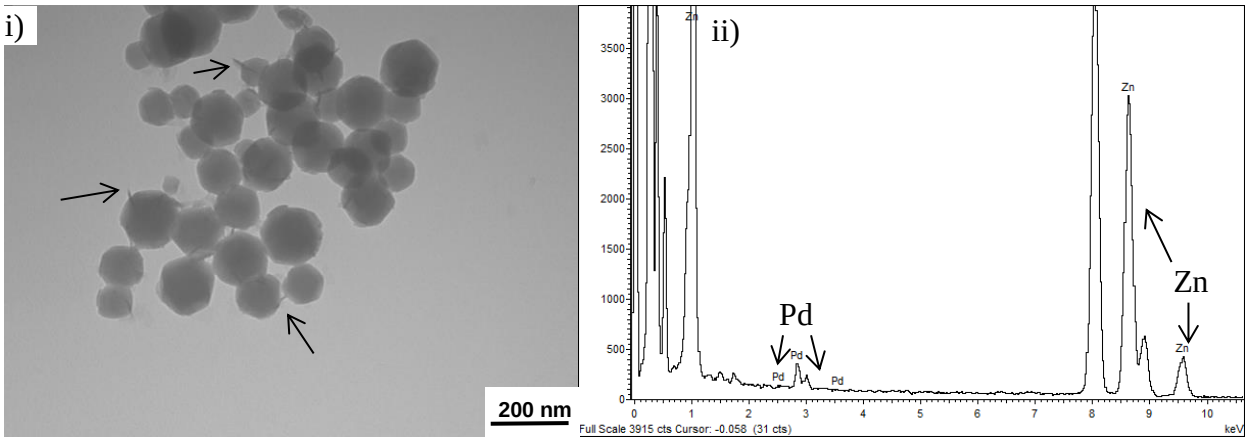

b) $Pd(OAc)_2$@nZIF-8

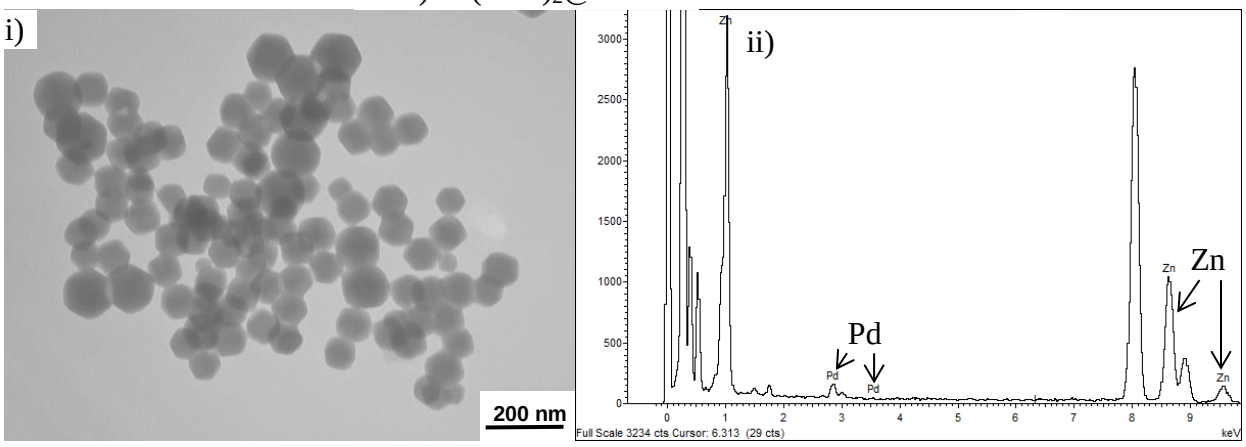

c) Pd@nZIF-8

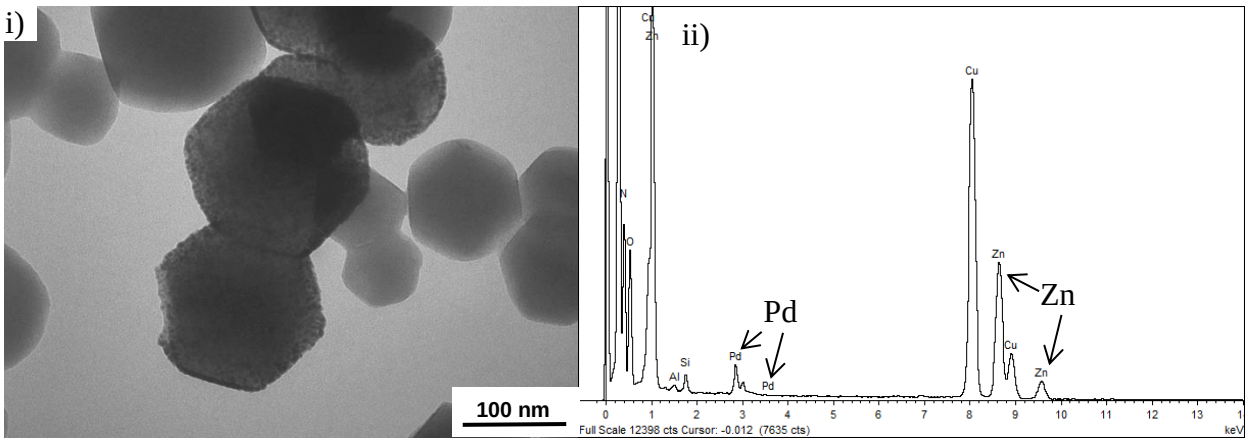

Figure 3.17 TEM images, accompanied by EDS spectra of a) $Pd(NO_3)_2$@nZIF-8, b) $Pd(OAc)_2$@nZIF-8 and c) Pd@nZIF-8 from $Pd(acac)_2$. acac = acetylacetonate.

After reduction of the impregnated $Pd(acac)_2$@nZIF-8 with $NaBH_4$, the TEM image of Pd@nZIF-8 (see **Figure 3.17.c**, p **65**) shows small palladium particles (~1 nm) well dispersed throughout the nZIF-8 framework. EDS (c.ii) confirmed that the particles are indeed palladium at ~2.9 keV. The $Pd(acac)_2$ was easily reduced by $NaBH_4$ with no influence on the nanoparticle structure. Very little agglomeration was observed for all palladium loaded nZIF-8 particles. The copper signal on all the EDS spectra originates from the sample holder grid.

X-ray Photoelectron Spectroscopy (XPS) of the palladium loaded nZIF-8 compounds, $Pd(NO_3)_2$@nZIF-8, $Pd(OAc)_2$@nZIF-8 and Pd@nZIF-8 gave qualitative as well as quantitative results in terms of the Pd content. The samples were not sputtered during the measurement resulting in large carbon and oxygen contents, with a negative influence on the accuracy of quantitative measurements. As example the wide scan survey of Pd@nZIF-8 is shown (see **Figure 3.18**, p **66**). For all the compounds the high resolution XPS scans for N and Zn were identical (see **Figure 3.19.a and b**, p **67**). The Pd signals for $Pd(NO_3)_2$@nZIF-8 (c), $Pd(OAc)_2$@nZIF-8 (d) and Pd@nZIF-8 (e) were strong enough for quantification purposes. The binding energies for the relevant elements are summarized in **Table 3.5** (p **68**).

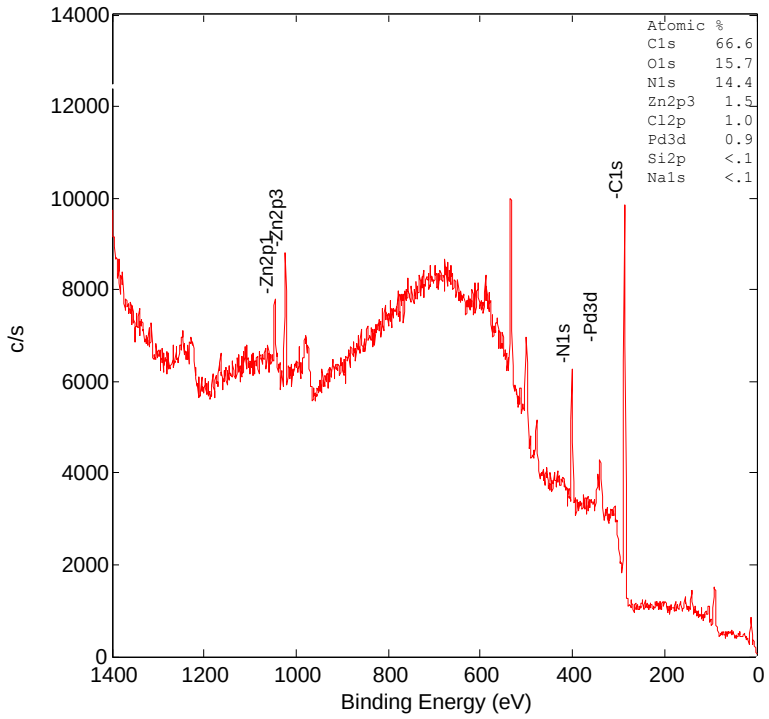

Figure 3.18 XPS Wide scan survey of Pd@nZIF-8 showing the photoelectron and Auger peaks. For clarity purposes the other peaks are not labeled.

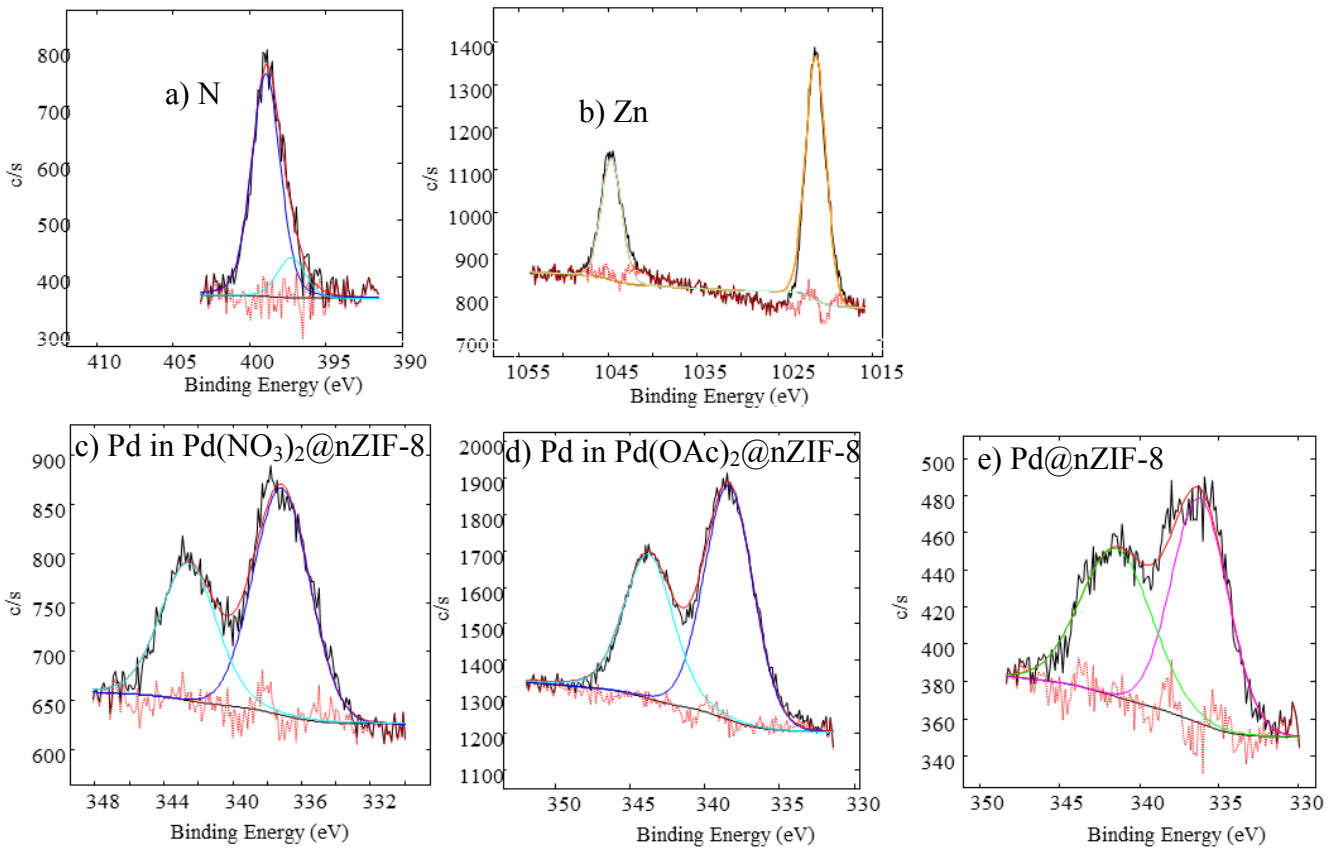

Figure 3.19 High resolution XPS scans of a) N and b) Zn for Pd@nZIF-8 with the XPS scans for Pd of c) $Pd(NO_3)_2$@nZIF-8; d) $Pd(OAc)_2$@nZIF-8 and e) Pd@nZIF-8.

The binding energy for 1s orbital of N and Zn were discussed in (**Chapter 3.3.2**, p **57**). The palladium signal appears as two peaks for $3d_{3/2}$ and $3d_{5/2}$ orbitals. The binding energies of these two peaks for Pd^{II} (present in $Pd(NO_3)_2$@nZIF-8 and $Pd(OAc)_2$@nZIF-8) are at 342.66 eV and 337.28 eV. Both peaks shift lower with ~1 eV upon reduction Pd^0 in Pd@nZIF-8 (see **Table 3.5**, p **68**). The presence of non-reduced palladium may have caused the peak broadening seen in **Figure 3.19.e** (p **67**). This is consistent with the non-reduced $Pd(acac)_2$ detected by TGA (see **Figure 3.16.d.iii**, p **64**) Minute amounts of sodium (<0.1 %) was detected in the wide scan which is attributed to the $NaBH_4$ used for reduction. From XPS data the Pd:Zn ratio could be determined for all three compounds as shown in **Table 3.5** (p **68**). The atomic ratio of Pd:Zn (0.25) is much larger than the Ag:Zn ratio (0.13) in **Chapter 3.3.2** (p **57**). This is due to the fact that the palladium nano particles (**Figure 3.17.c, p 65**) are smaller and better dispersed than the silver nano particles (**Figure 3.12.c, p 59**) which are larger and irregularly dispersed. Inductively Coupled Plasma (ICP) performed in duplicate on $Pd(NO_3)_2$@nZIF-8, $Pd(OAc)_2$@nZIF-8 and Pd@nZIF-8, gave a more accurate quantitative analysis than XPS with a 95 % confidence, as summarized in **Table 3.5** (p **68**). Palladium could be loaded into nZIF-8 to much higher levels

(3.3 %) than silver (1.3 %). A difference of wt % between XPS and ICP is due to the fact that XPS analyzed the surface and the ICP analyzed the bulk of the sample.

Table 3.5 The Pd content of the palladium impregnated derivatives of nZIF-8 as determined by XPS and ICP.

Element	Orbital	XPS: Binding Energy/ eV	XPS: atomic ratio Pd:Zn/ (wt %)	ICP/ (wt %)
N	1s	398.87	-	-
Zn	$2p_{1/2}$; $2p_{3/2}$	1044.62; 1021.49	-	-
Pd in $Pd(NO_3)_2$@nZIF-8	$3d_{3/2}$; $3d_{5/2}$	342.56; 337.17	0.25 (9.26)	3.3 (0)
Pd in $Pd(OAc)_2$@nZIF-8	$3d_{3/2}$; $3d_{5/2}$	342.76; 337.39	0.20 (7.75)	3.5 (5)
Pd in Pd@nZIF-8	$3d_{3/2}$; $3d_{5/2}$	341.40; 336.16	0.25 (10.38)	3.1 (1)

3.3.4 Porosity Analyses of Metal-loaded nZIF-8 Compounds

All metal salt and metal-containing nZIF-8 compounds (as described in **Section 3.3**) were activated at 150 °C for 16 hours prior to porosity analysis. All the silver loaded nZIF-8 compounds show typical Type-1 isotherms (**Figure 3.20**, p **69**) for the adsorption of nitrogen at 77 K, proving that nZIF-8 remains a microporous material after loading with $AgNO_3$ (a) as well as after reduction (b and c) remain porous. Only after doubling the load of silver, the amount of N_2 adsorped decreased significantly (c), a first indication that impregnation of nZIF-8 with $AgNO_3$, followed by reduction to Ag metal, reduced nZIF-8's adsorption capacity for N_2 at 77 K.

Upon comparison of the BET surface areas (see **Table 3.6**, p **69**) of the three silver loaded nZIF-8 compounds it is clear that the much larger silver loading in Ag_{high}@nZIF-8 lead to lower porosity than in the case of the other three compounds in the table. The high loading of silver in Ag_{high}@nZIF-8 caused a marked decrease in the amount of N_2 adsorbed (~100 cm^3 g^{-1}) as well as a decrease of the BET surface area by nearly 250 m^2 g^{-1}. This decrease in porosity of Ag_{high}@nZIF-8 could be caused by partial blocking of the pores of nZIF-8 by the well dispersed silver nanoparticles in the framework.

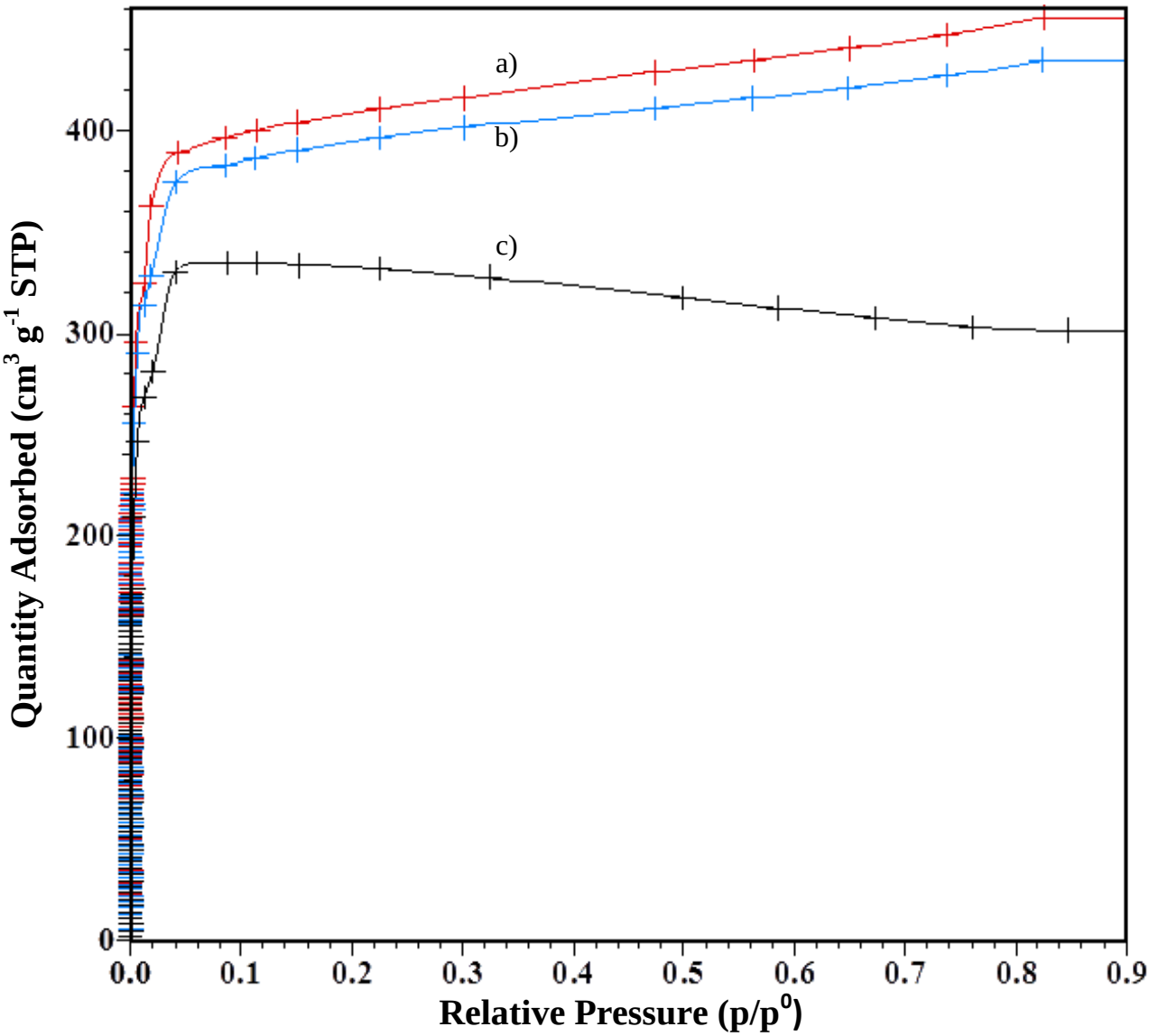

Figure 3.20 N_2 adsorption isotherms at 77 K of a) $AgNO_3$@nZIF-8 b) Ag@nZIF-8 and c) Ag_{high}@nZIF-8.

Table 3.6 N_2 porosity analysis at 77 K of silver loaded nZIF-8 compounds showing the quantity adsorbed ($cm^3\,g^{-1}$ at STP) at 0.9 p/p^0 and BET surface area ($m^2\,g^{-1}$).

Sample	Quantity Adsorbed/ $cm^3\,g^{-1}$	BET Surface Area/ $m^2\,g^{-1}$
nZIF-8 (bulk)	437	1705 ± 38
$AgNO_3$@nZIF-8	456	1681 ± 24
Ag@nZIF-8	435	1616 ± 42
Ag_{high}@nZIF-8	301	1440 ± 54

The typical type-1 isotherm obtained for Pd@nZIF-8 (**Figure 3.21.a**, p **70**) indicates that the nZIF-8 structure remains microporous after the impregnation with $Pd(acac)_2$ and its subsequent reduction with $NaBH_4$. Pd@nZIF-8 even shows an increase in uptake of N_2 from the 437 $cm^3\ g^{-1}$ of the empty nZIF-8 to 483 $cm^3\ g^{-1}$ (see **Table 3.7**, p **71**) which shows that the small palladium particles as seen in the TEM image (see **Figure 3.17**, p **65**) are able to provide additional adsorption sites. This increase capacity for N_2 adsorption on Pd@nZIF-8 is also confirmed by its slightly increased BET surface area (1770 $m^2\ g^{-1}$) compared to that of nZIF-8 (1705 $m^2\ g^{-1}$). The result for the unreduced $Pd(NO_3)_2$@nZIF-8 and $Pd(OAc)_2$@nZIF-8 in **Table 3.7** (p **71**) provides similar N_2 adsorption capacities to empty nZIF-8, except for $Pd(OAc)_2$@nZIF-8 which has a markedly smaller BET surface area (1455 $m^2\ g^{-1}$) compared to the rest of the palladium loaded nZIF-8 compounds.

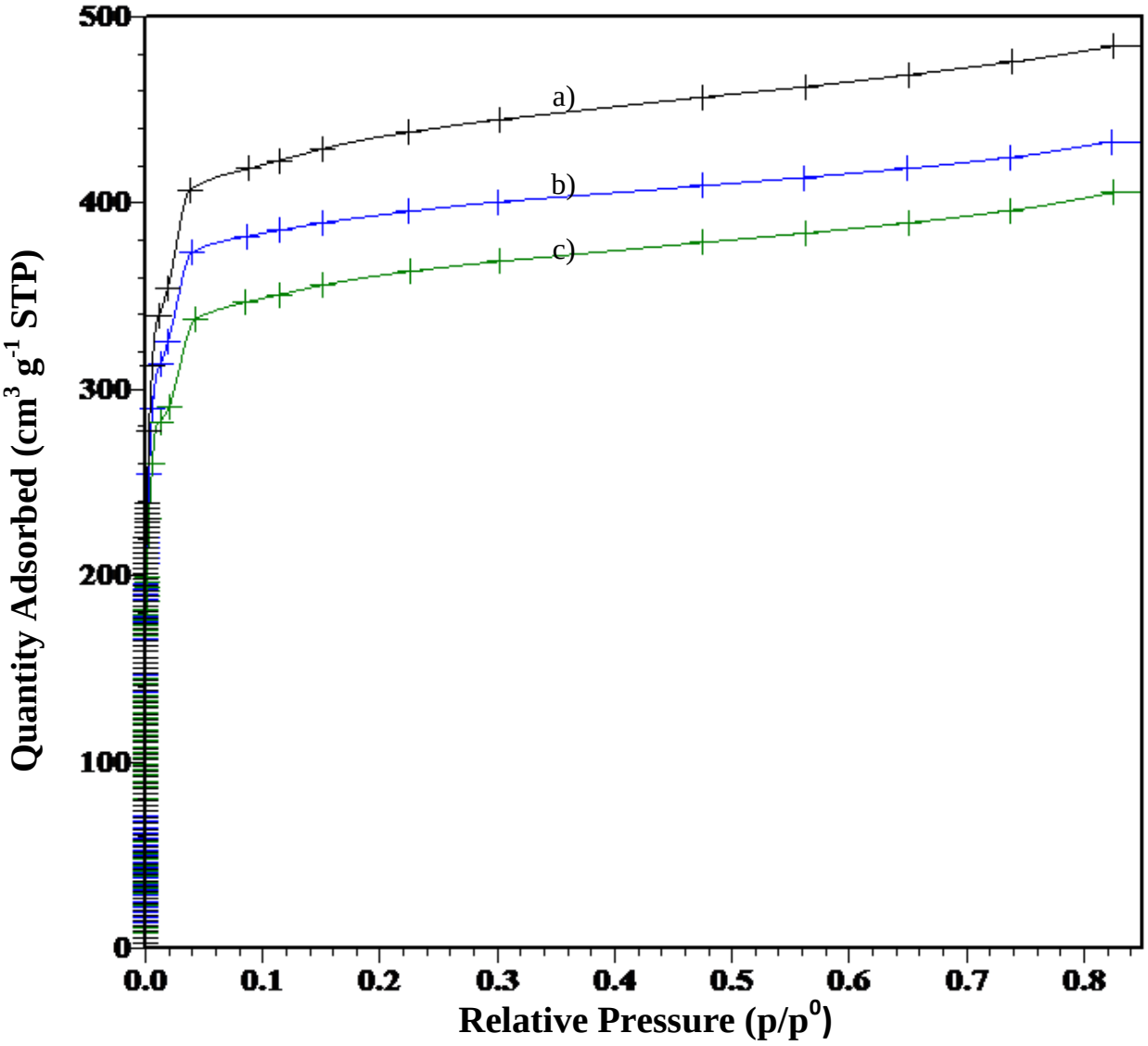

Figure 3.21 N_2 adsorption isotherms at 77 K of a) Pd@nZIF-8; b) $Pd(NO_3)_2$@nZIF-8 and c) Pd $(OAc)_2$@nZIF-8.

Table 3.7 N_2 porosity analysis at 77 K of palladium loaded in nZIF-8 compounds showing the quantity adsorbed ($cm^3 g^{-1}$ at STP) at 0.85 p/p^0 and BET surface area ($m^2 g^{-1}$).

Sample	Quantity Adsorbed/ $cm^3 g^{-1}$	BET Surface Area/ $m^2 g^{-1}$
nZIF-8 (bulk)	437	1705 ± 38
$Pd(NO_3)_2$@nZIF-8	428	1612 ± 50
$Pd(OAc)_2$@nZIF-8	405	1455 ± 47
Pd@nZIF-8	483	1770 ± 57

3.4 Time Resolved Solvent Assisted Ligand Exchange (SALE) of nZIF-8

3.4.1 Synthesis of SALEM-2

When micro-sized ZIF-8 was subjected to solvent assisted ligand exchange (SALE), the slow exchange process produced ZIF-8 particles with a high ratio of imidazole ligands (replacing 2-methylimidazole), while maintaining the SOD topology (see **Chapter 2.8**). In this study the 2-methylimidazole linker of the nano sized ZIF-8 was exchanged with imidazole by adapting the SALE process from Karagiaridi *et al.*, a time resolved exchange according to **Scheme 3.3** (p **71**).

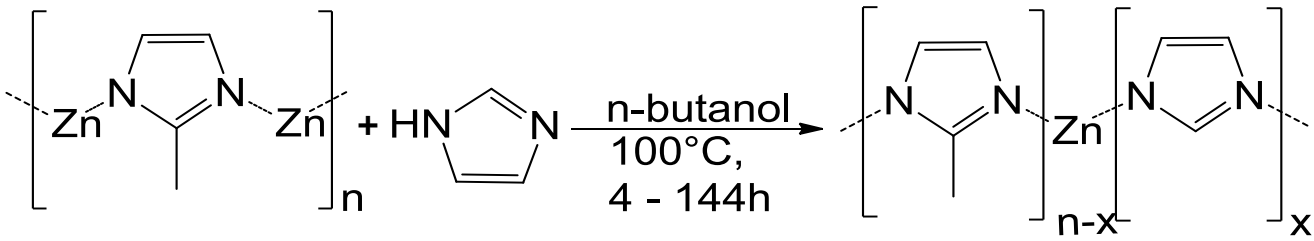

Scheme 3.3 General scheme of solvent assisted ligand exchange (SALE) of nZIF-8 with imidazole employing different time intervals where t = 4, 12, 24, 72, 144 hours.

The ligand exchange was carried out by first suspending activated nZIF-8 ultrasonically in *n*-butanol, before transferring it to a Teflon beaker containing a solution of excess (7 times) imidazole. After sealing the Teflon beaker in a stainless steel bomb reactor it was heated to 100 ℃ for different time intervals: 4, 12, 24, 72, 144 hours under solvothermal conditions. A consistent cooling time is essential since further exchange occurs during cooling. Similar to the original synthesis of nZIF-8, the exchange occurred by the deprotonation of the 2-

methylimidazole linker by the imidazole in the solution which then coordinates to the Zn in a tetrahedral manner. After isolation and drying high yields of the SALE product over 85 % was achieved (see **Table 3.8**, p **74**). The exchanged nZIF-8 (SALEM-2) compounds are fairly stable and can be stored with ease in ambient conditions.

Since a 100 % conversion was never achieved with the SALE process, the ZIF containing only imidazole linkers was synthesized using a rapid room temperature bench top reaction, similar to the synthesis of nZIF-8, using $Zn(NO_3)_2.4H_2O$ and imidazole as reagents in methanol (see **Scheme 3.4**, p **72)**. The white powder ($Zn(Im)_2$) obtained after isolation and activation was used as reference material in the characterization of the SALEM-2 products.

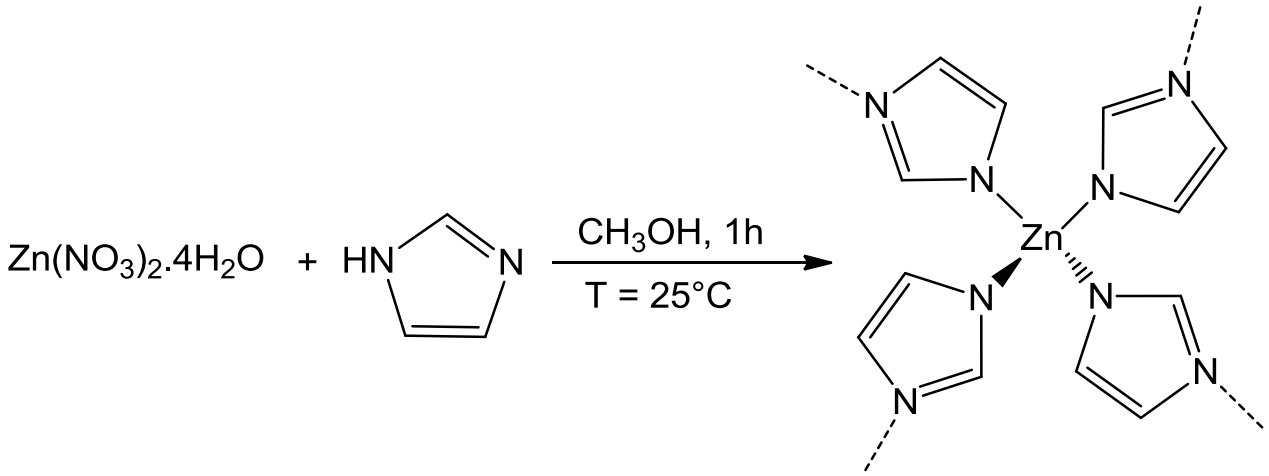

Scheme 3.4 Synthesis of $Zn(Im)_2$ particles at room temperature from imidazole tetrahedrally coordinated to zinc.

3.4.2 Characterization of SALEM-2

3.4.2.1 ^{1}H NMR

In order to determine the imidazole ligand content of the SALEM-2 compounds, they were characterized with ^{1}H NMR, after digesting these nZIF-8 derivatives in an acidic medium (a 9:1 ratio of D_2O and D_2SO_4). The ^{1}H NMR spectra for nZIF-8 (a) and SALEM-2_{12h} (b) are shown in **Figure 3.22** (p **73**). For the spectrum of nZIF-8 (a), two singlets are observed at 1.3 and 6 ppm representing the CH_3 and HC=CH protons of the 2-methylimidazole linker, respectively. For the SALEM-2 synthesized for 12 hours (b), 4 singlets were observed, the two singlets at 1.13 and 5.79 ppm belonging to the 2-methylimidazole linkers that were not exchanged and another two at 5.99 and 7.17 ppm for the exchanged imidazole ligand representing the HC=CH protons and the CH proton at position 2 on the ring, respectively.

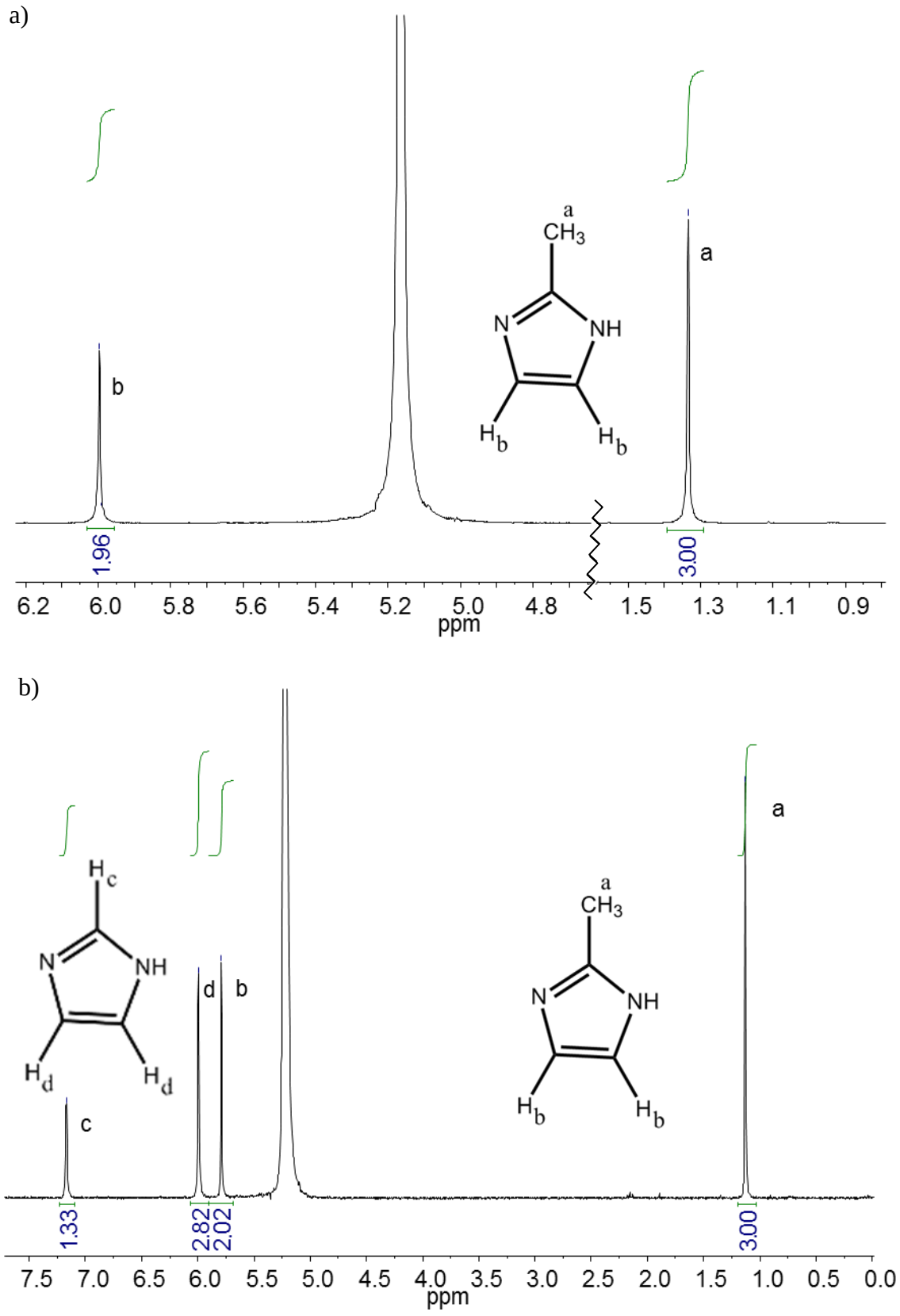

Figure 3.22 ^{1}H NMR spectra of: a) nZIF-8 and b) SALEM-2 (12h synthesis) digested in D_2O/D_2SO_4.

The ^{1}H NMR spectra for all the ligand exchanged SALEM-2 products from syntheses at different time intervals can be found in **Appendix D.2 to D.6**. Slight peak shifting is observed for the solvent and product due to small difference in the pH of the different batches. From the integration of the two sets of protons (from 2-methylimidazole and imidazole) the relative ratio of the two types of linkers could be determined and used to calculate the extent of conversion of 2-methylimidazole to imidazole in each of the SALEM-2 products in (see **Table 3.8**, p **74**). The maximum conversion percentage with nano-sized ZIF-8 was higher than that of micro-sized ZIF-8, reaching 90 % compared to the 85 % of the latter. The SALE rate of nZIF-8 was also much faster than that of the micro-sized ZIF-8, with the conversion reaching ~80 % in just 24 hours (see **Table 3.8**, p **74**), whereas 85 % the conversion of micro-sized ZIF-8 took 144 hours. [11]

Table 3.8 Solvent assisted ligand exchange (SALE) of nZIF-8 (1.3 mmol) with imidazole (8.9 mmol) in *n*-butanol at different synthesis times (see **Scheme 3.3**, p **71**). Conversion percentage of 2-methylimidazole linkers with imidazole was determined by ^{1}H NMR in D_2O/D_2SO_4 (9:1).

Synthesis Time/ h	Yield/ g (%)	Conversion/ %
144	0.233 (89)	90
72	0.226 (85)	91
24	0.219 (83)	79
12	0.231 (87)	58
4	0.225 (85)	31

The smaller diameter of the nanoparticles (nZIF-8) compared to that of the micro-sized ZIF-8 particles, allow for shorter diffusion time of the introduced imidazole linker to reach the insides of the particles, thus increasing the exchange rate. The faster SALE process could also be a result of the increases external surface area of nZIF-8 compared to that of micro-sized ZIF-8. The exchange percentage follow a trend as observed in **Figure 3.23** (p **75**) rising to a maximum conversion of 90 % after a 72 h synthesis time. The ligand exchange is possible because the large excess of imidazole ion in the slightly acidic solution. The pKa value of both 2-methylimidazole (7.52) and imidazole (6.97) are quite similar. The zinc nitrogen bonds of both ZIF-8 and SALEM-2 should be similar in strength.[11]

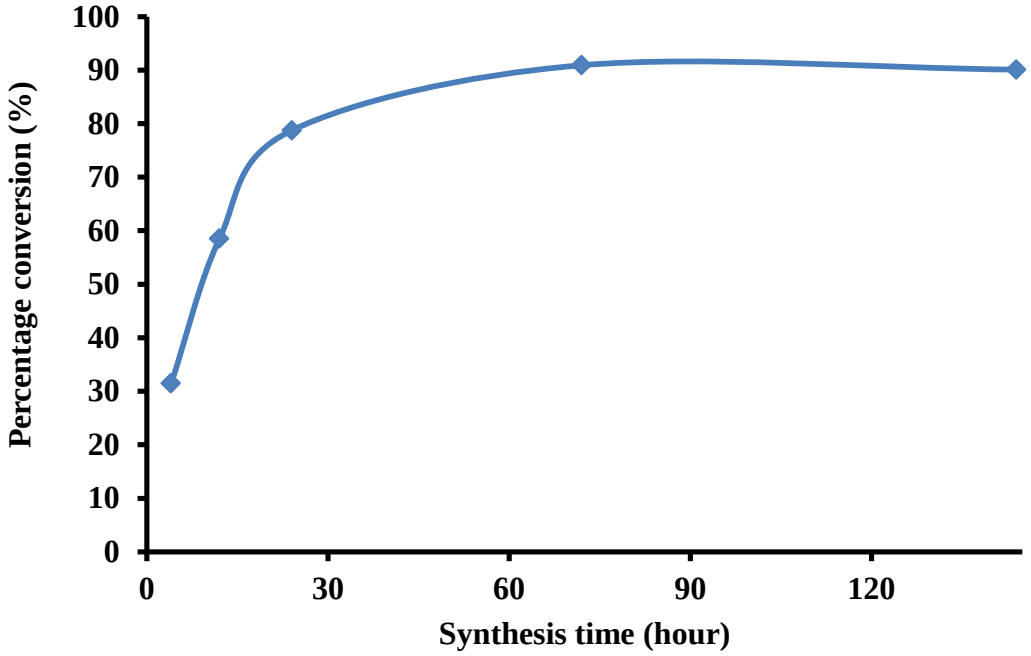

Figure 3.23 Trend of percentage conversion *vs.* synthesis time of solvent assisted ligand exchange (SALE) of nZIF-8 to SALEM-2.

3.4.2.2 ATR-FTIR

The progressive solvent assisted ligand exchange (SALE) of nZIF-8 by imidazole was followed by Fourier transform infrared spectrometry (FTIR) and represented in **Figure 3.24** (p **76**), together with the spectrum of the $Zn(Im)_2$ product (g). Original nZIF-8 (a) has a weak stretching frequency for the methyl group at 3136 cm^{-1} (marked i) which gradually disappeared with increasing replacement of 2-methylimidazole with imidazole. In the region between 1330 cm^{-1} and 1180 cm^{-1}, showing the ring deformation frequency due to the CH_3 groups, the appearance of a peak at 1245 cm^{-1} (marked ii) associated with the C-N stretching frequency, is observed to increase while the linker was exchanged with imidazole. The out of plane bending of the CH_3 group at 1146 cm^{-1} (iii) is gradually being replaced by the out of plane bending of the methine H (from imidazole) at 1034 cm^{-1} (iv) as seen by the disappearance of the peak at 1146 cm^{-1} and the appearance of a peak at 1084 cm^{-1}. The FTIR spectrum of the ZIF synthesized with the same bench top reaction as in ZIF-8, $Zn(Im)_2$ (g), obtained identical spectrum to the SALEM-2 after 72 hours (e).

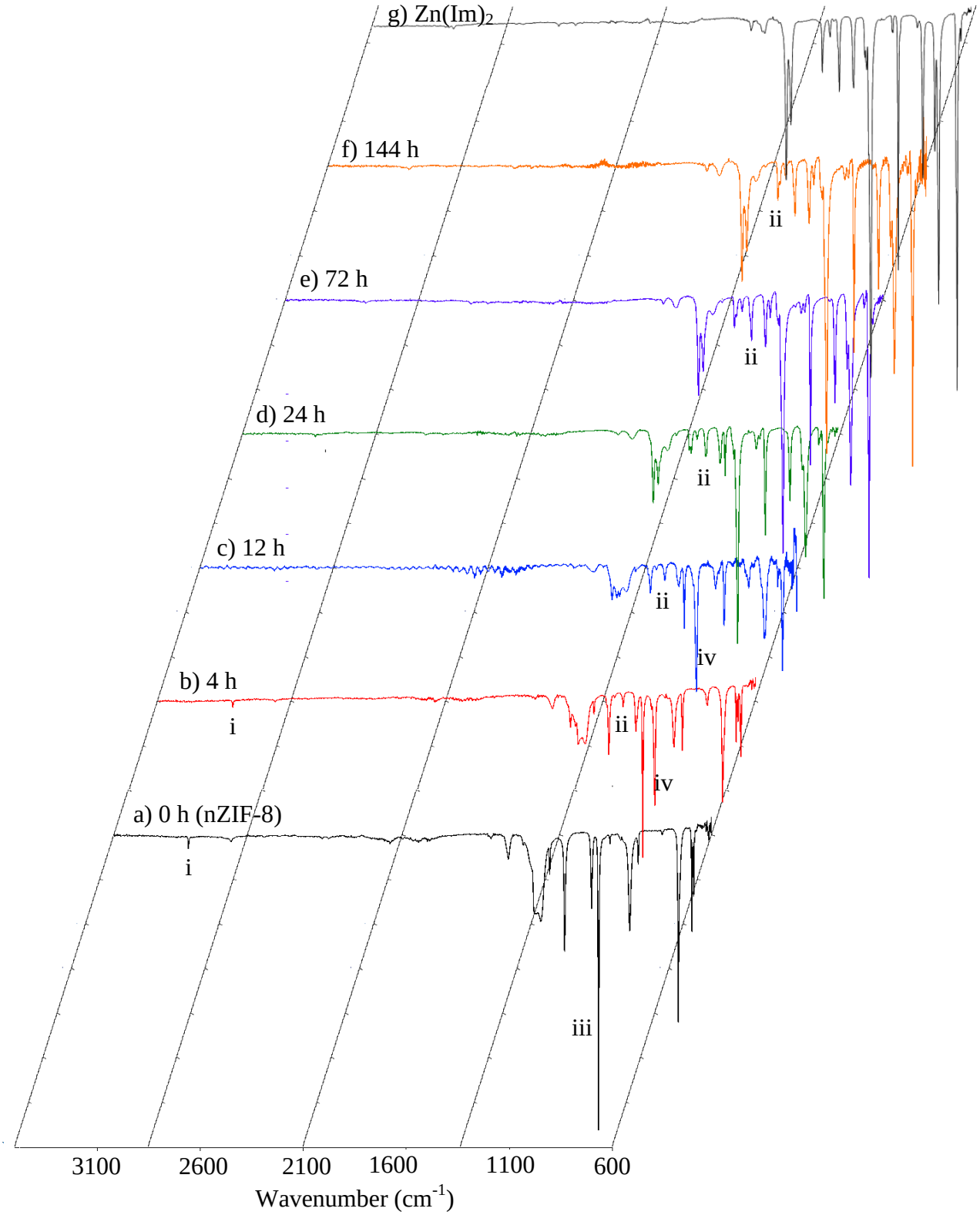

Figure 3.24 FTIR spectra of SALEM-2 products at different synthesis times: a) 0; b) 4; c) 12; d) 24; e) 72 and f) 144 hours, as well as (g) the ZIF product, $Zn(Im)_2$, from $Zn(NO_3)_2.4H_2O$ and imidazole.

3.4.2.3 PXRD

The structural integrity of the new SALEM-2 compounds was determined by PXRD measurements, showing that the SOD crystal structure of the nZIF-8 starting material is only maintained up to 24 hours (79 %) of exchange in this study (see **Figure 3.25**, p **78)**. The series of PXRD patterns shows that the structural integrity of the SALEM-2 products is dependent on the amount of 2-methylimidazole been exchanged. After 4 hours of exchange (b), the PXRD shows no additional peaks emerging thus representing a SOD topology. After 12 hours of exchange, reaching 58 % conversion (c) weak signals of new peaks at 14.6 º (i) and 18.8 º (ii) were observed, evidence of new crystal faces. After 24 hours of exchange (d) these peaks are now more intense, with the intensity of the original nZIF-8 peaks at 7.3 (iii), 10.2 (iv) and 12.6 º (v) decreased by half. The PXRD pattern at 24 hours (d) shows clearly that a combination of the original SOD structure (from nZIF-8) and a newly emerging crystal structure co-exist within the framework. After 72 hours and the conversion reaching 91 % (e) the three peaks between 7.3 and 12.6 º (marked iii, iv and v in d**)** have completely disappeared. This pattern remains identical after 144 hours of exchange (f**).** In the case of (e) and (f) it is clear that the SOD topology of the original nZIF-8 has been replaced with a new topology, signalling a breakdown in the structure integrity.

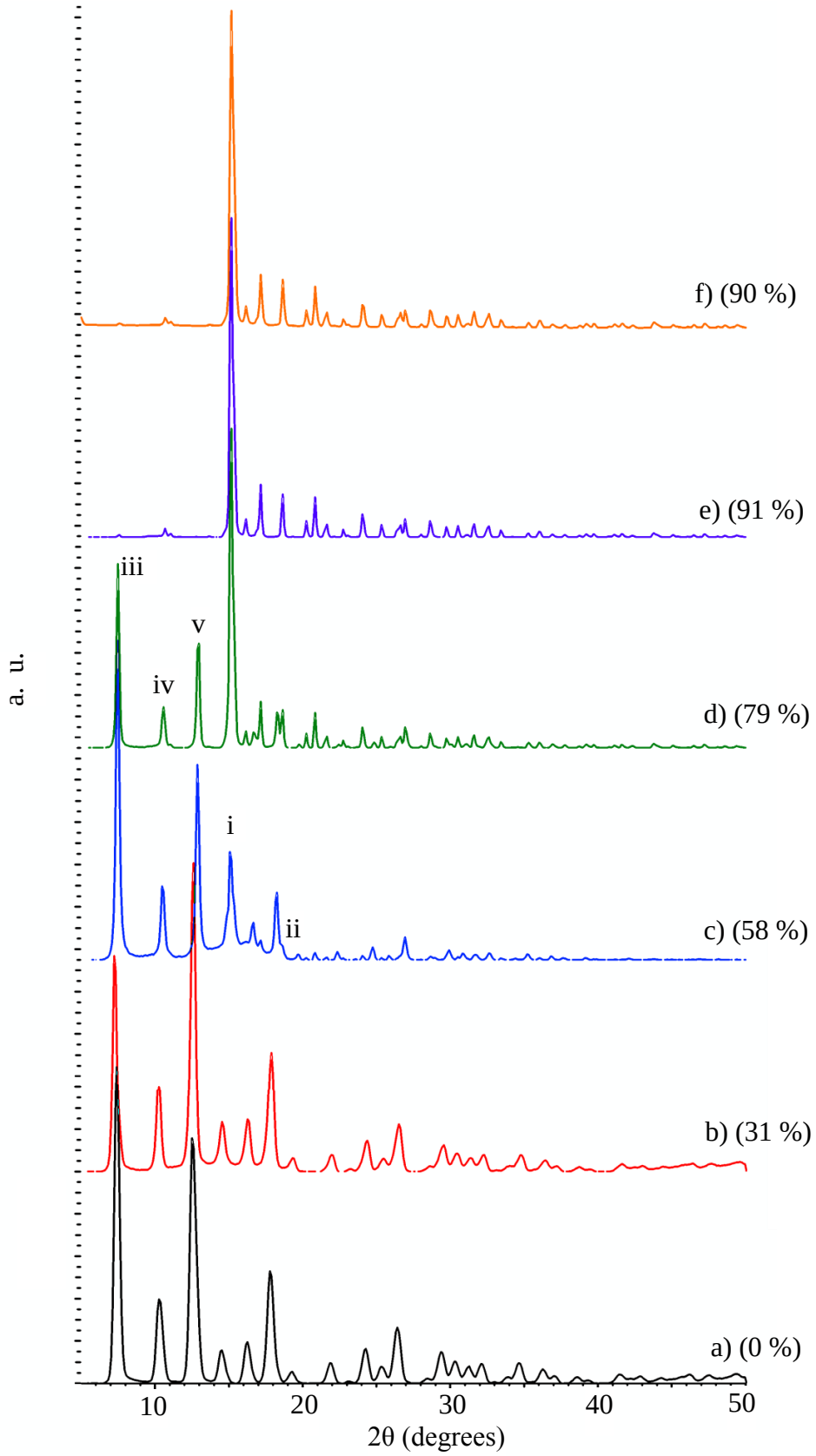

Figure 3.25 PXRD patterns of solvent assisted ligand exchange (SALE) products (SALEM-2) of nZIF-8 after different synthesis times a) 0; b) 4; c) 12; d) 24; e) 72 and f) 144 hours. The 2-methylimidazolate linkers of nZIF-8 were exchanged with imidazole in *n*-butanol. Each exchange percentage is given in brackets.

In order to verify this new structural topology of SALEM-2 products with conversion higher than 79 %, their PXRD patterns were compared to that of the $Zn(Im)_2$ (see **Figure 3.26**, p **79**) synthesized by bench top reaction (**Scheme 3.4**, p **70**)

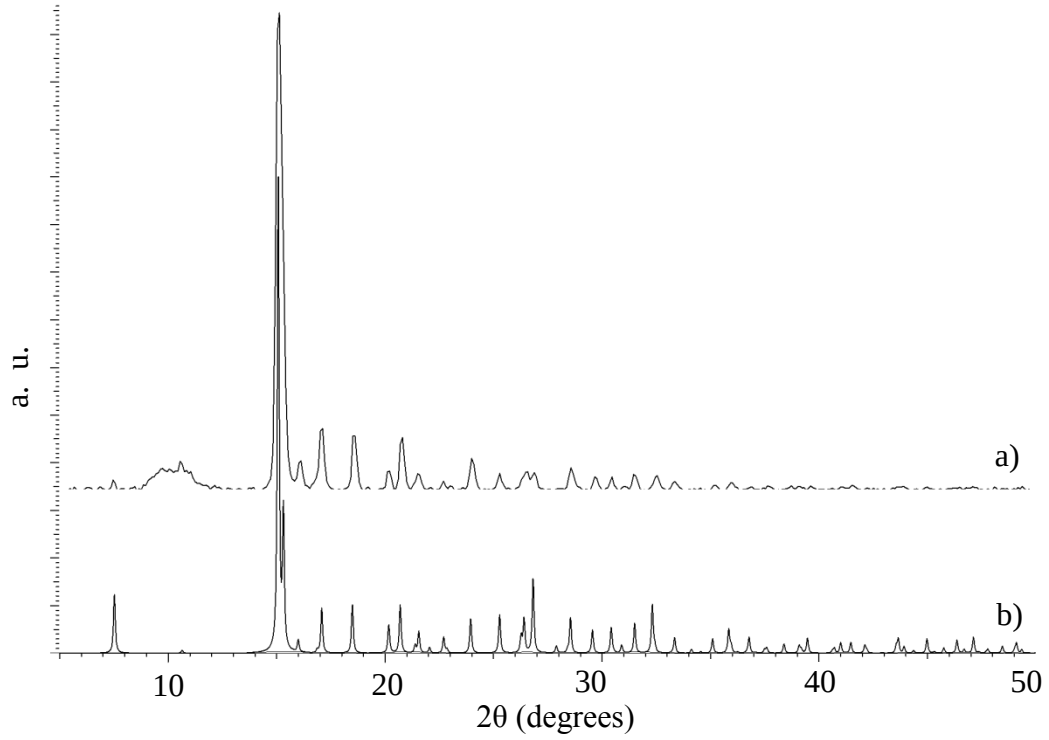

Figure 3.26 PXRD patterns of $Zn(Im)_2$: a) synthesized in methanol at room temperature, and b) simulated from single crystal XRD data, showing ZNI topology. [12]

The measured pattern of $Zn(Im)_2$ (a) is similar to that of the simulated pattern (b) obtained from single crystal XRD measurements.[12] With the crystal data the topology of $Zn(Im)_2$ was found to be ZNI (with a CCDC code of GITTAF), confirming the nonporous nature of $Zn(Im)_2$ or ZIF-ZNI.[13,14] It can be clearly seen from the similarity of the PXRD patterns (e) and (f) (see **Figure 3.25**, p **78**) and (a) (see **Figure 3.26**, p **79**) that the SALEM-2 products after 72 h and 144 h have ZNI topologies. The SALE reactions of nano sized ZIF-8 with imidazole gave a combination of both SOD and ZNI topologies after 12 hours and 24 hours (see **Figure 3.25**, (c) and (d) respectively, p **78**). The replacement of the 2-methylimidazolate linker in nZIF-8 with imidazole has thus a major impact on the topology of the resultant SALEM-2 products when the SOD structure is transformed to ZNI, during the exchange taking longer than 24 h.

3.4.2.4 Electron Microscopy

Solvent assisted ligand exchanged nZIF-8 nanoparticles (SALEM-2 products) were analysed with Transmission electron microscopy (TEM). From the TEM images it was observed that all the new SALEM-2 particles remain in the nano range with diameters of < 100 nm (see **Figure 3.27**, p **80** and **Appendix B.9 to B.13**). During exchange times longer than 24 h where the structure is transformed from the SOD to the ZNI topology, spherical irregular particles were obtained (see **Figure 3.27.b**, p **80**). With shorter exchange times the particles remained hexagonal as shown for the SALEM-2 product obtained after a 12 h exchange reaction, as in **Figure 3.27.a** (p **80**).

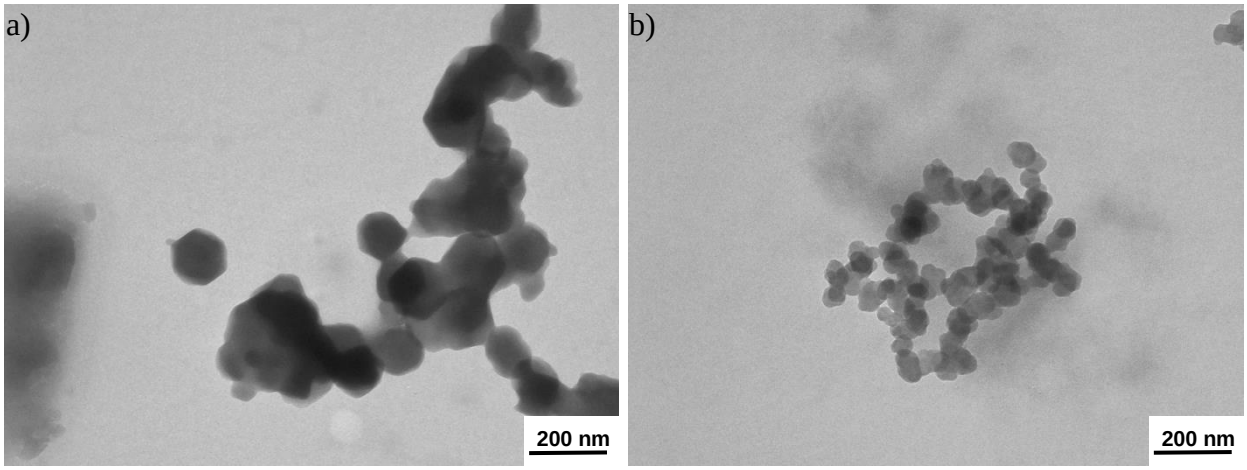

Figure 3.27 TEM images of SALEM-2 products obtained after a) 12 h and b) 72 h, of solvent assisted ligand exchange (SALE) of nZIF-8 particles with imidazole in methanol.

The ZIF-ZNI ($Zn(Im)_2$) synthesized with bench top reactions yielded rectangular micro-sized particles of 1320 nm in diameter.

3.4.3 Porosity Analysis of SALEM-2

The new SALEM-2 products were activated at 150 ℃ for 16 hours prior to porosity analysis. The SALEM-2 products obtained after exchange reactions of 24 h or shorter (see isotherms a – c, **Figure 3.28**, p **81**) show Type-1 isotherms, typical for microporous materials proving that the porosity of nZIF-8 is still present after up to 24 hours (79 %) of exchange. After 4 hours of SALE (solvent assisted ligand exchange) (a) and a 31 % conversion, the majority of the nZIF-8 porosity is maintained with the SALEM-2 product adsorbing 444 $cm^3 g^{-1}$ of N_2 at 77 K similar to the original nZIF-8(see **Table 3.9**, p **82**). An increased conversion with the exchange of 2-methylimidazole by imidazole leads to a decrease in porosity and surface area as seen in the table. After 24 hours of exchange the structure is fully transformed to the ZNI topology as

confirmed by PXRD measurements (see **Section 3.4.2.3**, p **77**) and a nonporous material was obtained (see isotherms d and e, **Figure 3.28**, p **81**).

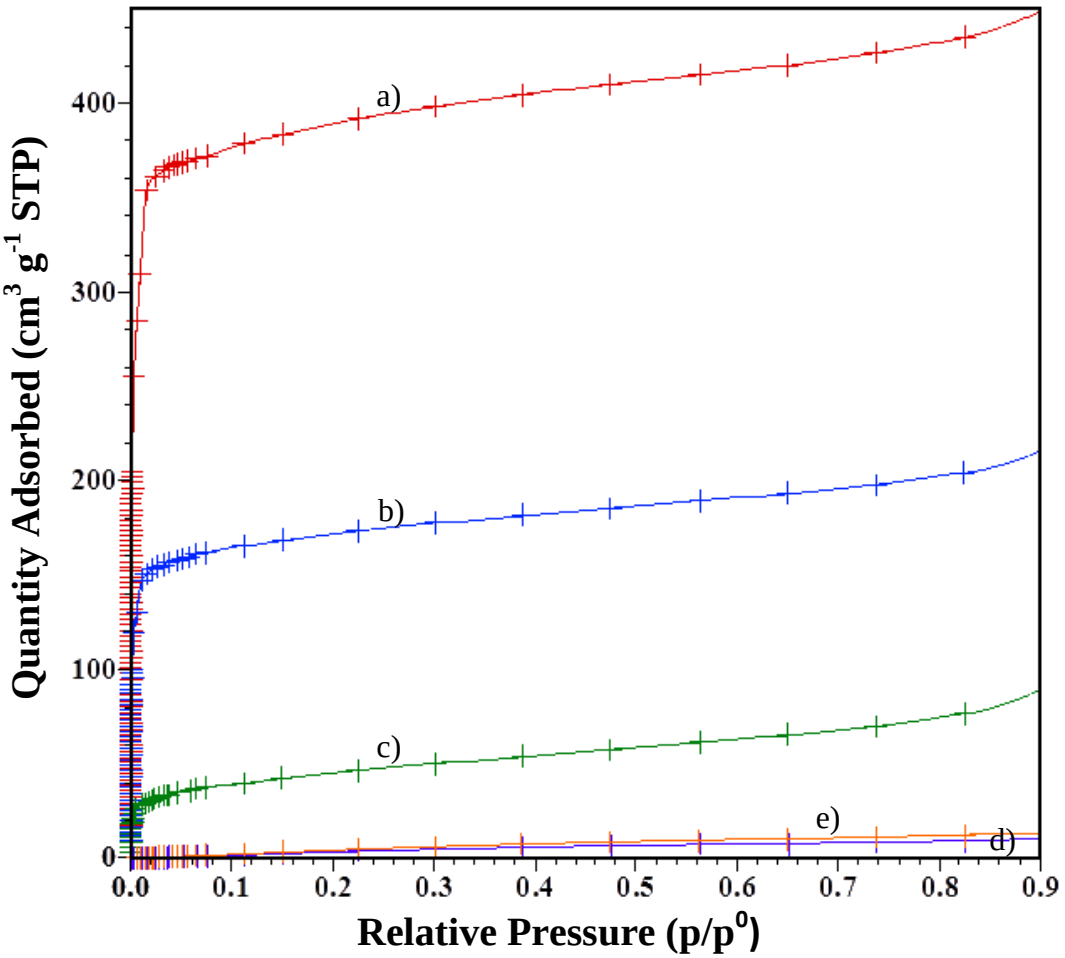

Figure 3.28 N_2 isotherms at 77 K of SALEM-2 products obtained after the following exchange times a) 4 hours (red); b) 12 hours (blue); c) 24 hours (green); d) 72 hours (purple); e) 144 hours (orange).

The BET surface areas of the new SALEM-2 products, summarized in **Table 3.9** (p **82**), were seen to decrease together with the quantity of N_2 adsorbed, as the percentage of conversion increases, and the porous SOD topology of the nZIF-8 starting material is replaced by the non-porous ZNI topology. After 72 hours of exchange, the amount of N_2 adsorbed and the BET surface areas of SALEM-2 are so low that the material can be regarded as non-porous. A trend was observed (see **Figure 3.29**, p **82**) that after a conversion of 31 %, the BET surface area begins to decrease up to a conversion of (79 %) where the SALEM-2 material becomes non-porous with very low BET surface area.

Table 3.9 N_2 porosity analysis (quantity adsorbed and BET surface area) at 77 K of SALEM-2 products obtained after different exchange times for Solvent assisted ligand exchange (SALE) of nZIF-8 with imidazole.

Compound	SALE reaction time/ h	Conversion/ %	Quantity Adsorbed/ $cm^3 g^{-1}$	BET Surface Area/ $m^2 g^{-1}$
nZIF-8	**0**	0	437	1704±37
SALEM-2	**4**	31	444	1579±14
SALEM-2	**12**	58	215	668±2
SALEM-2	**24**	79	90	145±1
SALEM-2	**72**	91	9	15±1
SALEM-2	**144**	90	12	20±2

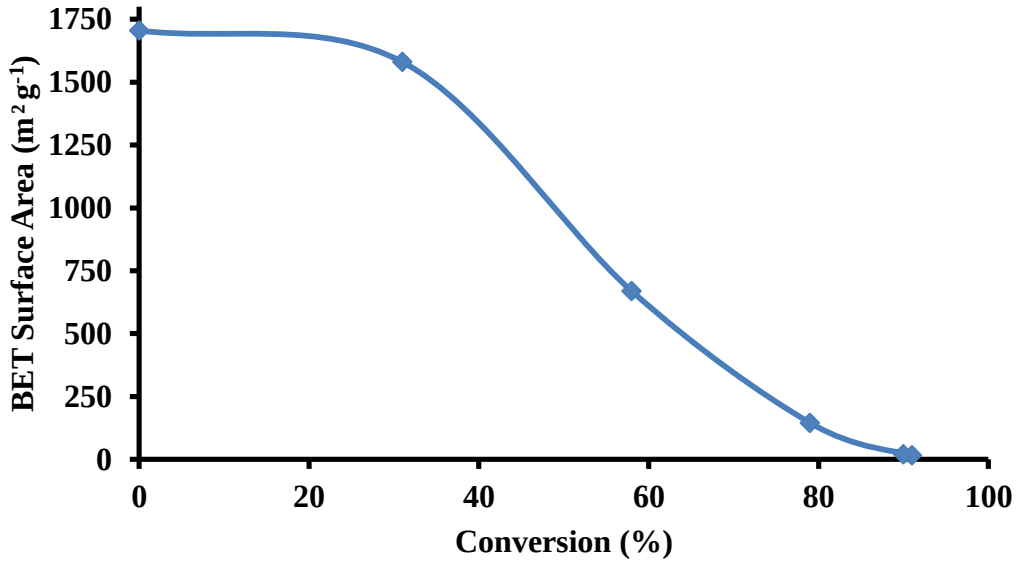

Figure 3.29 Trend of BET surface area *vs.* conversion of solvent assisted ligand exchange (SALE) of nZIF-8 to SALEM-2.

3.4.4 Thermal Analysis of SALEM-2

TGA thermograms of all the SALEM-2 products synthesized at different time intervals (see **Scheme 3.3**, p **71**) show identical thermal stability to that of the nZIF-8 starting material, as seen in **Figure 3.30** (p **83**). The thermogram or SALEM-2 after an exchange time of 12 h is displayed

as representative for all the SALEM-2 products, with the rest of the thermograms to be found in **Appendix E.9 to E.13**. All the SALEM-2 products show thermal stability up to 400 ℃ follow by an initial weight loss of ~6 % and continued gradual loss of the organic linker after ~650 ℃. SALEM-2 products show also identical thermal stability to the $Zn(Im)_2$ (ZIF-ZNI) synthesized at room temperature in methanol (**Appendix E.15**).

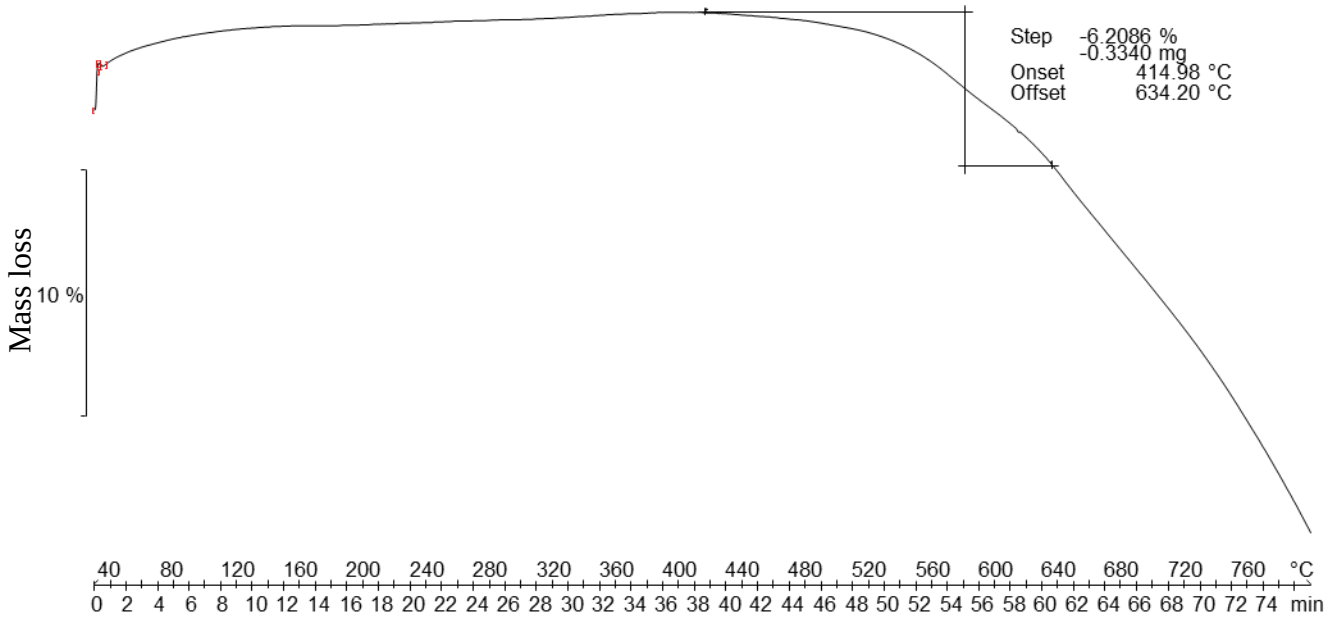

Figure 3.30 TGA thermogram in Argon of SALEM-2 obtained after 12 hours of solvent assisted ligand exchange (SALE) of nZIF-8 with imidazole.

3.5 Post Synthetic Modification of SALEM-2 through Lithiation

3.5.1 Synthesis

The post synthetic modification of SALEM-2 at the C2 position of the imidazole organic linker through lithiation reaction is known to produce N-heterocyclic carbene-like active sites on the external surface area of the micro-sized crystals (see **Chapter 2.9.3**). In this part of the study nano sized SALEM-2 with 69.6 % imidazole content was used for lithiation. The lithiation reaction step (see **Scheme 3.5**, p **84**) was followed by the attachment of a butane chain to the Lithium-activated imidazole linkers using 1-bromobutane.

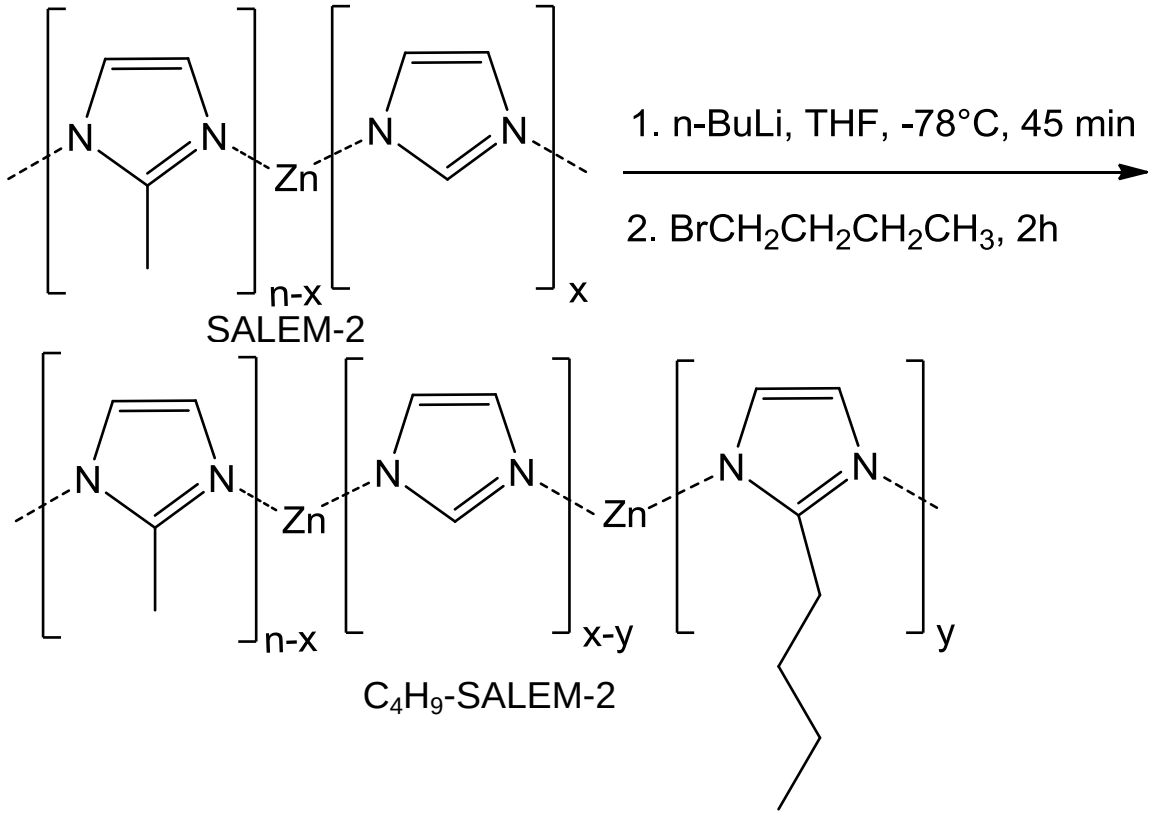

Scheme 3.5 A general scheme for the lithiation of nano SALEM-2 with *n*-BuLi followed by a reaction with 1-bromobutane on the lithiated C2 position.

Since the post synthetic modification of SALEM-2 involved lithiation it was performed under Schlenk conditions in dry THF with suspended SALEM-2 nanoparticles. During lithiation with *n*-butyllithium in hexane at -78 ℃ the SALEM-2 suspension solution turned slightly yellow, an indication that the imidazole was lithiated. After warming up to room temperature 1-bromobutane was added in excess to the suspension to produce C_4H_9-SALEM-2 during a 2 hours reaction period at room temperature. The C_4H_9-SALEM-2 nanoparticles were isolated, dried and activated under vacuum at 100 ℃ for 2 days to remove solvent and excess starting material within the pores. The C_4H_9-SALEM-2 nanoparticles, obtained in 76 % yield, are fairly stable and can be stored in ambient atmosphere without the need for further activation.

3.5.2 Characterization and Properties

Similar to SALEM-2 the C_4H_9-SALEM-2 could be characterized by digestive ^{1}H NMR in an acidic medium (D_2O/D_2SO_4 in a 9:1 ratio), giving a spectrum shown (in **Figure 3.31**, p **85**). After digestion, three different organic fragments could be identified: 2-methylimidazole (from the nZIF-8 starting material before SALE), imidazole (incorporated into the nZIF-8 structure during SALE) and 2-butylimidazole (obtained after lithiation and the reaction with 1-

bromobutane). For the 2-methylimdiazole fragment, two singlets are observed at 2.46 (a) and 7.12 ppm (b) representing the three CH_3 and two aromatic CH protons, respectively. For the imidazole fragment, two singlets at 7.32 and 8.51 ppm represent the two aromatic CH protons (d) and the CH proton at position 2 (c), respectively. For 2-butylimidazole the signals for the protons of the butyl chain are seen at 0.72 (δ, CH_3, triplet), 1.16 (γ, CH_2, multiplet), 1.36 (β, CH_2, multiplet) and 3.47 ppm (α, CH_2, triplet). The signals for the 2-butyl protons on the imidazole ring (marked ε) and the peak (marked b) are overlapping at 7.12 ppm. The integration values of the HC=CH protons were used to determine the relative abundance of the three imidazole fragments with 2-methylimdazole (69.3 %), imidazole (30.1 %) and 2-butylimidazole (0.6 %).

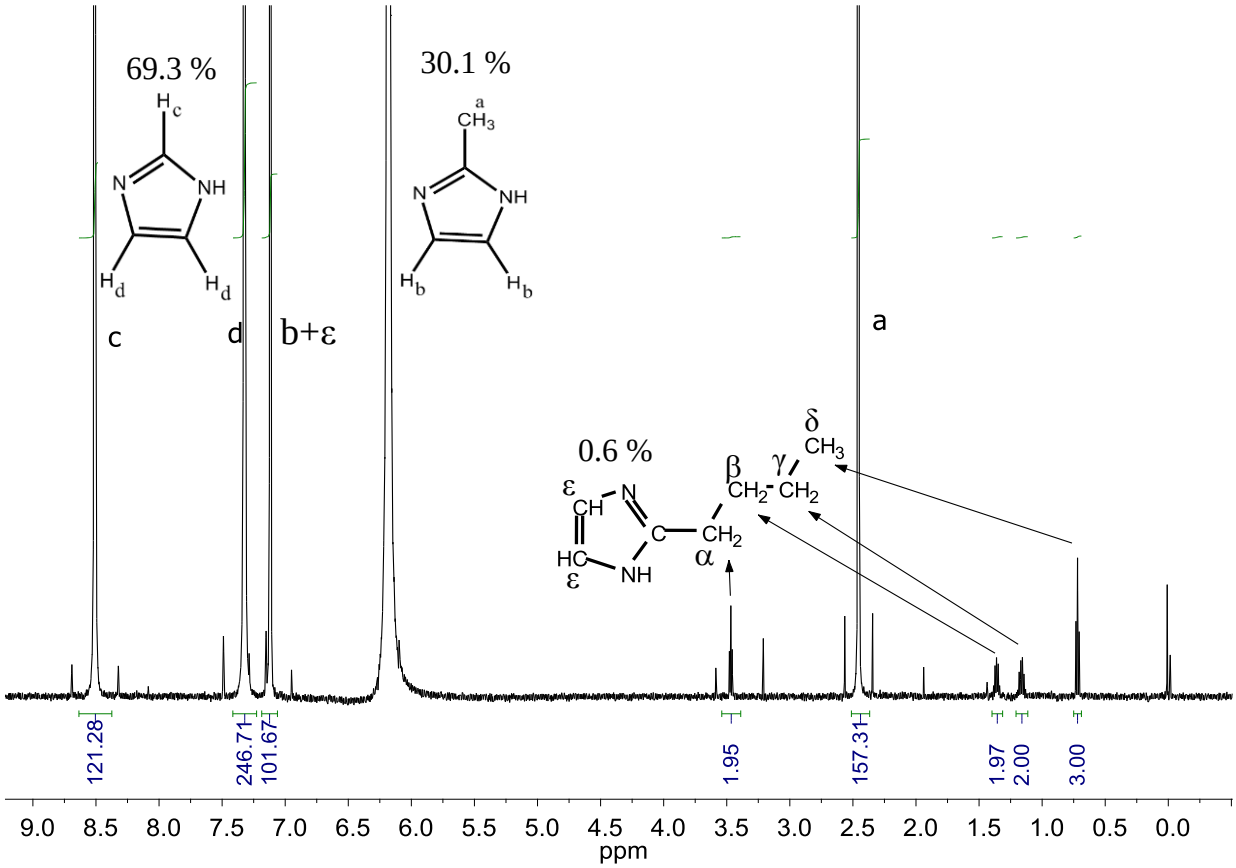

Figure 3.31 ^{1}H NMR spectrum obtained after digestion of C_4H_9-SALEM-2 in D_2O/D_2SO_4 (9:1). The relative abundance (%) of each fragment was calculated from the indicated integration values.

The 0.6 % of butyl groups in the structure of C_4H_9-SALEM-2 was too low to be detected by FTIR (see **Appendix A.8**). In **Figure 3.32** (p **86**) the PXRD pattern of C_4H_9-SALEM-2 is identical to that of SALEM-2 (a), existing as a mixture of SOD and ZNI topologies. No structural changes were detected after attachment of the butyl groups.

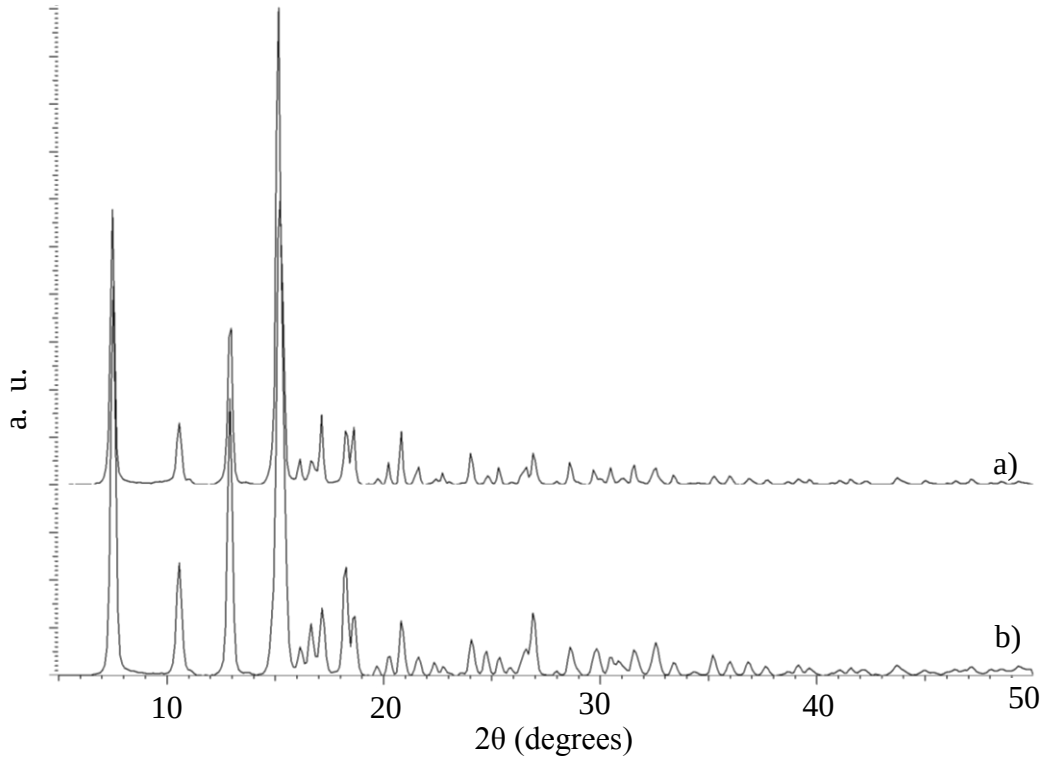

Figure 3.32 PXRD pattern of SALEM-2 (a) and C_4H_9-SALEM-2 (b) (obtained after lithiation and reaction of SALEM-2 with 1-bromobutane).

Porosity analysis of C_4H_9-SALEM-2 gave a type-1 isotherm (see **Figure 3.33**, p **87**) similar to that of the microporous SALEM-2 starting material (BET surface area of 365 m^2 g^{-1}). After lithiation of SALEM-2 and reaction with 1-bromobutane the C_4H_9-SALEM-2 product adsorbed 150 cm^3 g^{-1} of N_2 at 77 K and obtaining a BET surface area of 494 m^2 g^{-1}. It is thus possible to lithiate SALEM-2 and further react it with a brominated organic compound without changing the structure or porosity of the starting material.

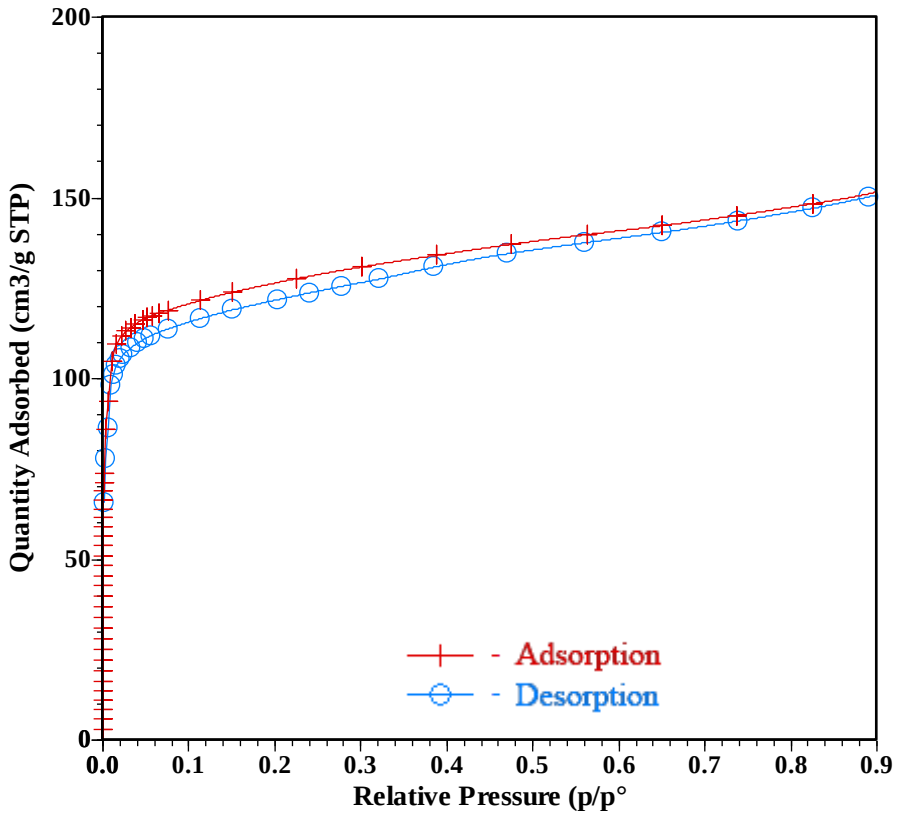

Figure 3.33 Adsorption and desorption N_2 isotherm at 77 K of C_4H_9-SALEM-2.

3.6 Catalytic Activity of nZIF-8

The catalytic activity of nZIF-8 was investigated using the Knoevenagel condensation reaction between ferrocenecarboxaldehyde (FcCHO) and malononitrile, and employing the smallest nZIF-8 nanoparticles (synthesized at 60 ℃, see **Scheme 3.1**, p **44**) as a heterogeneous catalyst with surface based Lewis basic sites. The catalytic activity of nZIF-8 will be compared to that of commercial, micro-sized ZIF-8 (Basolite Z1200) as well as without any catalyst.

The catalytic reaction (see **Scheme 3.6**, p **88**) was followed by Uv/Vis because of the high intensity adsorbance of the FcCHO and the product, 1,1-dicyanovinyl-2-ferrocene, in the visible region. Due to instrumental limitations and the exceptionally high intensities of both the reagent and the product relatively low concentrations of the reactants were used when compared to the procedure performed by Tran *et al.* (**Chapter 2.9.1**).[15] A 1:1 ratio of the two reactants was used for the Knoevenagel condensation and the sampling done at regular time intervals by extracting a small aliquot of 0.1 cm^3 for each analysis. Each aliquot was diluted 1000 times with 100 cm^3 of cold THF at 0 ℃ to ensure absorbance within instrumental limits and to slow down the reaction enough to allow for accurate measurement. The Uv/Vis spectrum of each sample was measured

at 3 ℃. Identical reaction conditions and measurements procedures were employed for micro-sized ZIF-8 (Basolite Z1200) as catalyst as well as without catalyst.

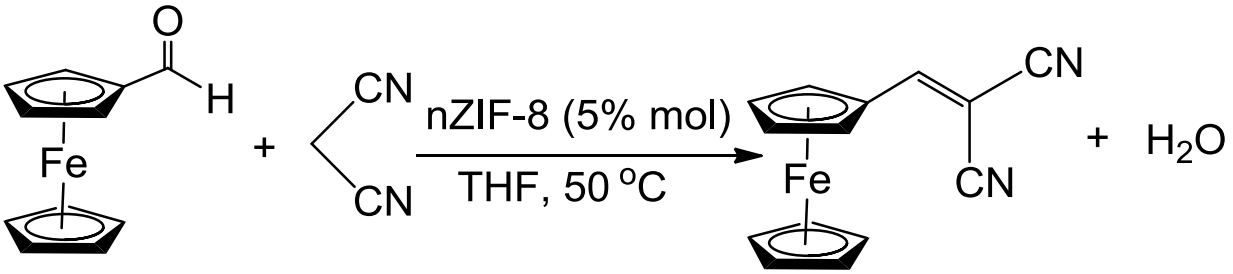

Scheme 3.6 Knoevenagel condensation reaction scheme of ferrocenecarboxaldehyde (FcCHO) and malononitrile with nZIF-8 as catalyst to yield 1,1-dicyanovinyl-2-ferrocene.

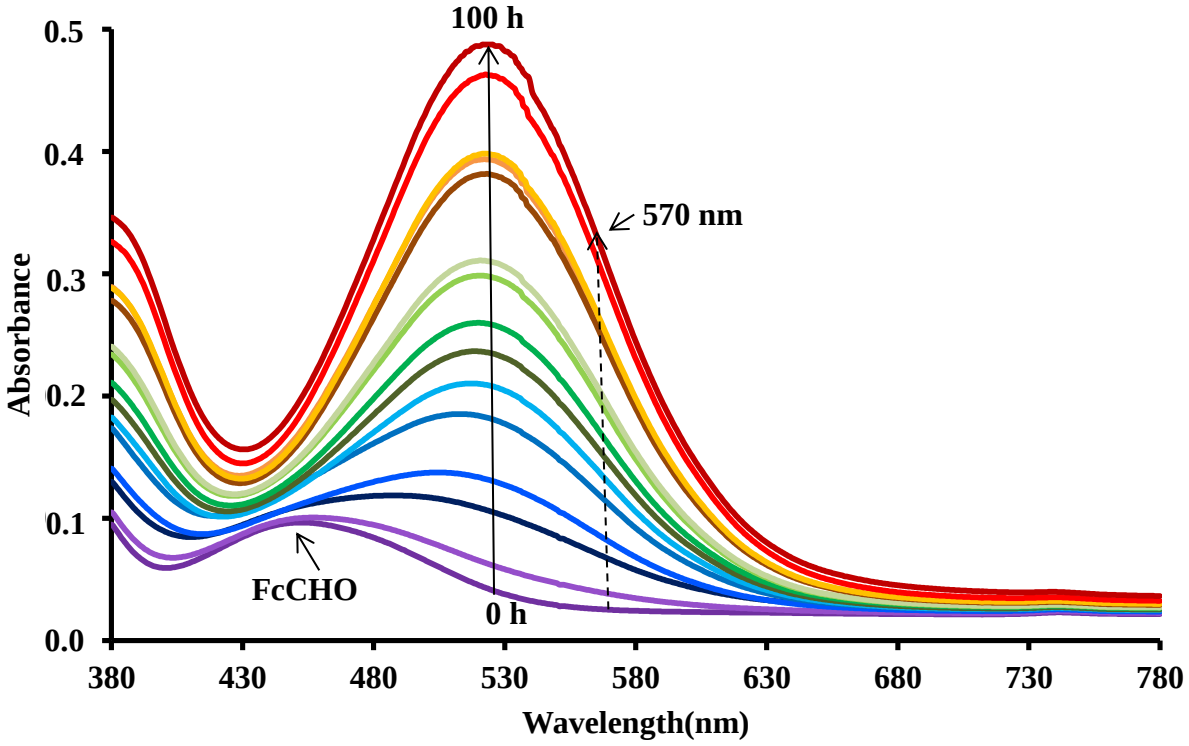

Figure 3.34 Uv/Vis absorbance specta *vs.* wavelength obtained between 0 and 100 h for the Knoevenagel condensation reaction between ferrocenecarboxaldehyde (FcCHO) and malononitrile with nZIF-8 as a catalyst to yield 1,1-dicyanovinyl-2-ferrocene.

The Uv/Vis absorbance spectrum (see **Figure 3.34**, p **88**) shows the peak at ~530 nm rising during the formation of 1,1-dicyanovinyl-2-ferrocene, but due to interference from the FcCHO peak, 570 nm was used to plot the progress of the Knoevenagel condensation reaction. The absorbance *vs.* time graph (see **Figure 3.35**, p **89**), obtained from these measurements, shows that with the use of nano-sized ZIF-8 the reaction reach completion after 140 hours, while the reaction catalysed by micro-sized ZIF-8 have not reached completion after 200 hours. Without a

catalyst, no product formation was detected as shown in (see **Figure 3.35**, p **89**). The turnover frequencies (TOF's) calculated for the first 25 h of the reactions were found to be 0.16 h^{-1} and 0.40 h^{-1} for ZIF-8 and nZIF-8 respectively. This correlates well with the t-plot external surface areas calculated in **Chapter 3.2.2.4** (p **51**) as 115 (ZIF-8) and 336 m^2 g^{-1} (nZIF-8). The 2.9 fold increase in external surface area from micro to nano sized ZIF-8 gave rise to a 2.5 fold increase of the TOF in catalytic activity, which is further proof that the catalytic reaction takes place on the external surface area of the ZIF-8 rather than within the pores.

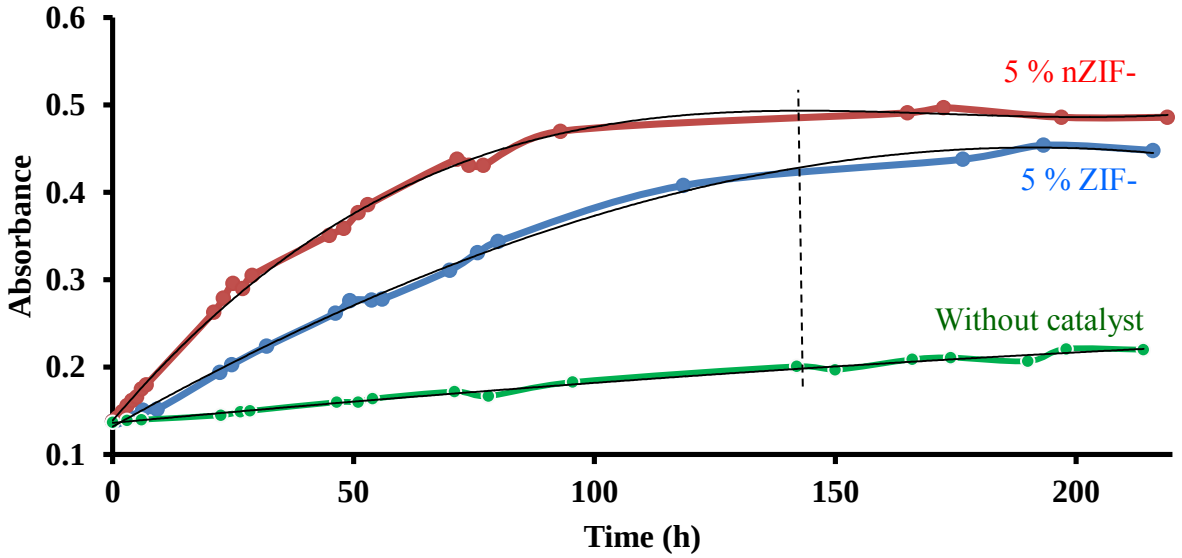

Figure 3.35 Absorbance (at 570 nm) *vs.* time plot of the Knoevenagel condensation between ferrocenecarboxaldehyde (FcCHO) and malononitrile, with nZIF-8 (red) and ZIF-8 (blue) as catalyst, as well as without catalyst (green).

This concludes the discussion of the research project. Chapter 4 will provide all the experimental details used to obtain these results.

References

[1] J. Cravillon, S. Münzer, K. Huber and M. Wiebcke, *Chem. Mater.*, 2009, **21**, 1410-1412.
[2] K. S. Park, Z. Ni, A. P. Cote, J. Yong, R. Huang, F. J. Uribe-Romo, H. K. Chae, M. O'Keeffe, O. M. Yaghi, *PNAS*, 2006, **103**, 10186-10191.
[3] J. Cravillon, R. Nayuk, S. Springer, A. Feldhoff, K. Huber and M. Wiebcke, *Chem. Mater.*, 2011, **23**, 2130-2141.
[4] J. Cravillon, R. Nayuk, S. Springer, A. Feldhoff, K. Huber and M. Wiebcke, *Chem. Mater.*, 2011, **23**, 2130-2141.
[5] P. A. Webb and C. Orr, *Analytical Methods in Fine Particle Technology (Micromeritics Instrument)*,1997, ch 3, 67-70.
[6] H-L Jiang, T. Akita, T. Ishida, M. Haruta and Q. Xu, *J. Am. Chem. Soc.*, 2010, **133**, 1304-1306
[7] J. T. Kummer, *J. Phys. Chem.*, 1956, **60(5)**, 666-670.

[8] N. Miyaura and A. Suzuki, *Chem. Rev.*, 1995, **95**, 2457-2483.
[9] M. C. McCarthy, V. Victor-Guerrero, G. V. Barnett, H. K. Jeong, *Langmuir*, 2010, **26**, 14636-14641.
[10] D. Esken, X. Zhang, O. I. Lebedev, F. Schroöder and R. A. Fischer, *J. Mater. Chem.*, 2009, **19**, 1314-1319.
[11] O. Karagiaridi, M. B. Lalonde, W. Bury, A. A. Sarjeant, O. K. Farha and J. T. Hupp, *J. Am. Chem. Soc.*, 2012, **134**, 18790−18796.
[12] V. R. Lehnert and F. Seel, *Z. anorg. allg. Chem.*, 1980, **464**, 187-194.
[13] J-P Zhang, Y-Biao Zhang, J-N Lin and X-M Chen, *Chem. Rev.*, 2012, **112**, 1001-1033.
[14] J. C. Tan, T. D. Bennett and A. K. Cheetham, *PNAS*, 2010, **107 (22)**, 9938-9943.
[15] U. P. N. Tran, K. K. A. Le and N. T. S. Phan , *ACS Catalysis.*, 2011, **1**, 120-127.

4 Experimental

4.1 Introduction

In this chapter, all chemicals, equipment, methods and procedures for synthesis characterization and analyses are described.

4.2 Chemicals

All synthesis reagents were purchased from Sigma-Aldrich and all solvents from Merck. These were used without further purification unless stated otherwise. When needed solvents were dried and distilled for further use. Double distilled water was used where necessary.

4.3 Equipment

Melting points were determined with an Olympus BX51 polarized microscope, fitted with a LINKAM THMS 600 heating stage. Transmission electron microscopy TEM was performed with a Philips (FEI) CM100 equipped with a Megaview III digital camera and coupled to an Oxford X-Max (80 mm^2), energy-dispersive X-ray spectroscope (EDS). TEM pictures were analysed utilizing Soft Imaging System (analySIS) software.

^1H Nuclear magnetic resonance (^1H NMR) spectra were measured on a Bruker Avance DPX 300 NMR or a Bruker Advance II 600 NMR spectrometer at 298 K. The ^1H chemical shifts were reported relative to $SiMe_4$ at 0.0 ppm as external standard and utilizing the solvent peak as internal standard were applicable. All insoluble ZIF-8 (5-10 mg) derivatives were suspended in D_2O (9 ml) by sonification. D_2SO_4 (1 ml) was added dropwise until a homogeneous solution was obtained for NMR measurements, taken after locking directly to D_2O.

All infrared spectra were measured on a Bruker Tensor 27 infrared spectrophotometer fitted with a Pike Miracle single bounce diamond ATR crystal or A Thermo Scientific Nicolet iS50 ATR Infrared Spectrometer with OMNIC v9.2.86 software. Uv/Vis spectra were measured on a Shimadzu UV-1650 PC UV-Visible spectrophotometer fitted with a 6 cell attachment and a Shimadzu CPS-240A Temperature controller. Spectra obtained were analysed with the UVProbe Version 2.20 software. All porosity and surface area measurements were performed on a

Micromeritics ASAP 2020 Surface Area and Porosity Analyzer and the data analysed with ASAP 2020 V2.0 for physisorption. The nZIF-8 was activated at 150 °C for 16 hours for porosity analysis and a typical amount of ~20 mg was used for each analysis with the warm and cold free space determined separately. Porosity results were refined by MicroActive V1.01 Software.

Powder X-ray diffraction patterns (PXRD) were collected on a Bruker D2 Phaser powder X-ray diffractometer at room temperature, employing a flat plate sample holder and Cu radiation (λ = 1.54 Å). Diffraction patterns were collected in the range 5° to 50° for 2θ, with a step size of 0.1° and a counting time of two seconds per step.

Thermo gravimetric analyses (TGA) was performed on a Mettler-Toledo TGA/SDTA851 under an argon atmosphere. The software STAR SW 8.10 was used to analyse TGA results. A temperature program was setup for the TGA analysis first the TGA was set to 30 ℃ for 30 minute to stabilize the TGA, then was heated to 800 ℃ at 10 ℃ min^{-1} and lastly set to rest at 800 ℃ for 1 min and cooled to 30 ℃ for further analysis.

X-ray Photoelectron Spectroscopy (XPS) data were recorded on a PHI 5000 Versaprobe system with a monochromatic AlK X-ray source. Spectra were obtained using the aluminium anode (Al Kα = 1486.6 eV) operating at 50 μm, 12.5 W and 15 kV energy (97 X-ray beam). The survey scans were recorded at constant pass energy of 187.85 eV and region scans at constant pass energy of 29.35 eV with the analyzer resolution ≤ 0.5 eV. The background pressure was 2 x 10^{-8} mbar. The XPS data were analysed utilizing Multipak version 8.2c computer software with Gaussian–Lorentz fits (the Gaussian/Lorentz ratios were always > 95 %).

A Shimadzu ICPS-7510 Inductively Coupled Plasma – Optical emission spectrometry (ICP-OES) with a radial-sequential plasma spectrometer was used for the wet chemical analysis of all the samples during the current study. The vertically oriented ICP-OES with the 'radial viewing' plasma was found to be suitable due to its better detection limits. The emission intensity measurements were made using the default conditions as indicated in (see **Table 4. 1**, p **92**).

Table 4. 1 ICP-OES operating conditions.

Parameter	Condition
RF power	1.2 kW
Coolant gas flow rate	14.0 L/min
Plasma gas flow rate	45 L/min
Auxiliary gas flow rate	0.5 L/min
Carrier gas flow rate	0.7 L/min

Sample uptake method	Peristaltic pump
Type of spray chamber	Glass cyclonic
Type of nebulizer	Concentric
Injector tube diameter	3.0 mm

4.4 Synthesis of Nano-sized 2-Methylimidazole Zinc Salt or Nano-ZIF-8 (nZIF-8)

4.4.1 Synthesis of nZIF-8 at Various Temperatures in Methanol

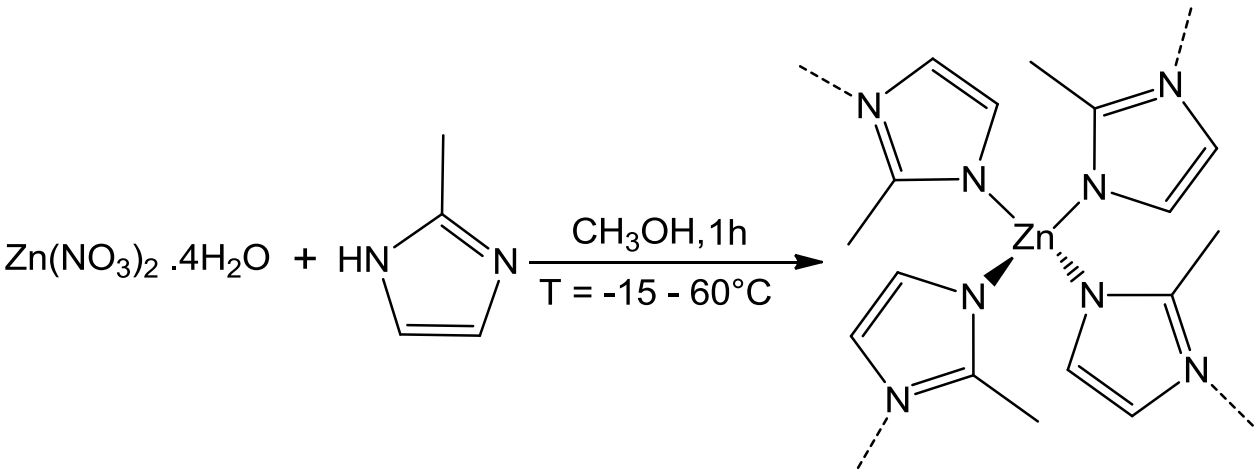

nZIF-8 was synthesized by the following adapted procedure.[1] A solution of $Zn(NO_3)_2.4H_2O$ (0.649 g, 2.48 mmol) in methanol (50 cm^3) at 25 $^oC^*$ was added rapidly to a solution of 2-methylimidazole (1.643 g, 19.99 mmol) in methanol (50 cm^3) at 25 $^oC^*$. The mixture was stirred for 1 hour at 25$^oC^*$. The precipitate was isolated by centrifugation (7000 rpm, 30 min, 15 ^{o}C). The solid product was washed with methanol (3 x 100 cm^3), isolated by centrifugation and dried in air overnight .The dried product was activated at 250 ^{o}C under nitrogen flow for 90 minutes to obtain a white powder (0.184 g, 32.6 %). ν_{max}/cm^{-1} (**Spectrum.A.1** and **Spectrum.A.2**): ν(C=N) = 1584, ν(C-H) = 3135; 2929. ^{1}H NMR: δ_H (300 MHz, D_2O)/ppm (**Spectrum D.1**): 6 (s, 2H, CH=CH), 1.33 (s, 3H, CH_3). PXRD (**Figure C.1)**.

Table 4.2 Synthesis of nZIF-8 at various Temperatures from $Zn(NO_3)_2.4H_2O$ (2.48 mmol) and 2-methylimidazole (20 mmol) in methanol.

*Synthesis Temperature ºC	Yield /g (%)
-15	0.023 (4.1)
-5	0.209 (36.7)
2	0.193 (33.9)
25	0.184 (32.3)
30	0.211 (37.1)
40	0.243 (43.0)
50	0.223 (39.3)
60	0.209 (36.7)

4.4.2 Bulk Synthesis of nZIF-8

A solution of $Zn(NO_3)_2.4H_2O$ (1.297 g, 4.96 mmol) was dissolved in methanol (50 cm^3) at room temperature and was added rapidly to a solution of 2-methylimidazole (3.306 g, 40.25 mmol) dissolved in methanol (50 cm^3). The mixture was stirred for 1 hour at room temperature. The nano crystals were isolated by centrifugation (7000 rpm, 30 min, 15 ºC), washed with methanol (3 x 100 cm^3) and isolated by centrifugation. The precipitate was dried in air overnight and activated by heating at 250 ^oC under nitrogen flow for 90 minutes to obtain a white powder (0.396 g, 34.8 %). ν_{max}/cm^{-1} (**Spectrum A.3**:): ν(C=N) = 1584, ν(C-H) = 3135; 2929. PXRD (**Figure C.1)**.

4.5 Metal Impregnation of nZIF-8 by Chemical Liquid Deposition

4.5.1 Ag@nZIF-8 *via* $AgNO_3$@nZIF-8[2]

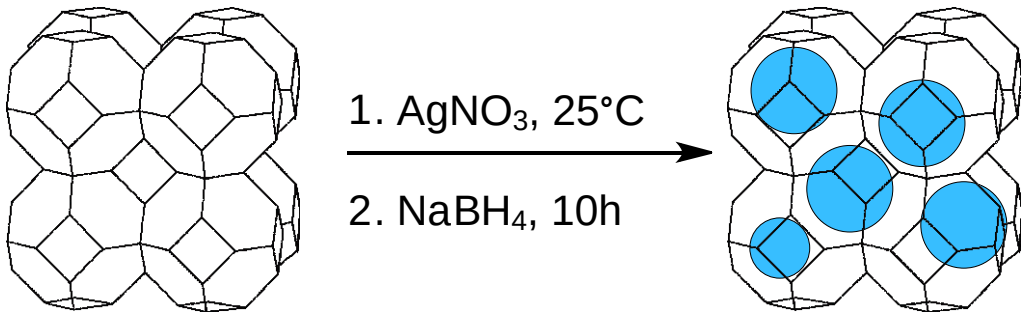

After preparation of nZIF-8 (0.700 g, 3.05 mmol) at 120 °C for 6 hours under vacuum, it was dispersed in methanol (11 cm^3) in an ultra-sonic bath for 3 minutes. The suspension was stirred vigorously while a solution of $AgNO_3$ (22.05 mg, 0.13 mmol) dissolved in methanol (3 cm^3) was added dropwise to the suspension. Vigorous stirring continued for 10 hours at room temperature while covered in foil. For characterization purposes nano crystals were isolated from a small portion of the suspension to obtain after workup, $AgNO_3$@nZIF-8 (FTIR **Spetrum A.5.a,** Ag – 0.6 wt %). To the rest of the suspension a solution of sodium borohydride (39.6 mg, 1.046 mmol) in methanol (5 cm^3) was added and stirred for 1 hour at room temperature. The nano crystals were isolated by centrifugation (7000 rpm, 30 min, 15 ^oC), washed with methanol (3 x 100 cm^3) and centrifugated. The solid product was dried in air to obtain the title light green powder (0.6395 g, 91 % base on nZIF-8). ν_{max}/cm^{-1} (**Spectrum A.4.b and c**): ν(C=N) = 1584, ν(C-H) = 3135; 2929. PXRD (**Figure 3.10)**. ICP: Ag – 3.8 wt %.

4.5.2 $Pd(NO_3)_2$@nZIF-8

The same procedure as in **4.5.1** was followed with pre-treated nZIF-8 (0.700 g, 3.05 mmol), $Pd(NO_3)_2.2H_2O$ (35.5 mg, 0.13 mmol). The solid product was isolated without reduction and dried in air to obtain the title light grey powder (0.6654 g, 95 % base on nZIF-8). ν_{max}/cm^{-1} (**Spectrum A.5.a**): ν(C=N) = 1584, ν(C-H) = 3135; 2929. ICP: Pd – 3.3 wt %. PXRD (**Figure 3.15)**.

4.5.3 $Pd(OAc)_2$@nZIF-8

The same procedure as in **4.5.1** was followed with pre-treated nZIF-8 (0.700 g, 3.05 mmol) and $Pd(O_2CCH_3)_2$ (29.2 mg, 0.13 mmol). The solid product was isolated without reduction and dried dried in air to obtain the title light grey powder (0.6690 g, 96 % base on nZIF-8). ν_{max}/cm^{-1} (**Spectrum A.5.b**): ν(C=N) = 1584, ν(C-H) = 3135; 2929. PXRD (**Figure 3.15)**. ICP: Pd – 3.5 wt %.

4.5.4 Pd@nZIF-8 via $Pd(acac)_2$@nZIF-8

In a typical synthesis pre-treated nZIF-8 (0.700 g, 3.05 mmol) and $Pd(C_5H_7O_2)_2$ (34.9 mg, 0.13 mmol) with sodium borohydride (40 mg, 1.057 mmol) was prepared in the same procedure as **4.5.1**. The dried powder was washed and dried in air to obtain the title dark grey powder (0.6661 g, 95 % base on nZIF-8). ν_{max}/cm^{-1} (**Spectrum A.5.c**): ν(C=N) = 1584, ν(C-H) = 3135; 2929. PXRD (**Figure 3.15)**. ICP: Pd – 3.1 wt %.

4.6 Solvent Assisted Ligand Exchange (SALE) Derivatives of nZIF-8

4.6.1 Time-resolved Ligand Exchange of nZIF-8 with Imidazole to Synthesize SALEM-2[3]

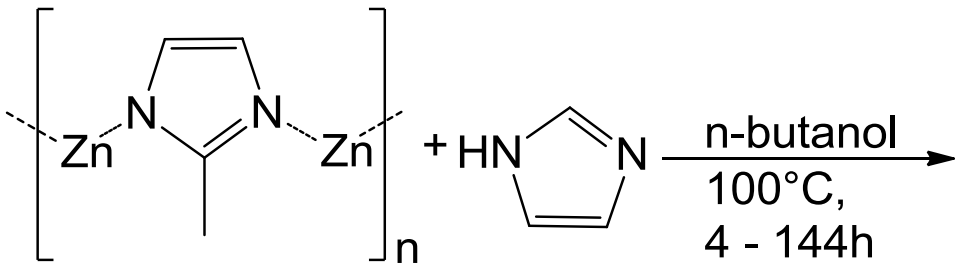

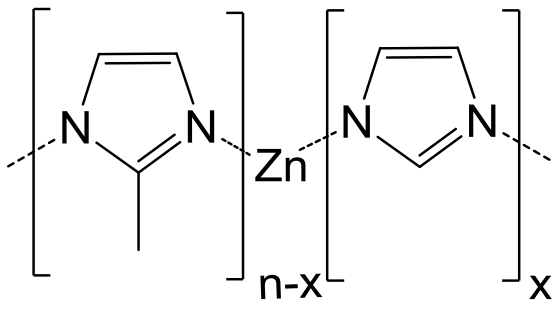

nZIF-8 (0.300 g, 1.306 mmol) was suspended in *n*-butanol (30 cm^3) in an ultra-sonic bath for 5 minutes and transferred into a stainless steel reactor. Imidazole (0.603 g, 8.858 mmol), dissolved in *n*-butanol (30 cm^3) was mixed with the nZIF-8 suspension. The reactor was sealed and heated at 100 ℃ for 144* hours. After cooling the nano crystals were isolated by centrifugation (7000 rpm, 30 min, 15 ℃), washed with methanol (3 x 100 cm^3) centrifugated, dried in air overnight and obtained as a white powder SALEM-2_{144h} (0.233 g, 89 % based on nZIF-8). ^{1}H NMR: δ_H (300 MHz, D_2O)/ppm (**Spectrum D.6**): 7.54 (s, 8.94H, CH), 6.36 (s, 18.48H, CH=CH), 6.15 (s, 2H, CH=CH), 1.49 (s, 3H, CH_3)

Table 4.3 Ligand exchange at different times with reagent of nZIF-8 (1.3 mmol) and imidazole (8.9 mmol) in *n*-butanol.

Product	***Time**	**Yield/ g (%)**	**Conversion (%)**	**^{1}H NMR Spectrum**	**PXRD Spectrum**
SALEM-2_{144h}	144 Hours	0.233 (89)	90	**D.6**	**Figure 3.40.f**
SALEM-2_{72h}	72 Hours	0.226 (85)	91	**D.5**	**Figure 3.40.e**
SALEM-2_{24h}	24 Hours	0.219 (83)	79	**D.4**	**Figure 3.40.d**
SALEM-2_{12h}	12 Hours	0.231 (87)	58	**D.3**	**Figure 3.40.c**
SALEM-2_{4h}	4 Hours	0.225 (85)	31	**D.2**	**Figure 3.40.b**

4.6.2 Synthesis of ZIF-ZNI

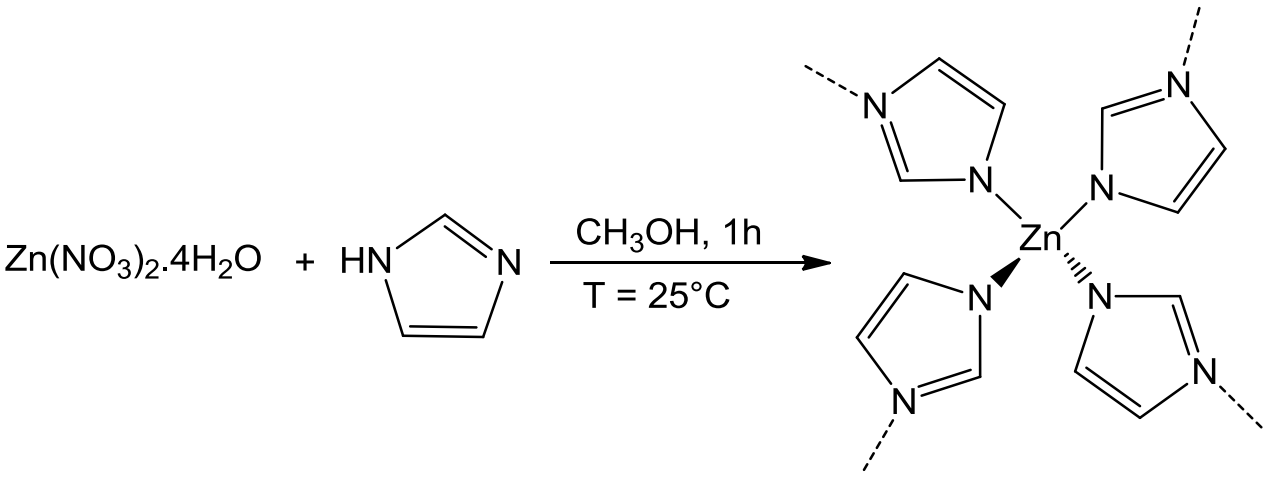

A solution of $Zn(NO_3)_2.4H_2O$ (0.643 g, 2.46 mmol) in methanol (50 cm^3) at 25^{o}C was added rapidly to a solution of imidazole (1.368 g, 20.09 mmol) in methanol (50 cm^3) at 25℃. The mixture was stirred for 1 hour at 25℃. The nano crystals were isolated by centrifugation (7000 rpm, 30 min, 15^{o}C), washed with methanol (3 x 100 cm^3) and centrifugated. A small part of the colloidal suspension (5 cm^3) was collected and the remainder was dried in air overnight to obtain

a white powder (0.1 g, 20 % based on zinc). ν_{max}/cm^{-1} (**Spectrum A.7**): (C=C) = 1616, ν(C-H) = 1085. PXRD (**Figure 3.41)**

4.6.3 Synthesis of Ligand Exchange nZIF-8 Butane (C_4H_9-SALEM-2)

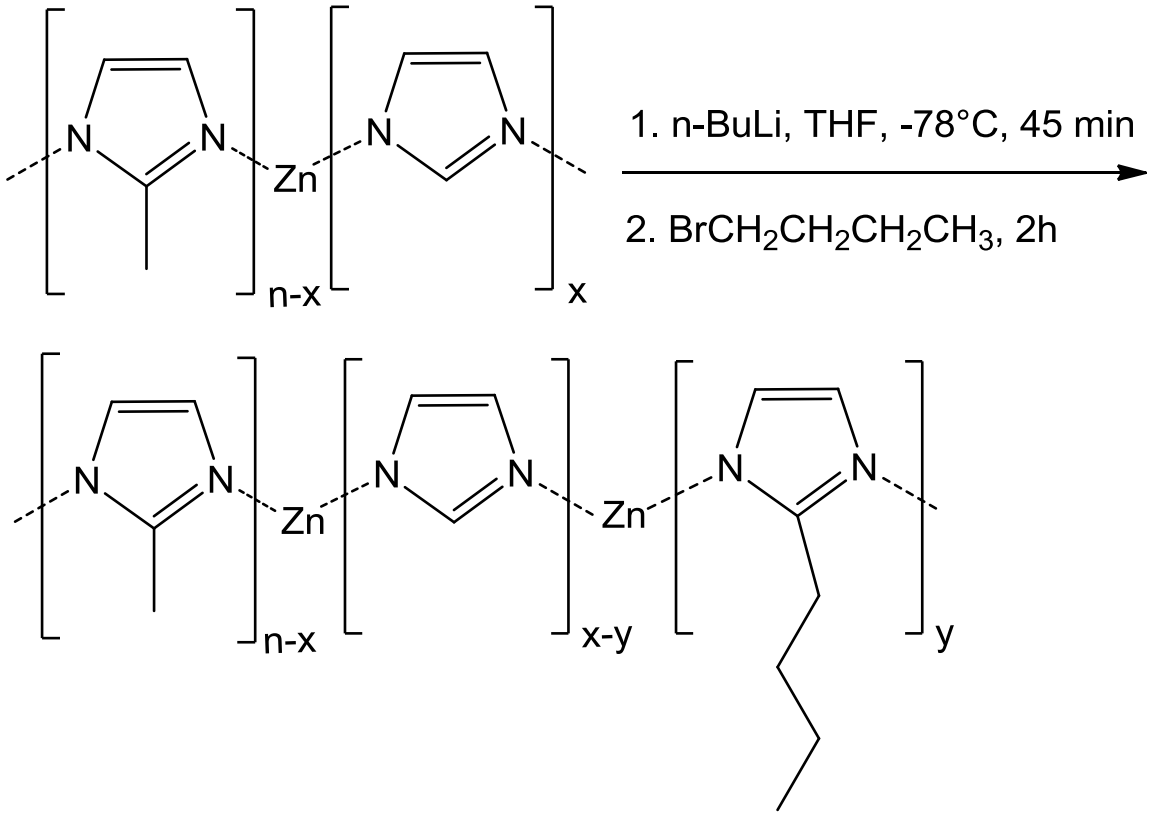

As-synthesized SALEM-2_{12h} (0.210 g) was heated at 100 ^oC for 1 day under vacuum and then suspended in THF (20 cm^3) with ultra-sonication under argon flow. While stirring under argon, the solution was cooled to -78 °C before 2.5 M *n*-butyllithium in hexane (0.8 cm^3) was added dropwise over 5 minutes. The stirred solution was allowed to warm up to room temperature. After 45 minutes 1-bromobutane (0.2 cm^3, 1.85 mmol) was added drop-wise over 5 minutes and stirred for 2 hours at room temperature. The nano crystals were isolated by centrifugation (7000 rpm, 30 min, 15^oC), washed with methanol (100 cm^3), water/methanol (50 cm^3/50 cm^3), methanol (2 x 100 cm^3) and centrifugated. The white powder was dried in air overnight before it was activated at 100 °C under vacuum for 2 days to obtain the powder product (0.1600 g, 0.8 % conversion by ^1H NMR). ^1H NMR: δ_H (600 MHz, D_2O)/ppm (**Spectrum D.7**): 8.51 (s, 2.31H, CH), 7.32 (s, 4.71H, CH=CH), 7.12 (s, 1.95H, CH=CH), 3.47 (t, 0.04H, CH_2), 2.43 (s, 3H, CH_3), 1.36 (m, 0.04H, CH_2), 1.2 (m, 0.04H, CH_2), 0.7 (t, 0.08H, CH_3). PXRD (**Figure 3.48)**

4.7 Heterogeneous Catalysis: Knoevenagel Condensation

4.7.1 Synthesis of 1,1-Dicyanovinyl-2-ferrocene with nZIF-8 as Catalyst

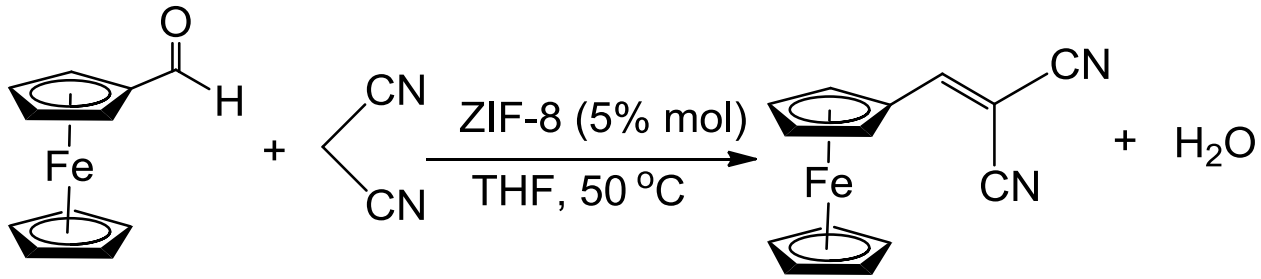

Ferrocenecarboxaldehyde (0.407 g, 1.9 mmol) was dissolved and nZIF-8 (0.02 g, 0.087 mmol) dispersed in tetrahydrofuran (THF) (4 cm^3). Malononitrile (0.379 g, 5.74 mmol) was dissolved in THF (1 cm^3). Both solutions were heated to 50 ℃ before adding the malononitrile solution to the ferrocenecarboxaldehyde solution. The reaction was stirred overnight and turned to dark purple. The crude product was purified with column chromatography (hexane:ether 1:1 on silica) and dried in air at room temperature to obtain a fine purple crystals (0.3083 g, 55 % based on ferrocenecarboxaldehyde); Melting point 96 ℃, R_f = 0.35 (hexane:ether = 1:1) ν_{max}/cm^{-1} (**Spectrum A.10**): 2218 (C≡N), 1103/986 (C-C, Cp-ring). ^1H NMR: δ_H (300 MHz, $CDCl_3$)/ppm (**Spectrum D.8**): 7.73 (s, 1H, CH), 4.35 (s, 5H, C_5H_5), 4.8 (t, 2H, C_5H_4), 5 (t, 2H, C_5H_4).

4.7.2 Time Resolved Synthesis of 1,1-Dicyanovinyl-2-ferrocene with nZIF-8 as Catalyst

The kinetics of the Knoevenagel condensation reaction between ferrocenecarboxaldehyde and malononitrile was monitored by Uv/Vis spectrophotometer (by monitoring the change of absorbance at 570 nm) at 3°C. THF was used as solvent. The reactant was diluted 1000 times with cold THF after extraction and immediately measured on the Uv/Vis spectrophotometer. All kinetic measurements were done in a 1:1 molar ratio of ferrocenecarboxaldehyde and malononitrile.

In a typical synthesis ferrocenecarboxaldehyde (0.856 g, 4 mmol) and nZIF-8 (0.04 g, 0.174 mmol) was dispersed in tetrahydrofuran (THF) (10 cm^3) and malononitrile (0.264 g, 4 mmol) was dissolved in THF (10 cm^3). Both solutions were heated to 50℃ before adding the

malononitrile solution to the ferrocenecarboxaldehyde solution while stirring at 50 ℃. A small aliquot (0.1 cm^3) was extracted at each measuring interval, cooled to 0 ℃, diluted with cold THF (100 cm^3) and transferred to a glass cuvette for Uv/Vis spectrum measurement. The procedure was repeated with micro sized ZIF-8 as well as without any catalyst.

1 J. Cravillon, S. Münzer, K. Huber and M. Wiebcke, *Chem. Mater.*, 2009, **21**, 1410-1412.
2 H-L Jiang, T. Akita, T. Ishida, M. Haruta and Q. Xu, *J. Am. Chem. Soc.*, 2010, **133**, 1304-1306.
3 O. Karagiaridi, M. B. Lalonde, W. Bury, A. A. Sarjeant, O. K. Farha and J. T. Hupp, *J. Am. Chem. Soc*., 2012, **134**, 18790−18796.

5 Conclusion and Future Perspectives

5.1 Conclusion

In this study, the particle size control of nano sized ZIF-8 (between 25 and 85 nm) was successfully achieved by applying different synthesis temperatures: -15, -5, 2, 25, 30, 40, 50, 60 ℃ during simple bench top reactions in methanol. Real particle sizes were determined by statistical measurement of TEM pictures, giving a particle size distribution. The Scherrer equation was applied to PXRD data peak broadening as a theoretical method to calculate the minimum size of the nano particles. From TEM analysis it was found that a synthesis temperature as low as -15 ℃ yields nZIF-8 particles with sizes of 85 nm and a wide particle size distribution, while a synthesis temperature as high as 60 ℃ yield particle with sizes of 25 nm and a narrow particle size distribution. The increase in synthesis temperatures, within the limits for methanol, lead to smaller particle sizes with a narrower particle size distribution. The PXRD results, giving the minimum particle size of the synthesized nZIF-8, were in agreement with the results from TEM measurements. FTIR confirmed the chemical structure and PXRD the SOD topology of the synthesized nZIF-8 material. Porosity analyses showed that all nZIF-8 particles were capable of adsorbing more than 400 $cm^3\ g^{-1}$ of N_2 (STP) at 77 K, with BET surface areas of more than 1600 $m^2\ g^{-1}$. The external surface area of nano particles was calculated for each batch using t-plot analysis and found to be in a range between 254 and 336 $m^2\ g^{-1}$. As the particle size decreases the external surface increases. The smallest nanoparticles, synthesized at 60 ℃ have an external surface area 3 times larger than the commercial ZIF-8. Thermal analysis showed that nZIF-8 particles are stable up to 450 ℃ before structural breakdown.

The evacuated porous nZIF-8 particles were loaded with Ag and Pd salts using chemical liquid deposition (CLD) methods. These salts were chemically reduced by $NaBH_4$ after impregnation to give Ag@nZIF-8 and Pd@nZIF-8 while maintain the SOD topology as shown by PXRD. By using a high concentration of $Ag(NO)_3$ (18.56 mM) during impregnation, a 3.8 wt % of Ag was found in Ag_{high}@nZIF-8, as determined by ICP after reduction. The presence of these silver particles in nZIF-8 was confirmed by EDS and XPS measurements, while TEM images showed that the Ag nanoparticles are mostly found on the external surface of the nZIF-8 particles. Of the three different palladium precursors, $Pd(NO_3)_2$, $Pd(OAc)_2$ and $Pd(acac)_2$, used for impregnation

of nZIF-8, only $Pd(acac)_2$ resulted in Pd nanoparticles of ~1 nm distributed throughout Pd@nZIF-8 after reduction with $NaBH_4$, as shown by TEM. Qualitative analysis with EDS and XPS confirmed the presence of Pd^0 in the ZIF-8 material, while ICP analysis showed a loading of ~3.5 wt % Pd in Pd@nZIF-8. Porosity analysis of Ag@nZIF-8 revealed a decrease in BET surface area (from 1705 $m^2 g^{-1}$ of nZIF-8 to 1440 $m^2 g^{-1}$ of Ag_{high}@nZIF-8) as well as the amount of N_2 adsorped (from 437 $cm^3 g^{-1}$ of nZIF-8 to 301 $cm^3 g^{-1}$ of Ag_{high}@nZIF-8) after loading the pores with silver particles. This could be due to the silver particles on the external surface of nZIF-8 partially blocking the pores. In the case of Pd@nZIF-8 an increase in BET surface area (from 1705 $m^2 g^{-1}$ of nZIF-8 to 1770 $m^2 g^{-1}$ of Pd@nZIF-8) as well as the uptake of N_2 (from 437 $cm^3 g^{-1}$ of nZIF-8 to 483 $cm^3 g^{-1}$ of Pd@nZIF-8) was observed. This confirmed the distribution o the Pd particles inside the pores of nZIF-8. Metal impregnation had no appreciable effect on the thermal stability of the original unloaded nZIF-8.

A high percentage of the 2-methylimidazole linkers of nZIF-8 were successfully replaced with imidazole during a solvent assisted ligand exchange (SALE) procedure without changing the SOD topology of the nanoparticles. A maximum exchange of 80 % was reached after 24 hours of SALE. It was also demonstrated that the percentage of ligand exchange can be controlled by reaction time, with shorter SALE times giving lower exchange percentages. The ligand-exchanged products, SALEM-2, were characterized by ^1H NMR (digested in a 9:1 ratio of D_2O and D_2SO_4), giving clear quantification of the exchange of 2-methylimidazolate linkers by imidazole. PXRD measurements were used to successfully follow changes to the SOD topology of nZIF-8 during the SALE process. It showed that the SOD topology was maintained till an 80 % conversion, with ZNI topology observed at higher conversion percentages. TEM analysis was used to prove that the SALEM-2 products are still nano-sized after the solvothermal procedure. The type-1 isotherms of SALEM-2 obtained during ASAP measurements, showed that an increase in ligand exchange lead to a decrease in adsorption from 444 $cm^3 g^{-1}$ (of N_2 at STP) at 31 % exchange, to 90 $cm^3 g^{-1}$ after 80 % conversion. Further exchange of 2-methylimidazolate linkers with imidazole leads to a nonporous material with no N_2 adsorption. Similarly the BET surface area of the SALEM-2 products decreases with an increase in conversion. The SALEM-2 products remained thermally stable up to 450 ℃, similar to the nZIF-8 starting material.

Post synthetic modification (PSM) of the SALEM-2 products containing ~60 % imidazole linkers, was successfully performed by lithiation of the carbon atom in the 2-position of the imidazole. After lithiation, butyl chains were attached to the lithiated active sites with a 0.6 %

success rate with respect to the total number of linkers. Throughout the PSM process, the topology (mixed SOD and ZNI topology) was maintained.

nZIF-8 synthesized at 60 ℃ with an average particle size of 26 nm showed a 2.5 fold increase in turnover frequency in the Knoevenagel condensation reaction between ferrocenecarboxaldehyde and malononitrile as compared to micro sized commercial ZIF-8. As the catalytic sites occur only on the external surface area of ZIF-8, this result is in excellent agreement with the fact that the nZIF-8 nanoparticles have a 2.9 times larger external surface than commercial ZIF-8. The increased external surface area of the nZIF-8 is thus a direct cause for the increased turnover frequency observed.

5.2 Future Perspectives

In this study the author has shown important ways to improve and modify ZIF-8 nanoparticles for applications in the fields like catalysis. This study can lead to further investigation like the following:

I. The sized-control achieved by synthesis temperature can be combined with other techniques such as the addition of surfactants to synthesize smaller ZIF-8 nanoparticles with much narrower size distribution, which can be used to improve catalytic activity on the external surface area or as additive to oil to enhance lubrication.

II. Ag@nZIF-8 and Pd@nZIF-8 can be evaluated for catalytic activity using reactions like oxidation reaction for Ag@nZIF-8 and Suzuki and hydrogenation reactions for Pd@nZIF-8.

III. A series of solvent exchanged ligand exchange reactions using other imidazole derivatives (e.g. benzimidazole and 2-aminoimidazole) as well as the exchange of the metal centres can be performed for nZIF-8.

IV. Kinetic studies on the time resolved SALE reactions can be performed to determine the rate. The use of techniques such as PXRD, FTIR and ^{1}H NMR can be investigated for these studies.

V. Computer simulations to determine the mechanism of the ligand exchange process. This will aim to explain the effect it has on the SOD topology of the nZIF-8 structure.

VI. By attaching butyl groups to the surface of the SALEM-2 nanoparticles, it was demonstrated that post synthetic modifications of the nanoparticles can used to add additional functional groups to influence properties such as gas adsorption or facilitate catalysis.

CONCLUSION

Appendix

A. ATR-FTIR Spectra

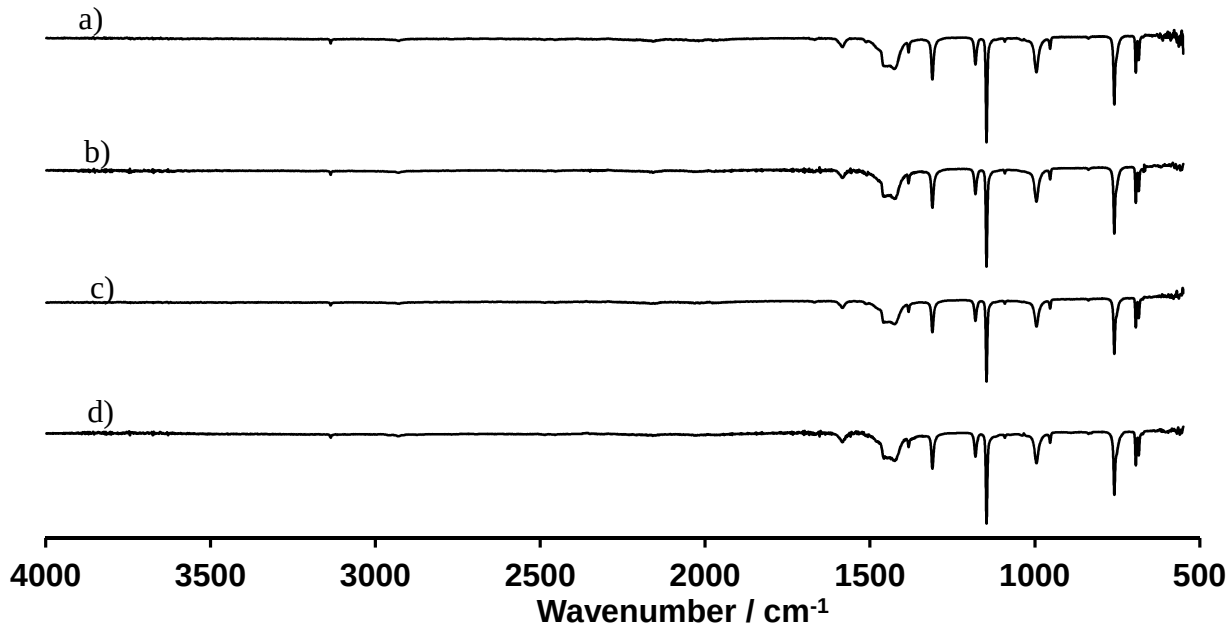

Spectrum A.1 FTIR spectra of nZIF-8 synthesized at a) 25 °C; b) 2 °C; c) -5 °C and d) -15 °C.

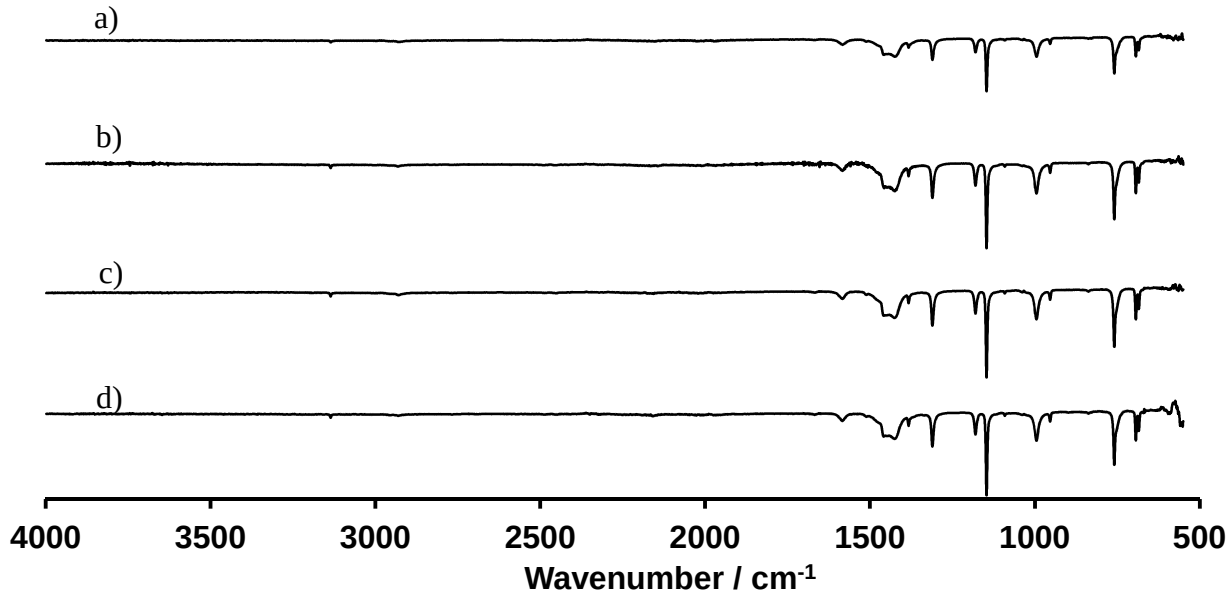

Spectrum A.2 FTIR spectra of nZIF-8 synthesized at a) 30 °C; b) 40 °C; c) 50 °C and d) 60 °C.

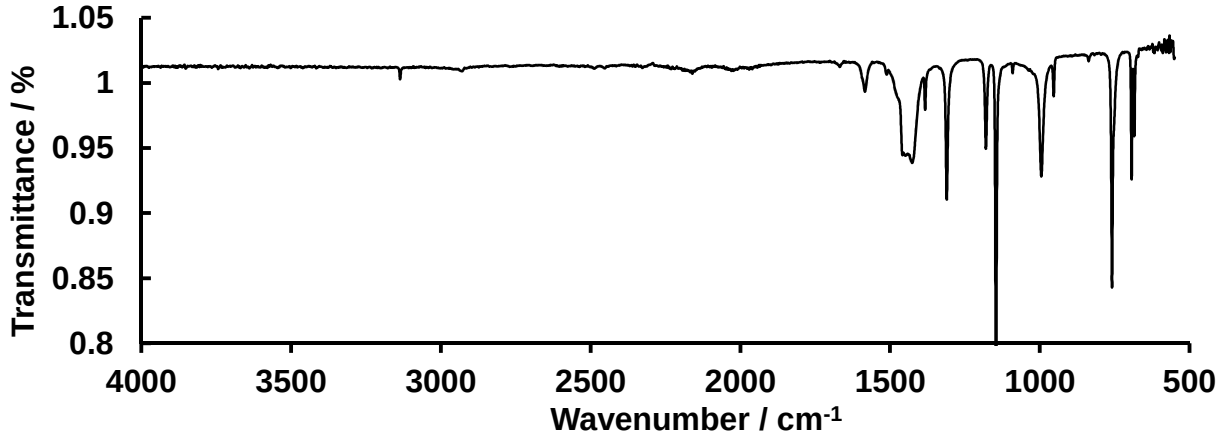

Spectrum A.3 FTIR spectra of nZIF-8 (Bulk synthesis at 25 °C).

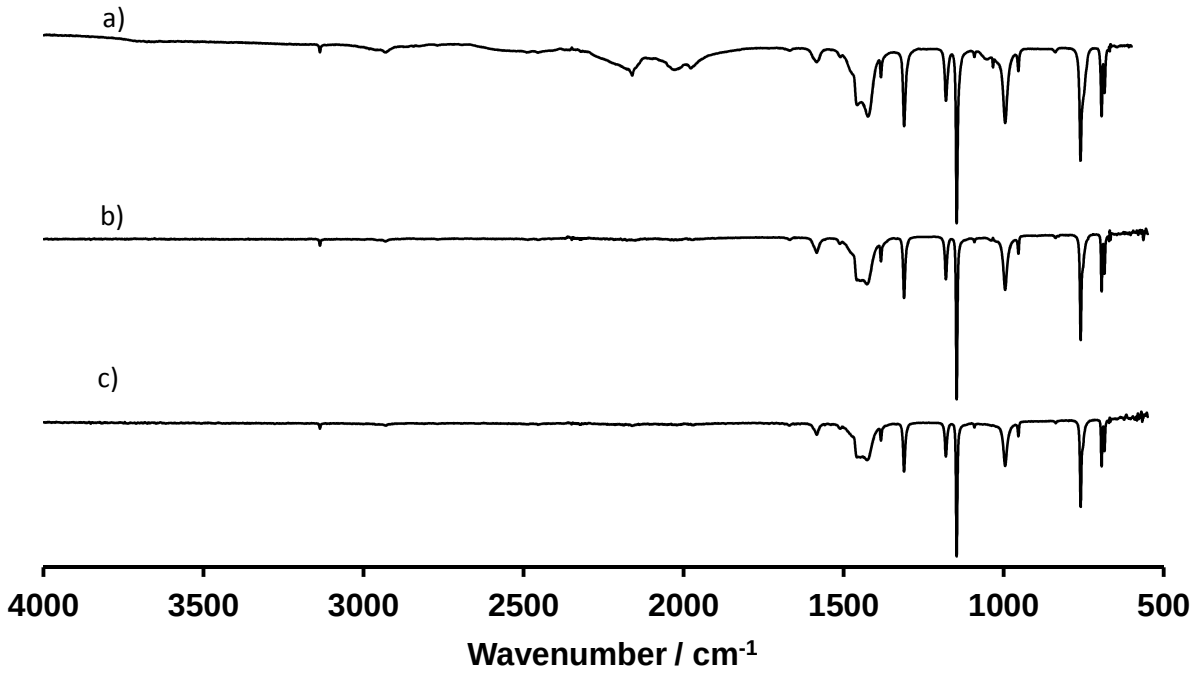

Spectrum A.4 FTIR spectra of silver loaded in nZIF-8 a) $Ag(NO_3)_2$@nZIF-8; b) Ag@nZIF-8 and c) Ag_{high}@nZIF-8.

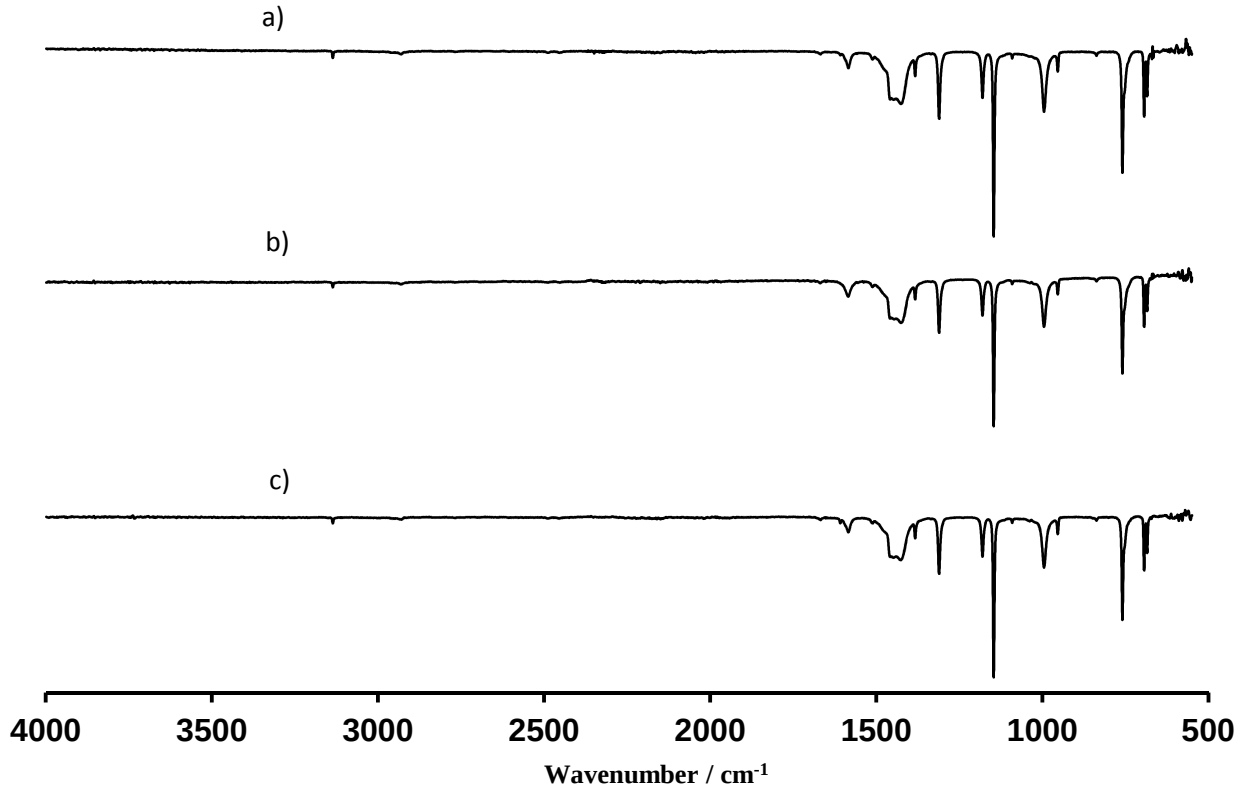

Spectrum A.5 FTIR spectra of palladium loaded in nZIF-8 a) $Pd(NO_3)_2$@nZIF-8; b) $Pd(OAc)_2$ @nZIF-8 and c) Pd@nZIF-8 (acac).

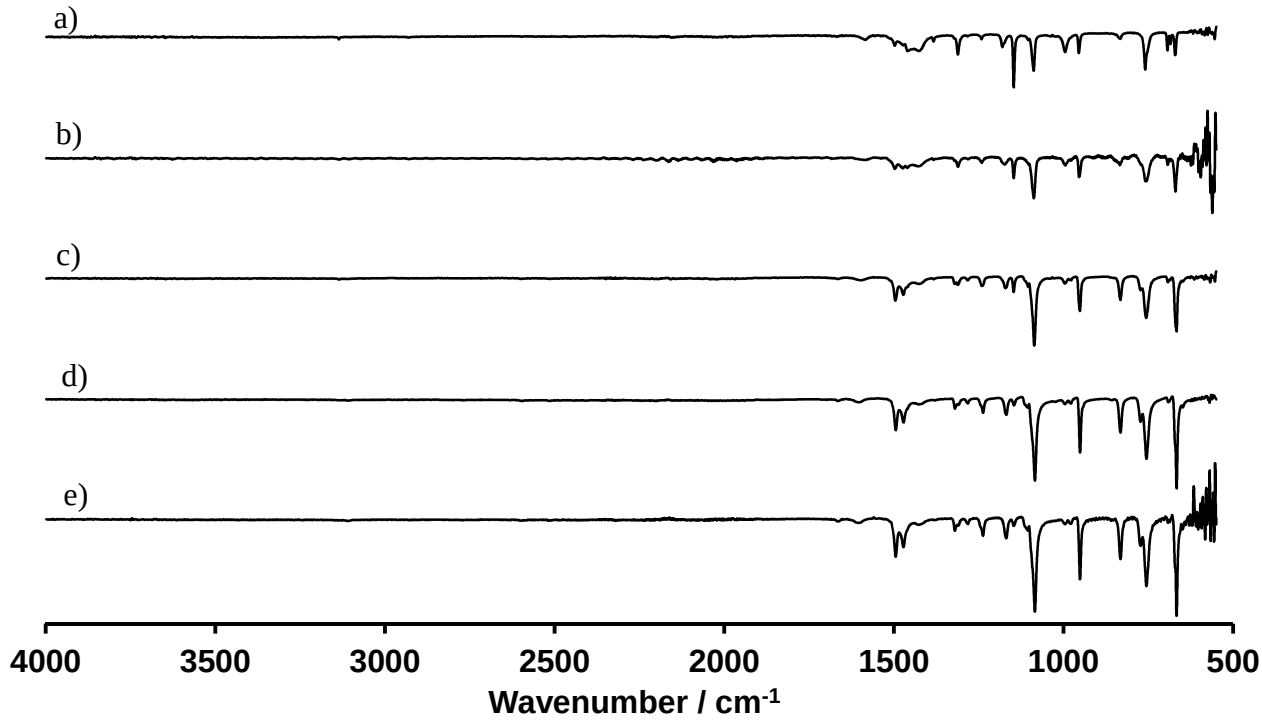

Spectrum A.6 FTIR spectra of ligand exchanged products of nZIF-8 synthesized at different time intervals of exposure to an imidazole solution a) 144 hours; b) 72 hours; c) 24 hours; d) 12 hours and e) 4 hours.

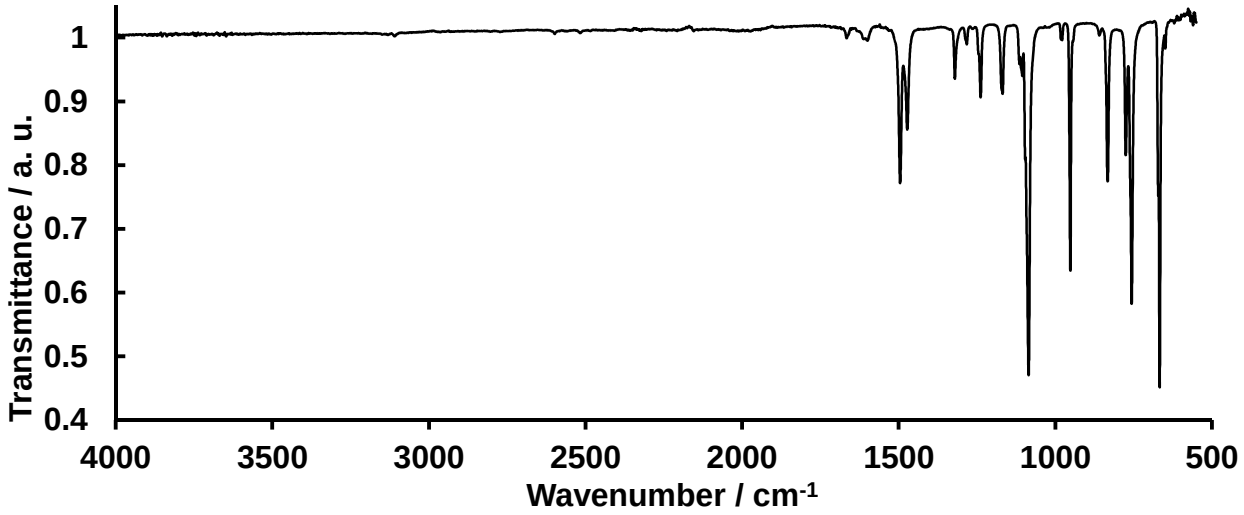

Spectrum A.7 FTIR spectrum of $Zn(Im)_2$ synthesized with Methanol at room temperature.

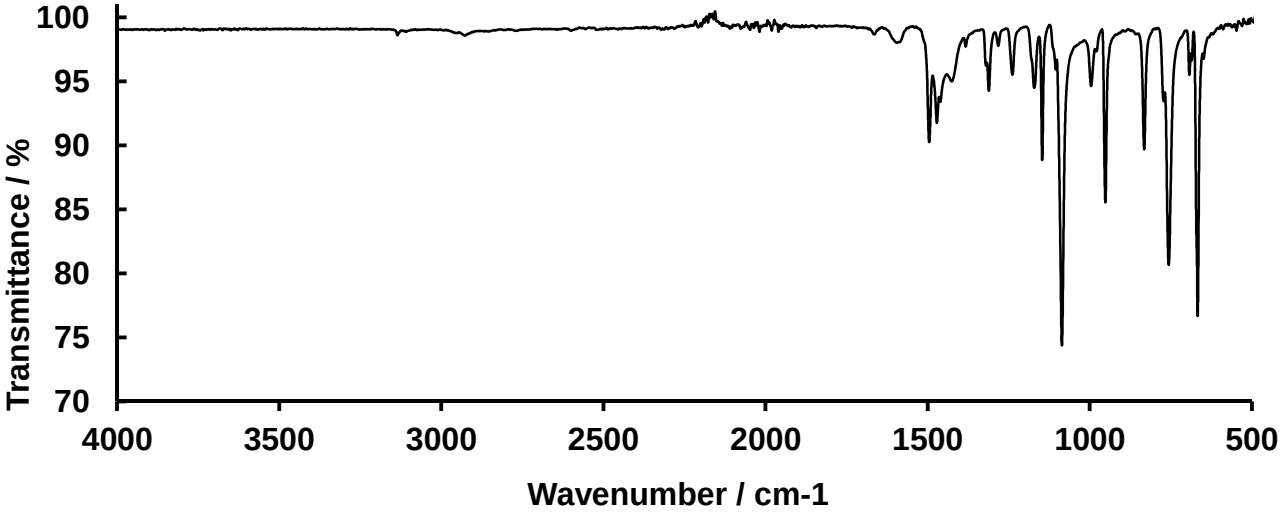

Spectrum A.8 FTIR spectrum of SALEM-2_{12h}-C_4H_9 for 12 hours and after reaction with 1-bromobutane.

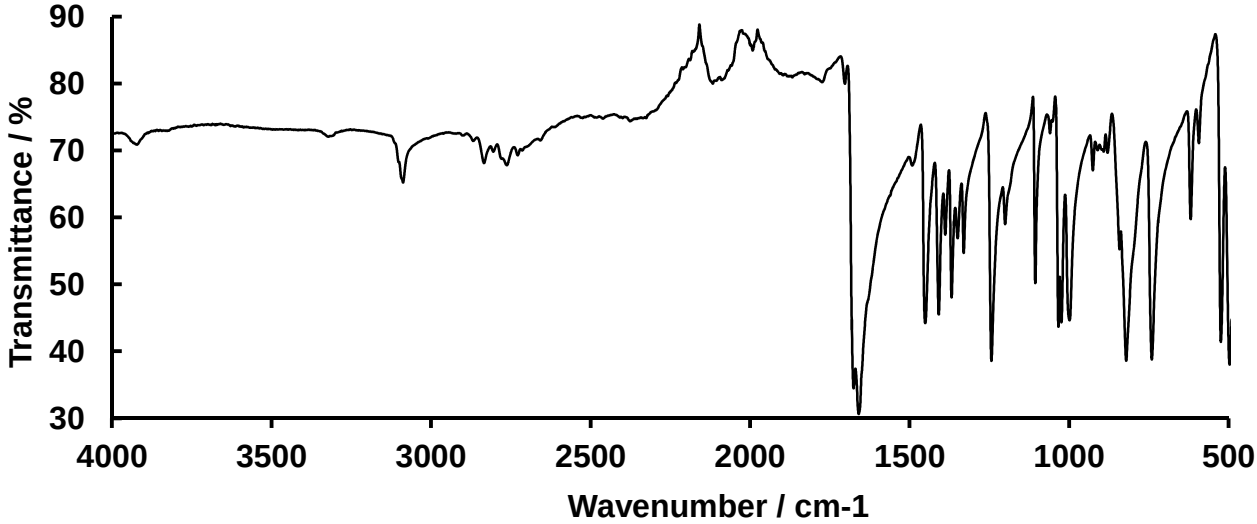

Spectrum A.9 FTIR spectrum of Ferrocenecarboxaldehyde.

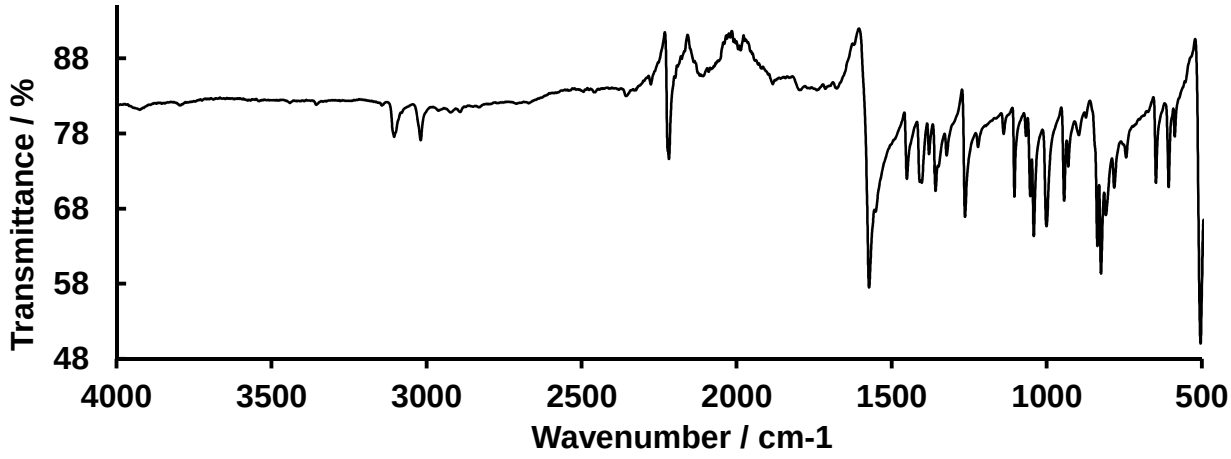

Spectrum A.10 FTIR spectrum of 1,1-dicyanovinylferrocene.

B. TEM Images

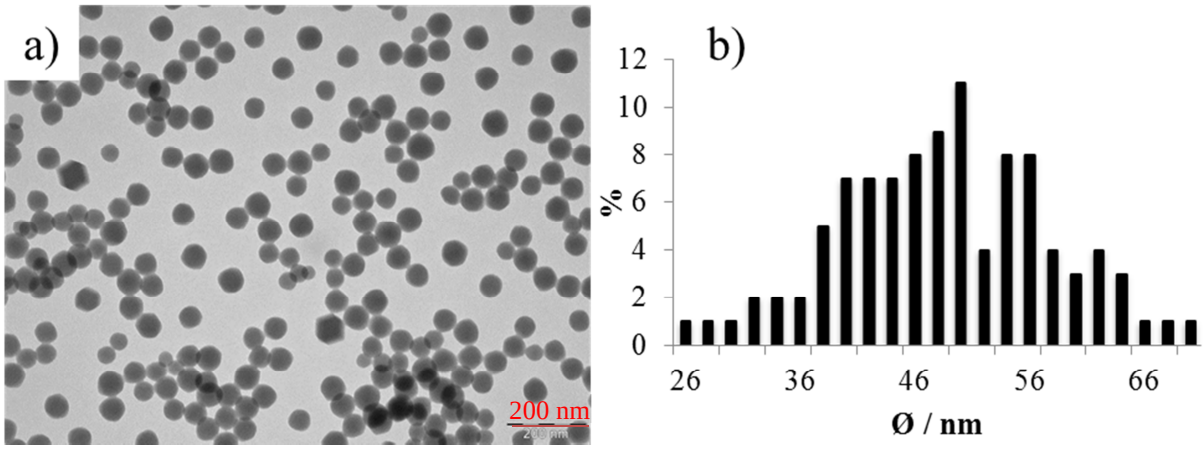

Figure B.1 a) TEM image and b) particle size distribution of nZIF-8 synthesized at -15 °C

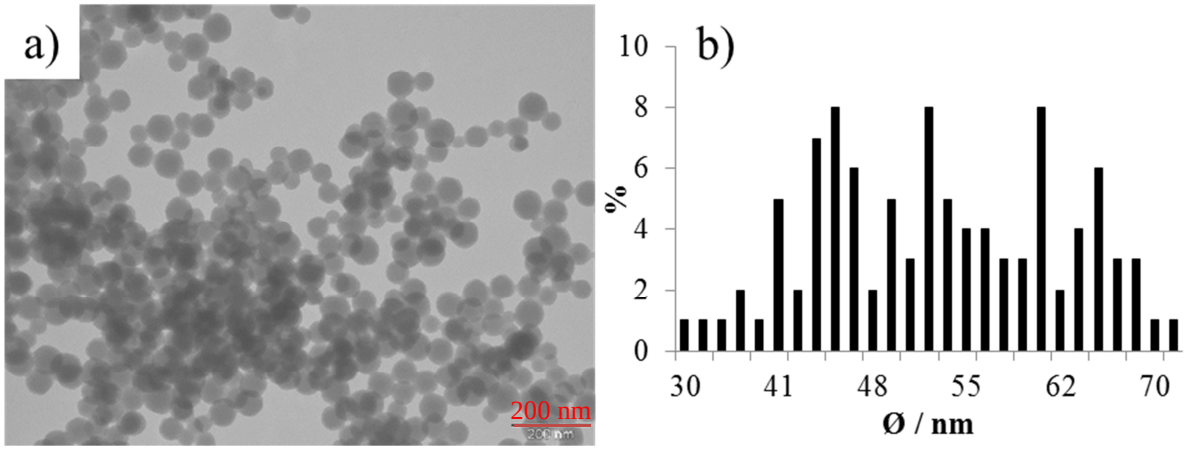

Figure B.2 a) TEM image and b) particle size distribution of nZIF-8 synthesized at -5 °C.

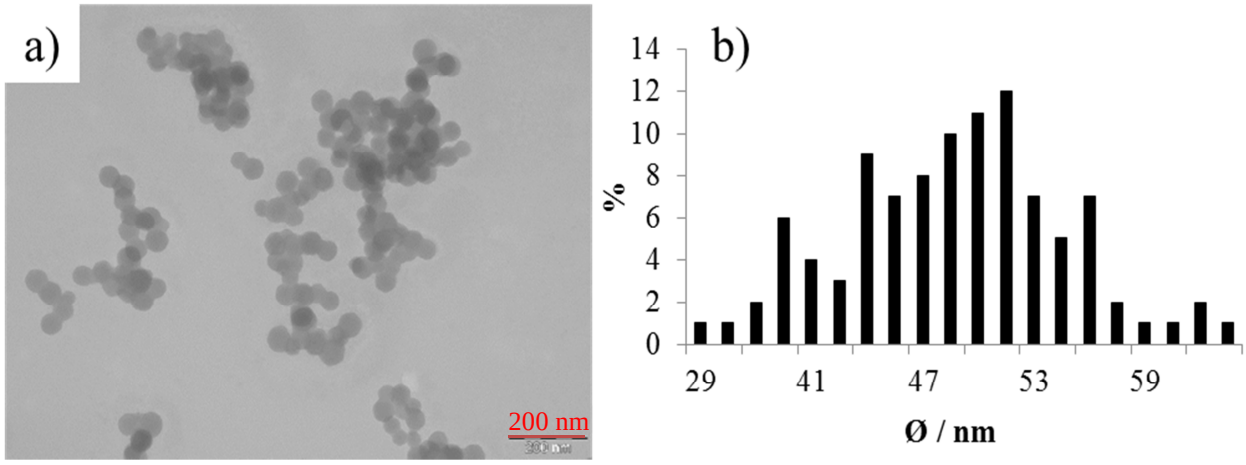

Figure B.3 a) TEM image and b) particle size distribution of nZIF-8 synthesized at 2 °C.

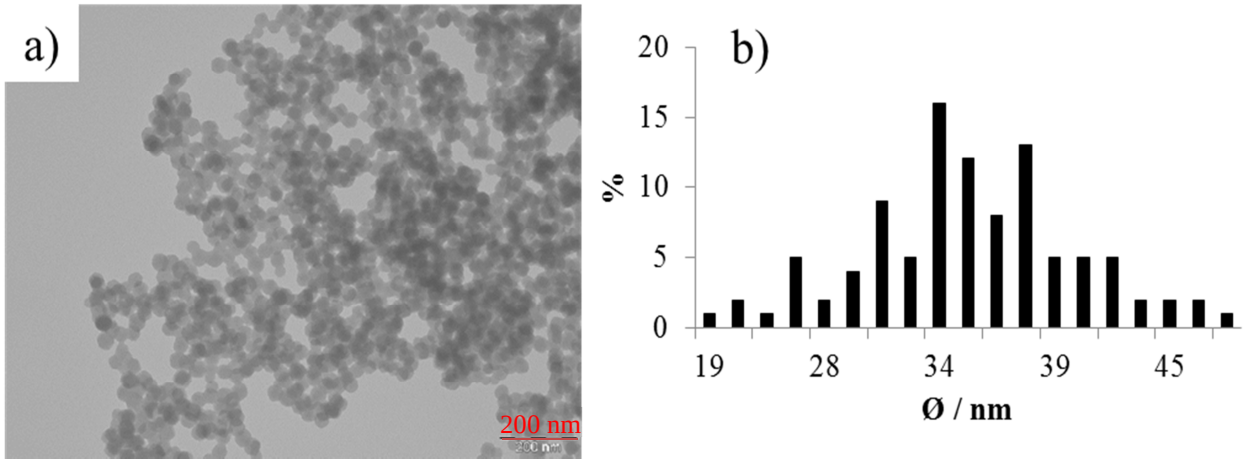

Figure B.4 a) TEM image and b) particle size distribution of nZIF-8 synthesized at 25 °C.

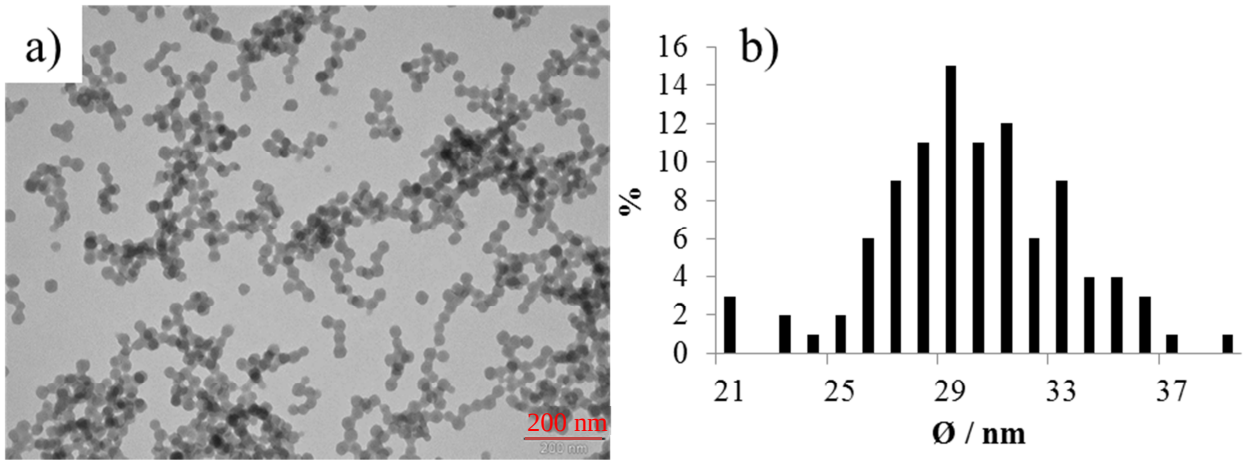

Figure B.5 a) TEM image and b) particle size distribution of nZIF-8 synthesized at 30 °C.

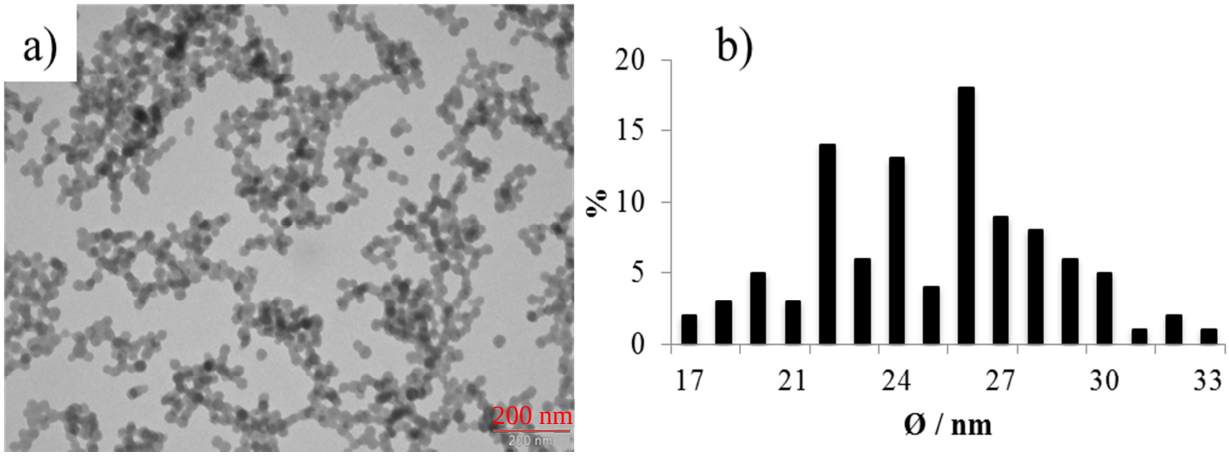

Figure B.6 a) TEM image and b) particle size distribution of nZIF-8 synthesized at 40 °C.

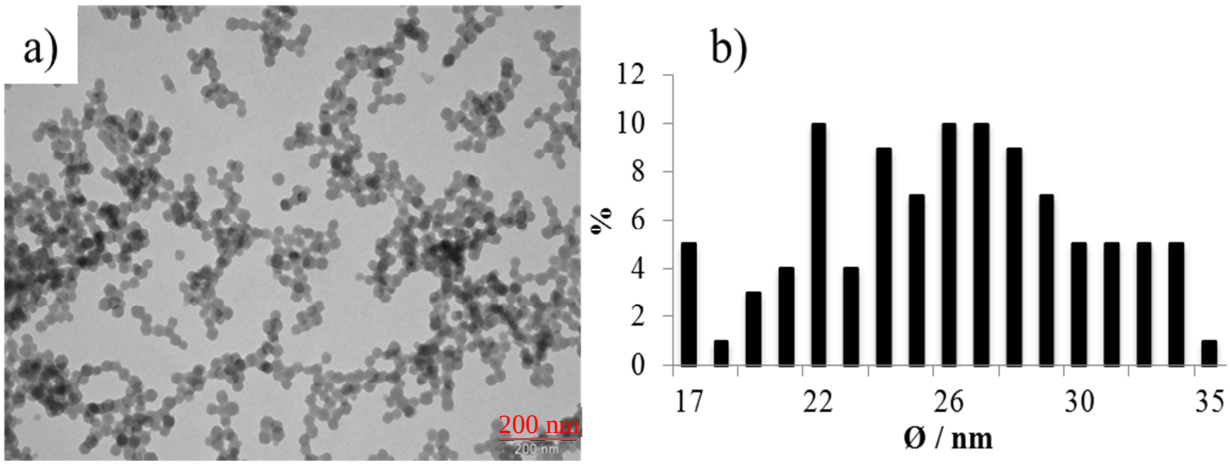

Figure B.7 a) TEM image and b) particle size distribution of nZIF-8 synthesized at 50 °C.

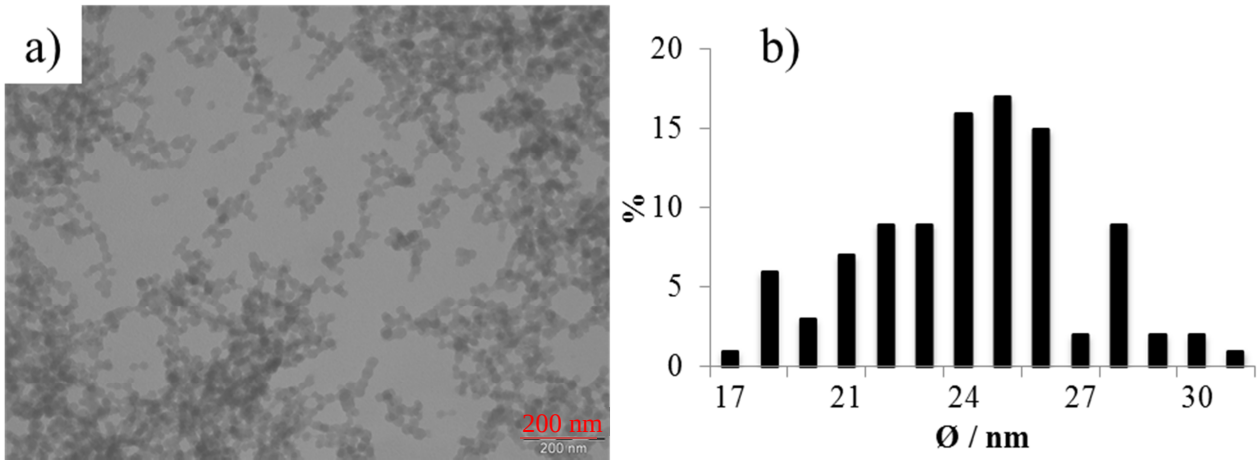

Figure B.8 a) TEM image and b) particle size distribution of nZIF-8 synthesized at 60 °C.

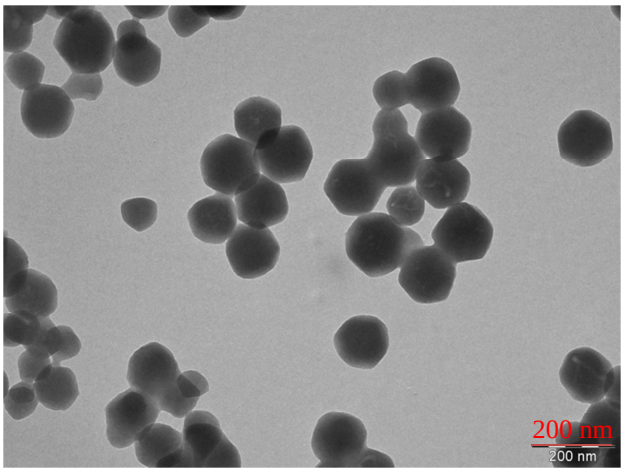

Figure B.9 TEM images of SALEM-2_{4h} after 4 hours exchange.

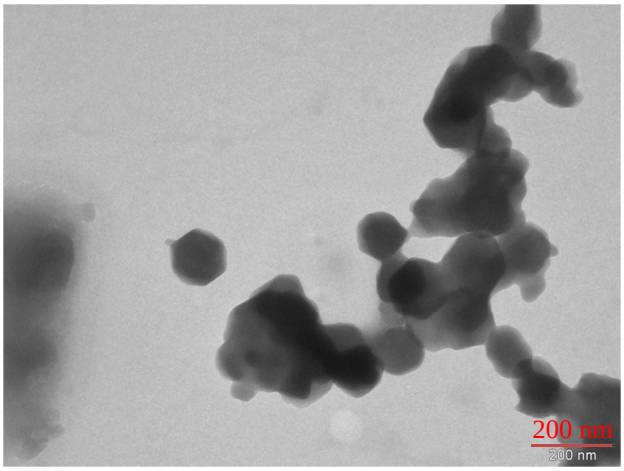

Figure B.10 TEM images of SALEM-2_{12h} after 12 hours exchange.

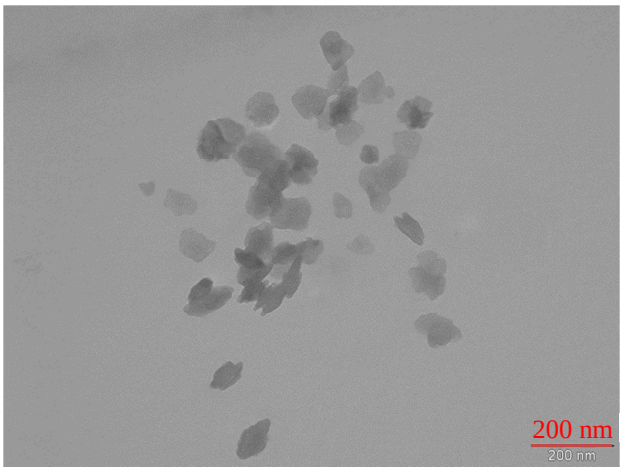

Figure B.11 TEM images of SALEM-2_{24h} after 24 hours exchange.

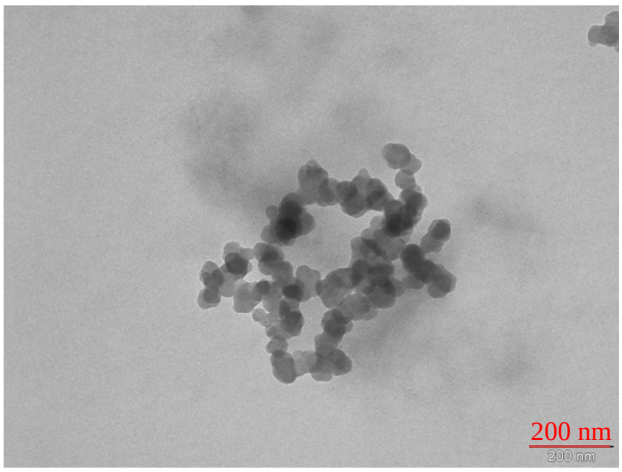

Figure B.12 TEM images of SALEM-2_{72h} after 72 hours exchange.

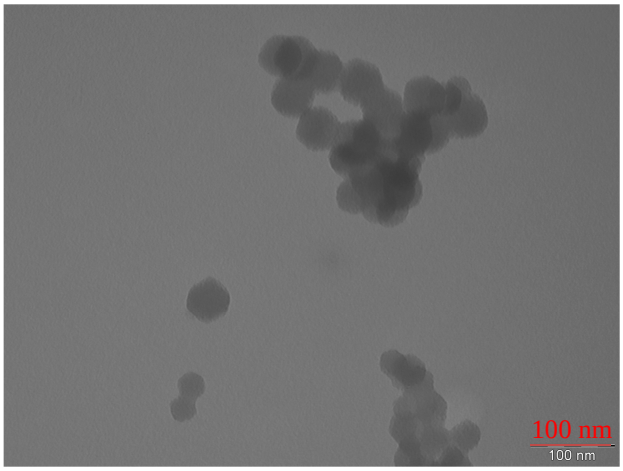

Figure B.13 TEM images of SALEM-2_{144h} after 144 hours exchange.

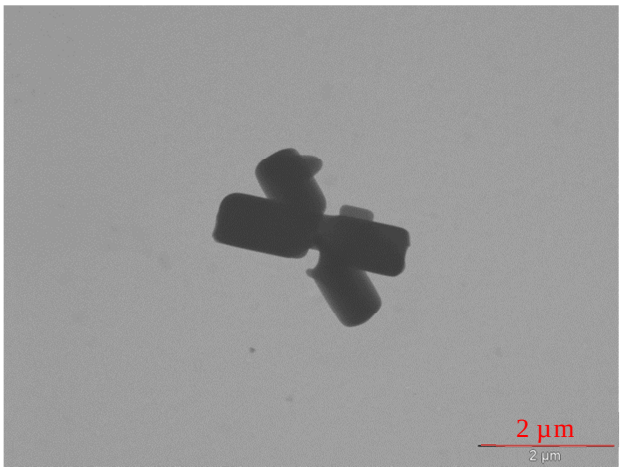

Figure B.14 TEM images of ZIF-ZNI synthesis in methanol at room temperature.

C. Crystallographic Data

The ZIF-8 structure was solved to be in the cubic *I*-43m space group with Z = 4 using direct methods with the following crystal data with a unit cell dimension of 16.32 Å .

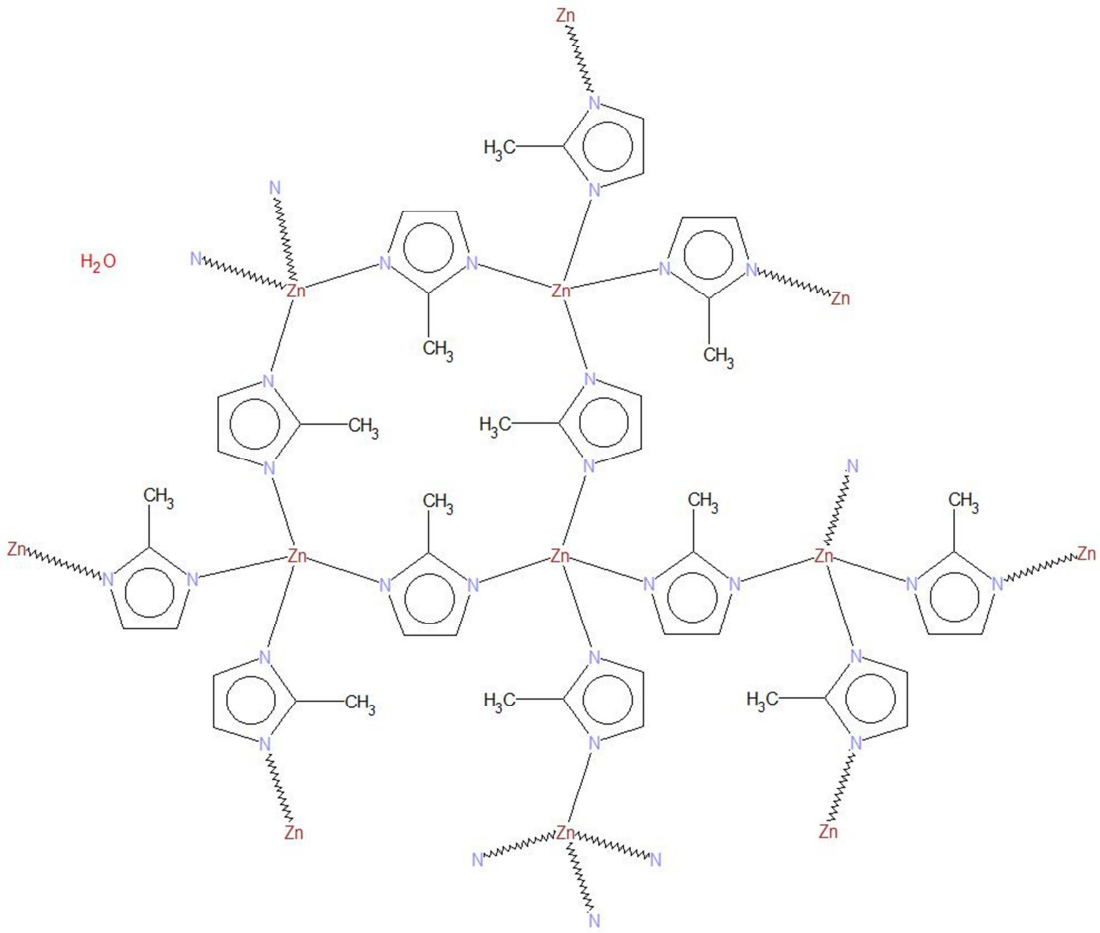

Figure C.1 Crystal structure of ZIF-8 (FAWCEN).

Table C.1 Crystal Data of ZIF-8.

Unit Cell dimension	a = 16.9910(12) Å	α= 90°.
	b = 16.9910(12) Å	β= 90°.
	c = 16.9910(12) Å	γ = 90°.
Volume	4905.2(6) Å	
Density (calculated)	1.141 mg m^{-3}	

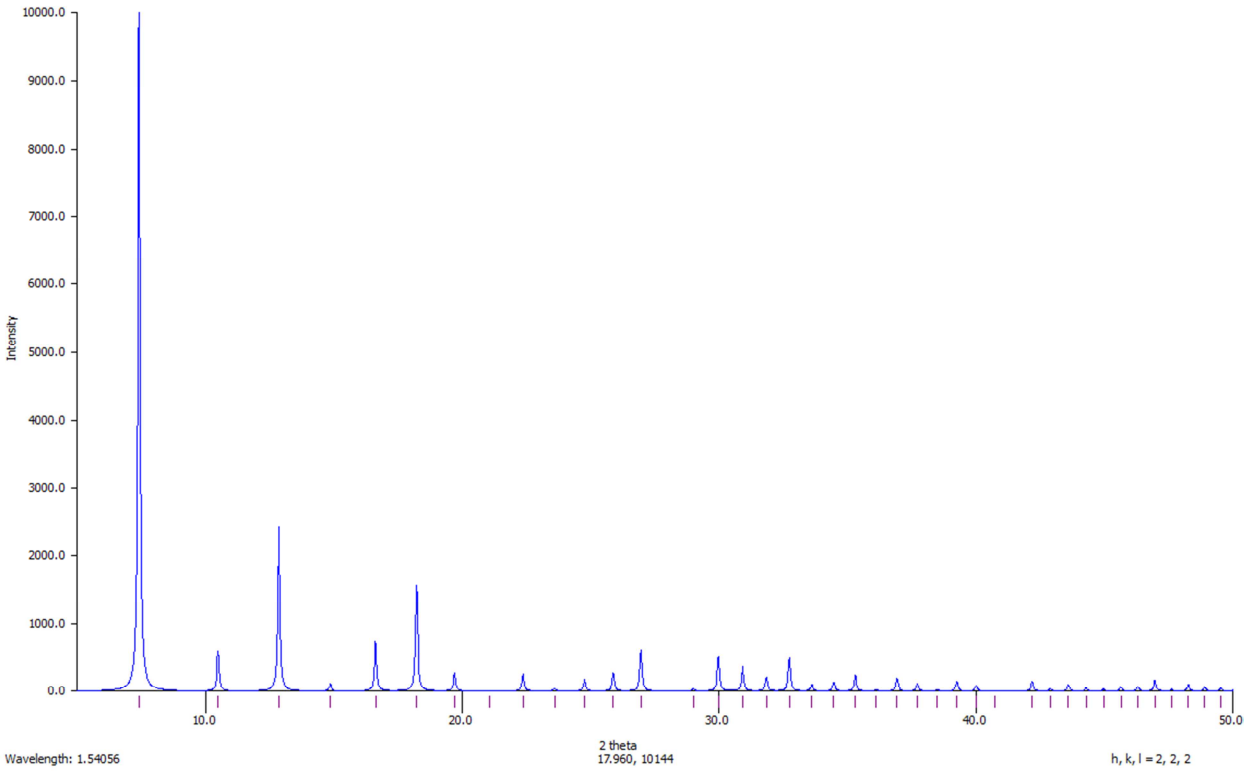

Figure C.2 Simulated PXRD pattern of ZIF-8 from single crystal X-ray crystallography (FAWCEN).

Table C.2 PXRD Positions of as-synthesized ZIF-8 and simulated peak positions with indices of diffraction.

As-synthesized PXRD		Simulated PXRD		Indices
2-Theta	**d**	**2-Theta**	**d**	**hkl**
7.31	12.085	7.35	12.015	011
10.24	8.629	10.40	8.496	002
12.65	6.994	12.75	6.937	112
14.67	6.035	14.73	6.007	022
16.03	5.433	16.48	5.373	013
17.84	4.905	18.07	4.905	222
22.02	4.033	22.18	4.005	114
24.38	3.648	24.55	3.623	233
26.64	3.343	26.73	3.332	134
29.72	3.004	29.72	3.004	044
30.44	2.934	30.65	2.914	334
31.69	2.821	31.57	2.832	244
32.41	2.760	32.46	2.756	235

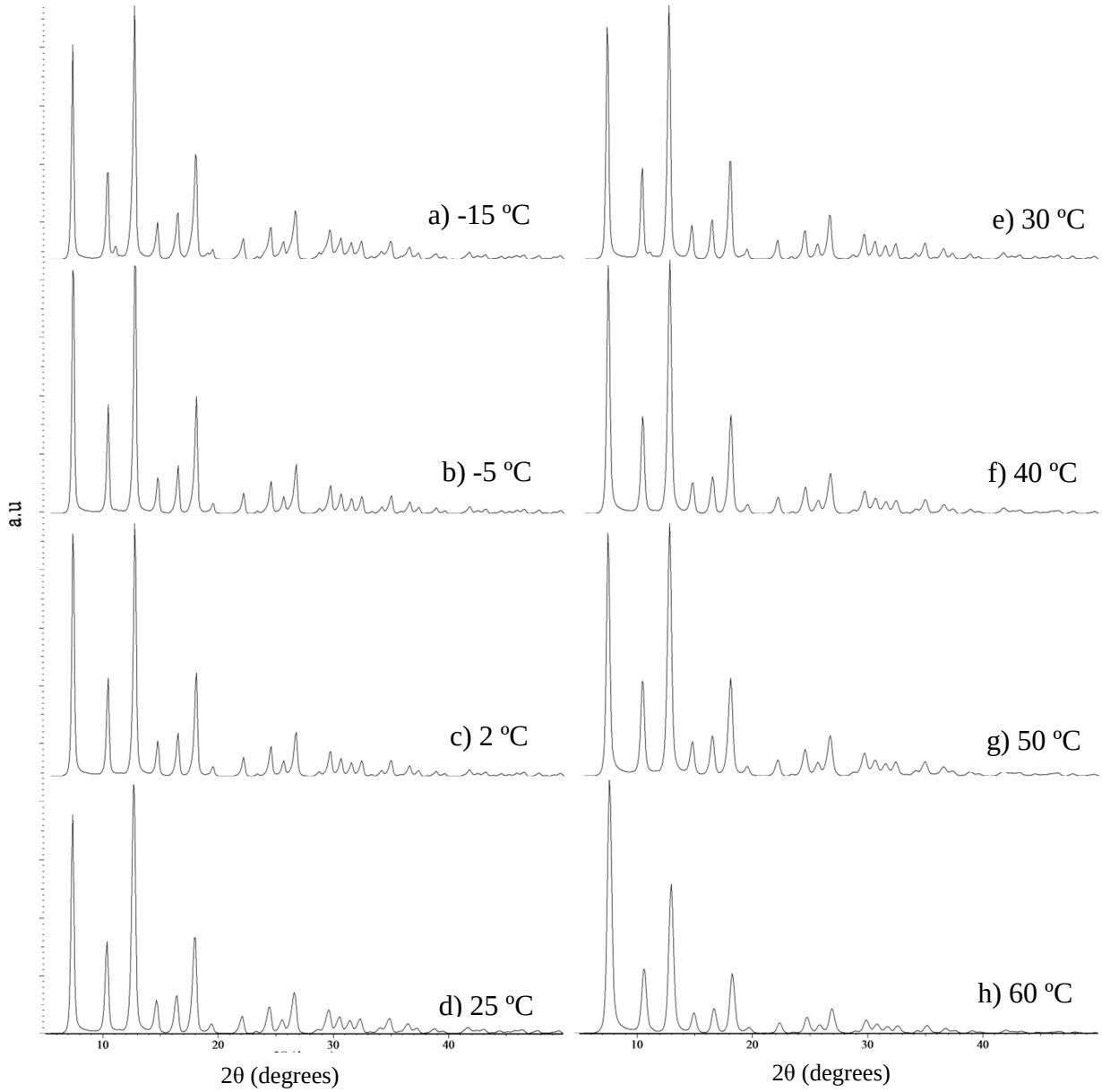

Figure C.1 Powder X-ray Diffraction patterns of as-synthesized nZIF-8 synthesized at a) -15 ºC b) -5 ºC c) 2 ºC d) 25 ºC e) 30 ºC f) 40 ºC g) 50 ºC and h) 60 ºC.

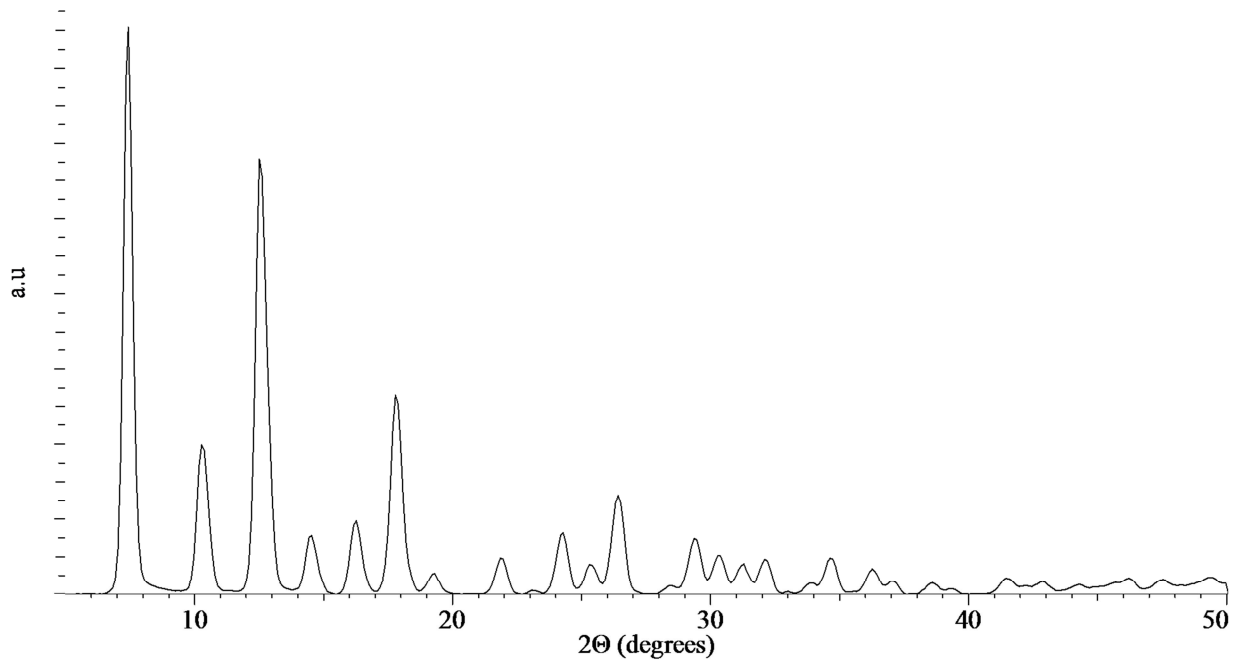

Figure C.2 PXRD pattern of nZIF-8 (bulk) synthesized in methanol at room temperature.

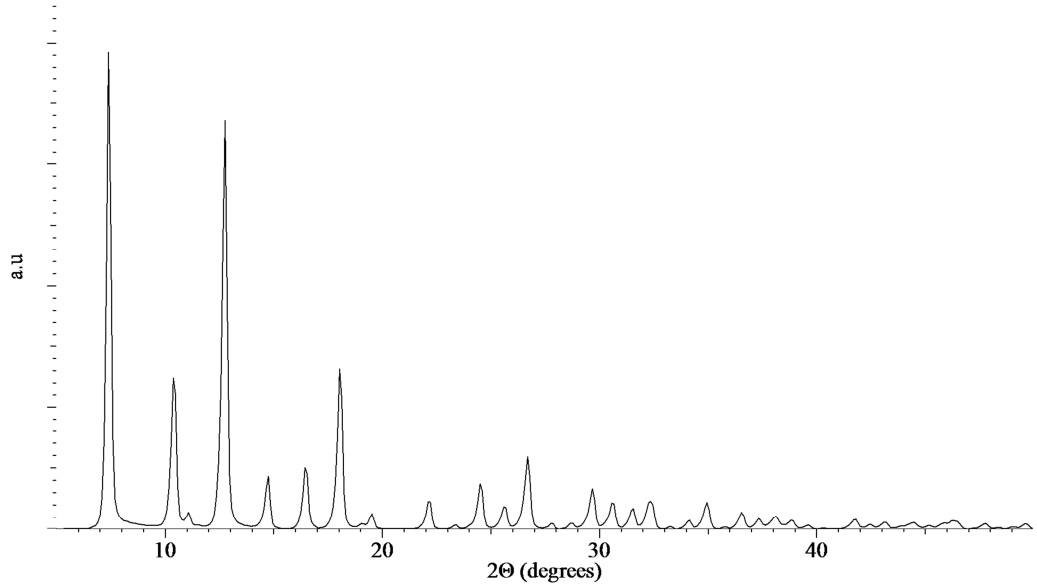

Figure C.3 PXRD patterns of silver loaded in nZIF-8 (Ag@nZIF-8).

D. ^{1}H NMR Spectrum

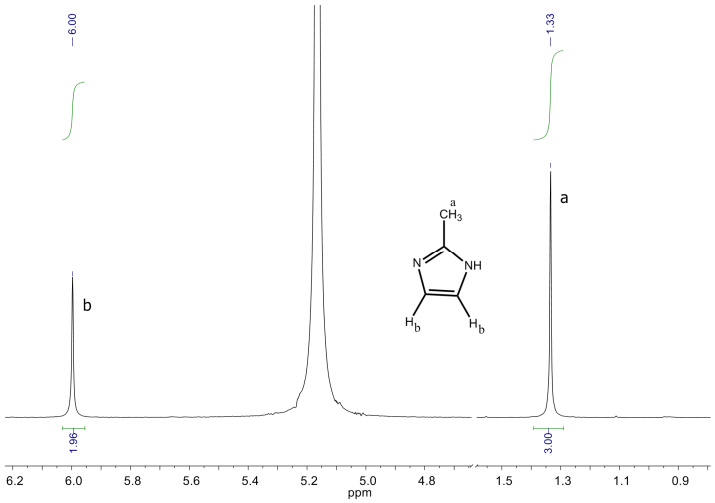

Spectrum D.1 ^{1}H NMR spectrum of nZIF-8, digested in D_2SO_4/D_2O.

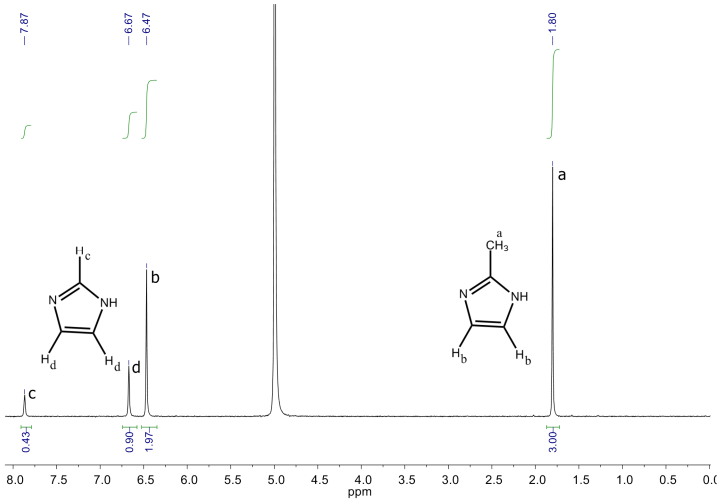

Spectrum D.2 ^{1}H NMR spectrum of SALEM-2_{4h}, digested in D_2SO_4/D_2O.

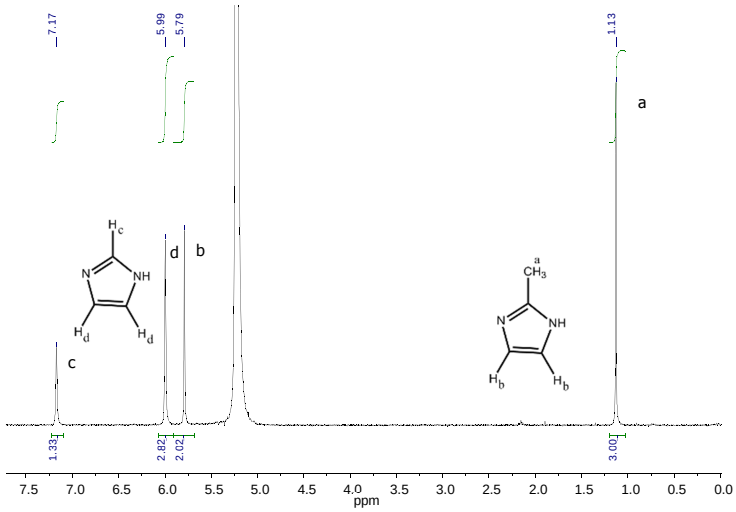

Spectrum D.3 ^{1}H NMR spectrum of SALEM-2_{12h}, digested in D_2SO_4/D_2O.

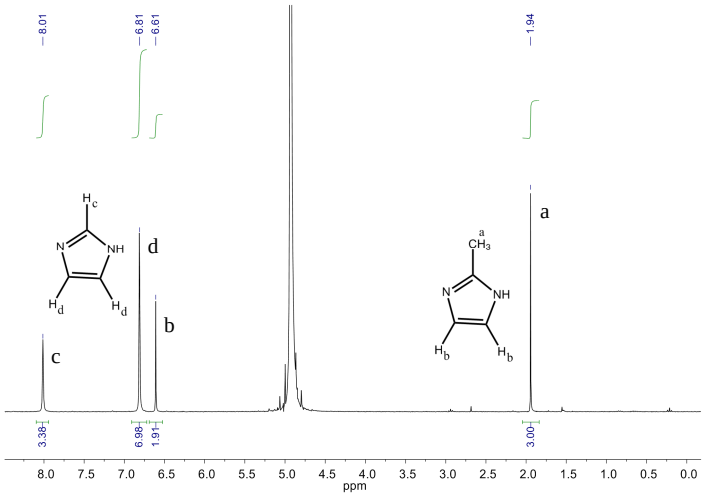

Spectrum D.4 ^{1}H NMR spectrum of SALEM-$_{24h}$, digested in D_2SO_4/D_2O.

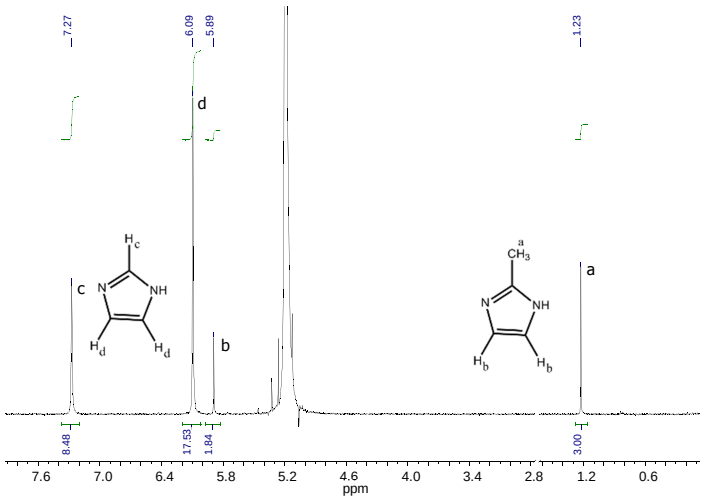

Spectrum D.5 ^{1}H NMR spectrum of SALEM-$_{24h}$, digested in D_2SO_4/D_2O.

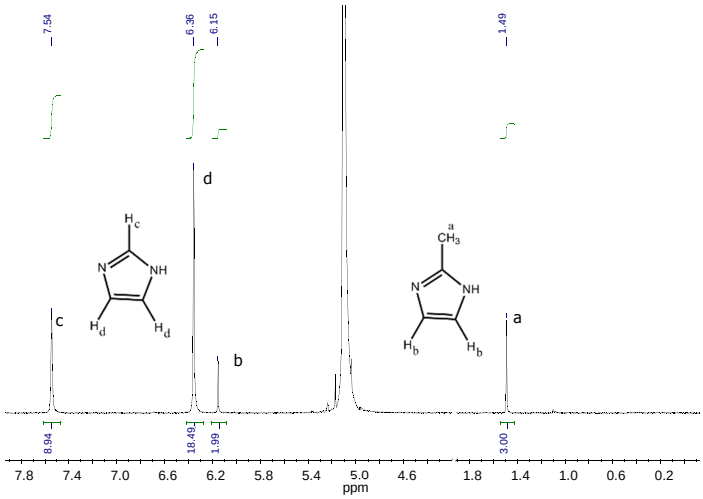

Spectrum D.6 ^{1}H NMR spectrum of SALEM-$_{144h}$, digested in D_2SO_4/D_2O.

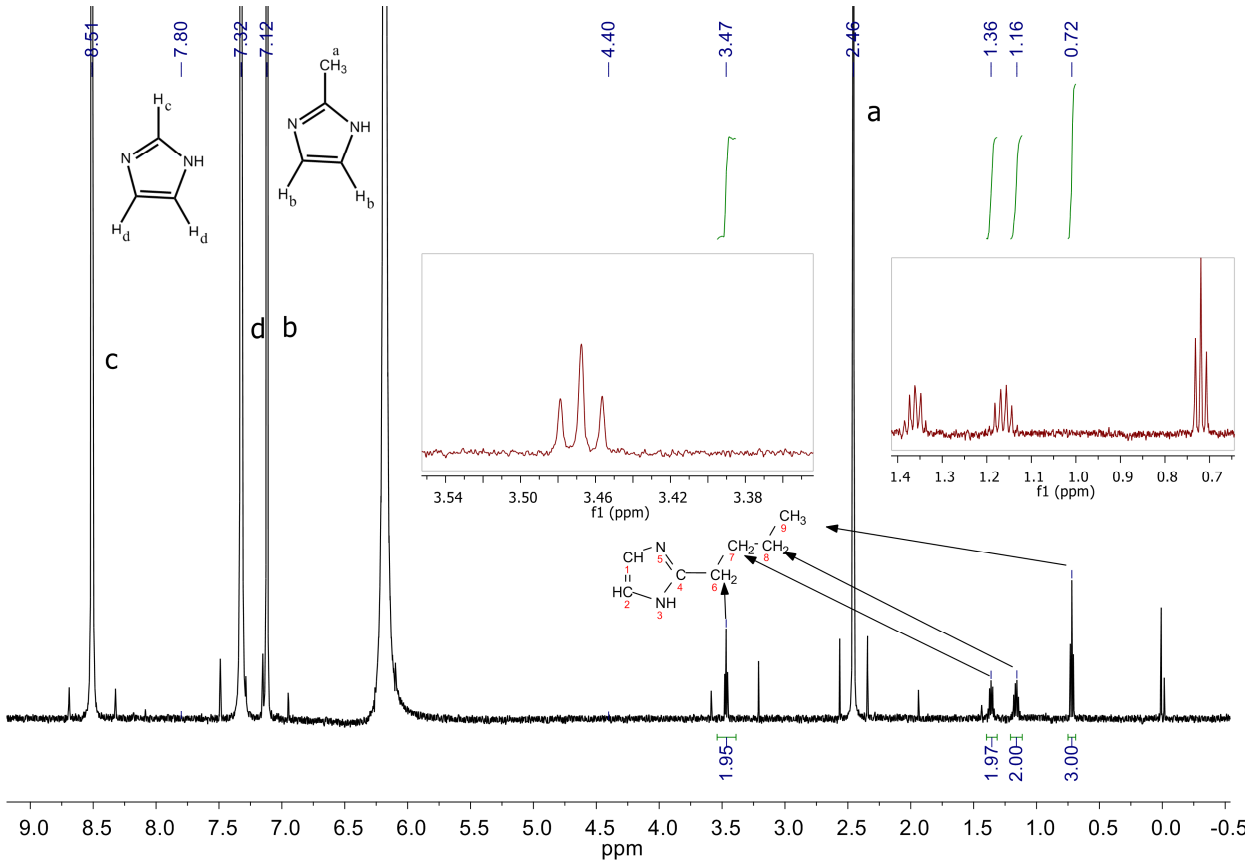

Spectrum D.7 ^{1}H NMR spectrum of SALEM-2_{12h}-C_4H_9 for 12 hours and after reaction with 1-bromobutane, digested in D_2SO_4/D_2O

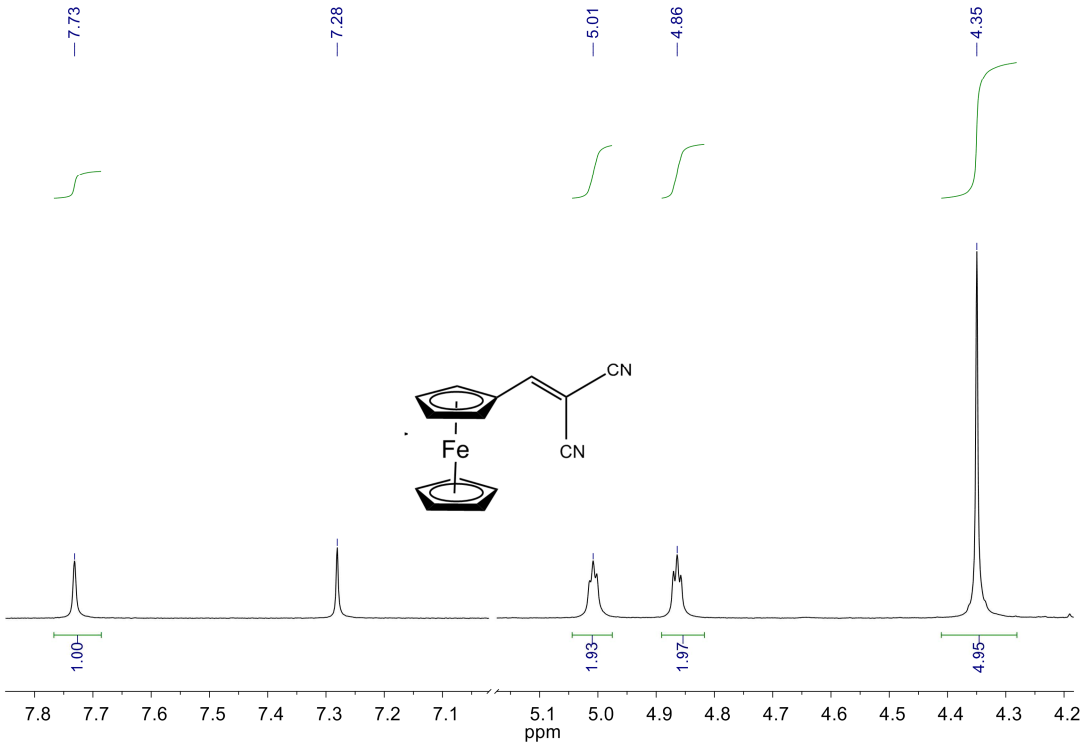

Spectrum D.8 ^{1}H NMR spectrum of 1,1-dicyanovinylferrocene in $CDCl_3$

E. Thermal Gravimetric Analysis

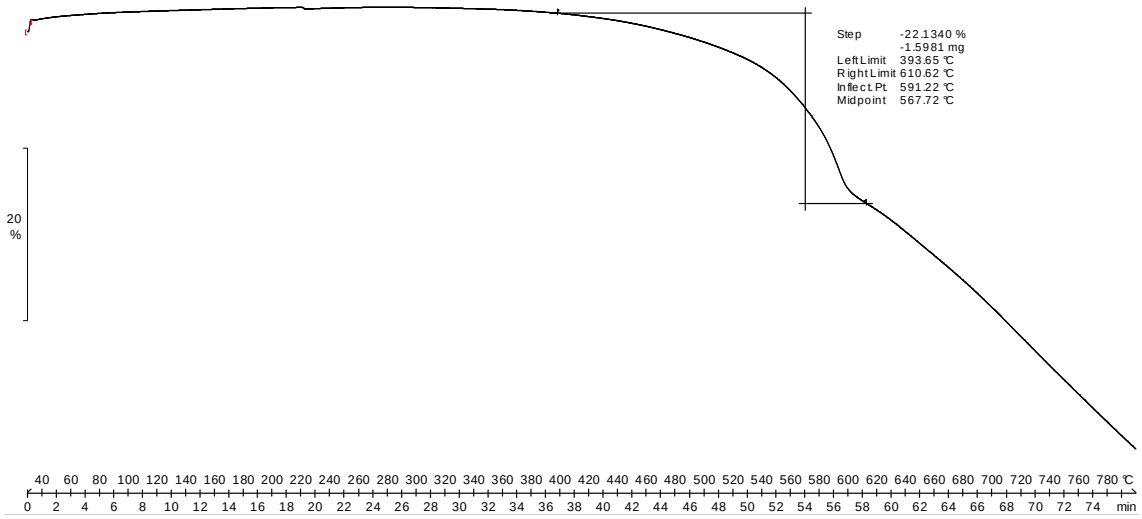

Figure E.1 TGA thermogram of nZIF-8 synthesized at -15 ºC in Ar.

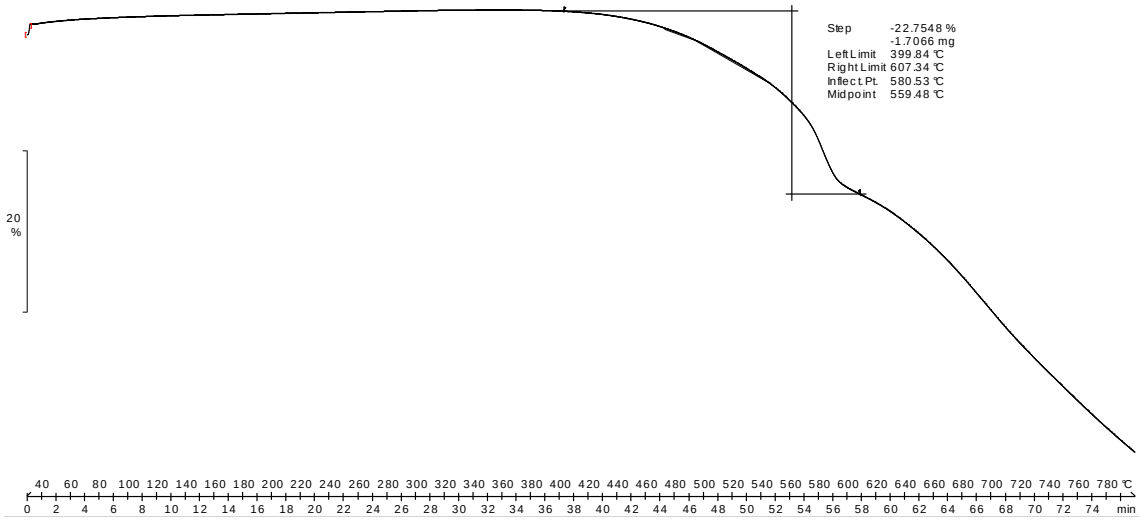

Figure E.2 TGA thermogram of nZIF-8 synthesized at -5 ºC in Ar.

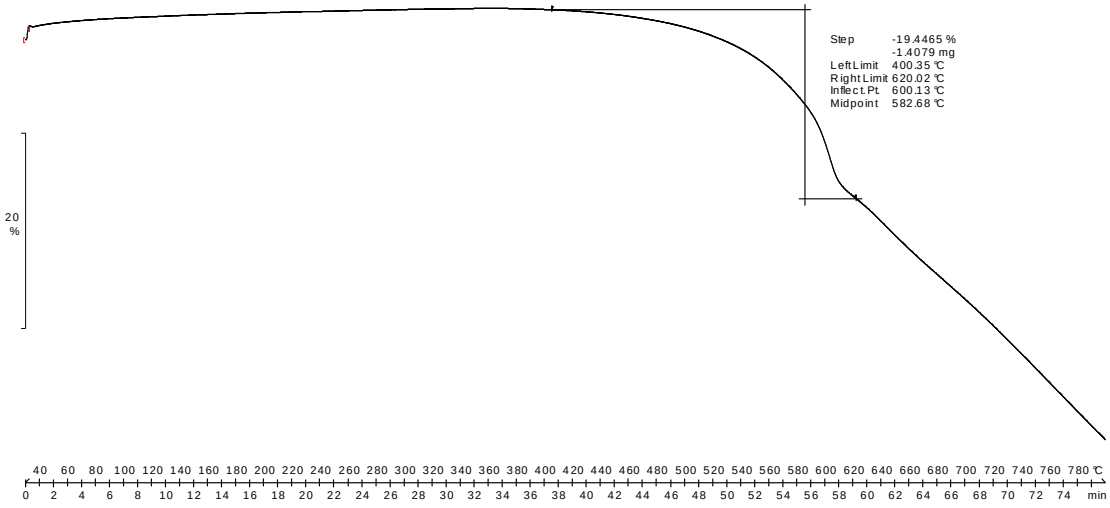

Figure E.3 TGA thermogram of nZIF-8 synthesized at 2 ºC in Ar.

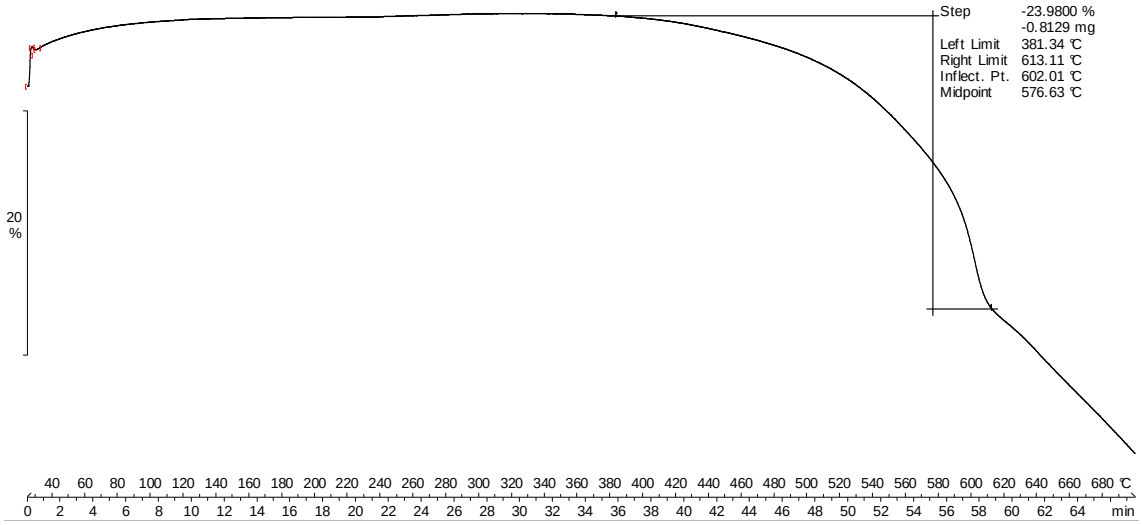

Figure E.4 TGA thermogram of nZIF-8 synthesized at 25 ºC in Ar.

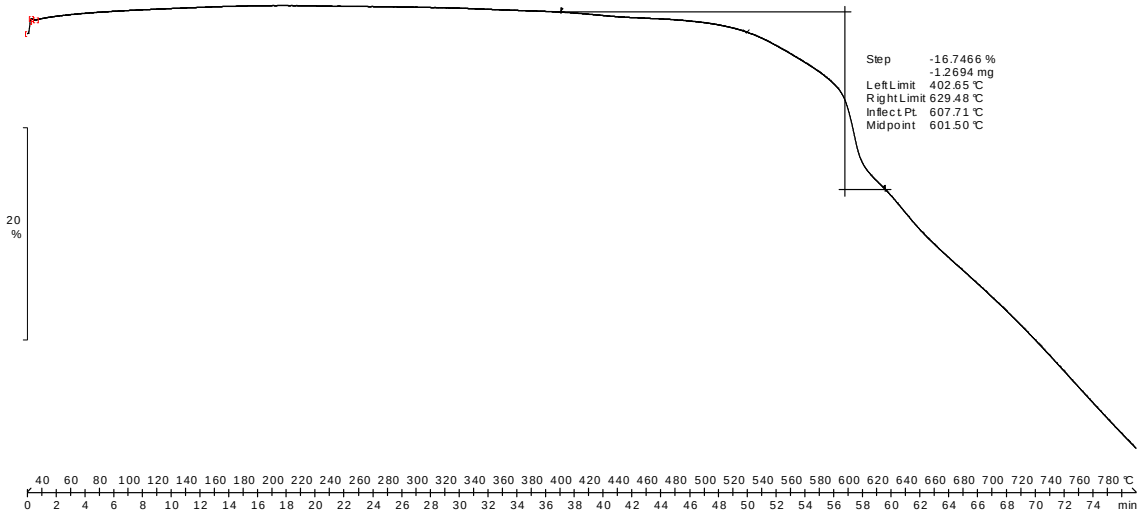

Figure E.5 TGA thermogram of nZIF-8 synthesized at 30 ºC in Ar.

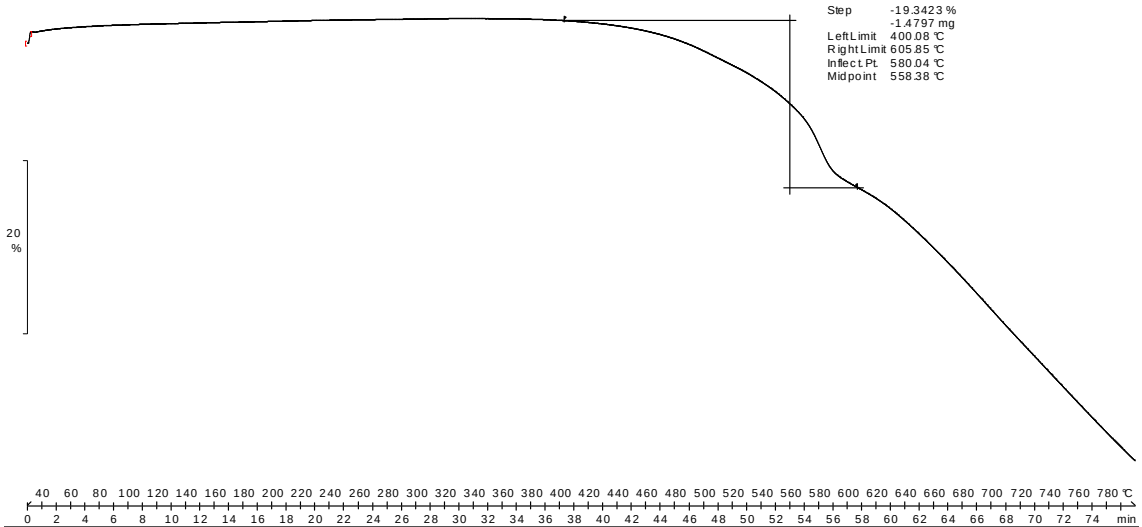

Figure E.6 TGA thermogram of nZIF-8 synthesized at 40 ºC in Ar.

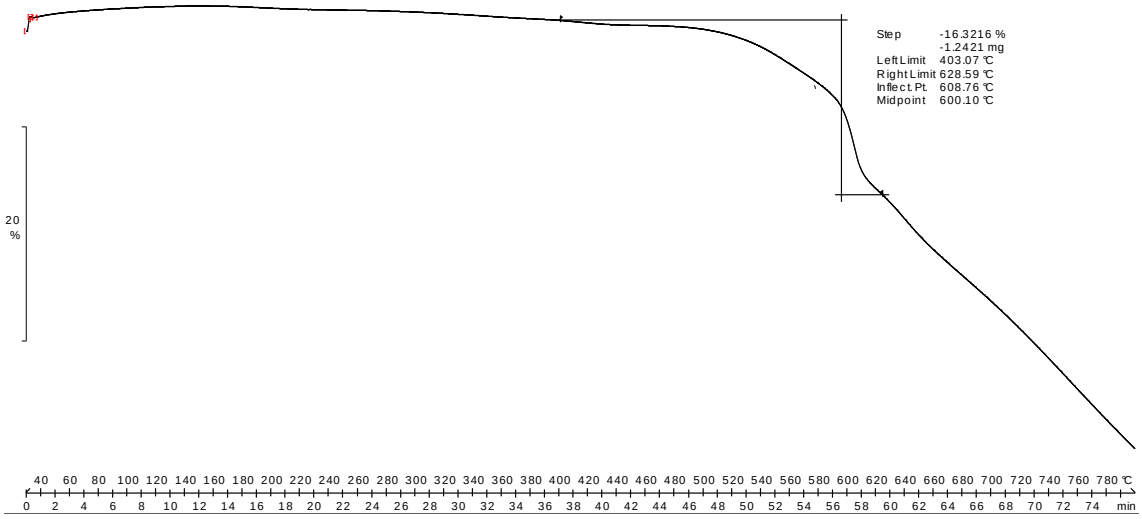

Figure E.7 TGA thermogram of nZIF-8 synthesized at 50 ºC in Ar.

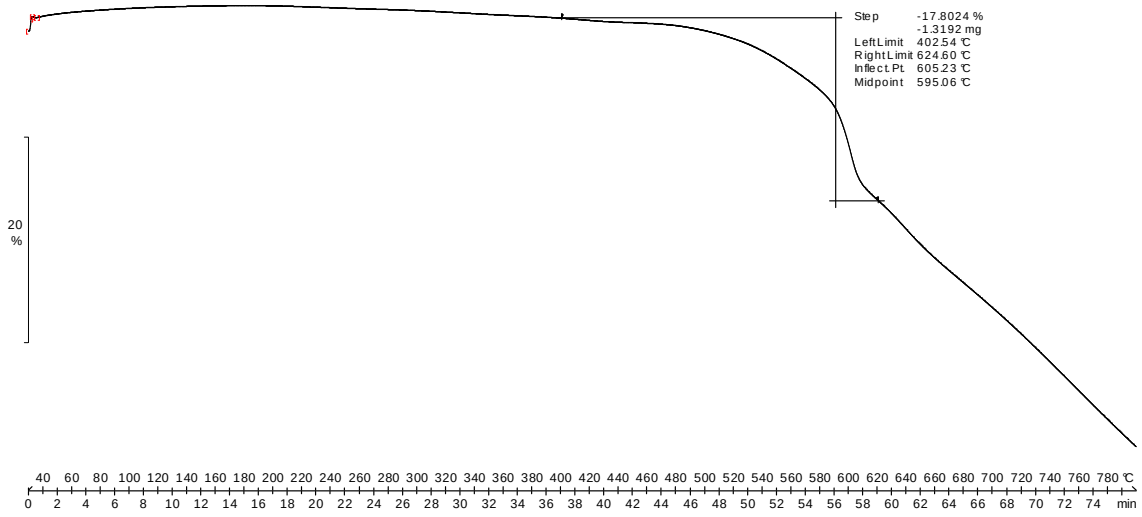

Figure E.8 TGA thermogram of nZIF-8 synthesized at 60 ºC in Ar.

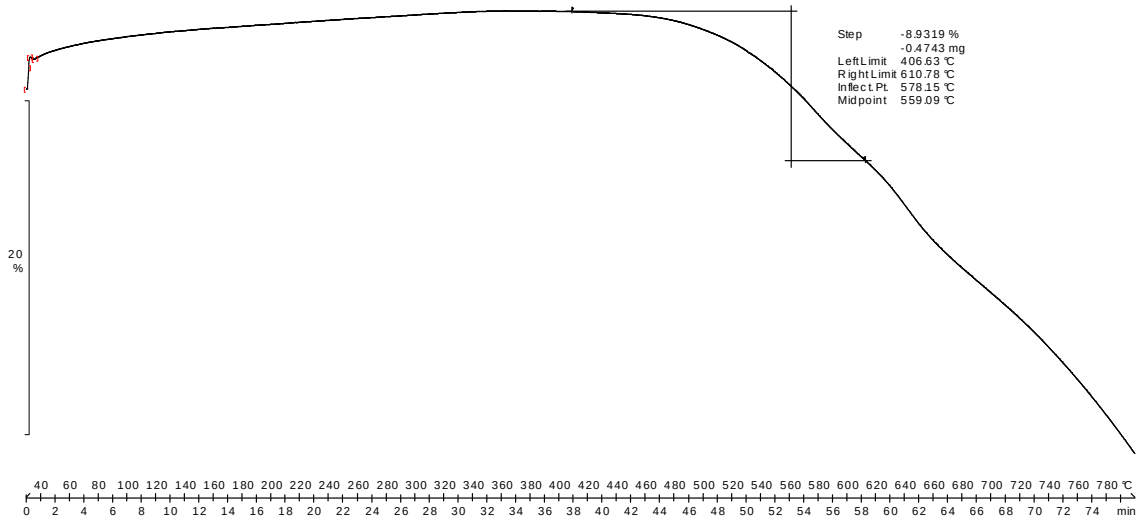

Figure E.9 TGA thermogram of SALEM-2 after 4 hours of SALE in Ar.

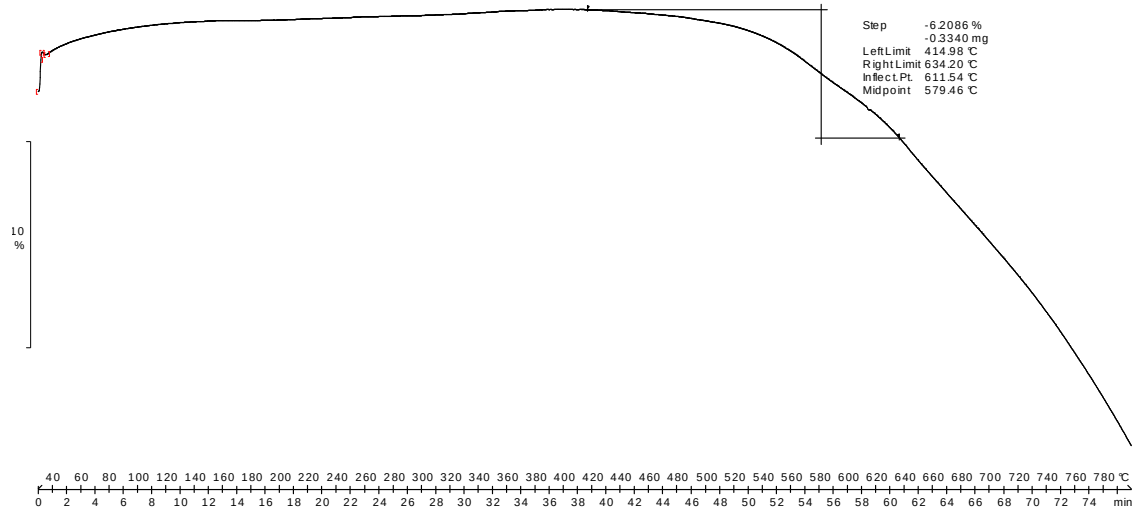

Figure E.10 TGA thermogram of SALEM-2 after 12 hours of SALE in Ar.

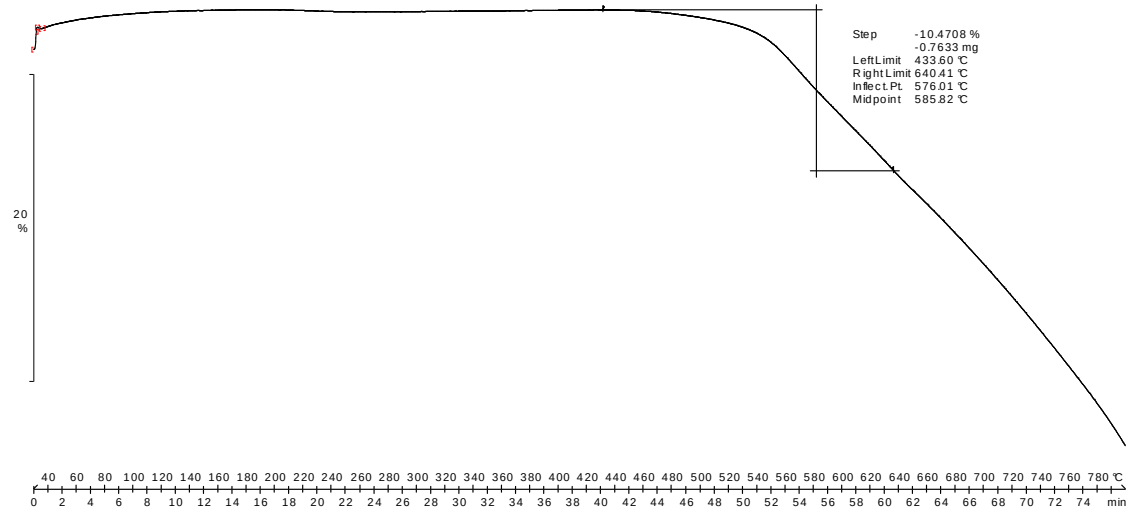

Figure E.11 TGA thermogram of SALEM-2 after 24 hours SALE in Ar.

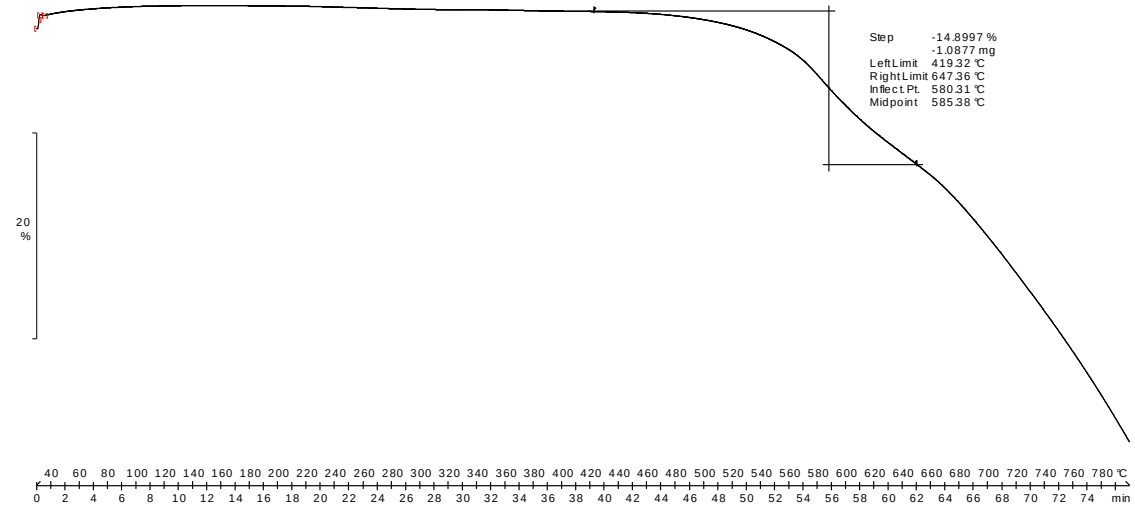

Figure E.12 TGA thermogram of SALEM-2 after 72 hours SALE in Ar.

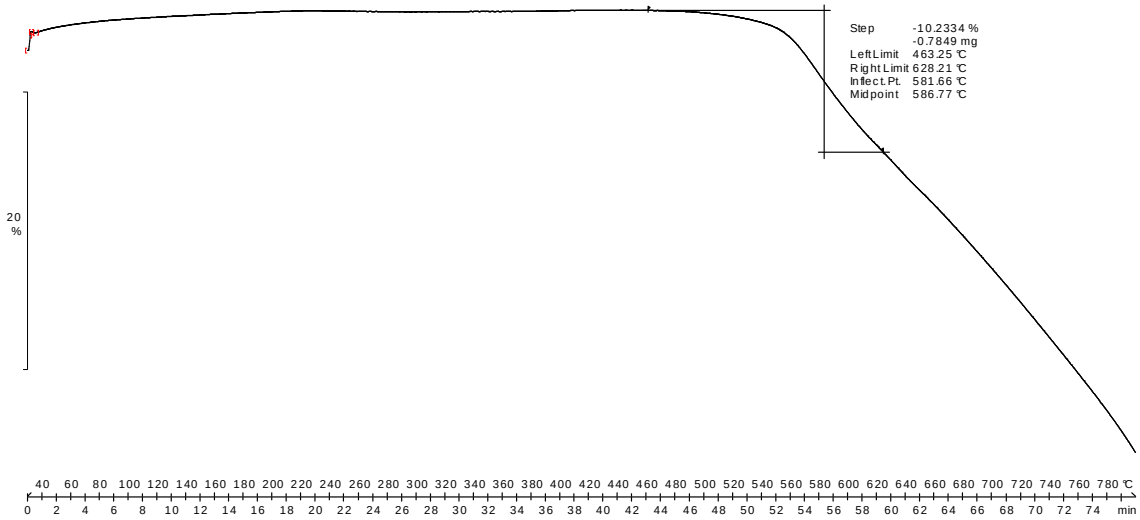

Figure E.13 TGA thermogram of SALEM-2 after 144 hours SALE in Ar.

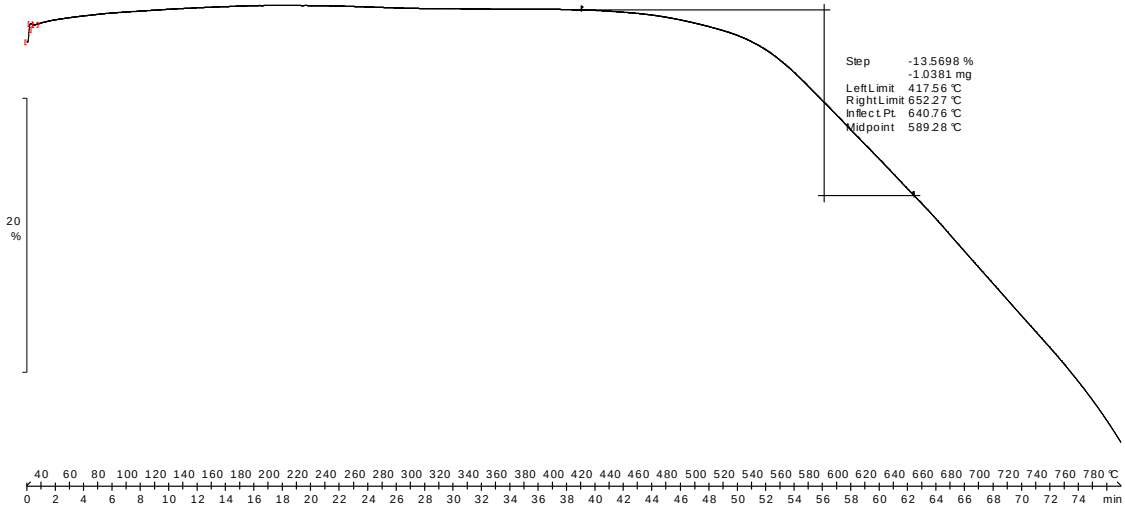

Figure E.14 TGA thermogram of C_4H_9-SALEM-2 for 12 hours after lithiation with 1-bromobutane in Ar.

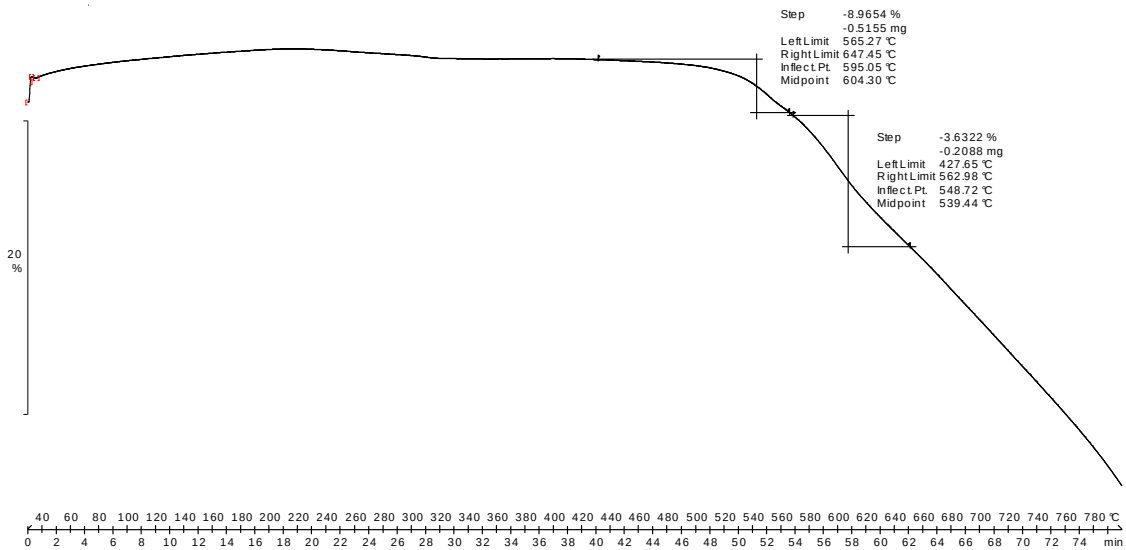

Figure E.15 TGA thermogram of ZIF-ZNI synthesis in methanol at room temperature in Ar.

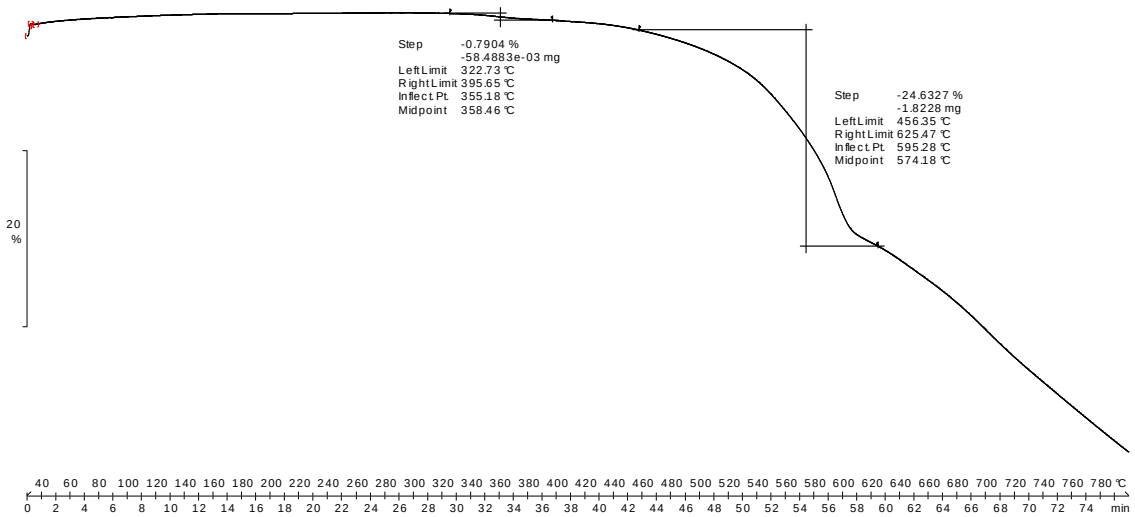

Figure E.16 TGA thermogram of Ag@nZIF-8 taken in an Argon atmosphere in Ar.

F. Synthesis Results

Table F.1 Results of nZIF-8 synthesized at various temperatures from $Zn(NO_3)_2.4H_2O$ (2.48 mmol) and 2-methylimidazole (20 mmol) in methanol (100 cm^3). Syntheses were performed in triplicate to obtain average values.

Synthesis Temperature/ ^oC	Batch 1 Yield/ g (%)	Batch 2 Yield/ g (%)	Batch 3 Yield/ g (%)	Average Yield/ g (%)
-15	0.023 g (4.1)	0.065 g (11.4)	0.066 g (11.6)	0.051 g (9)
-5	0.209 g (36.7)	0.164 g (28.9)	0.114 g (19.9)	0.162 g (28.5)
2	0.193 g (33.9)	0.136 g (23.9)	0.152 g (26.7)	0.160 g (28.2)
25	0.184 g (32.3)	0.215 g (37.8)	0.193 g (33.8)	0.197 g (34.6)
30	0.211 g (37.1)	0.198 g (34.8)	0.200 g (35.2)	0.203 g (35.7)
40	0.243 g (43.0)	0.224 g (39.3)	0.242 g (42.6)	0.236(41.5)
50	0.223 g (39.3)	0.232 g (40.7)	0.223 g (39.2)	0.226 g (39.7)
60	0.209 g (36.7)	0.327 g (57.4)	0.247 g (43.3)	0.261 g (45.8)

Table F.2 The PXRD particle diameter Ø (nm) of batch 1 calculated from the Scherrer equation where K= 0.94 and λ = 1.541.

Temperature/ °C	-15	-5	2	25	30	40	50	60
FWHM: Average	0.39	0.37	0.38	0.30	0.41	0.44	0.44	0.48
PXRD: Average	21.43	23.11	23.9	27.9	20.52	19.15	19.37	17.48
Std. Dev. (nm)	2.61	4.33	7.98	0.54	3.21	2,68	2.72	2.30

Table F.3 The PXRD particle diameter Ø (nm) of batch 2 calculated from the Scherrer equation where K= 0.94 and λ = 1.541.

Temperature/ °C	-15	-5	2	25	30	40	50	60
FWHM: Average	0.25	0.26	0.26	0.31	0.31	0.33	0.37	0.35
PXRD: Average	33.18	32.59	32.72	27.32	27.23	25.71	22.50	23.68
Std. Dev. (nm)	3.11	2.44	2.56	1.94	2.21	1.96	1.54	0.99

Table F.4 The PXRD particle diameter Ø (nm) of batch 3 calculated from the Scherrer equation where K= 0.94 and λ = 1.541.

Temperature/ °C	-15	-5	2	25	30	40	50	60
FWHM: Average	0.25	0.25	0.27	0.33	0.29	0.34	0.37	0.46
PXRD: Average	33.84	33.11	31.38	25.37	28.96	24.42	22.73	18.27
Std. Dev. (nm)	3.93	2.57	2.09	2.60	1.99	1.80	1.77	0.73

Table F.5 The TEM particle diameter Ø (nm) of batch 1 measured statistically.

Temperature/ °C	-15	-5	2	17	30	40	50	60
TEM: Average	48.93	52.96	48.84	35.09	29.91	24.85	25.97	24.07
TEM: Minimum	26.13	30.43	29.41	18.98	21.11	17.28	17.28	17.3
TEM: Maximum	84.43	72.46	66.18	55.47	39.2	33.47	34.55	32.39
Std. Dev. (nm)	9.59	9.53	6.22	5.8	3.46	3.58	4.37	2.89

Table F.6 The TEM particle diameter Ø (nm) of batch 2 measured statistically.

Temperature/ °C	-15	-5	2	25	30	40	50	60
TEM: Average	91.77	40.71	57.70	41.33	43.90	33.20	25.95	29.07
TEM: Minimum	39.95	19.44	31.31	24.84	23.76	12.96	18.36	15.12
TEM: Maximum	127.42	60.47	78.83	54.09	60.47	43.19	34.55	48.59
Std. Dev. (nm)	17.41	9.53	10.86	7.33	8.54	5.78	3.37	4.95

Table F.7 The TEM particle diameter Ø (nm) of batch 3 measured statistically.

Temperature/ °C	-15	-5	2	25	30	40	50	60
TEM: Average	92.59	82.84	60.72	48.98	47.26	32.97	26.75	26.96
TEM: Minimum	50.97	44.86	28.55	24.47	20.39	14.27	11.88	12.23
TEM: Maximum	134.57	114.18	83.60	67.29	67.29	53.01	38.87	36.70
Std. Dev. (nm)	19.34	15.73	12.07	10.23	11.86	6.73	4.58	4.41

G. N_2 Isotherms

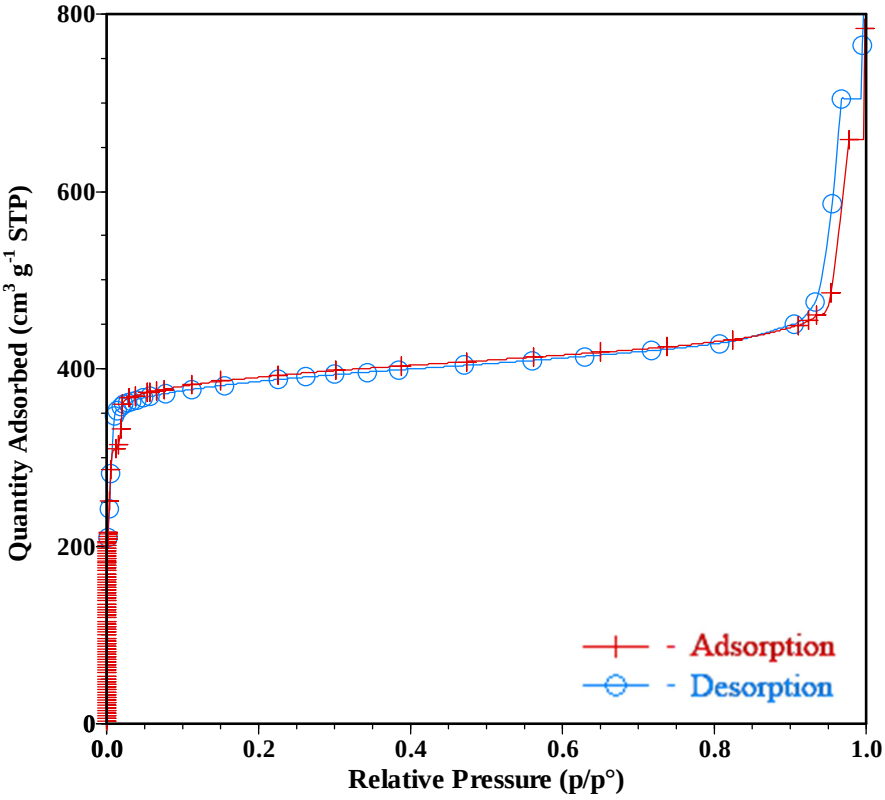

Figure G.1 Adsorption and desorption N_2 isotherm at 77 K of nZIF-8 synthesized at -15 °C.

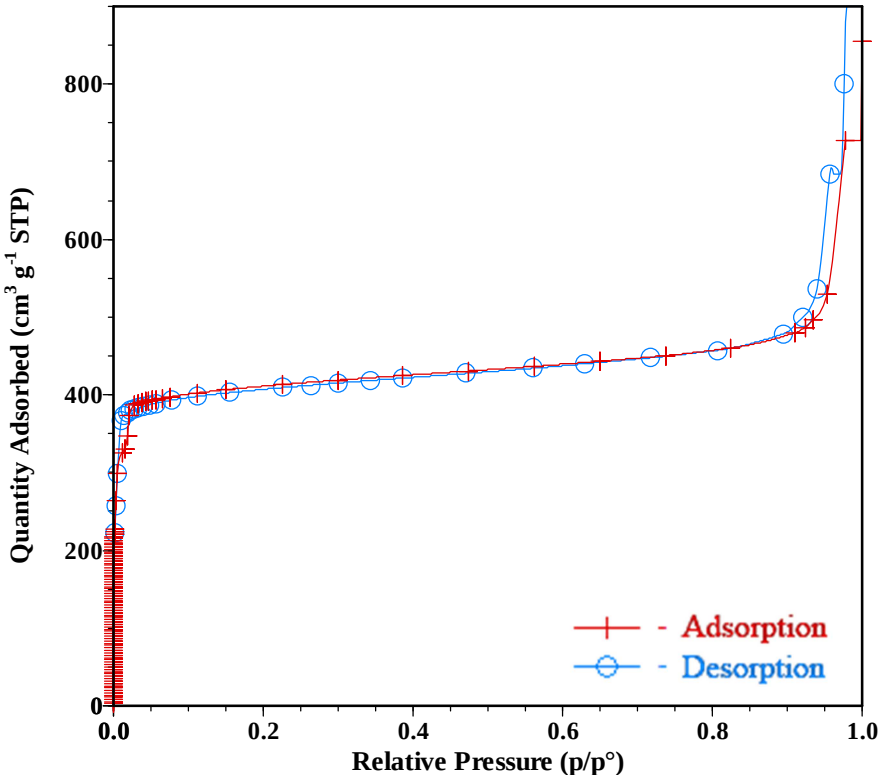

Figure G.2 Adsorption and desorption N_2 isotherm at 77 K of nZIF-8 synthesized at -5 °C.

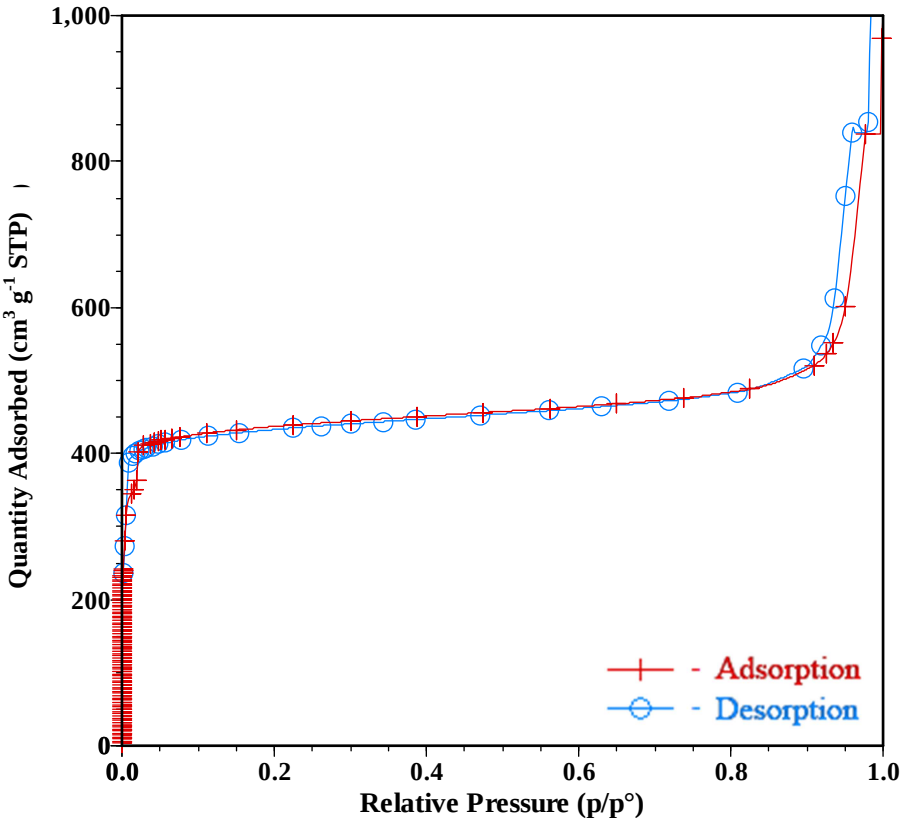

Figure G.3 Adsorption and desorption N_2 isotherm at 77 K of nZIF-8 synthesized at 2 °C.

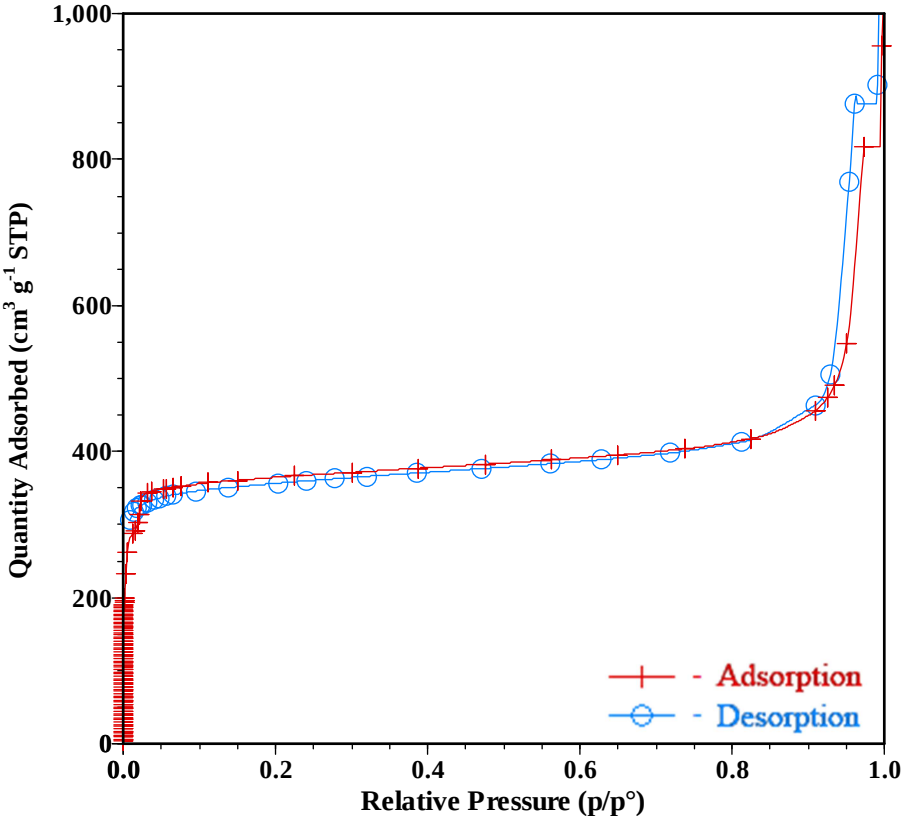

Figure G.4 Adsorption and desorption N_2 isotherm at 77 K of nZIF-8 synthesized at 25 °C.

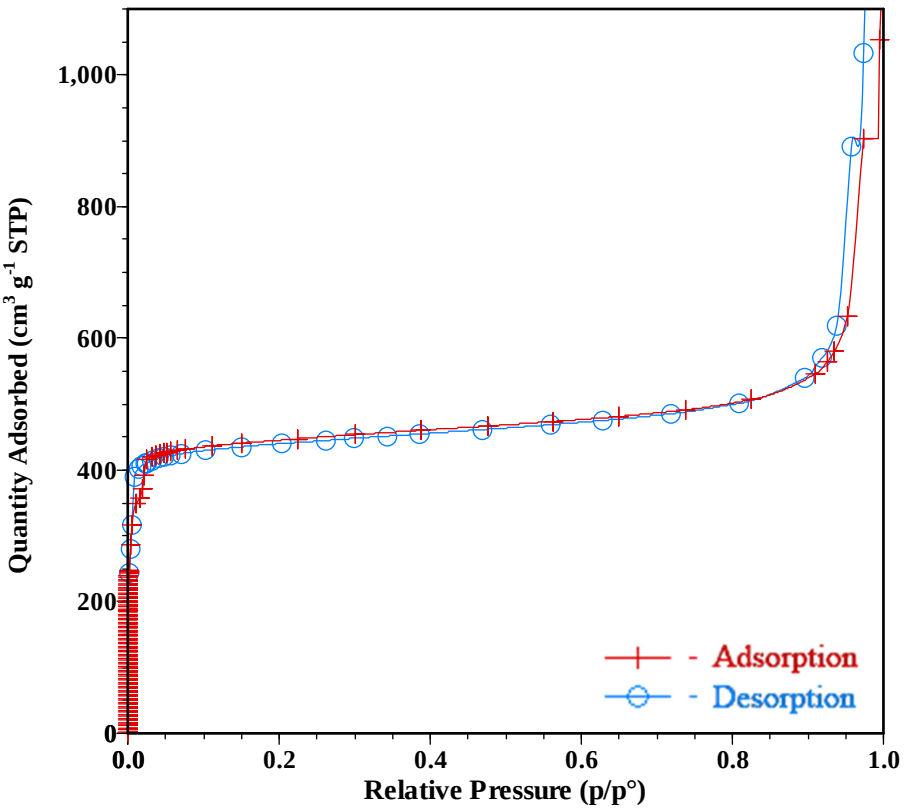

Figure G.5 Adsorption and desorption N_2 isotherm at 77 K of nZIF-8 synthesized at 30 °C.

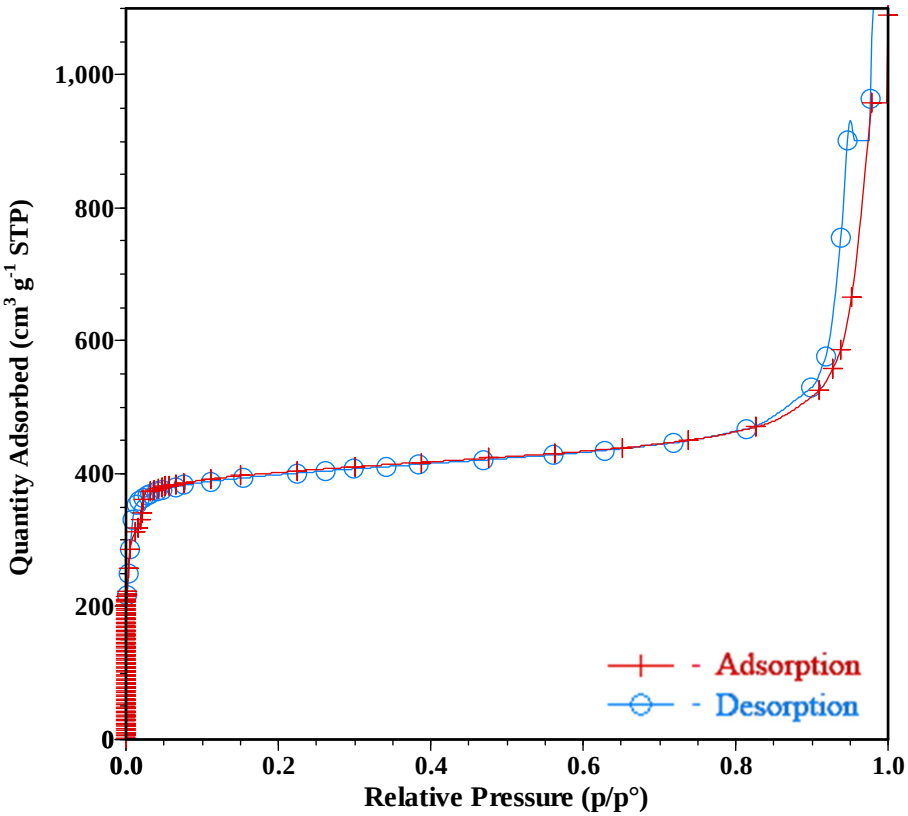

Figure G.6 Adsorption and desorption N_2 isotherm at 77 K of nZIF-8 synthesized at 40 °C.

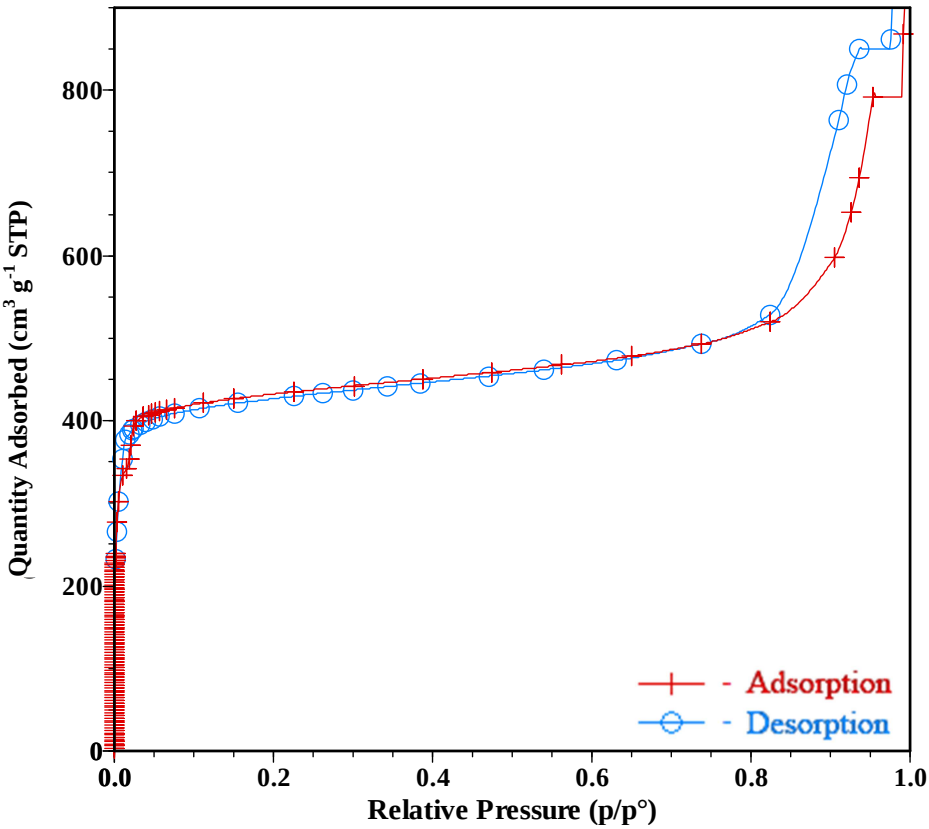

Figure G.7 Adsorption and desorption N_2 isotherm at 77 K of nZIF-8 synthesized at 50 °C.

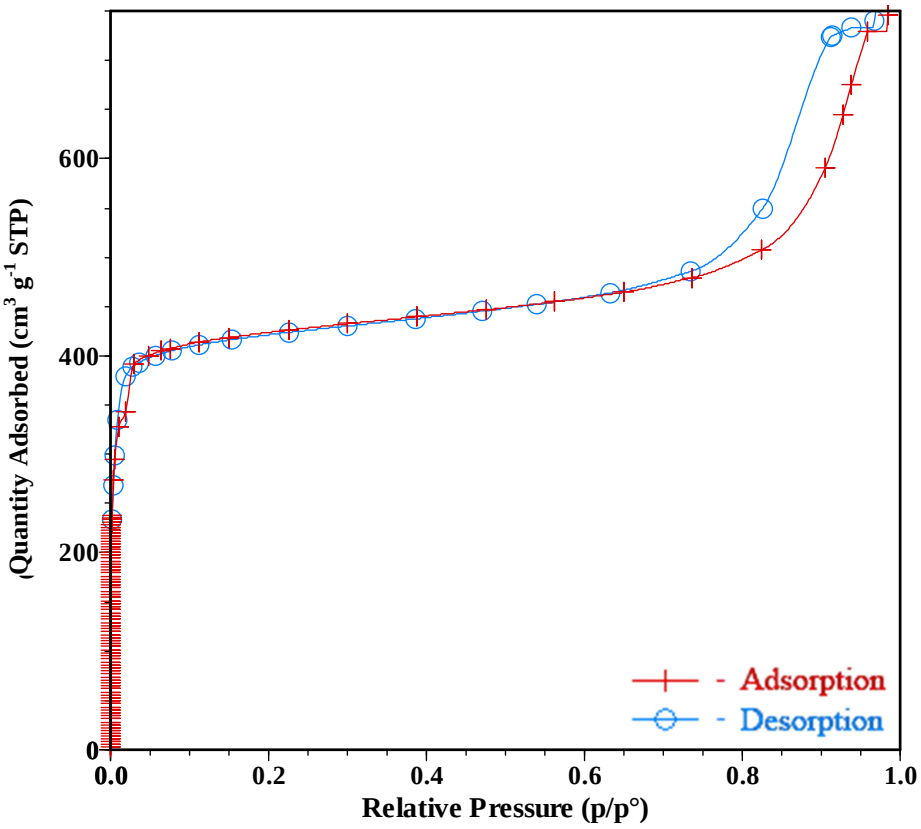

Figure G.8 Adsorption and desorption N_2 isotherm at 77 K of nZIF-8 synthesized at 60 °C.

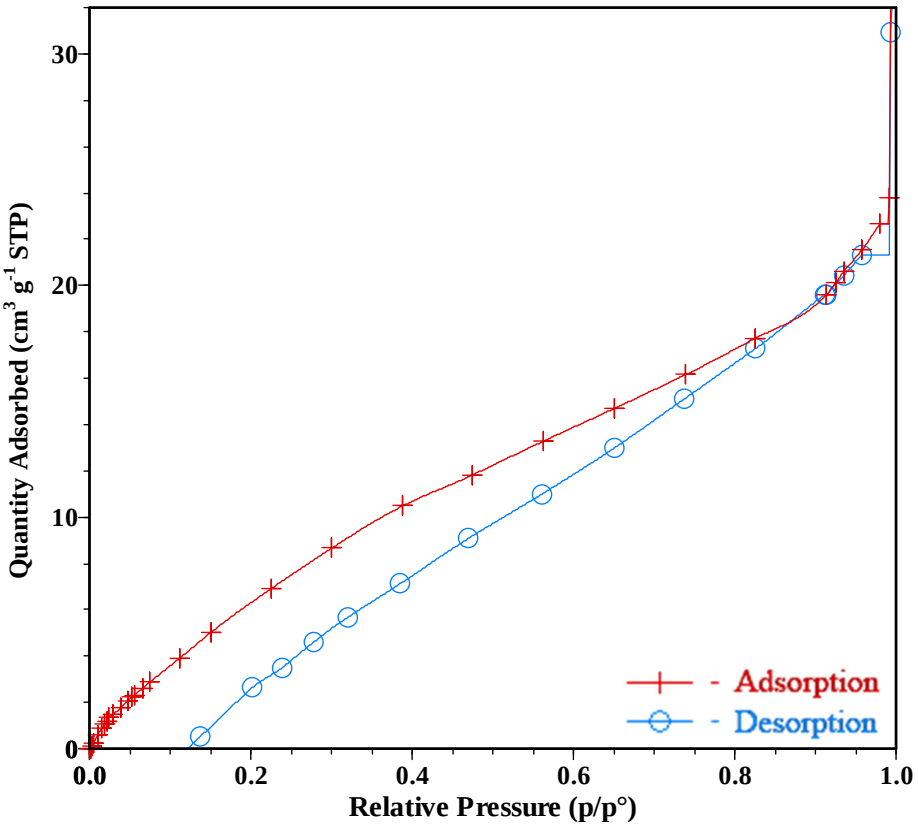

Figure G.9 Adsorption and desorption N_2 isotherm at 77 K of ZIF-ZNI.

Abstract

Zeolitic Imidazole Framework-8 nanoparticles, a subclass of Metal Organic Frameworks, were successfully synthesized with particle size control by temperature, using isothermal benchtop reactions in methanol. As the synthesis temperature was increased from -15 ℃ to 60 ℃, the average nanoparticle sizes decreased from 78 nm to 26 nm, with a simultaneous narrowing of the particle size distribution. Porosity analysis showed that the external surface area of the nanoparticles increases from 254 $m^2 g^{-1}$ till 336 $m^2 g^{-1}$, as the particle size decreases from 78 nm till 26 nm. This increased external surface area led to a significant increase in the catalytic activity of the ZIF-8 nanoparticles in a Knoevenagel condensation test reaction.

nZIF-8 was impregnated with silver and palladium salts, $AgNO_3$ and $Pd(acac)_2$, which after reduction with $NaBH_4$ gave Ag@nZIF-8 and Pd@nZIF-8 respectively. In Ag@nZIF-8 the reduced silver metal nanoparticles (3.8 wt %) are situated on the external surface of nZIF-8, while in Pd@nZIF-8, the ~1 nm palladium metal cluster (3.1 wt %) were well dispersed throughout the porous structure of nZIF-8. While Ag_{high}@nZIF-8 showed a decrease in BET surface area, Pd@nZIF-8 showed an increase in BET surface area, with respect to the nZIF-8 starting material.

nZIF-8 subjected to time resolved solvent assisted ligand exchange (SALE) with imidazole, gave a maximum conversion of 90 % after 72 hours. The ratio of 2-methylimidazole and imidazole linkers within the SALEM-2 products was determined by digestive ^1H NMR for each timed exchange reaction. PXRD studies showed that the SOD topology of nZIF-8 starting material is retained till 24 h (or 58 %) of exchange, after which the structure begins to transform from SOD to ZNI topology. With the change to the non-porous ZNI topology, the porosity of the SALEM-2 compounds decreased. During post synthetic modification by lithiation of the C2 postion of the imidazole linkers a butyl chain was attached to SALEM-2 with a 0.6 % loading

.

Keywords: ZIF-8, nanoparticles, particle size control, external surface area, metal impregnation, solvent assisted ligand exchange, post synthetic modification, heterogeneous catalysis, Knoevenagel condensation.

Opsomming

Nanodeeltjies van Zeolitiese Imidasool Netwerk-8 (ZIF-8), 'n bekende Metaal Organiese Netwerk (MOF), waarvan die deeltjiegrootte met sintesetemperatuur gereguleer is, is suksesvol tydens isotermiese mengreaksies in metanol gesintetiseer. Soos die sintesetemperatuur van -15 ℃ na 60 ℃ verhoog is, het die gemiddelde grootte van die nanodeeltjies afgeneem van 78 nm na 26 nm, met 'n gelyktydige vernouing van die deeltjiegrootte verspreiding. Porositeitsanalises het getoon dat die eksterne oppervlakarea van die nanodeeltjies van 254 $m^2\ g^{-1}$ na 336 $m^2\ g^{-1}$ vergroot soos die deeltjiegrootte afneem van 78 nm na 26 nm. Dié vergrote eksterne oppervlakarea het gelei tot 'n beduidende toename in die katalitiese aktiwiteit van die ZIF-8 nanodeeltjies (nZIF-8) tydens 'n Knoevenagel kondensasie toetsreaksie.

nZIF-8, geïmpregneer met silwer- en palladiumsoute, $AgNO_3$ and $Pd(acac)_2$, het, na reduksie met $NaBH_4$, Ag@nZIF-8 en Pd@nZIF-8 onderskeidelik gegee. In Ag_{high}@nZIF-8 word die gereduseerde silwermetaal nanodeeltjies (3.8 massa %) op die buite-oppervlak van nZIF-8 gevind, terwyl die ~1 nm palladium metaalklontjies (3.1 massa %) in Pd@nZIF-8 goed regdeur die poreuse struktuur van nZIF-8 versprei is. Met Ag_{high}@nZIF-8 is 'n afname, en met Pd@nZIF-8 'n toename van BET oppervlakarea, met betrekking tot die nZIF-8 uitgangstof, gemeet.

nZIF-8 het 'n maksimum omskakeling van 90 % na 72 h bereik tydens 'n tydsveranderlike, oplosmiddelgesteunde liganduitruiling (SALE) met imidasool in metanol. Die relatiewe hoeveelhede van 2-metielimidasool- en imidasoolskakels in die SALEM-2 produkte is, na suurvertering, met ^1H KMR vir elke tydgemete uitruilingsreaksie bepaal. PXRD studies het getoon dat die SOD topologie van die nZIF-8 uitgangstof behoue bly tot met 'n 24 h (of 58 %) uitruiling, waarna die struktuur begin oorgaan van SOD na ZNI topologie. Met die oorgang na die nie-poreuse ZNI topologie, het die porositeit van die SALEM-2 verbindings dramaties afgeneem. Tydens na-sintese aanpassing deur litiëring van die C2 posisie van die imidasool skakel, is butielkettings met 'n 0.6 % sukseskoers aan SALEM-2 geheg.

Sleutelwoorde: ZIF-8, nanodeeltjies, isotermiese sintese, eksterne oppervlakarea, metaalimpregnering, oplosmiddelgesteunde liganduitruiling, na-sintese aanpassing, katalitiese aktiwiteit, Knoevenagel kondensasie.

Declaration

I, Chih-Wei Tsai, declare that the dissertation/thesis hereby handed in for the qualification Magister Scientiae in Chemistry at the University of the Free State is my own independent work and that I have not previously submitted the same work for a qualification at/in another university/faculty. I furthermore cede copyright of the thesis in favour of the University of the Free State.

Signed

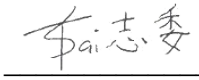

Date

4 June 2014